NanoImprint Lithography: Developments and nanodevice fabrication

Irene Fernández Cuesta

PhD Thesis

March, 2009

Departament de Física

Centro Nacional de Microelectrónica IMB

CSIC

NanoImprint Lithography:
Developments and nanodevice fabrication

Memoria presentada para optar al título de:

Doctor en Física

Por:

Irene Fernández Cuesta

Directores:

Xavier Borrisé Nogué

Francesc Pérez Murano

Tutor:
Jordi Pascual Gainza

Marzo 2009

La presente tesis doctoral titulada: “*NanoImprint Lithography: developments and nanodevice fabrication*” ha sido realizada por Irene Fernández Cuesta como Trabajo de Investigación dentro del programa de Tercer Ciclo de Ciencia de Materiales (Física) bajo la dirección del Dr. Xavier Borrisé Nogué y del Dr. Francesc Pérez Murano, en el Centro Nacional de Microelectrónica - Instituto de Microelectrónica de Barcelona (IMB-CNM, CSIC) y bajo la tutela de Dr. Jordi Pascual Gainza (departamento de Física de la Universidad Autónoma de Barcelona).

Bellaterra, Febrero de 2009.

Los directores:		El tutor:
Xavier Borrisé	Francesc Pérez	Jordi Pascual

Acknowledgements

This thesis work wouldn't have been possible without the help and support of many people that have directly or indirectly collaborated, with its development. I would like to dedicate these few lines to acknowledge their support.

Mi primer y más sincero agradecimiento es para mis directores de tesis, Francesc y Xevi, por haberme dado esta oportunidad. Profesionalmente, gracias por los consejos, las ideas y las soluciones a los problemas que he ido encontrando. Y personalmente, gracias por la ayuda, por el apoyo continuo, por vuestra paciencia (especialmente en estos últimos meses), y porque aún siendo lo negativa que soy, me habéis animado siempre.

Quiero dar las gracias también a todo el personal del CNM, en especial al equipo de Sala Blanca, por su profesionalidad y disposición. Especialmente a Liber y Marta, que han sido a las que más guerra he dado, y que siempre me han recibido con una sonrisa (y con los procesos hechos poco después).

During these years, I also had the opportunity of working and living in Denmark. I would like acknowledge Anders Kristensen, for trusting and hosting me at MIC. And, together with him, all the people in the Optofluidics group, and especially Sasha and Rasmus, that introduced me in the plasmonics world. I would like to thank also Jan and Jordi, for the beers (not only in the Friday bar), for all the trainings in the cleanroom, and the company during those dark but not cold months.

También quiero dar las gracias a los investigadores que han ayudado y hecho posible la obtención de muchos de los resultados aquí presentados. A Niek van Hulst y Dominique Heinis por las medidas de SNOM en el ICFO, y a Sergei Bozhevolnyi por las de Aalborg. A David Mendels, por las simulaciones del proceso de impresión. A Alfredo de la Escosura y Arben Mercoçi, por las nanopartículas de oro y las ideas para funcionalizarlas. A Alessandra Bonanni y Manel del Valle, por la colaboración para inmovilizar ADN y la interpretación de los resultados obtenidos después de hibridizar. Y a Santos Merino y Aritz Retolaza por los RIEs para hacer los moldes, las impresiones para las medidas del frozen-in stress, etc.

Otra gran parte de la tesis se la debo a la ayuda de César Fernández y Toni Baldi, que me descubrieron un mundo nuevo, extraño y desconocido para mí: *la química*. Gracias por enseñarme lo interesante que puede ser la electroquímica e introducirme en el mundo de los sensores. Gracias por la ayuda con las medidas y con la interpretación de los resultados, y porque siempre que he ido con el "*pasa una cosa rara*" habéis tenido una solución.

An important part of these years went by around one thing: the NaPa project. As Marc said, it was a "one-of-a-kind" experience. Here, I had the opportunity to learn about all the different aspects of nanotechnology in the meetings, during the coffees, and in the summer school. I also made jealous most of my friends because of the trips. But, what I think was more interesting was the people I met: Helmut, that saw me "growing up", since I couldn't speak English and could not distinguish the stamp from the imprint, until now....and also Vincent and Niko, with whom I had drinks and discussions about NIL and e-beam in whatever place....And a special thanks to Paul, for co-chairing the bar sessions :)

Además del trabajo en el laboratorio, durante la tesis, uno pasa mucho tiempo delante del ordenador y en el despacho (especialmente a la hora de escribirla). Gracias a toda la gente que ha hecho del sitio de trabajo un lugar agradable: Marc Sansa, Marc Serra, Giordano, Nerea, Marta, Jesús, Jahir, Julien, etc.
Gracias también a Juan Pablo E, Juan Pablo B, Diana, Picón, Íñigo G, Jordi....A Jorge, por dejarme el día 27, por ser Friki, y por enseñarme que yo también lo soy, más de lo que parezco :P. A Albert, por las clases magistrales sobre impedancias, los consejos, y porque poco a poco voy aprendiendo que primero es lo importante, y después lo urgente. A Amelia, porque siempre está ahí...por el apoyo, por

saber escuchar, por los fines de semana, por las fiestas.... A Íñigo, por tener taaanta paciencia conmigo, por aguantarme las pataletas, por la ayuda con el word, por aguantarme las pataletas, por escucharme las charlas (del CNM y las de no del CNM), por los congresos y por aguantarme las pataletas (lo he dicho ya?). Tú sí que vales mucho :) Gracias a todos por ser como sois, y porque igual se puede hablar de la radiación Cherenkov que de cómo tratar adiabáticamente un ordenador para que haga un pdf, del hombre ovejo, sobre la extinción de los dinosaurios por culpa de las flores, del funcionamiento de un pato termodinámico, etc.

Quiero dar las gracias a Roger, por presentarme a la Colla, y a la Colla, por integrarme desde el primer momento. Gracias Neus, Roger, Cris, Gemma, Dave, Gemmeta, Toni, Jessi, Pau, Toni, Nuria, Ginés, Alberto, Roberto y Eduard, por tantos buenos momentos, por los 3 Vilas, las casas rurales, los partidos de la Champions, Croacia, Servi, las bodas, las bacanales, etc. Y gracias Roger también por presentarme a tu familia, jajajajaja. Gracias Ferran por saber escuchar, y por tener la habilidad de hacer que de cualquier problema se pueda sacar algo positivo :)

No quiero olvidarme de los que ya no andan por Barcelona, pero con los que he pasado muuucho tiempo :) Gracias a Asun, por los vinitos, y por "no ser normal" y no querer estar todo el día en casa. A Mariajo, por tantos días de "ponernos al día"...y por las visitas que ya nos hemos hecho, y las que nos haremos. Y a Javi, por haberme aguantado tantas veces....por los buenos momentos y por los malos. Y por habernos engañado tantos días entre semana, y por convertir una en un montón :)

Quiero agradecer también a mis compañeros de piso la compañía durante estos años. Gracias a Mark por no entender a las mujeres, a Dani, for being noiseless, y a Carlos, por haberme enseñado a apreciar una de las cosas más sencillas de la vida: el silencio. Gracias por haber sido mi "pareja de hecho" durante tanto tiempo.

Y gracias también al *núcleo duro*....Javi, Rafa y Sergio....Por el piano (el de Javi, y con el que se pilla Rafa), por las cenas (las de fiesta en casa de Sergio, las de antes de las fiestas, y en las que no hay fiesta y nos confesamos), por los fines de semana en los que nunca falta plan, por las pelis (las de leer de los Verdi, las de Kurosawa de casa de Rafa y las de terror nuestras), por las partidas de Monopoly y de parchís, por las conversaciones radicales, sobre sexo, y sobre el sexo de los radicales, por los conflictos entre hardware y software, por ser de abogados del diablo cuando hace falta, por los consejos buenos y los *atropellaaarpon*, por los Bonis que nunca llegaron y por los que con tanto esfuerzo hemos trabajado (y tanto hubiéramos merecido muchas veces), por los viajecillos a Pals, Menorca, Oporto, Berlín, y por Calderón de la Barca....

Aunque en la distancia, también he tenido el apoyo de Silvia, Inés, Lucy, Susana e Inma. Gracias por seguir ahí....por las visitas y por tantas y tantas horas de teléfono, para contarnos algo *superimportante*, o para contarnos *pues yo poco tengo que contarte*. Espero seguir contando con vosotras, y nos vemos en Dinamarca :D

Gracias también a mi familia. En especial, a mis padres por su cariño, porque me han apoyado y ayudado con todas las decisiones que he tomado, y siempre han confiado en mí....y por hacerme ver que, aunque a veces parezca que no, los esfuerzos tienen su recompensa. Y a mi hermano, que, a su manera, sé que también me tiene algo de cariño :D y al que animo a seguir con la decisión que ha tomado.

Y gracias al otro Sergio.... a la parte que he descubierto hace poco. En estos meses, has evitado muchas veces que siguiera escarbando (como dicen en Italia). Y, sobre todo, gracias por darme la razón: sabía que merecías la pena.

...Si fuéramos robots, sería todo mucho más aburrido.

Contents

SECTION 1: CONTRIBUTIONS TO NIL TECHNOLOGY DEVELOPMENT

SECTION 2: PLASMON CONFINEMENT IN V-GROOVES FABRICATED BY NIL

SECTION 3: INTERDIGITATED NANOELECTRODES FOR (BIO)SENSING

Motivation

In 1959, Richard Feynman envisioned the new possibilities arising from miniaturization and down-scaling of devices in his very famous talk "*There is plenty of room at the bottom*"[1] . Since then, Nanotechnology has become a hot-topic not only in research labs, but also for industry. The study of matter when the typical dimensions of the structures are reduced down to the nanoscale have academic interest, as it exhibits new properties, and, taking advantage of that, potential applications can be found in many different fields, such as physics, biology, chemistry, medicine, electronics, material science, pharmaceutical, environmental control, etc.

Nanotechnology presents several challenges. The study and characterization of features with very small dimensions needs to be tackled different from those with macroscale dimensions. Even further, nanotechnology also involves manipulation and control of the matter at the nanoscale. These leaded to the development of new tools the last decades, such as new microscopy and/or fabrication techniques.

Concerning the fabrication, there are mainly two approaches: bottom-up, and top-down. In the first, small "seeds" are used for the assisted growth or creation of the structures (e.g., growth of silicon nanowires using gold nanoparticles as catalysts, or creation of complex structures emulating natural motors starting from self-assembled molecules). The second approach consists on starting at the top of the blank piece and work the way down removing or depositing material from where it is not required.

Top-down Nanofabrication

Figure 1 shows a scheme of a conventional fabrication process, based on silicon technologies. Two parts can be distinguised: the **lithography**, where the features are defined in a resist (or other material) deposited onto *the substrate* where the features need to be defined, and that will used as a mask for the second part: the **post-process**. This depends on the objective of the sample, and can range from an etching to define structures in 3 dimensions, a metallization, to define metallic structures, or local modification (e.g. ion implantation) for CMOS fabrication.

The processes used for fabrication of devices in the nanoscale based on the top-down technologies needs to be adapted and often completely changed from those used for microfabrication.

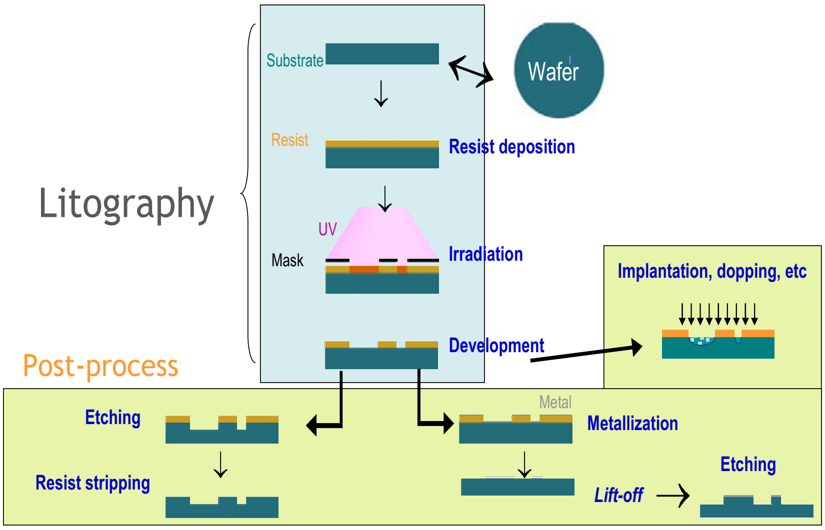

Figure 1. Top-down fabrication approach, consisting on a lithography step and post-process.

In general microfabrication, optical lithography is used to define a resist mask onto the substrate (silicon wafer), where the features are defined by local exposure to UV-light, using a mask. Several post-processes are possible, attending to the final purpose of the sample: metallization, etching, ion implantation, etc.

---

[1] "*There is plenty of room at the bottom*", talk given by the physicist Richard Feynman in an American Physical Society meeting at Caltech on December 29, 1959

Defects related to border effects, lateral underetching, light diffraction, etc that have typical sizes of nanometers, do not have relevance in the micrometric fabrication. But, when the dimensions of the structures are shrunk down, they become important. Figure 2 shows examples of defects encountered when using conventional recipes and processes to fabricate structures with few microns of lateral size and below. In general, the metallization and etching processes can be conveniently optimized to obtain structures with nanometric dimensions. But, as far as lithography is concerned, optical lithography cannot be used, as the wavelength of the light sources are larger than the dimensions of the structures.

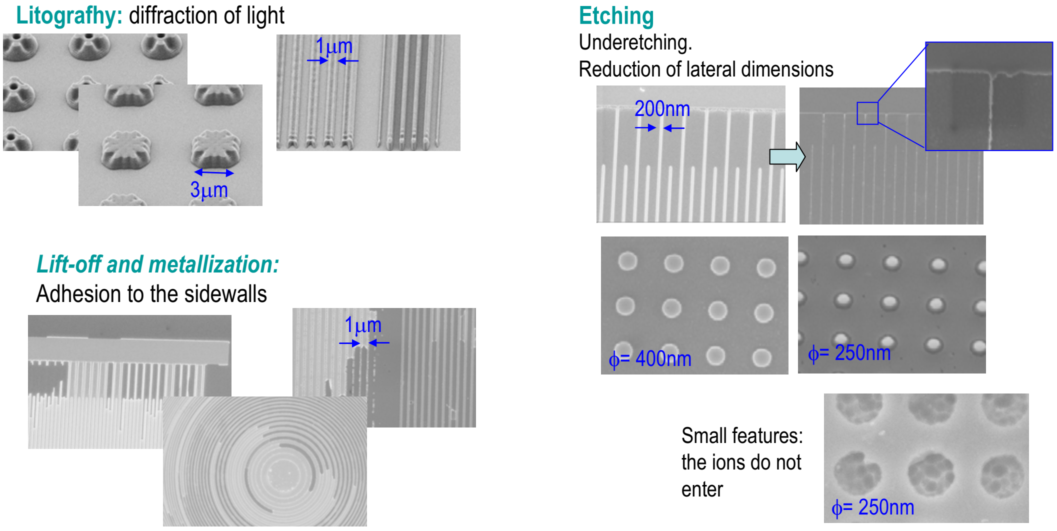

Figure 2. SEM images of defectuous structures obtained when using conventional microfabrication techniques to define patterns with lateral dimensions in the sub-micrometric range. The use of light for optical lithography leads to diffraction-related defects; the adhesion of the metal to the sidewalls of dense arrays difficults the lift-off process, and the lateral underetching, that is in the order of tens of nanometers, may lead to the collapse of the structures, to a non-desired reduction in the dimensions, or inhibit the penetration of the ions.

Nanolithography

There are now-a-days several lithographic techniques that allow overcoming the diffraction limit of light, and allow the definition of features in the nanometric scale.

Figure **3** shows a scheme of the different techniques that are most commonly used, where the minimum resolution achievable is plotted as a function of the areal throughput. Thus, depending on the application and the requirements of the pattern, a trade-off between cost, efficiency and resolution can be achieved.

One of the most extended techniques is electron beam lithography (EBL), that is commonly used to pattern nanometric features in several types of resists. Never the less, it is rather slow. For this reason, nanoimprint lithography (NIL) is emerging as an alternative, as the resolution is also very high, and, as it is a parallel method, it allows fabrication with high throughput.

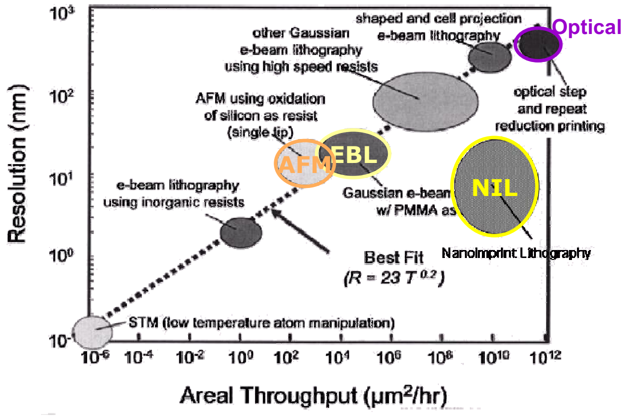

Figure 3. Scheme of the different nanolithography methods. The resolution achievable is plotted as a function of the throughput. The techniques used along this thesis work have been overlighted.

C. R. K. Marrian and D. M. Tennant: *Nanofabrication*, J. Vac. Sci. Technol. A, Vol. 21, No. 5, 2003

Summary

This thesis is devoted to nanoimprint lithography (NIL), from **process study** and optimization, to its application for the **fabrication of different types of nanodevices** in the area of micro and nano systems engineering. The work was started right after the arrival of the first NIL equipment to the cleanroom of CNM. Along these years, the international activity within NIL has evolved from being a promising technique, to be a well-know method, that allows robust nanofabrication. This evolution can be also observed in the development of the thesis work.

The memory is divided in **three sections,** each sub-divided in several chapters. Technology and *nanofabrication* (especially nanoimprint lithography, NIL, process study) are the topics of the first section. The fabrication of *plasmonic waveguides* devices and the optical characterization to proof their good performance are shown in the second one. The fabrication of sensors based on *interdigitated nanoelectrodes*, together with the electrochemical and impedimetric measurements and applications are detailed in the third section.

The **first section** is devoted to NIL technology. Different aspects of the technology have been studied and optimized, which, in many cases resulted in original works that have been published in international scientific journal of international and/or contributions to international conferences. The studied aspects of the NIL technology vary from the stamp fabrication and antisticking coating, to the optimization of the imprinting recipes for different geometries and the post-processing depending on the final application. Once the technology was settled, several different groups demanded nanoimprinted structures for different applications, what leaded to national and international collaborations. The section is divided in four chapters:

- In Chapter 1, the state of the art of nanoimprint is summarized. A picture of the different imprinting-based nanofabrication processes is given as well as a description of specific equipments and materials available in the market. An important part of the development of NIL within this thesis work was done thanks to the participation in a european project (NaPa), that actively advanced the state of the art of NIL in the European research community. Some of the main activities will be listed, to conclude the summary of the current status of NIL.
- Chapter 2 describes different approaches to fabricate stamps for NIL. Electron-beam lithography was the main technique used. On the other hand, AFM local anodic oxidation was originally applied for the fast fabrication of stamps. For this, the oxidation mechanism of very thin layers of Si_3N_4 was deeply studied A especial effort was done towards the fabrication of triangular-shaped lines, with very smooth sidewalls. Also, a novel method for the antisticking coating of the stamps at room temperature was developed and the functional properties of the obtained mono-layers characterized in several ways. This procedure was also used for local deposition of different types of silanes.
- Chapter 3 resumes the studies done in order to optimize the imprinting parameters especially regarding polymer rheology. Here, an especial attention was given to the cooling step: the residual stress in the polymeric structures was studied as a function of the cooling ratio and stamp-substrate separation temperature. For this, special stamps were fabricated, and AFM measurements were brought to their limit. The residual layer was measured, studied and compared in the micrometric and nanometric ranges for different equipments, within a benchmarking task in the NaPa project.

- To explore potential applications of NIL technology, in Chapter 4 collaborations arising from the possibility of using NIL to fabricate nanostructures with high throughput, and using various different substrates will be explained.

In **section two**, NIL is used to fabricate devices to be used in the optics and plasmonics field. Novel waveguiding devices, based on plasmon confinement in V-grooves will be introduced: from the NIL-based fabrication of the samples to the optical characterizations performed to show plasmon confinement and propagation. This section is divided in three chapters:

- In Chapter 5, the basic notions about plasmons, surface plasmons and confined plasmons (chanel plasmons) will be detailed
- In Chapter 6, different strategies followed to fabricate V-groove based plasmonic waveguides will be described. Nanoimprint was the preferred tool to structure the polymeric substrates, that were later covered with a gold layer, where the plasmons would be excited.
- In Chapter 7, the optical characterization will be shown. Near optical field microscopy shows effectively that the imprinted V-grooves support channel-plasmon-polariton propagation. Far field images allow to qualitatively study the modal shape for different excitation conditions. To conclude the section, the results of introducing fluorescent nanoparticles inside the channels will be shown. This allows studying the propagation mechanism just by using a conventional optical microscope.

The **third section** is devoted to the fabrication and characterization of interdigitated arrays of nanoelectrodes (IDEs). In this part of the work, the NIL-based fabrication was developed in parallel to the characterization of the devices. This section is also divided in three chapters:

- In Chapter 8 different process flows to fabricate the IDEs are described. The most efficient technique was a combination of electron beam and optical lithography. Devices with large active areas were fabricated as well using a new equipment that arrived at CNM by the end of this thesis. In parallel, the nanoimprint-based fabrication was studied and optimized to reduce the number of defects in the structures. Independently on the fabrication technique, a passivation, wire bonding and encapsulation process was finally developed and used, in order to have the devices ready-to-use, even in liquid media.
- In Chapter 9, the performance of the devices as electrochemical sensors will be described. Different substances were used, as well as different methods, which allowed to calibrate the sensors, and to study the minimum detection limit, and the sensitivity. It was also observed that the electrodes having a small width and large gap showed an ultra-micro-electrode behaviour.
- In Chapter 10, impedimetric spectroscopy measurements will be shown. An electric model is proposed, and standard characterizations performed, in order to check its validity: the response to solutions with different conductivities and different permittivity validates the model. Finally, two original applications are described: the detection (and quantification) of nanoparticles of different natures (conductive and insulating), and the detection of specific DNA hybridization.

The initial objectives of the thesis were the development of nanoimprint lithography at CNM and its applications in the area of micro/nano systems technology. These objectives were fulfilled. During the thesis work, significative advances were achieved. In addition, it leaves several research lines open. The availability of new fabrication processes and the demonstration of the improved properties of the (nano) devices compared to the previously existing (micro) devices, open a broadband of possibilities (maybe in the biosensing world).

Section 1

Contributions to NIL technology development

"Give me 10% of the money that you've spent on next-generation lithography and we'll give you an imprint system that will do that job."

Steve Dwyer, vice president of EV Group

Schärding, Austria, 2006

The possibility of replication of the nanostructures of a hard stamp into a polymer was first proposed by S. Chou et. al. in 1995 [1]. Since then, Nanoimprint Lithography (NIL) has evolved from being a promising alternative method for nanofabrication [2, 3], to be, nowadays, a mature technique that allows obtaining nanometer scale features at wafer scale, with high reproducibility and throughput [4]. The applications taking advantage of NIL fabricated structures range from micro/nano electronics, material sciences, or biology, just to cite some examples.

Nanoimprint Lithography

Since the dawn of the human civilization, the possibility of replication the features previously patterned on a mold or a stamp in different materials has been widely exploded. Mint of coins may be one of the first examples, dating from thousands of years ago. The printing press or even waffle cooking are just some other examples of replication processes used in day by day life.

These methods have been somehow adapted for the fabrication also in the micro and nanoscale. Depending on the application, there are several different possibilities for replication, varying the material, the nature of the stamp, or the replication process itself.

Nanoimprint lithography has the main advantage, compared to other nanofabrication processes, that is a parallel process, that allows multiple device fabrication and processing in one single step, with high throughput, which is cost-effective, and maintaining the nanometric resolution of the features of the stamp. For all these reasons, in the last 10 years, it has been widely spread, both in research labs, and in industry, to take advantage of the new possibilities that it offers.

As there are several variants of the process, the fields where NIL applies are not restricted to micro-nano/electronics or CMOS technology, but also, material sciences, biology or medicine take advantage of nanoimprint lithography.

In this section, the different processes most commonly used and the equipments and materials especially developed for NIL will be gathered in the state-of-the art (Chapter 1). Then, the original contributions developed during this work will be described: stamps fabrication (Chapter 2), rheology studies (Chapter 3) and examples of applications (Chapter 4).

Minting Press, year 1913.
Coin (Asia Minor), year 660 BC.

Guthemberg's printing press, year 1450.
Letters to conform the stamp.

Sealing wax, 16th century

Rubber stamp, and imprint. 20th century

Waffle cooking

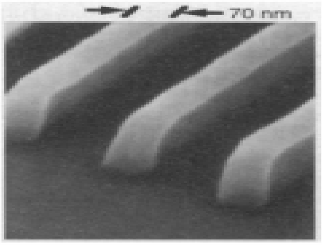

Nanoimprinted lines, year 2006

Index of Section 1

Contributions to NIL technology development

Chapter 1

NanoImprint Lithography: Introduction and state of the art

Nowadays, there is a huge variety of nanoimprint processes, materials, equipments and special tools, that, together with the theoretical studies and modellizations, are contributing to the development of NIL and to its consolidation as a standard nanofabrication process.

In this chapter, the main processes of replication of structures from a stamp into a substrate will be explained. We will next focus the attention in thermal NIL, that is the technology that was used and developed along this thesis work. The different materials that can be used, the equipments that are commercially available and the special characteristics of each one will be commented. Some hot applications will be cited as well, to show the potential of this nanofabrication technique.

1.1.- METHODS

The creation of structures by nanoimprint is based on mechanical deformation of a patterning media, that can be a polymer, a resin, silicon or even a metal. This is radically different from other methods (electron-beam lithography and optical lithography), which rely on chemical modifications of the material. The first imprinting method was based on heating a polymer up to a low viscous state, but soon other methods aroused, each having specific advantages for specific applications. However, all of them share common characteristics: they use a 3-dimensional stamp and pressure (high or low) to create the structures.

1.1-1. Thermal NIL

The first nanoimprint lithography (NIL) process reported by Chou et al. [5] was done by applying heat and pressure to a thermoplastic material. In general terms, this **thermal NIL** process consists on embossing a deformable polymer above its *glass transition temperature* (T_g) with a hard stamp, cooling-down the system and releasing the pressure when the polymer is solid again. Figure 4 shows the different steps:

a. A hard (silicon) stamp with the features to be replicated is fabricated.

b. A thermoplastic polymer is coated onto a substrate.

c. The stamp and the substrate are brought into contact. The system is heated up to the "**imprinting temperature**" (**T_i**), which is above the T_g of the polymer. Thermoplastic materials can flow when heated above their T_g, as they enter the viscous regime.

d. By applying pressure ("**imprinting pressure", P_i**), the resist is displaced by squeeze flow, until it conforms to the surface relief of the stamp. The temperature and pressure are kept at constant values during the so called "**imprinting time"** (**t_i**).

e. The pressure is maintained during the cooling down, until the temperature is below T_g, so the polymer is solid again. The temperature at which the mold is released is called "**demolding temperature**" (T_D).

f. When the stamp is separated from the sample, the polymer maintains the shape of the features of the stamp.

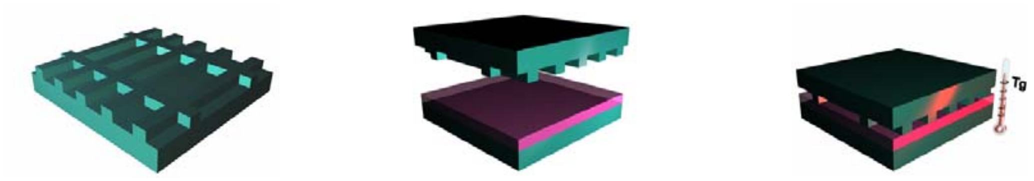

(a) Hard stamp

(b) Substrate, with a thermoplastic polymer

(c) Heat (above T_g)

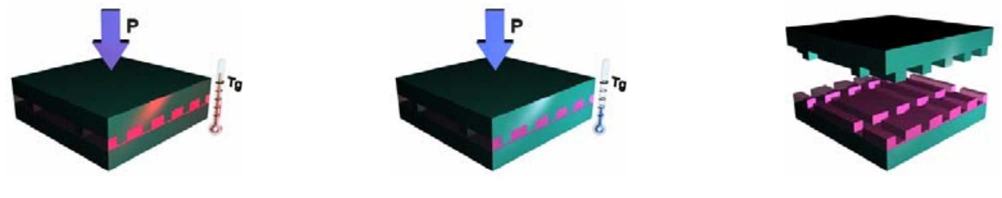

(d) Pressure

(e) Cooling down

(f) Demolding

Figure 4. Scheme of the NIL process and its different steps. Starts with a hard stamp (a), and a substrate, where a thermoplastic polymer has been spin-coated (b). The system is heated up above the T_g of the polymer (c), and, by applying a pressure (d), the material is forced to flow. The system is cooled down (e), and when the temperature is below T_g, the mold is released, so the polymer has been structured (f).

1.1-2. UV-NIL

Later in 1996, Haisma et al. [6] reported on the possibility of performing replications by UV-curing of a pre-polymer, spun onto a hard substrate and molded with a transparent stamp. The steps of this process, called **UV-NIL**, are shown in Figure 5.

a. A *transparent* stamp is approached to the substrate, which is coated with the liquid photocurable pre-polymer or a very low molecular weight resist.
b. A soft pressure is applied to fill the cavities with the liquid. Then, the system is exposed to UV light, so the polymer is cured.
c. After releasing the stamp, the features are replicated in the polymer onto the substrate.

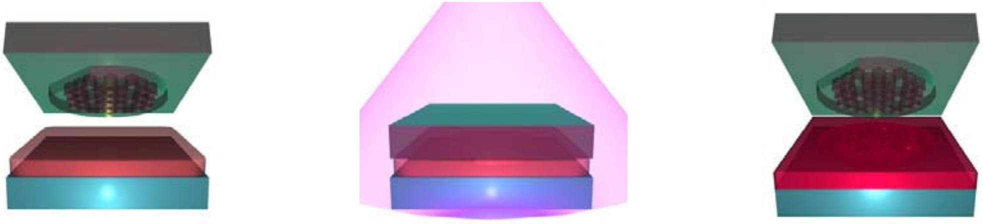

(a) (b) (c)

Figure 5. Scheme of the UV-NIL process. A transparent stamp (a) is pressed against a photocurable resist. After UV-curing (b), the features are transferred to the polymer (c).

One of the requirements of this process is that the stamp (or the substrate) has to be transparent to UV light. Thus, the stamps are commonly made of SiO_2, which makes its fabrication process trickier than the standard silicon-based fabrication. As an alternative to silica stamps, replication of stamps in photocurable hybrid polymers [7-9], can be considered.

1.1-3. Micro Contact Printing

Another imprinting-based method for pattern replication consists on using a flexible stamp, and do an inking-and-stamping process [10]. This method is commonly used to pattern a substrate with *proteins* or other *biological material*. Even further, by using the appropriate ink, applications in many other fields can be found [11, 12].

There are various approaches for soft patterning of bio-materials. In all of them, a flexible stamp is used (PDMS, generally), where the liquid ink is absorbed and afterwards stamped onto the substrate surface, just by applying soft (contact) pressure. Figure 6 shows the steps of the process, where the inking of the liquid material is done by pressing the stamp onto another substrate, coated with the ink. Figure 7 shows another approach, where the absorption of the material is done by dropping the liquid on the stamp and drying the solvent.

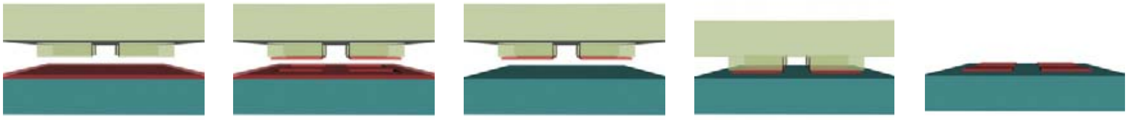

(a) (b) (c) (d) (e)

Figure 6. Scheme of the ink-stamp process. The process starts with a soft stamp and a substrate, spin-coated with the biological ink (a). The stamp is pressed against the substrate, so the protusions are inked with the material (b). The stamp is approached to another (clean) substrate (c), so, after contact (d), the features are patterned onto this new substrate (e)

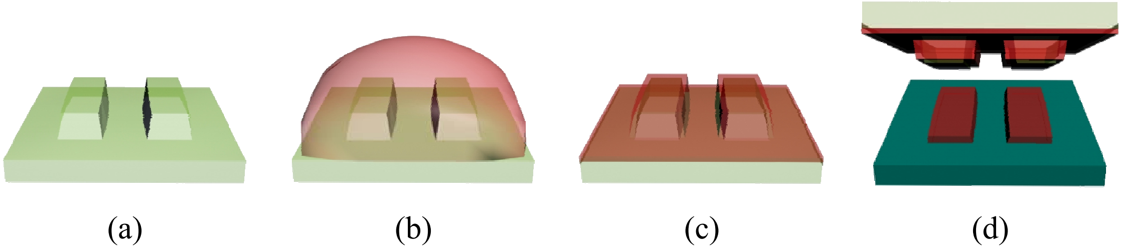

Figure 7. Scheme of the soft lithography process. A flexible stamp (a) is wetted with the ink (b). After drying the solvent, the biological material conforms the stamp surface (c). Then, with a soft contact, the features can be patterned onto a hard substrate (d).

In the soft lithography process, the stamping step is manually done (generally). This, along with defects due to the bending of the stamp, limit the resolution of the patterned structures to the micrometric range. Stamp production and design optimization [13] together with improvements in the printing conditions make possible to shrink the size of the patterns to the nanoscale [10].

1.1-4. Others

One of the signs that points to an increasing in the world wide activity in using nanoimprint lithography for nanofabrication is the huge number of process variants. Direct imprint of other materials (such as SiO_2, silicon [14] or metals [15, 16]), hybrid processes combinations (photolithography, thermal and UV [17, 18]) to combine different sizes, and even reversal imprint for 3D fabrication [19, 20] are some of the examples of different processes that can be found in the literature that show the versatility of imprinting-based fabrication.

During this thesis work, **thermal NIL** was **started up** at the working institute (**IMB-CNM**). Several different associated processes had to be developed, such as those related to stamp fabrication and antisticking coating (Chapter 2).The imprinting process itself had to be studied and understood for the used equipment, what leaded to rheological studies, necessary to optimize the imprinting recipes (Chapter 3). The participation in a EU Project allowed to collaborate with many other european groups, and to be involved in benchmarking tasks, developing studies towards standardization of nanoimprint lithography, as described also in Chapter 3. The optimizations were needed not only to study the process itself, but also for the complete fabrication of devices towards different kind of applications, as will be sumarizzed in Chapter 4.

1.2.- THERMAL NIL-BASED NANOFABRICATION

Nanoimprint can be used either **to structure (functional) polymers** or as an **actual lithographic technique**, using the different height features as a mask for a post-processing.

Examples of the first case are the fabrication of photonic crystals [21], micro/nano fluidic channels [22] or plastic electronics [23, 24]. The possibility of fabrication of multilevel structures in the same imprinting step and the ability of imprinting onto pre-structured substrates makes this technique preferred for lab-on-a-chip fabrication [17, 25, 26].

In the second case, NIL is commonly used as an alternative to the time-consuming electron beam lithography (EBL). The first stamp with the desired nano/micro-metric features needs often to be fabricated by EBL. Afterwards, the features can be replicated many times with a simple parallel and fast NIL step. Prior to using the structures as a mask, a short O_2 plasma reactive ion etching is needed to remove the **residual layer** that remains in the buried areas. Figure 8 shows a typical NIL-based process, where the structures are used to define a metallic pattern by lift-off. The use of functionalized polymers as imprinting materials allows direct patterning of structures with functional properties [27], as will be described later on.

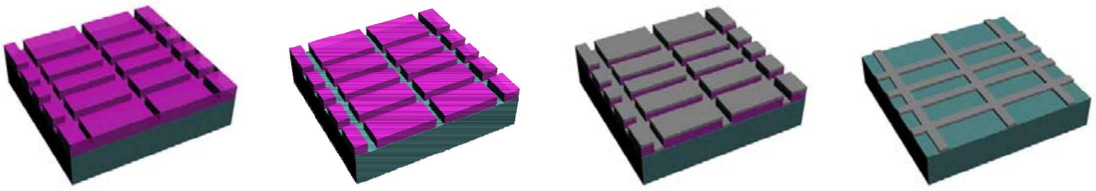

(a) Nanoimprint Lithography (b) Residual Layer etching (c) Metallization (d) Lift-off

Figure 8. Example of post process of a sample: defining the pattern in metal. After imprinting the features (a), the residual layer is removed with a short oxygen plasma (b). The metal is deposited (c), and, after lift-off, the metal pattern is fabricated onto the substrate (d).

In this thesis, both approaches were used for the fabrication of devices. Section 2 will describe an application based on *direct structuring of polymers* to fabricate plasmonic waveguides. Section 3 will describe an application where *the imprinted features are used as a mask* (substituting e-beam) to define metallic nanoelectrodes.

1.2-1. Resists

The increasing interest for NIL as a novel lithography technique entails an increase in the demand of the polymers and resists used as imprinting material. Their development and improvements are currently taking place both in research labs, and also in companies, that then commercialize the developed products for public supply.

Nowadays, there is a high number of polymers available, with different properties [28] devoted to several different NIL applications. There are resists that have especial **processing parameters** (tailored for the specific needs), **post-processing** special issues (such as high etching resistivity) or **functional properties** for different applications. Polymers with different T_g, high or low viscosity, ordered internal structures (cristallinity), low [29] or high [30, 31] surface energy and an increased or decreased etch resistivity are commercially available to obtain the most suitable processing and post processing conditions. The polymers can be also functionalized to obtain very interesting properties for a wide range of applications: conductive polymers (for flexible electronics or solar cells), polymers with selective affinities (for biosensing or specific recognition) [32, 33], dyed materials for lasers fabrication, incorporation of functional nanoparticles [34], modified polymers with special optical properties [35, 36] (such as high transparency, variable refractive index), etc.

A more detailed study of the thermoplastic materials used during this work for thermal NIL, as well as their main rheological issues will be reported in Chapter 3.

1.2-2. Equipments for thermal NIL

There is also a large number of companies involved in the development and fabrication of equipments for nanoimprint. Obducat, EVG, Molecular Imprints, Jenoptik, Nanonex, SussMicrotec and SET are some of the most important ones in the thermal-NIL area.

1.2-2:a.- Parallel press equipments

Commercial thermal NIL equipments consist basically on a *chamber*, where the substrate and the stamp are introduced, and the heat and pressure applied. It is connected to a *computer* to control the imprinting recipes and to monitorize the process status in real time. The equipments allow parallel wafer-scale fabrication, and, in general, depending on the holder, the maximum sample size can vary from 2 up to 8 inch in diameter.

Figure 9 (a) shows the *Obducat 4 inch* equipment used during this work, placed at CNM's cleanroom. Here, the imprinting system can be seen next to the computer. Figure 9 (b) shows a detail of the chamber, with the 4 inch sample holder.

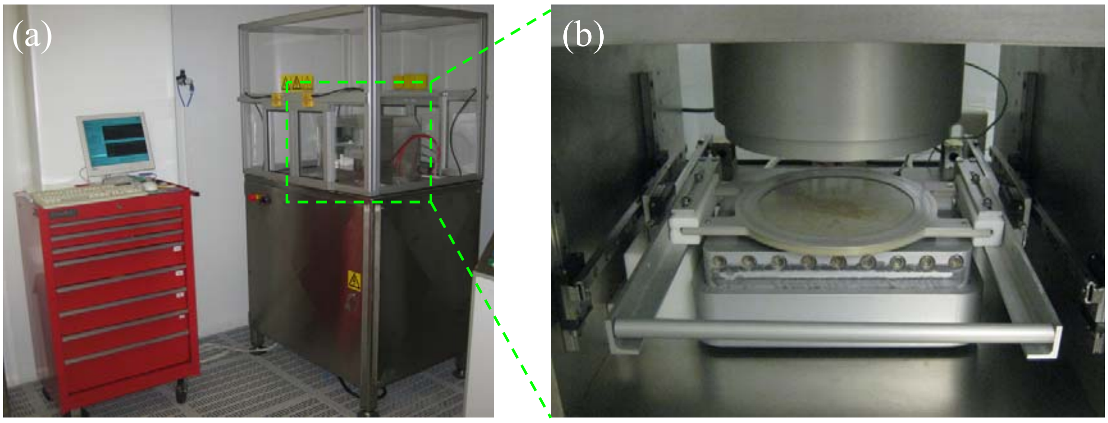

Figure 9. Obducact, 4 inch NIL equipment. General view (a) at CNM's cleanroom, and detail of the imprinting chamber (b).

Generally, a **compliance layer** is placed in-between the stamp and the holder. It homogenizes the pressure and softens the mechanical contact, minimizing the risk of breaking the samples. This layer can be an aluminium or plastic thin foil, a PDMS sheet, etc.

The commercial equipments may present differences in some of their characteristics, depending on the fabricant. For example, the **pressure** can be applied *mechanically* (Figure 10(a)) or by *air pumping* (Figure 10(b)). This last was patented by Obducat (*Soft Press* ®). The requirements for the compliance layer change for both cases. In the first one, it has to be flexible and soft, to homogenize the pressure. PDMS sheets are generally used. In the second one, it needs to be ductile, to cover and conform the back-side of the sample, to keep the air in-between the chamber and the sample, as schematized in Figure 10(b). Aluminum or PMMA thin foils are often utilized. It has been reported recently that the distribution of the pressure is one order of magnitude more homogeneous in this second case [37].

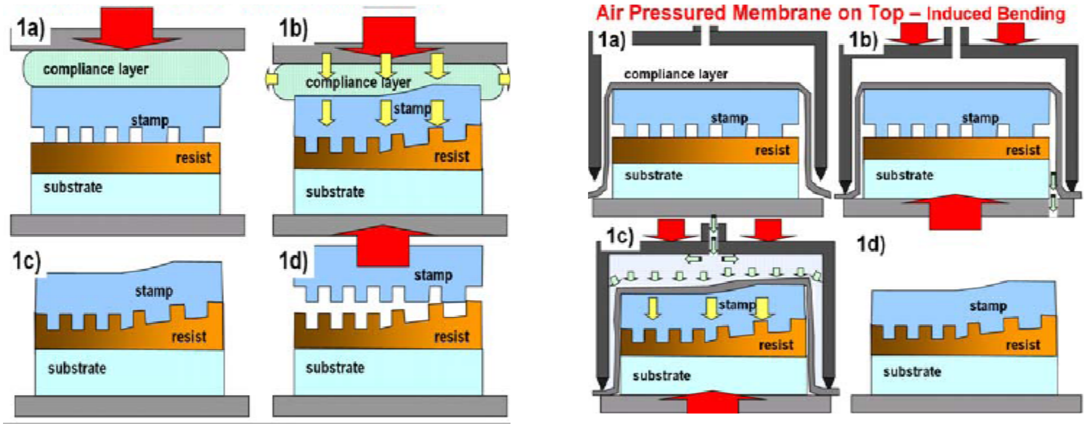

(a) Mechanical pressure (b) Air Pressure

Figure 10. Scheme of two different types of chambers: mechanically applied pressure (a) and air-induced pressure (b). [38]

Figure 11 (a) shows the imprinting chamber of the Obducat equipments, (air-induced pressure, also called *Soft Press*®), with the aluminum foils covering the sample and the stamp. During the imprint process (Figure 11 (b)) the foils protect the samples from mechanical damage and serve to keep the pressure and homogenize its distribution, as already mentioned, and induce the bending and process. After the process, the shape of the backside of the stamp onto the sample can be seen in the foil (Figure 11 (c)).

(a) Before (b) During (c) After imprinting

Figure 11. Compilance (aluminium) layers used in the Obducat equipment. The layers lye onto the sample (a), and serve to maintain and homogenize the pressure during the imprinting process (b), by conforming the back-side shape of the system substrate-stamp, as can be seen in (c).

Another characteristic that may vary from one equipment to another is the **cooling system**. It can be done just by turning off the heating, by air flowing inside the holder plate, or, to achieve a faster ratio, with liquid nitrogen flow.

Also, some of the equipments have special holders, that allow (vertical) **automatic demolding**. Figure 12 shows a scheme of a stamp holder, adapted for vertical demolding.

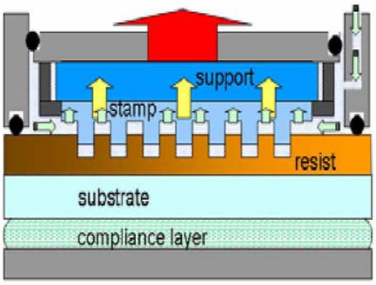

Figure 12. Scheme a chamber, with the possibility of automatic demolding. A special holder is used to control the vertical movement of the stamp. [38].

1.2-2:b.- Other Special equipments

Apart from these parallel presses, there are some other special equipments available for thermal NIL, that generally allow larger scale fabrication but that are more complex.

One case is the **step-and-stamp NIL**, schematized in Figure 13 (a). Here, the wafer-scale fabrication is not done in parallel using a wafer-scale stamp, but a smaller one is imprinted several times. For this, an equipment with stepper motors is needed. Local heating is important, as rewarming of the already imprinted structures can cause distortions, so it is generally done by heating up the stamp. This process can be also performed for UV-NIL (the so-called *step-and-flash*). In this case, the liquid resist is locally dispensed to avoid exposure of non-patterned areas. An important advantage is that *alignment* is possible, with an accuracy of few hundreds of nanometres [39], demonstrated even when using non-transparent substrates for *thermal* step-and-stamp NIL [40]. These equipments are much more complex than the conventional parallel presses, used for thermal or UV NIL described above, as complicated engines and mechanics for moving the stamp with the necessary accuracy are involved. Figure 13 shows a NPS equipment, from SET*, that allows step-and-imprint and step-and-flash processes, also installed at CNM's cleanroom.

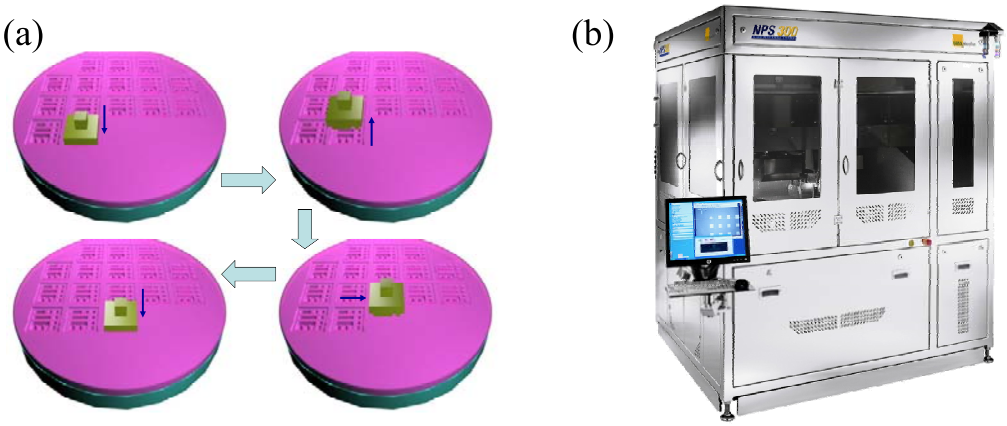

Figure 13. Scheme of Step and Imprint NIL (a): a small stamp is imprinted several times, to full-fill a larger wafer. Photo of a NPS equipment (b).

Another special large-scale process is the **roll-to-roll** nanoimprint [41]. In this case, a cylindrical stamp is rolled and pressed onto a long polymeric film, locally heated (Figure 14(a)). It has demonstrated nanometric resolution (200 nm period, 70 nm line width [41]) along several centimetres. The main drawbacks are the complexity of the machine (Figure 14(b)), and the fabrication of the rounded stamp. Nevertheless, this method is already been used by industry (Hewlett Packard, HP) to

---

* SET – Smart Equipment Technology (France) - www.set-sas.fr/

produce prototypes of all-polymeric electronic devices and optical displays, fabricated entirely by a roll-to-roll based NIL process.

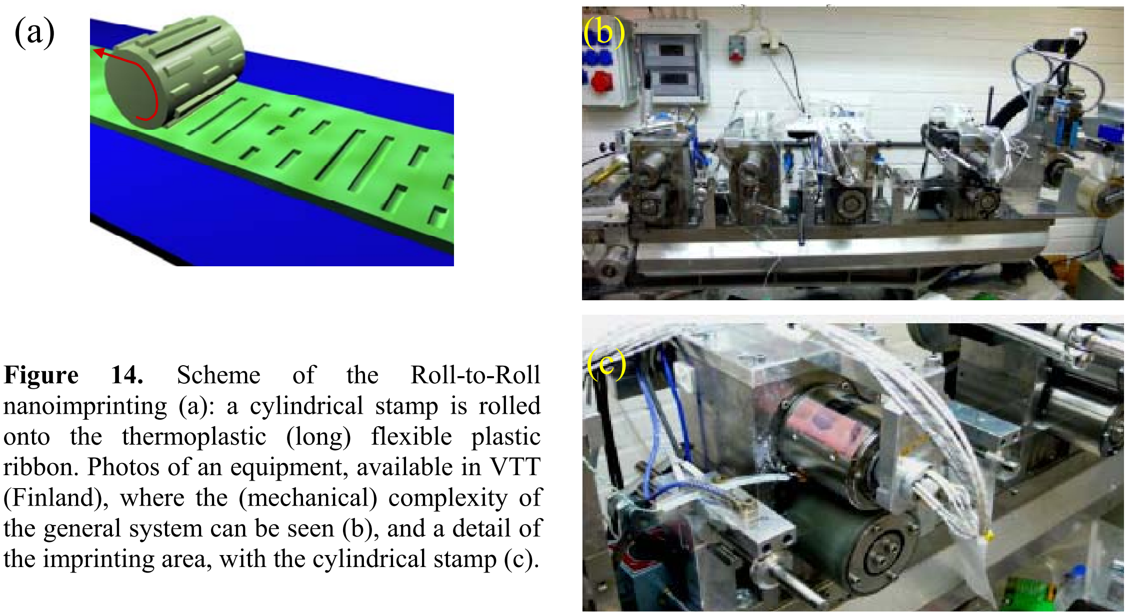

Figure 14. Scheme of the Roll-to-Roll nanoimprinting (a): a cylindrical stamp is rolled onto the thermoplastic (long) flexible plastic ribbon. Photos of an equipment, available in VTT (Finland), where the (mechanical) complexity of the general system can be seen (b), and a detail of the imprinting area, with the cylindrical stamp (c).

During the development of this thesis, an **Obducat parallel 4 inch equipment**, with an *air pressure chamber*, and *air cooling* (Figure 9), placed at CNM's cleanroom, was used. Also, we had the opportunity of using an EVG nanoimprint tool [†] in the cleanroom of the Technical University of Denmark, and a HEX03 tool from Jenoptik [‡], in TEKNIKER.

Even further, in the framework of a european project, we have had also the possibility of comparing the imprinting systems, recipes and conditions, together with the results, advantages and main drawbacks for several different equipments. The details of these benchmarking tasks will be described in Chapter 3.

1.3.- STATE OF THE ART

Fabrication by means of nanoimprint showed, since its beginning, that a **resolution** of few nanometers was achievable. Figure 15 [1, 42] shows a stamp consisting on an array of pillars, 10 nm diameter (a), the imprinted pattern in PMMA (b) and the features after a metallization and lift-off (c), reported by Chou et al. in 1997. More recently, the possibility of achieving *molecular scale* resolution by replication methods was reported by Hoff et al. [43], achieved by imprinting stamps made of carbon nanotubes. Figure 16 shows AFM images of the soft stamp (a) and the replication (b). This proves that the resolution achievable by NIL is limited by the stamp and not by the replication processes themselves.

Regarding **alignment**, UV-NIL allows high accuracy, as the stamps used are generally transparent. Figure 17 shows a finFET[§] transistor [44] fabricated in various steps by UV-NIL, where the gate was aligned within 20 nm on the 19 nm small fin. Nowadays, some thermal NIL equipments incorporate alignment capabilities, with an accuracy of ~ 100 nm [39].

[†] 520HE parallel press from EVG – EvgGroup - http://www.evgroup.com/en

[‡] HEX03, from Jenoptik - http://www.jo-mt.de/

[§] finFET: nonplanar, double-gate transistor built on an SOI substrate. The conducting channel is wrapped around a thin silicon "fin", which forms the body of the device.

The high **throughput** of this technique has also been widely demonstrated up to date. Imprinting of a full 8 inch wafer with nanometric features has widely been proved [45]: Figure 18 shows a 8 inch wafer, fully imprinted with lines (optical encoders) with different widths and pitch, down to 200 nm.

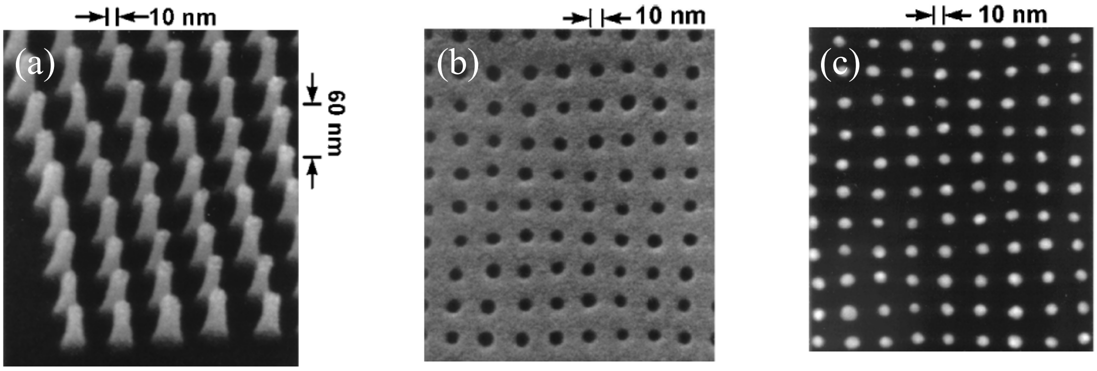

Figure 15. Minimum resolution, obtained by Chou et al.. The stamp (a) was patterned with an array of dots, 10 nm diameter, imprinted in PMMA (b), and the features successfully transferred by metallization and lift-off onto the substrate (c). [42].

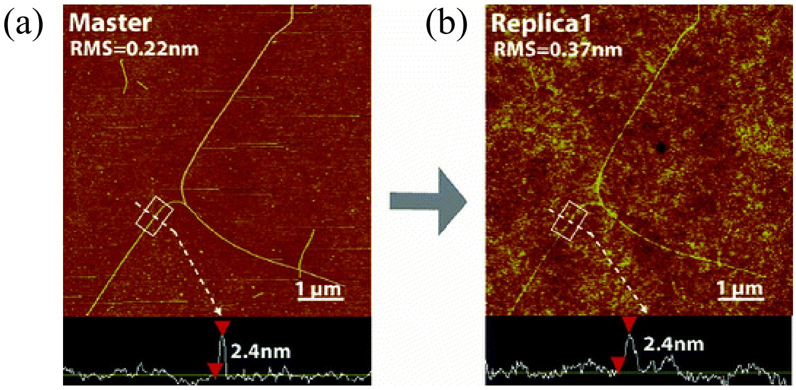

Figure 16. Molecular resolution obtained by Hoff et al. by imprinting a carbon nanotube, previously replicated by using PDMS. (a), AFM image of the stamp, and (b), imprinted replica. [43].

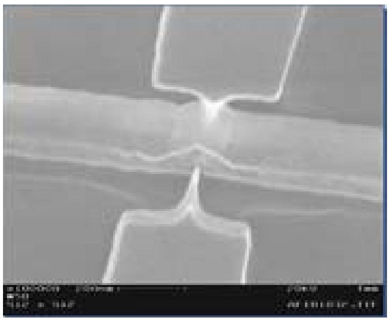

Figure 17. Alignment in UV-NIL. A finFET transistor fabricated only using UV-NIL. The gate was aligned within 20 nm on the 19 nm small fin. [44].

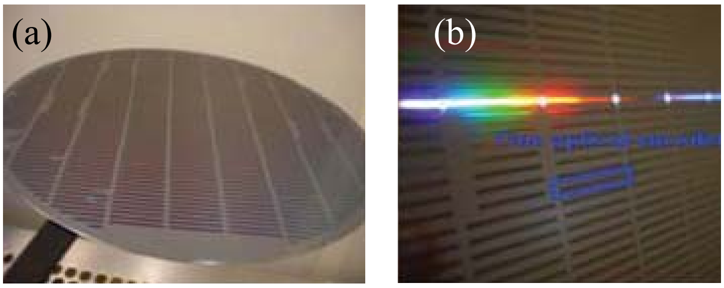

Figure 18. 8 inch wafers imprinted at CEA-LETI (France). Full eight inches silicon stamps (a) and closer view of several optical encoders (b). The width of the features is 250 nm. [45]

Thermal NIL is nowadays a well-known process, and the research activities towards process study and optimization (polymer rheology, modellization or defects study) are appearing less often than those related to applications, where the structures and devices used in other research areas, such as biology, optics or medicine, were fabricated by NIL.

NIL was added to the International Technology Roadmap for Semiconductors (ITRS) [46] for the 32 and 22 nm nodes some years ago. But, according to the last results presented by companies in international scientific conferences, NIL is not really being developed to substitute Optical Lithography in the semiconductor industry. Massive fabrication of nanostructured magnetic media for information storage [47] (Figure 19 (a)), and the fabrication of optical devices [48] [49] (Figure 19 (b)) look like the preferred industrial applications for NIL.

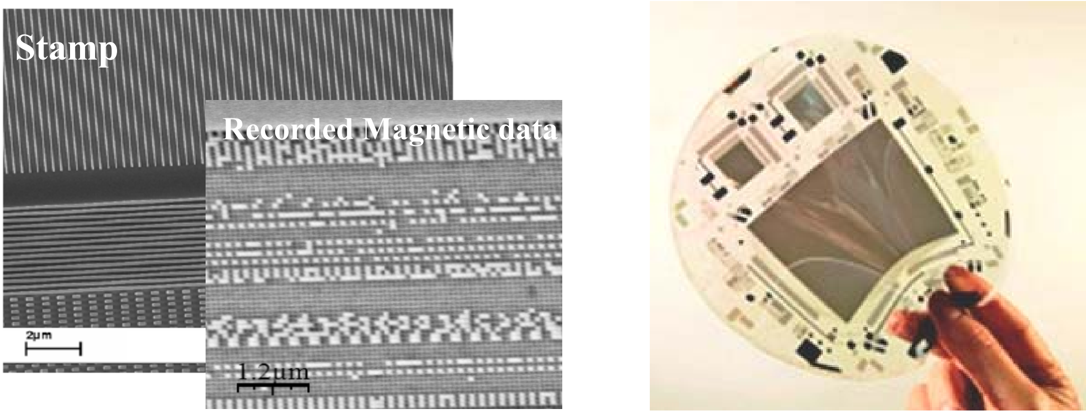

(a) Hitachi Global Storage Technologies (b) Prototype of flexible display, HP Labs

Figure 19. Photos of two devices under development by industry: NIL-based nanofabrication for magnetic storage (a), and for flexible electronics and displays (b).

Maybe, one of the most interesting and amazing applications of NIL is the fabrication of **memristors**[**] by NIL, as an alternative to conventional CMOS circuitry, that is being developed at HP Labs [50]. These consist on metallic nanoscaled cross-bars, where the dimensions have to be in the sub-100 nm range. The junctions of the lines form the memristor matrix [51, 52]. The combination of the report on the viability of the performance of memristor-based devices and the high throughput of NIL-based fabrication technology can make it possible to develop far more energy-efficient computing systems with memories that retain information even after the power is off, so there's no wait for the system to boot up after turning the computer on. It may even be possible to create systems with some of the pattern-matching abilities of the human brain. Figure 20 shows two images of the cross bars, 32 nm pitch, fabricated recently by UV-NIL in titanium dioxide, at HP labs in California.

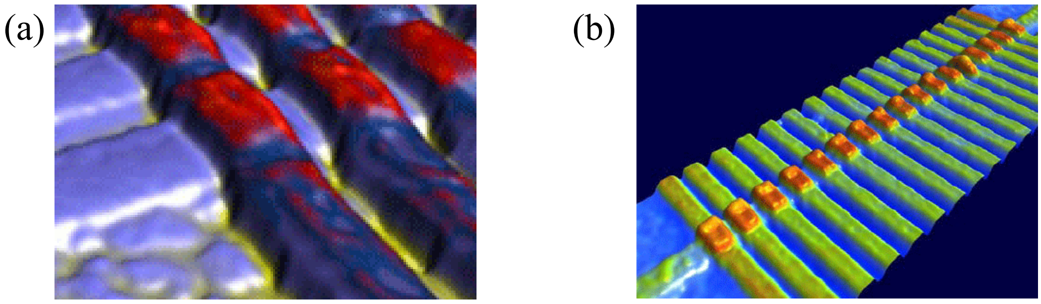

Figure 20. AFM images of cross-bars of titanium dioxide, fabricated by UV-NIL, that behave as memristors matrix. The pitch of the lines is 32 nm. They have been fabricated at HP labs (CA - USA).

[**] Memristor: passive two terminals circuit element, which resistance is variable, and its status can act as a memory or as an electronic switch.

1.4.- PROJECTS

1.4-1. NaPa: Nanopatterning Emerging Methods

An important part of the work related to *NIL-process* developed during this thesis was done in the framework of the European Project NaPa - *Emerging Nanopatterning Methods*[††], where 35 research groups from 14 different countries from Europe (Figure 21(a)) were working together towards the development, optimization and combination of the different emerging nanopatterning methods.

The project was formed by 3 sub-projects (Micro/Nano Electro Mechanical Systems-*MEMS*, Soft Lithography and Self Assembly-*SLASA*, and Nanoimprint Lithography-*NIL*), complemented by other 3 (*Materials*, *Tools* and *Simulations*), as is schematized in Figure 21(b).

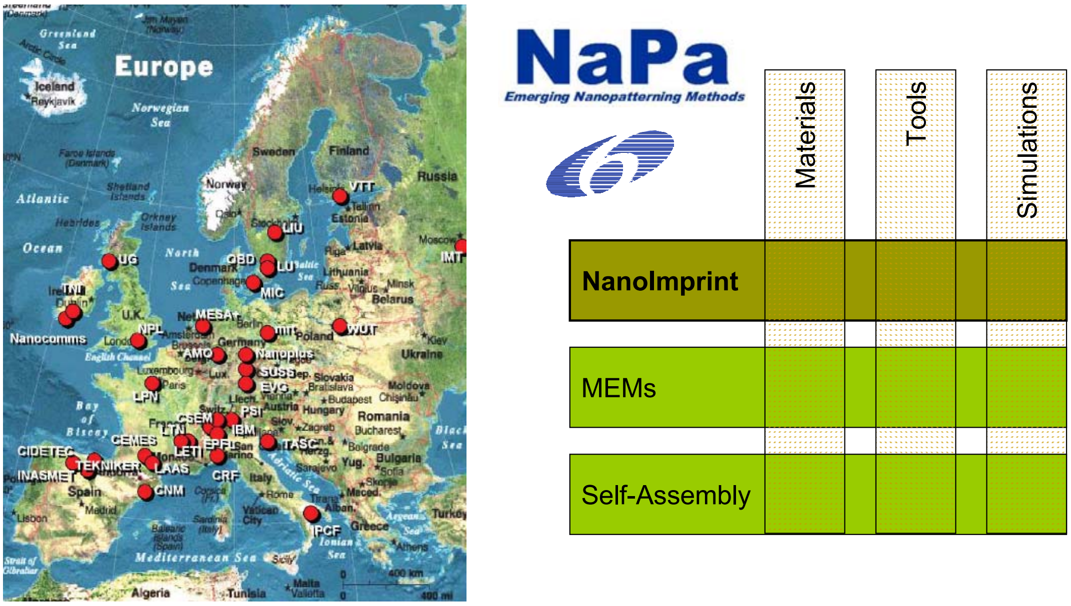

Figure 21. NaPa project: Map of the distribution of the 35 partners all around Europe (left), Logo and scheme of the sub-projects and their inter-relationships (right).

The tasks in the NIL sub-project covered all the NIL issues, ranging from the most basic studies of the polymer behaviour, to the development and fabrication of complex devices devoted to optics or biology, covering also the fabrication of stamps, optimizing the resolution and exploring new materials or 3D shapes, and benchmarking.

Taking advantage of the huge number of laboratories involved, one of the goals of the project was to standardize the NIL process and recipes, and do a “cooking book” for NIL, gathering the know-how and expertise of the researchers involved. For this, some important tasks consisted on benchmarking the process, both for micro and nano structures.

As a summary of the developments achieved during the 4 years of the project, and as a proof of the valuable work done towards standarization of nanotechnology (not only NIL), a handbook consisting on a library of the processes utilized and developed by the project members, was recently published (Figure 21) [53]. This book is also a good example of the intense activity of the research labs within the emerging nanopatterning methods study and development. As an example (related to NIL), several

---

[††] NaPa –Emmerging Nanopatterning Methods. 6th European Sixth Framework Programme. NMP4-CT-2003-500120.

different imprinting recipes, processes and variants, already optimized and commonly used by the members are gathered here.

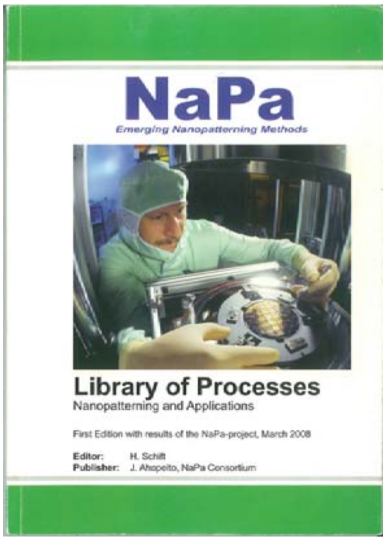

Figure 22. NaPa Library of processes, edited by H. Schift. This book gathers the different types of processes developed and used by the members of the project. [53]

During this thesis, an important part of the work related to *the basics of nanoimprint* (*optimization and rheology*) was done in relation to the sub-project devoted to the thermal-NIL process study. More specifically, our main tasks within NaPa were the study of the internal stress and related strain induced in the polymeric structures during the cooling step [54]. Some contributions for benchmarking tasks were also done. Their objective was comparing the results and the homogeneity at wafer-scale for imprints done with different equipments in the micro [55] and nanoscale [56], as will be described in Chapter 3.

1.4-2. NILSIS: Micro/Nano Devices fabricated by NIL

Part of the work related to *the use of NIL technology for the fabrication of structures and/or devices* (more specifically interdigitated nanoelectrodes) was developed in the frame of the national project NILSIS[‡‡] (Micro/Nanodevices fabricated using emerging lithographic techniques), that aims to establish NIL as a common nanofabrication method in the Spanish research and industrial community. These activities are coordinated with other two partners, as will be described along the thesis: Gaiker and Tekniker.

The robustness and viability of NIL-based fabrication is shown by developing 4 different applications, which prototypes are shown in:

i) Linear encoders with accuracy and resolution on the nanometer range

ii) Biochips for protein recognition, with high density and functionality

iii) Nanoelectromechanical device based on Silicon nanowires

iv) Interdigitated Electrode Arrays, with nanometric resolution and high sensibility.

[‡‡] NILSIS - *Micro/Nano Dispositivos Fabricados Mediante Técnicas Litográficas Emergentes- MCYT* - TEC2006-13910-C03-01/MIC (2006 – 2009).

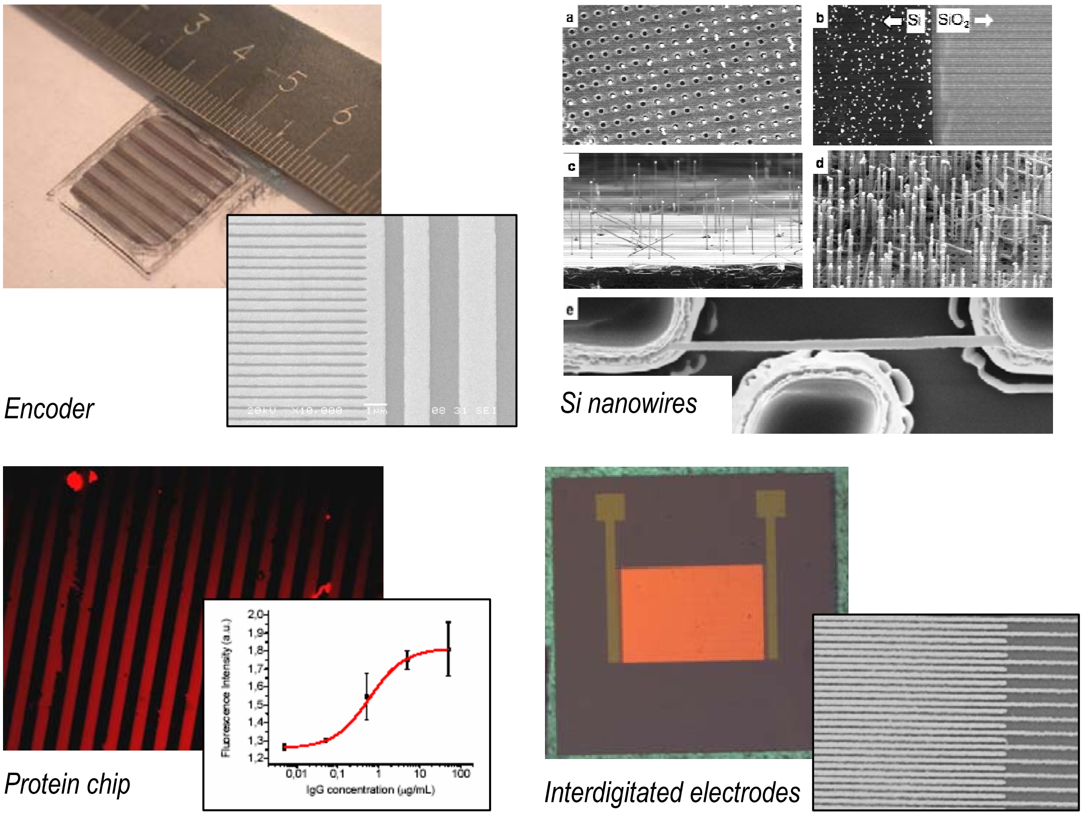

Figure 23. Images of the demonstrators and prototypes proposed within the NILSIS project: encoders, silicon nanowire-based MEMS/NEMS, protein chips and interdigitated arrays of nanoelectrodes.

In parallel with the development of micro and nano systems and devices with a valuable industrial interest and biomedical and pharmaceutical applications, technological issues were also addressed, for the development of general NIL technology, or applied to the specific fabrication of the devices (Figure 24). During this thesis, we also participated in the fabrication of molds, and in the selective deposition of nanoparticles for ordered growth of silicon nanowires.

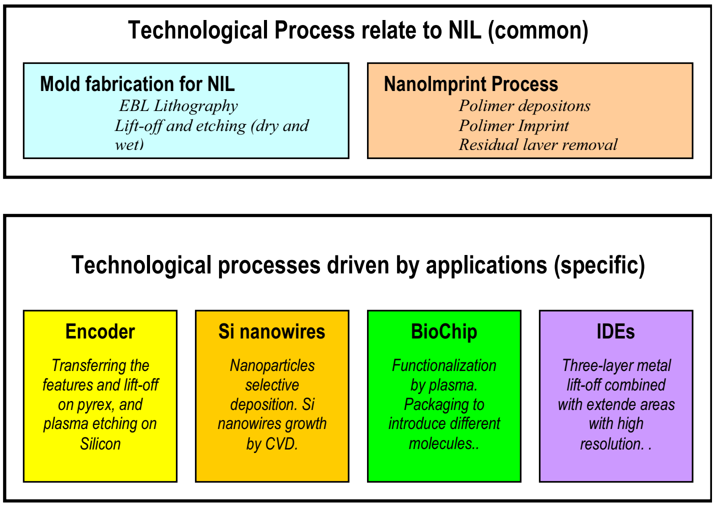

Figure 24. NILSIS: development of technologic issues within the different tasks, and towards the fabrication of demonstrators with interest in industry and/or biosensing.

1.4-3. NanoBioMed: Nanotechnologies in Biomedical applications

This project aims to set a research team in the emerging field of nanoscience and nanotechnology towards biomedical applications (NANOBIOMED[§§]). The project is based on the develop of micro a nanofabrication processes based on Top-down techniques and the fabrication of nanomaterials with different functionalities (Bottom-up approach) with the ultimate objective to achieve significant applications in biomedicine. Here, the developed nanotechnologies are applied to advanced therapies as the local drug delivery, and the improvement of the early diagnosis "in-vivo" by the enhance of the magnetic resonance imaging (MRI) contrast by targeting of the contrast agent and also "in-vitro" by the design and fabrication of biosensors and multi-sensor platforms (lab-on-chip) for early diagnosis of diseases at the point of care.

Within this project, we had the opportunity of collaborate with groups with large expertise in biosensing, so, after the fabrication of the biosensors (interdigitated nanoelectrodes) different types of *characterization and applications of biomedical interest* were developed, such as *nanoparticle quantification* and *DNA hybridization detection*.

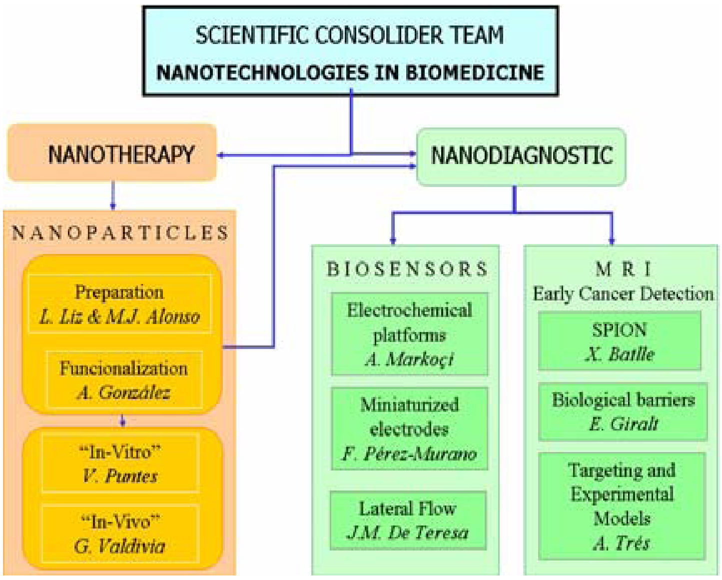

Figure 25. NanoBioMed: scheme of the different research lines, where nanoparticles play one of the most important roles: synthesis, functionalization, detection and quantification, and use for diagnostic, drug delivery or treatment of diseases.

[§§] Consolider NanoBioMed - *Nanotecnologías en Biomedicina* **-** PROYECTO CONSOLIDER-INGENIO 2010. CSD00C-06-04615 (2006 – 2010)

1.5.- REFERENCES

[1] Chou, S.Y., Krauss, P.R. and Renstrom, P.J.,
Imprint of Sub-25 Nm Vias and Trenches in Polymers.
Applied Physics Letters, 1995. **67**(21): p. 3114-3116.

[2] Chou, S.Y. and Krauss, P.R.,
Imprint lithography with sub-10 nm feature size and high throughput.
Microelectronic Engineering, 1997. **35**(1-4): p. 237-240.

[3] Guo, L.J., Krauss, P.R. and Chou, S.Y.,
Nanoscale silicon field effect transistors fabricated using imprint lithography.
Applied Physics Letters, 1997. **71**(13): p. 1881-1883.

[4] Luesebrink, H.,
Nanoimprint lithography: the semiconductor industry and beyond.
Microlithography World, 2006. **15**(1): p. 4-+.

[5] Chou, S.Y., Krauss, P.R. and Renstrom, P.J.,
Nanoimprint lithography.
Journal of Vacuum Science & Technology B, 1996. **14**(6): p. 4129-4133.

[6] Haisma, J., Verheijen, M., Heuvel, K.v.d. and Berg, J.v.d.,
Mold-assisted nanolithography: A process for reliable pattern replication.
Journal of Vacuum Science & Technology B, 1996. **14**(6): p. 4124-4128.

[7] Himmelhuber, R., Fink, M., Pfeiffer, K., Ostrzinski, U., Klukowska, A., et al.
Innovative materials tailored for advanced microoptic applications. in *Proceedings of SPIE--the international society for optical engineering*. 2007.

[8] Klukowska, A., Posset, U., Schottner, G., Wis, M.L., Salemi-Delvaux, C., and Maeatesta, V.,
Photochromic hybrid sol-gel coatings: Preparation, properties, and applications.
Materials science, 2002. **20**(1): p. 95-104.

[9] *microresist technology, GmbH (Berlin). www.microresist.de.*

[10] Kumar, A. and Whitesides, G.M.,
Features of gold having micrometer to centimeter dimensions can be formed through a combination of stamping with an elastomeric stamp and an alkanethiol ``ink'' followed by chemical etching.
Applied Physics Letters, 1993. **63**(14): p. 2002-2004.

[11] Geissler, M., Wolf, H., Stutz, R., Delamarche, E., Grummt, U.-W., et al.,
Fabrication of Metal Nanowires Using Microcontact Printing.
Langmuir, 2003. **19**(15): p. 6301-6311.

[12] Kunnavakkam, M.V., Houlihan, F.M., Schlax, M., Liddle, J.A., Kolodner, P., et al.,
Low-cost, low-loss microlens arrays fabricated by soft-lithography replication process.
Applied Physics Letters, 2003. **82**(8): p. 1152-1154.

[13] Hull, R., Chraska, T., Liu, Y. and Longo, D.,
Microcontact printing: new mastering and transfer techniques for high throughput, resolution and depth of focus.
Materials Science and Engineering: C, 2002. **19**: p. 383-392.

[14] Chou, S.Y., Keimel, C. and Gu, J.,
Ultrafast and direct imprint of nanostructures in silicon.
Nature, 2002. **417**(6891): p. 835-837.

[15] Choi, J., Nielsch, K., Reiche, M., Wehrspohn, R.B. and Gosele, U.,
Fabrication of monodomain alumina pore arrays with an interpore distance smaller than the lattice constant of the imprint stamp.
Journal of Vacuum Science and Technology B, 2003. **21**(2): p. 763-766.

[16] Hideki, M., Haruki, Y., Masahiro, S., Hidetaka, A., Masashi, N., and Toshiaki, T.,
Highly ordered nanochannel-array architecture in anodic alumina.
Applied Physics Letters, 1997. **71**(19): p. 2770-2772.

[17] Christiansen, M.B., Schøler, M. and Kristensen, A.,
Integration of active and passive polymer optics.
Optics Express, 2007. **15**(7): p. 3931-3939.

[18] Cheng, X. and Guo, L.J.,
A combined-nanoimprint-and-photolithography patterning technique.
Microelectronic Engineering, 2004. **71**(3-4): p. 277-282.

[19] Kehagias, N., Reboud, V., Chansin, G., Zelsmann, M., Jeppesen, C., et al.,
Reverse-contact UV nanoimprint lithography for multilayered structure fabrication.
Nanotechnology, 2007. **18**(17): p. 175303.

[20] Yang, B. and Pang, S.W.,
Multiple level nanochannels fabricated using reversal UV nanoimprint.
Journal of Vac. Sci. Technol. B, 2006. **24**(6): p. 2984-2987.

[21] Sang Hoon, K., Ki-Dong, L., Ja-Yeon, K., Min-Ki, K. and Seong-Ju, P.,
Fabrication of photonic crystal structures on light emitting diodes by nanoimprint lithography.
Nanotechnology, 2007. **18**(5): p. 055306.

[22] Thamdrup, L.H., Klukowska, A. and Kristensen, A.,
Stretching DNA in polymer nanochannels fabricated by thermal imprint in PMMA.
Nanotechnology, 2008. **19**(12): p. 125301.

[23] Behl, M., Seekamp, J., Zankovych, S., Sotomayor Torres, C.M., Zentel, R., and Ahopelto, J.,
Towards Plastic Electronics: Patterning Semiconducting Polymers by Nanoimprint Lithography.
Advanced Materials, 2002. **14**(8): p. 588-591.

[24] Mcalpine, M.C., Friedman, R.S. and Lieber, C.M.,
High-Performance Nanowire Electronics and Photonics and Nanoscale Patterning on Flexible Plastic Substrates.
Proceedings of the IEEE, 2005. **93**(7): p. 1357.

[25] Hansen, M., Nilsson, D., Johansen, D.M., Balslev, S. and Kristensen, A.,
A nanoimprinted polymer lab-on-a-chip with integrated optics.
Proc. SPIE, 2005. **5872**(1): p. 58720A.

[26] Balslev, S., Jorgensen, A.M., Bilenberg, B., Mogensen, K.B., Snakenborg, D., et al.,
Lab-on-a-chip with integrated optical transducers.
Lab on a Chip, 2006. **6**(2): p. 213-217.

[27] Kehagias, N., Hu, W., Reboud, V., Lu, N., Dong, B., et al.,
Nanoimprint lithography and surface modification as prospective technologies for heterogeneous integration.
physica status solidi (c), 2008. **5**(12): p. 3571-3575.

[28] Scheer, H.-C., Bogdanski, N., Wissen, M. and Möllenbeck, S.,
Imprintability of polymers for thermal nanoimprint.
Microelectronic Engineering
Proceedings of the Micro- and Nano-Engineering 2007 Conference - MNE 2007, 2008. **85**(5-6): p. 890-896.

[29] Obieta, I. and Arroyo, O.,
Plasma Treatments of NIL Polymers to enhance Anti-Adhesion Properties, in *Litho2006*. 2006: Marseille (France).

[30] Egitto, F.D. and Matienzo, L.J.,
Plasma modification of polymer surfaces for adhesion improvement.
IBM Journal of Research and Development, 1994. **38**(4): p. 423-439.

[31] Hegemann, D., Brunner, H. and Oehr, C.,
Plasma treatment of polymers for surface and adhesion improvement.
Nuclear Instruments and Methods in Physics Research Section B: Beam Interactions with Materials and Atoms, 2003. **208**: p. 281-286.

[32] Maury, P.A.,
Fabrication of nanoparticle and protein nanostructures using nanoimprint lithography, in *U. Twente*. 2007: Enschede. p. 154.

[33] Merino, S., Retolaza, A., Trabadelo, V., Cruz, A., Heredia, P., et al.
Protein patterning on the micro and nanoscale by thermal nanoimprint lithography on a new functionalized copolymer. in *International Conference on Micro- and Nano-Engineering (MNE)*. 2008. Athens (Greece): Poster.

[34] Tamborra, M., Striccoli, M., Curri, M.L., Alducin, Juan A., Mecerreyes, D., et al.,
Nanocrystal-Based Luminescent Composites for Nanoimprinting Lithography.
Small, 2007. **3**(5): p. 822-828.

[35] Tamborra, M., Striccoli, M., Curri, M.L., Alducin, J.A., Mecerreyes, D., et al.,
Nanocrystal-Based Luminescent Composites for Nanoimprinting Lithography13.
Small, 2007. **3**(5): p. 822-828.

[36] Reboud, V., Kehagias, N., Striccoli, M., Placido, T., Panniello, A., et al.,
Photoluminescence enhancement in metallic nanocomposite printable polymer.
Journal of Vacuum Science and Technology B, 2007. **25**(6): p. 2642-2644.

[37] Gao, H., Tan, H., Zhang, W., Morton, K. and Chou, S.Y.,
Air Cushion Press for Excellent Uniformity, High Yield, and Fast Nanoimprint Across a 100 mm Field.
Nano Letters, 2006. **6**(11): p. 2438-2441.

[38] Schift, H.,
Nanoimprint lithography: An old story in modern times? A review.
Journal of vacuum science & technology. B, Microelectronics and nanometer structures, 2008. **26**(2): p. 458-480.

[39] *NPS300 technical specifications - http://www.set-sas.fr/en/multipage.xml?pg=1&id=176707*.

[40] Haatainen, T., Majander, P., Riekkinen, T. and Ahopelto, J.,
Nickel stamp fabrication using step & stamp imprint lithography.
Microelectronic Engineering, 2006. **83**(4-9): p. 948-950.

[41] Se Hyun Ahn, L.J.G.,
High-Speed Roll-to-Roll Nanoimprint Lithography on Flexible Plastic Substrates.
Advanced Materials, 2008. **20**(11): p. 2044-2049.

[42] Chou, S.Y., Krauss, P.R., Zhang, W., Guo, L.J. and Zhuang, L.,
Sub-10 nm imprint lithography and applications.
Journal of Vacuum Science & Technology B, 1997. **15**(6): p. 2897-2904.

[43] Hoff, J.D., Cheng, L.-J., Meyhofer, E., Guo, L.J. and Hunt, A.J.,
Nanoscale Protein Patterning by Imprint Lithography.
Nano Letters, 2004. **4**(5): p. 853-857.

[44] Choi, Y., Lindert, N., Xuan, P., Tang, S., Ha, D., et al.,
Sub-20nm CMOS Fin-FET Technologies.
International Electron Devices Meeting, 2001: p. 421-424.

[45] Landis, S., Chaix, N., Gourgon, C., Perret, C. and Leveder, T.,
Stamp design effect on 100 nm feature size for 8 inch NanoImprint lithography. 2006. p. 2701.

[46] *International Technology Roadmap for Semiconductors* - www.itrs.net/.

[47] Albrecht (Hitachi Global Storage Technologies), T.R.,
Patterned Magnetic Recording Media, in *International Conference on Electron, Ion and Photon Beam Technology and Nanofabrication*. 2008: Portland, OR (USA).

[48] Stanley Electric Co., L.J.,
Improvement of the external extraction efficiency of OLED by using a pyramid array.

[49] Lambertini, V.,
Double Side Patterned OLED, in *Developed within the NaPa Project*,
I. FIAT Research Center (Torino, Editor. 2007.

[50] Kuekes, P.J.,
Molecular crossbar latch in *United States Patent*. 2003, Hewlett Packard Development Company LP (Houston, TX) USA.

[51] Tour, J.M. and He, T.,
Electronics: The fourth element.
Nature, 2008. **453**(7191): p. 42-43.

[52] Strukov, D.B., Snider, G.S., Stewart, D.R. and Williams, R.S.,
The missing memristor found.
Nature, 2008. **453**(7191): p. 80-83.

[53] Schift, H.,
NaPa Library of Processes. First Edition with results of the Napa-project. 2008: J. Ahopelto, NaPa Consortium.

[54] Fernandez-Cuesta, I., Nielsen, R.B., Heinis, D., Boltasseva, A., Borrisé, X., et al.
Plasmon confinement in V-groove waveguides fabricated by NanoImprint Lithography. in *NanoSpain*. 2008. Braga (Portugal): Oral.

[55] Kristensen, A.,
NaPa Residual layer thickness benchmarking. 2005, MIC: Copenhagen. p. 67.

[56] Gourgon, C., Chaix, N., Schift, H., Tormen, M., Landis, S., et al.,
Benchmarking of 50 nm features in thermal nanoimprint.
Journal of Vacuum Science & Technology B, 2007. **25**(6): p. 2373-2378.

Chapter 2

Stamp Fabrication

The capability of fast fabrication of stamps with different feature sizes, depths, designs and geometries is of crucial importance for the study and optimization of the NIL technology. Different approaches for the fabrication of stamps were addressed during the starting-up and optimization of the NIL process at CNM, first, to study the polymer rheology and process, and, finally, to develop functional devices.

The geometric design, the lithographic technique used together with the etching process, as well as the antisticking coating are the main issues that were addressed in this work concerning stamp preparation.

2.1.- NANOPATTERING FOR STAMP FABRICATION

Stamp design and fabrication is one of the key issues in NIL technology, as the quality of the final structures will strongly depend on it. The imprinting process parameters will be influenced by its geometry: size, gap between protrusions, presence of compensation structures, roughness and slope of the sidewalls, homogeneity of the depth, etc.

During this thesis work, electron beam lithography (EBL) was mainly used for most of the featured stamps. In addition, as an original work, we demonstrated that lithography with the atomic force microscopy is a powerful method as well.

2.1-1. Electron Beam Lithography

2.1-1:a.- Patterning with an electron beam

The most extended procedure to fabricate silicon stamps is by defining the structures in a polymer, and to use this polymer (or a thin film of some other material underneath it, like SiO_2) as a mask for a reactive ion etching (RIE), to carve the structures into the substrate. Attending to their geometry, extension and resolution, the process chosen to write the pattern in the polymer can be a conventional **optical lithography** (OL) for micrometric structures, or **electron beam lithography** (EBL) for sub-micrometric and high resolution patterns (down to ~ 50 nm lateral size). As the wavelength associated to an electron is much shorter than that of a photon, "writing" with electrons allows overcoming the diffraction limits arising from the use of light, thus, improving the maximum resolution [1].

For EBL, a thin film of a resist sensitive to the electron radiation is spun onto the substrate (Figure 26(a)), and the pattern is defined by locally exposing the resist to a focused electron beam (Figure 26(b)). Depending on the nature of the resist, the developer dissolves the exposed areas in a **positive resist** (Figure 26(c-top)) or the non-exposed ones in a **negative resist** (Figure 26(c-bottom)). In the first case, the material is a polymer with high molecular weight, which chains are broken by the exposition to the electron gun into smaller ones, that are soluble in the developer. In the second case, the initial material is generally a pre-polymer that polymerizes when exposed to the electrons radiation, becoming un-soluble in the developer.

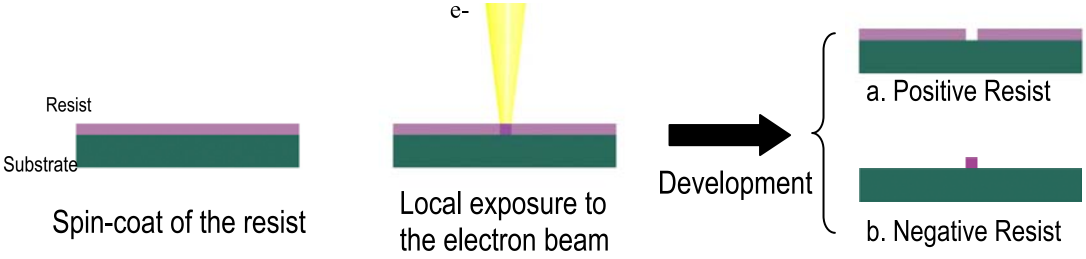

Figure 26. Scheme of e-beam lithography: a material, sensitive to the electron radiation is spin coated onto the substrate. Then, it is exposed to a focused beam of electrons. Finally, depending on the nature of the resist used, the developer removes the exposed patterns (positive resists) or the non-exposed areas (negative resist).

Positive resists are most frequently used, but also negative ones were used in this work, as will be described further in this chapter. *Poly(methyl methacrylate) – **PMMA***, is generally used as e-beam resist. During this thesis, a 100 nm thick film of PMMA with a molecular weight of 950 k was used for e-beam writing. The exposure parameters were varied depending on the pattern specifications. The typical parameters used are listed in Table 1. When the dimensions of the structures were critical, a previous calibration test to find the optimal dose was done. The exposed areas were developed in methyl isobutyl ketone (MIBK) diluted in isopropanol (IPA), MIBK:IPA (1:3), during 45 s, cleaned in IPA and dried with a nitrogen gun. Eventually, other resists (negative) or different molecular weights were also used.

Table 1. Typical parameters used to expose PMMA, 100 nm thick.

Voltage	Areas Dose ($\mu C/cm^2$)	Lines Dose (pC/cm)	Dots dwell time (ms)
10 kV	120	330	0.01 – 1
20 kV	220	700	0.05 – 1

2.1-1:b.- Pattern transfer

After the lithographic step, the structures are commonly etched into the silicon by means of a dry **reactive ion etching** (RIE) or by **wet etching**. Figure 27 shows two examples of structures fabricated by dry (a) and wet etching (b).

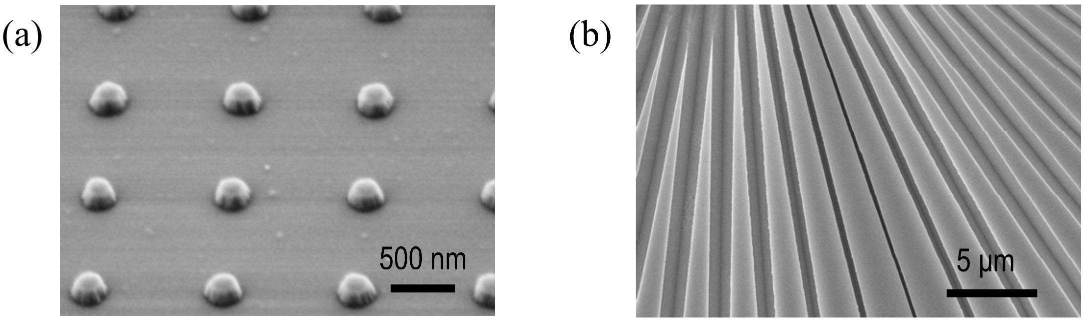

Figure 27. Examples of silicon structures fabricated by ebeam and RIE (a) or wet etching (b). In the first case, with a RIE* process vertical sidewalls can be obtained (a). In the second case, the sidewalls orientation depend on the orientation of the silicon wafer. The image shown in (b) corresponds to a pattern defined in a (110) wafer, and etched in TMAH†. This solvent leads to anistropic wet etching of silicon. The slope of the sidewalls depends on the orientation of the mask with respect to the crystallographic planes.

Apart from EBL, other patterning methods were also used, studied and optimized during the work.

---

[*] RIE: C_4F_8 + SF_6 plasma for *Silicon* reactive ion etching.

[†] TMAH - Tetramethylammonium hydroxide, for anisotropic wet etching of silicon. Processing conditions: 25% at 80ºC.

2.1-2. AFM Local Anodic Oxidation

Atomic force microscope (AFM) local anodic oxidation (LAO) [2] is a very versatile method to define structures at the nanoscale in the surface of anodizable materials: the application of a positive voltage to the surface with respect to the tip in an atmosphere with a presence of humidity induces the oxidation of the surface (Figure 28).

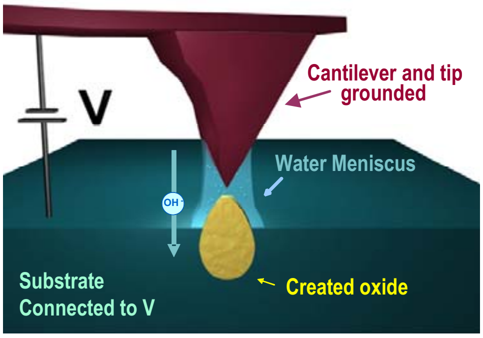

Figure 28. Local anodic oxication with AFM. Due to the ambient humidity, a water meniscus is created between the tip and the sample surface. When the substrate is polarized (and the tip virtually grounded), the ions in the water are accelerated, and react with the material of the substrate, that is chemically modifyied (it is oxidized generally).

LAO can been applied to define a fairly large range of structures and devices, like single electron transistors [3], nanomechanical structures [4], quantum electronic devices [5] and molecular templates [6]. The kinetics and mechanism of the oxidation process on bulk materials like silicon have been already studied in detail. The ambient humidity forms a water meniscus that enfolds the AFM tip and the surface. The application of the voltage ionizes the water molecules producing OH^- ions that are accelerated towards the surface where the oxidation reaction occurs [7]. In consequence, extension of the water meniscus, electrical field magnitude and ionic concentration are the key parameters that determine the kinetics of the oxidation reaction [8].

Up-to-date, most of the studies have been carried out in bulk materials. When LAO is performed in samples with a thin layer of material on the surface, the mechanism and kinetics are modified and new phenomena arises, like increased oxidation rate or electrical charging [9-12].

In this work, a detailed study of the oxidation mechanism in thin films of Si_3N_4 was carried out. For this, the consumed material was estimated from AFM topographical images after oxidation and after removing the created oxide. Afterwards, the current flow during the process was also studied, to get a deeper insight of the processes taking place. The results were compared to local oxidation of bulk silicon.

A commercial AFM from Veeco Instruments[‡] was used. LAO was performed by operating the AFM in contact mode using Pt/Ir coated tips (constant force ~ 0.2 N/m) at the laboratory environmental conditions (temperature = 21 ºC, humidity ≈ 40 %). Imaging was performed by operating the AFM in dynamic mode using standard AFM non-contact silicon cantilevers. Electrical current measurements were performed using a trans-impedance amplifier connected to the AFM tip with a gain of 1 pA/V. The voltage was always applied to the bottom of the sample and the tip was virtually grounded.

For a selective removing of the materials, different etching solutions were used, as shown in Table 2. TMAH solution (25 %, at 80 ºC) was used for silicon etching, Sioetch[§] [12] for silicon oxide etch, and H_3PO_4 (80 %, at 165ºC) to remove silicon nitride.

[‡] Nanoscope IV and Dimension 3100, from Veeco Instruments.

[§] *Sioetch*: MT 06/01 VLSI, Merck KGaA. NH4F (25%) and HF (6%) tamponed solution.

Table 2 – Chemicals used for selective wet etching. The etching velocities and relative selectivities are shown.

		Si	**SiO_2**	**Si_3N_4**
TMAH	Relative etch rate	>25000	20	1
(25% 80ºC)	Etch velocity	430 nm/min	0.3 nm/min	0.015 nm/min
***Sioetch*§**	Relative etch rate	-	>100	1
	Etch velocity	-	184 nm/min	1.4 nm/min
H_3PO_4	Relative etch rate	1	2.5	30
(80% 165ºC)	Etch velocity	0.12 nm/min	0.3 nm/min	4 nm/min

2.1-2:a.- Characterization of the Si_3N_4 films

Thin films with two different thicknesses of silicon nitride were deposited by low pressure chemical vapour deposition (LPCVD), using a mixture of $SiCl_2H_2$ and NH_3, at 800 ºC and 150 mtorr on p-type, 0.1-1.4 Ω·cm, (100)-oriented and p-type 24-30 Ω·cm (110)-oriented Si wafers. The films were characterized by ellipsometry to determine the film thickness, and X-Ray PhotoSpectroscopy (XPS). Ellipsometry measures revealed thicknesses of 4.4 nm and 9.8 nm for the two kind of samples prepared. XPS measurement (Figure 29) showed that the silicon nitride composition was stoichiometric (Si_3N_4) except on the surface of the film, which appeared oxidized. Table 3 summarizes the percentages of each element for different depths of the film.

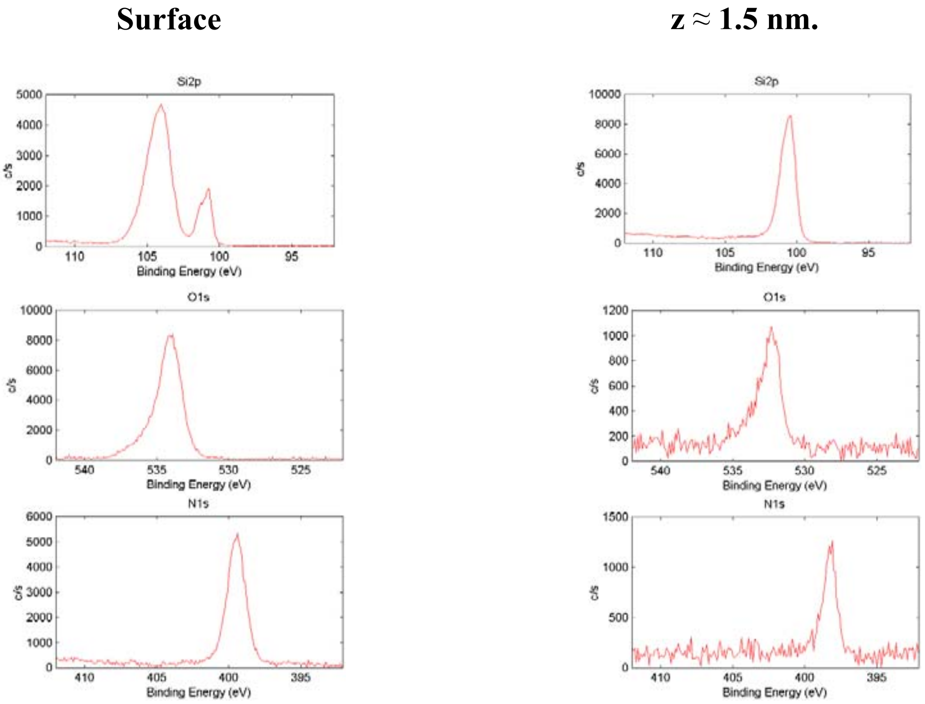

Figure 29. Results of the XPS measurements, performed in a thin film of 4 nm thick of Silicon nitride, deposited onto a Silicon substrate, with a surface orientation of (110). On the left column, the results obtained at the surface are shown. On the right one, inside the Silicon nitride film. Each spectrum corresponds to one of the elements present in the samples: silicon, oxygen and nitrogen (from top to bottom, respectively).

Table 3. Percentages of each element presento at the different depths at which the measurements were done. The last row corresponds to the substrate, and the one befote that, to the interface.

Depth	N 1s (%)	O 1s (%)	Si 2p (%)	C 1s (%)
surface (z = 0)	29.36	21.42	37.35	11.86
1.5 nm	8.17	3.36	88.47	0.00
3 nm	2.18	0.87	96.94	0.00
4.5 nm	0.48	0.63	98.88	0.00
6 nm	0.00	0.00	100	0.00

The roughness of the surface of the Si_3N_4 after the deposition was less than 0.22 nm, as evaluated from AFM measurements.

For the comparison with LAO of bulk silicon, experiments on clean silicon wafers were also performed. In this case, the native oxide was not eliminated before doing the LAO experiments.

2.1-2:b.- Local Anodic Oxidation of Si_3N_4

Figure 30 (left) shows a scheme of the different steps of the LAO experiments.

1. The thin Si_3N_4 films were deposited by LPCVD, and characterized, as already described before.
2. Areas of 1 µm x 1 µm were scanned with the AFM tip while applying a constant voltage. The resulting height was determined from AFM images.
3. The created oxide was removed selectively in Sioetch, and the depth measured with AFM images.
4. Two different processes were performed afterwards:

    4a. The pattern could be transferred into the silicon by a wet etching in TMAH, using the non-patterned silicon nitride as a mask.

    4.b The silicon nitride layer could be removed, to analyze the properties of the underlying substrate.

Figure 30 (right) shows AFM images obtained after each step, that were used to determine the thickness of the silicon nitride layer that it is oxidized and the quantity of silicon from the substrate that it is consumed.

With these steps, the result of the LAO process was analyzed by quantifying the height of the oxidized area by AFM, the extension of the oxide into the silicon nitride layer, the consumption of silicon from the substrate, and the properties of the remaining silicon nitride when the layer was not completely oxidized.

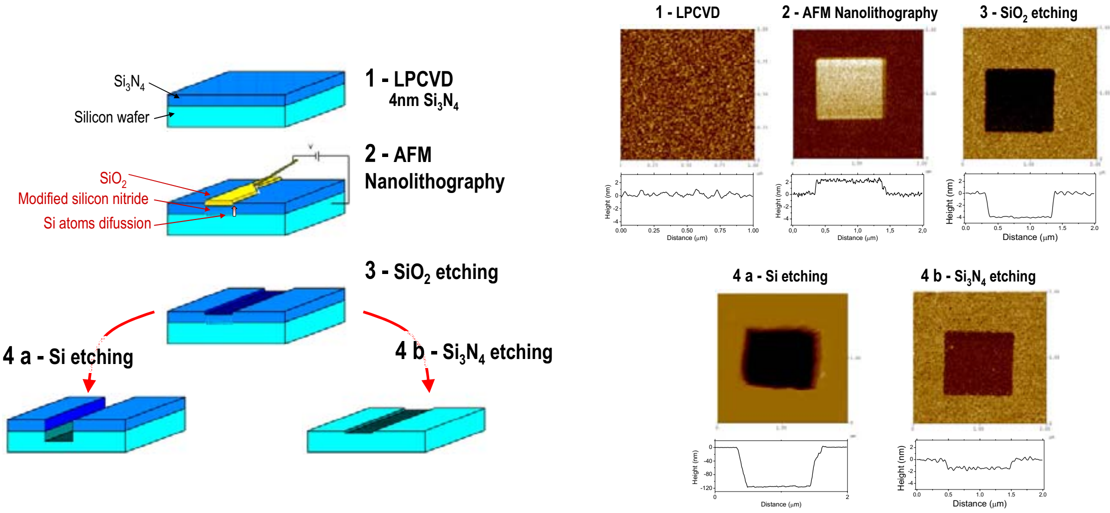

Figure 30. Scheme (left) and AFM images and profiles (right) of the process, showing the different materials created and consumed. After the deposition of the thin film of Si3N4 by LPCVD (step 1), it was oxidized with the AFM (step 2). The created oxide was removed in an HF solution (step 3). Then, the features can be transferred into the substrate, using the non-modified material as a mask (step 4a) or, on the other hand, the non-modified material can be removed, and, unexpectedly, a hole appeared (step 4b).

First, the dependence of the **oxide growth** on the applied voltage was obtained (step 1). Figure 31 shows the resulting oxide height as a function of applied voltage for different scanning velocities. Experiments were performed for both films thicknesses. The dependence of oxide growth on the applied voltage was linear for low voltages, as it had been reported before [13]. We observed that for higher voltages it got to a saturation point, from which the dependence of oxide height on voltage decreased. For the sample with the thinner film, appreciable oxide growth appeared for lower voltages (4V) than those needed for the 10 nm film (8V). But the saturation point was reached at the same oxide height in both samples. It is remarkable that the saturation height is the same, indicating that the saturation is not related with the fact that the silicon nitride layer is completely oxidized. We attribute this behavior to a space charge effect that decreases the oxidation rate. The transport of oxyanions is hindered by the space charge build-up. Consequently, not all of the available reactants convert into oxide, resulting in self-limiting behavior [14].

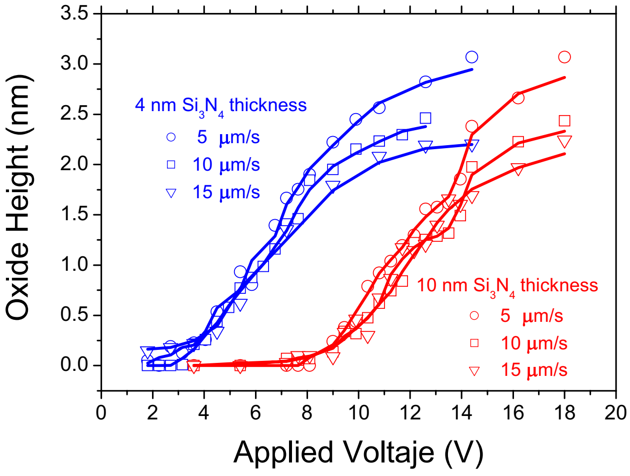

Figure 31. Oxide height as a function of the applied voltage for different velocities of the tip, and for two different thickness of the layer (4nm, blue lines; 10 nm, red lines).

By repeating these experiments for different conditions (tip velocity and applied voltage) in all the steps, the proportion of SiO_2 created (onto and inside the thin film) and the consumed silicon into the Si_3N_4 could be plotted. Figure 32 shows the results for the sample of 4 nm thickness as a function of the applied voltage. It can be observed how silicon nitride and substrate silicon are modified simultaneously for increasing voltages.

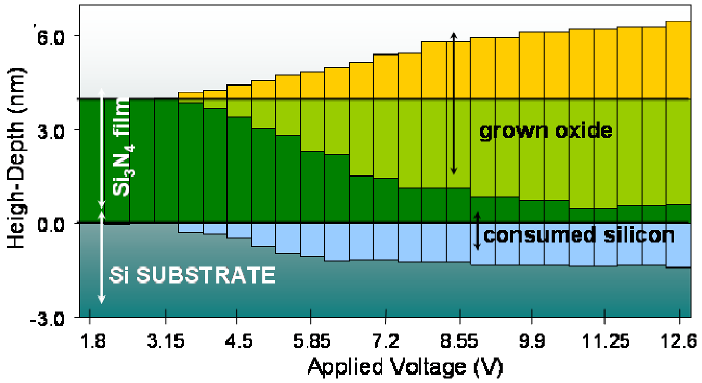

Figure 32. Scheme of the materials created and consumed, as a function of the applied voltage, constructed from the AFM topographical images after each process step.

The AFM images revealed that after etching the oxidized area with *sioetch*, the resulting hole was shallower than the thickness of the film, indicating that some material remained on top of the silicon surface. It is remarkable that this remaining material was modified with respect to the initial silicon nitride because it did not sustain the TMAH etching (Figure 33). SEM images revealed that the unmodified silicon nitride film remains after the etching. It was also remarkable that even in this case, the underlying silicon in the substrate was consumed, because a depression appeared in the silicon surface after removing the silicon nitride. Figure 33(a) shows an AFM image of a sample, where small areas were oxidized at different conditions (voltages and tip velocities), thus, obtaining different thicknesses of SiO_2. After removing the oxide, the sample was immersed in TMAH. The SEM image of Figure 33(b), obtained afterwards, shows that the areas are etched into the substrate even for the thinnest oxide. This means that the underlying Si_3N4 is not acting as a mask against the TMAH anymore, what is caused by enrichment in Si, what leads to a poorer selectivity. This is a huge advantage, as there is no need to oxidize the whole film, which makes the process faster and improves the resolution.

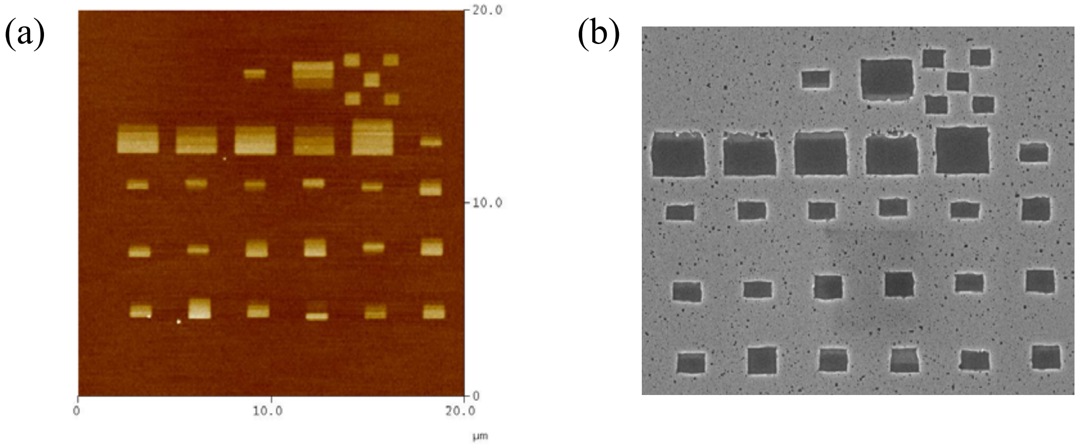

Figure 33. (a) AFM image of various areas of 1 x 1 µm^2, 2 x 2µm^2 and 0.5 x 0.5 µm^2 oxidized with the described process, by varying the applied voltage and the scanning velocity. (b) SEM image of the same area, after a Sioetch etching (6 seconds long), and a TMAH etching (30 seconds long). In all the cases, it can be observed that the oxide growth is correlated to the features transfer into the substrate.

In consequence, different kinds of reactions seemed to be taking place during the LAO process. In order to gain more insight into the process, the kinetics of the oxidation and the flowing of the electrical current during the oxidation were studied.

2.1-2:c.- Current measurements and LAO mechanism

Monitoring of the electrical current during the oxidation showed that, under these conditions, the measured current is kept constant when the voltage is constant (i.e, the oxidation was performed at constant electrochemical current). This situation allows a better characterization of the electrochemical current than in previous reported studies, where the current showed spikes due to the transient when switching on the voltage [15-17].

The electrical current was acquired while scanning the 1µm x 1 µm areas. The voltage was kept constant for ¼ of the area, and changed for every quarter until the full area was scanned. As a result, oxidized squared areas with different height stripes were obtained. Figure 34(a) shows the topographic image of one of these areas (top view on the left, 3 dimensional view on the right), obtained at a tip velocity of 15 µm/s. Steps can be observed as a consequence of voltage variations; from top to bottom 5.4, 7.2, 9 and 10.8 volts were applied, resulting in 0.6, 1.2, 1.8 and 2.2 nm oxide height respectively. Figure 34(b) shows electrical current measured during the oxidation process. For a certain tip velocity, when voltage is kept constant, the electrical current intensity remains also constant. In the case of figure 3, the current levels vary from 1.2 to 3 pA.

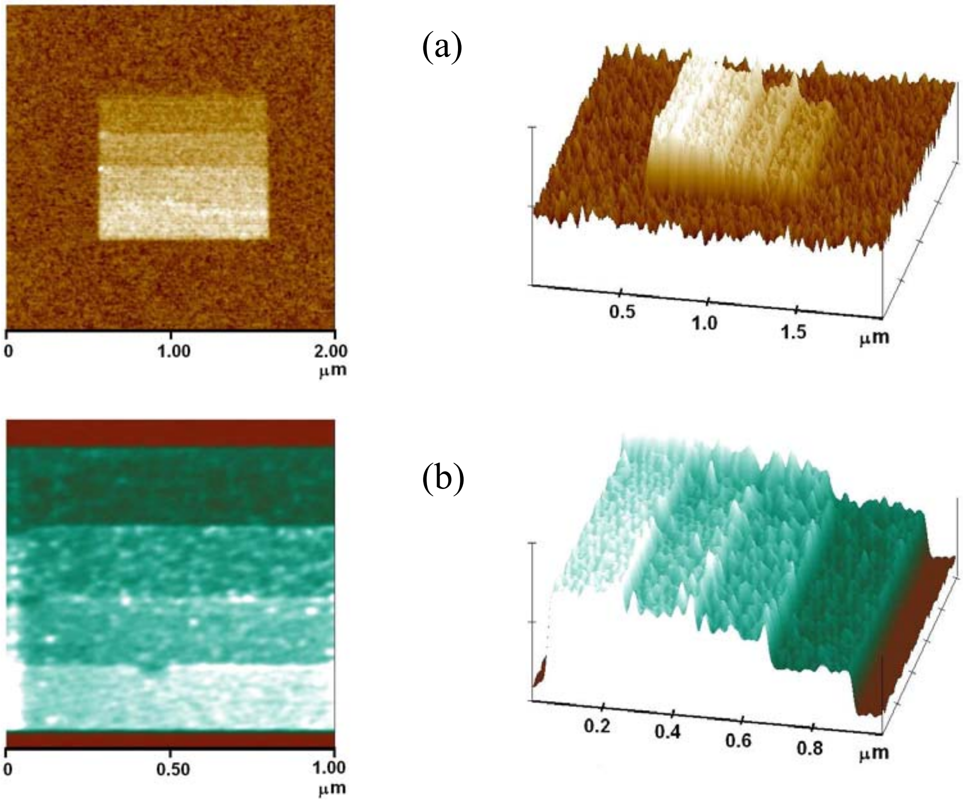

Figure 34. AFM image of the oxidation results of LAO, obtained changing the applied voltage while scanning at 15 µm/s. The voltages are 5.4, 7.2, 9 and 10.8 V, and the measured oxide heights are 0.6, 1.2, 1.8 and 2.2 nm respectively. (b) The corresponding electrical currents measured simultaneously to the LAO of pattern in figure 3.a. The current varies from 1.2 to 3 pA.

Figure 35(a) shows the relation between the resulting oxide height and the measured electrical current for different scanning velocities.

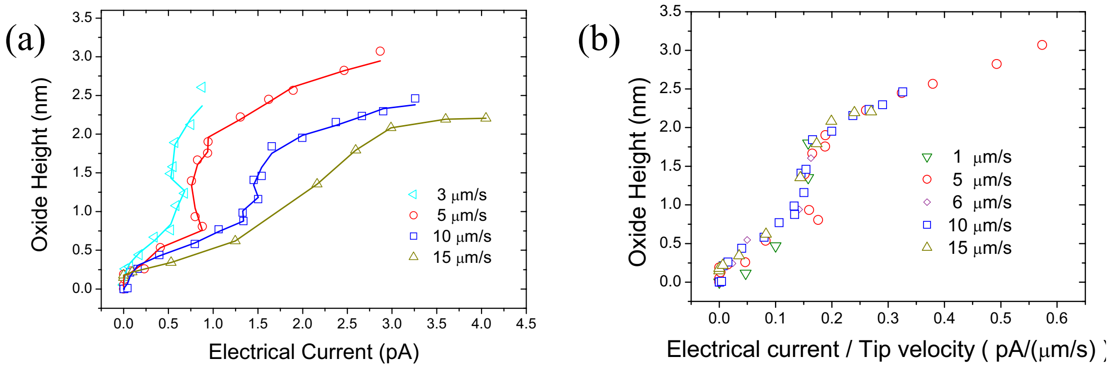

Figure 35. Oxide height dependence on electrical current (a) and on injected charge (b) for different tip velocities.

If we divide the current intensity (I) by tip velocity (v), we obtain a measure of the total injected charge (Q). As we observe that the current I is constant during the oxidation, we can assume that:

$$Q = I \cdot t \qquad (1)$$

then, the oxidation time, t, can be calculated from *v* and the dimensions of the oxidized area,

$$t = scanned\_lenght / v \qquad (2)$$

and finally, the total injected charge can be written as:

$$Q \propto I / v \qquad (3)$$

We obtained that curves corresponding to current measurements taken at different velocities follow exactly the same trend, as can be seen in Figure 35(b). This is an evidence of the reliability of the measures and that all the measured electrical current is due to the electrochemical reaction. Compared to current detection during oxidation in other systems [18] [19], tunnelling current was not present at low voltages, because of the insulating characteristics of the SiN layer. In consequence, additional information about the oxidation process could obtained from the analysis of the electrochemical current detection.

It is remarkable that the curves in Figure 35(b) show a fast increase of height between 1 nm and 2 nm. To understand this behaviour, we had to attend to the different electrochemical reactions taking place. The first reaction to consider consists on the conversion of Si_3N_4 to SiO_x. This reaction, considering that most of the created oxide corresponds to SiO_2 can be described as follows [20]:

$$Si_3N_4 + 6OH^- \rightarrow 3SiO_2 + 2N_2 + 6e^- \qquad (4)$$

We also observed that substrate silicon was consumed during the LAO process. It could be due to two reasons: silicon oxidation or silicon incorporation into the Si_3N_4 film.

Oxidation of silicon could be possible assuming that the accelerated OH were able to go thorough the film and react with the underlying silicon. Then, the observed hole in Figure 32 (step 4b) should be due to the eliminated SiO_2 by the H_3PO_4 etching. This reaction has been reported before [7], and it is described as follows:

$$Si + 2OH^- \rightarrow SiO_2 + 2e^- + H_2 \qquad (5)$$

Both reactions introduce 2 electrons for each molecule of SiO_2 produced, but the volume expansion is different in each case.

The measured hole both in silicon nitride film and in silicon substrate (after Sioetch and H_3PO_4 dipping, respectively) can be related to the consumed volume of silicon and silicon nitride to create the oxide. Figure 36 (a) and (b) show the comparison between the expected current, calculated from the volume measurements extracted from the data of figure 2 (assuming that consumed silicon is converted into silicon oxide) and the detected current acquired at a tip velocity of 5 µm/s and 10 µm/s, respectively.

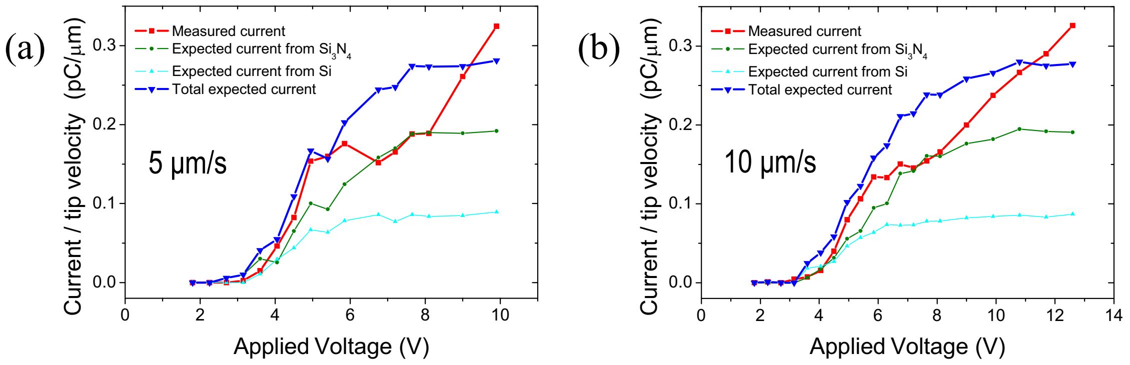

Figure 36. Expected current is plotted for the individual current components (Si oxidation and Si_3N_4 transformation to SiO_2), as well as their sum, and the measured current, for patterns made at a tip velocity of 5 µm/s in (a) and 10 µm/s (b).

We represent the fraction of the current for silicon and silicon nitride oxidation, as well as its sum. The measured current and the total expected current coincide until the oxide height reaches 0.85 nm. For voltages higher than 4 volts, both curves starts to diverge, that corresponds to the voltage when silicon consumption is already maximum, as can be seen in Figure 32. In consequence, current measurements do not support the idea that the silicon consumption is due to silicon oxidation.

Chemical etching is another evidence of substrate silicon atoms incorporation into the silicon nitride film. If the underlying silicon would be oxidized, it wouldn't be possible to transfer the lines to the substrate as shown Figure 30 (step 4a) because of the high selectivity of TMAH between silicon and silicon oxide as it is shown in table 1 in the experimental section. So we can conclude that substrate silicon is not oxidized.

On the other hand, the second possible reaction involves the **incorporation of silicon atoms into the silicon nitride film**. This behaviour has been reported before. Gritsenko et al. [21] measured Si-Si bonds in the Si_3N_4/thermal SiO_2 interface, what indicates a Si excess in the silicon nitride. Gwo et al [20] , also observed this excess of silicon in the silicon nitride layer after LAO. This description fits our experimental results. The incorporation of silicon into the film would explain the hole shown in Figure 30 (step 4b). Silicon atoms are incorporated into the silicon nitride film, modifying its composition from Si_3N_4 to Si_xN_4 ($x>3$) and leaving a hole in the substrate. This modification of the film by an excess of silicon would explain the fact that the bottom modified silicon nitride sustains the *Sioetch* but not the TMAH etching.

2.1-2:d.- Comparison with LAO in bulk silicon

With these studies, it was found that LAO of thin films of Si_3N_4 was a very robust and reliable process. These diffusion processes of the silicon atoms from the substrate into the Si_3N_4 film had an important impact on the processing conditions for further fabrication of stamps: low voltages and fast velocities could be used, as, for etching into the silicon, there was no need to oxidize the complete film.

In order to prove the clear advantages of performing LAO using a thin film of silicon nitride, compared to bulk materials, the same procedure was followed on bare silicon wafers. Figure 37 shows the total oxide thickness (h+d) obtained for bulk silicon and for a 4 nm Si_3N_4 layer. It is relevant to observe that LAO of thin silicon nitride films require the use of lower voltages than for LAO of silicon. This is quite remarkable taking into account that the silicon nitride layer is insulating, and in consequence the electrical field is lower in the case of oxidation of silicon nitride compared to the oxidation of silicon surfaces.

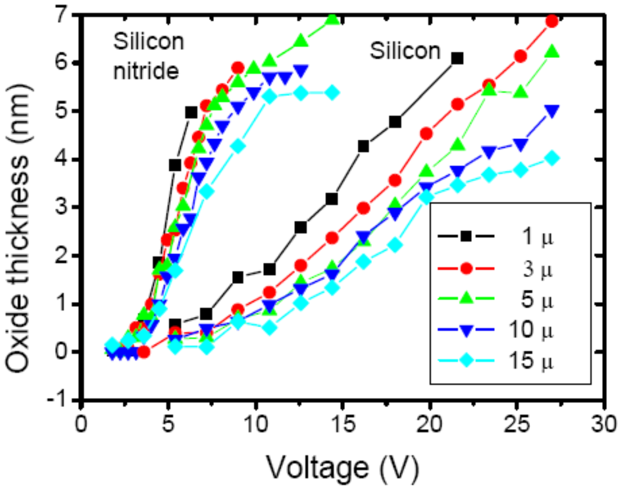

Figure 37. Comparison of total oxide thickness dependence on voltage for LAO of bulk silicon and silicon nitride thin film, for different tip velocities. For silicon, the dependence is lineal, but for the Si_3N_4 the dependence decreases for higher oxide thickness. Silicon nitride oxidizes for lower voltages and faster tip velocities than those required for silicon.

From the relation between the height of the oxidized area (h) and the depth of the hole (d) after a selective etching of the silicon nitride layer, we can get insight into the composition of the oxide. Figure 38 shows the result for oxidation of silicon and silicon nitride. We obtain a volume expansion factor (h+d)/d of 1.8 for the oxidation of silicon nitride, close to the expected value for the thermal oxidation of silicon nitride (1.64). On the other hand, we obtain an expansion factor for silicon oxidation of 2.6, much larger than the one corresponding to the thermal oxidation of silicon (2.27). This indicates that the silicon oxide corresponding to the oxidation of the silicon nitride is closer to the expected density (thermal oxidation) than the oxide resulting from oxidizing silicon surfaces.

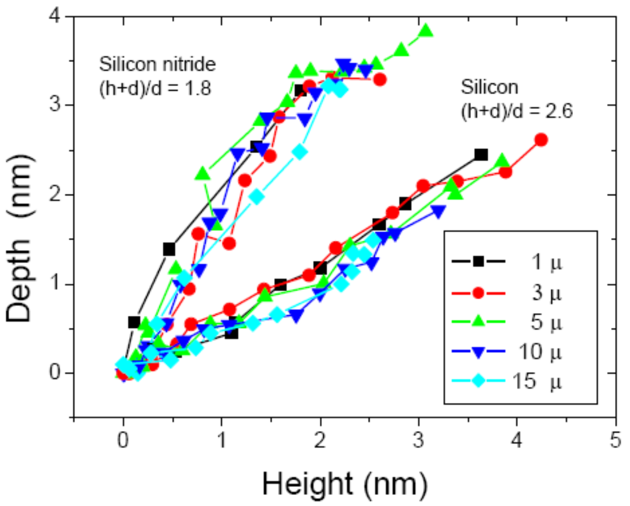

Figure 38. Comparison of the consumed silicon or silicon nitride (d: depth of the hole after the etching) as a function of oxide height (h) for different tip velocities. Average slopes are 1.25 for silicon nitride and 0.62 for silicon. The ratio (h+d)/d indicates the volume expansion factor. For silicon, a 2.6 factor is obtained (2.27 is the value for the thermal grown oxide), and 1.8 for silicon nitride (1.64 for thermal grown oxide).

Once again, to obtain more information about the oxidation mechanism the relation between oxide thickness (which is proportional to the total volume of oxide assuming a constant height on the whole squared pattern) and total injected charge (electrical current/ tip velocity) was studied. Figure 39 shows the data obtained from silicon nitride film at different scanning velocities, compared with data obtained from the oxidation of silicon surfaces). It is remarkable that for small oxide thicknesses (that corresponds to low voltages) we observe that the oxide height is independent of tip velocity, so that we can conclude that all the measured current is originated from an electrochemical reaction. For oxidation of silicon nitride, two regimes can be observed, separated by a jump between 3 and 5 nm of the oxide thickness. This makes evident that the oxidation process is difference compared to the oxidation of silicon. We already attributed above the jump to the regime when the oxidation of silicon nitride is dominant (smaller thickness) to the regime when the incorporation of silicon to the films is dominating.

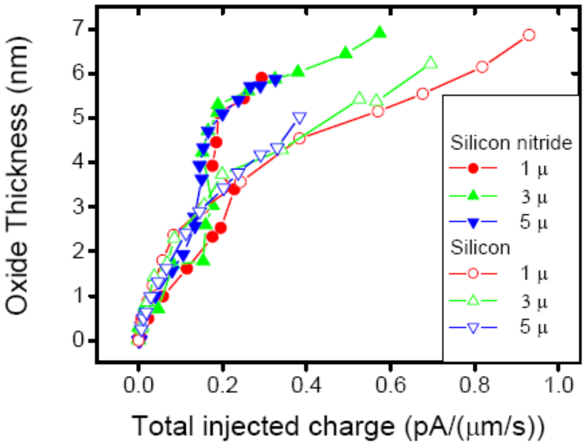

Figure 39. Comparison of oxide thickness dependence on total injected charge (measured current/tip velocity) for silicon and silicon nitride thin film for different tip velocities. Data at different velocity follow the same trend for low oxide thicknesses, but diverge for higher. For silicon nitride, two regimes appear, indicating the existence of two different phenomena/reactions that are taking place simultaneously.

From the above experiments, we can draw an overall view of the main aspects of the LAO of thin silicon nitride layers. Compared to the oxidation of silicon, it proceeds at lower voltages and the final density of the oxide is closer than the expected from thermal oxidation. Moreover, the whole thickness of the thin layer is modified even for low voltages. These observations indicate that the ionic transport through the silicon nitride layer (which is required for the electrochemical reaction to take place) is enhanced compared to LAO of silicon. A plausible explanation can be found attending to the role of space-charge build-up during the oxide growth [7, 22], which is decreased in the case of the oxidation of silicon nitride, and in consequence, the ionic transport is enhanced and less charge-related defects are created.

All these observations and results allowed to draw an overall view on the basics and details of this technique, and showed that is a very appropriate technique for rapid prototyping of nanofeatures.

2.2.- EXAMPLES OF STAMPS FABRICATION

Once the most suitable method for patterning has been chosen, attending to the stamp requirements (size, resolution, extension of the patterned area, etc), the post process has to be optimized (dry or wet), to successfully achieve the desired structures.

Next, we show some examples of stamps fabrication, that will be used for different types of applications. Various patterning techniques and post-processing were chosen to achieve the optimal compromise between robustness, resolution, reproducibility and troughput.

2.2-1. Pillars arrays fabricated by e-beam, RIE and oxidation

Dots or pillars of a given diameter are often needed for several applications (as will be described in chapter 4). The most direct and simple approach is to define the dots by e-beam, and then do lift-off and/or a RIE, to define the pillars. Figure 40 shows the scheme of this direct fabrication process (a-e) as well as a SEM image of a stamp obtained following these steps (f).

(a) EBL (b) Metallization (c) Lift-off

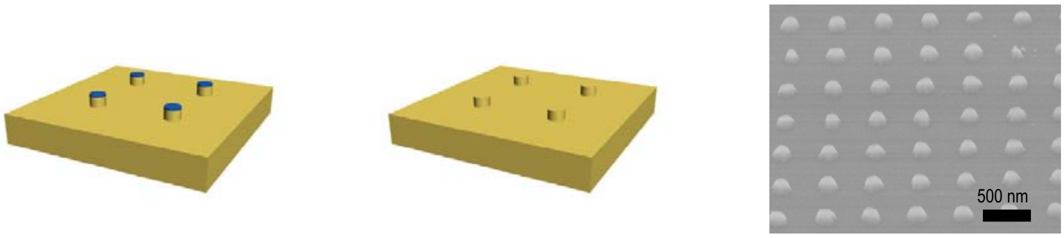

(d) RIE (e) Metal removing (f) Example

Figure 40. Scheme of the fabrication of pillars. The mask for the etching of the pillars is defined by EBL (a), metallization (b), and lift-off (c). Then, a RIE transfers the pattern into the substrate (d). After removing the remaining metal (e), the stamp is fabricated. (f) shows a SEM image of a pillar array fabricated following this procedure.

For certain applications, very small dimensions are required. Figure 41 shows SEM of pillars fabricated following this method, that have a pitch of 200 nm and a diameter of 100 nm.

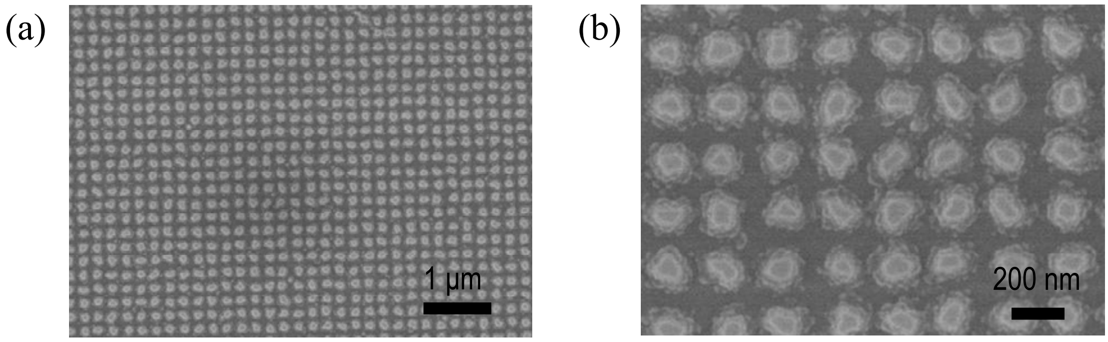

Figure 41. SEM images with different magnifications of the stamp containing the pillars.

It can be seen that the shape of the dots with very small diameters (~ 100 nm) is not very rounded nor smooth. The beam instability may affect their shape and current oscillation may lead to variations in the diameter. Even further, the sputtering equipment often used for metallization and the RIE recipes to etch the structures into the substrate were not very well adapted for nanoscale dimensions, leaving to rough and inhomogeneous patterns.

A different approach, reliable to improve the quality, consists on starting from wider pillars fabricated following the same procedure, and use them as a master stamp to do several replications (via imprinting, and lift.off). Each of this replicas can be oxidized, and the oxide selectively removed in *sioetch*. This reduces the diameter of the pillars, so several stamps containing similar features with different lateral sizes can be easily fabricated. Figure 42 shows SEM images of a master stamp (a) (400 nm diameter) and the replicas, where the lateral dimensions have been reduced down to 200 nm in (b) and 100 nm in (c).

A drawback of this method is that the pitch cannot be varied.

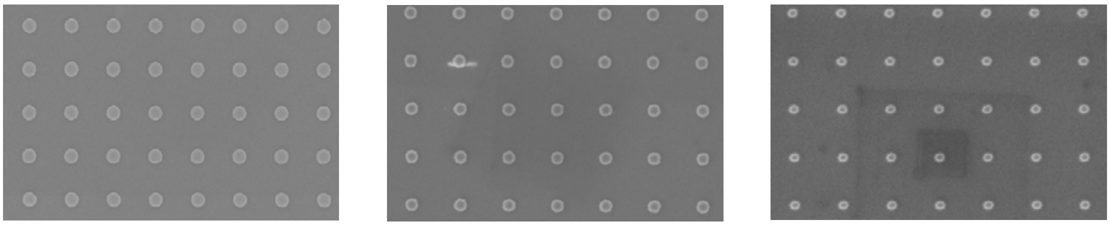

(a) Master Stamp,
$\phi \approx 400$nm

(b) Replica 1,
30 min of oxidation
$\phi \approx 250$nm

(c) Replica 2,
60 min of oxidation
$\phi \approx 100$nm

Figure 42. Oxidation of silicon pillars. The starting master silicon stamp (top) had pillars of 400 nm diameter. The obtained replicas were 250 nm diameter, after a wet oxidation of 1h, and 100nm diameter, after 2 hours oxidation.

2.2-2. Fabrication of triangular shaped lines

As will be described in Chapter 3, triangular-shaped channels with very smooth sidewalls and a well-know (and preferably fix) angle were needed for rheological measurements. The geometry and smoothness were very important, so the stamp design and the optimization of the fabrication process had to be carefully studied. This task was developed in collaboration with MIC[**], and some of the steps needed for the fabrication were done by using their cleanroom facilities.

2.2-2:a.- Anisotropic etching of silicon

Although triangular shape structures could be obtained by dry etching (Figure 43), the geometry and the slope of the structures were not precisely controlled. Instead, anisotropic wet etching of silicon was a robust and suitable method for this purpose: the structures result in a well-defined slope.

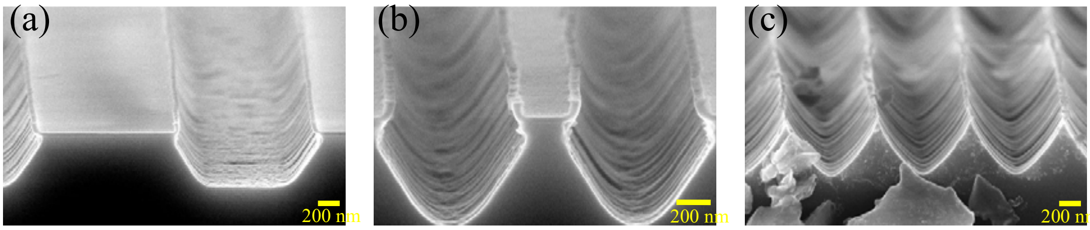

Figure 43. Dry etching of Silicon, for various recipes, in order to obtain non-vertical sidewalls.

The etching step was crucial in the fabrication process, and alignment between the crystallographic planes of the substrate and the mask strongly influences the quality of the obtained structures. In principle, it is limited by the alignment accuracy between the wafer flat and the silicon crystal directions when defining the mask by EBL. Suppliers claim that this accuracy is better than 1°. Even for this slight misalignment, rough sidewalls appeared, as can be seen in the SEM image of Figure 44.

[**] MIC, now DTU•Nanotech, Technical University of Denmark. 2800 Kogens Lyngby (Denmark)

Figure 44. SEM image of triangular shaped channels, fabricated by anisotropic wet etching of silicon, where the mask is not aligned with respect to the crystallographic planes of the silicon substrate. Rough sidewalls appear as a consequence.

A detailed study of the silicon wet etching was carried out with the help of models and simulations, in order to get a deeper insight in the process.

2.2-2:b.- Alignment and simulations

Anisotropic etching simulations were done using a program called "Anisotropic Crystalline Etching Simulation – ACES[††]". It can simulate silicon etching with different front-surface orientations in different etchants, for wet or dry processing. The etching time and the mask are defined by the user.

Figure 45 shows the simulations of an anisotropic wet etching process of a silicon (100) substrate, obtained for two different line-shaped masks, as shown in the first image: aligned (left) and 2º misaligned (right) with respect to the crystallographic planes. For the reactives commonly used for wet etching (i.e. TMAH and KOH) the etching ratio of the (100) planes is much faster than for the (111) planes. Thus, the etch in depth "stops" when the (111) planes meet (at t_3, in the simulations), what leads to the typicall triangular shape when using (100) silicon wafers. In the aligned structure, the process finishes at this point, and the shape does not change for longer etching times, as can be seen in Figure 45 for t4, t5 and t6[‡‡]. In the misaligned one, also, the depth does not change from that obtained at t3. In this case, as a result of the misalignment, "steps" appear in the sidewalls. For **longer processing times**, these **steps are etched away**, and the final line broadens. For t4, t5 and t6, the evolution of one of the steps has been marked with an arrow. Thus, by enlarging the etching time, very smooth sidewalls can be obtained even if the mask is not perfectly aligned, as shown in Figure 45 (t6).

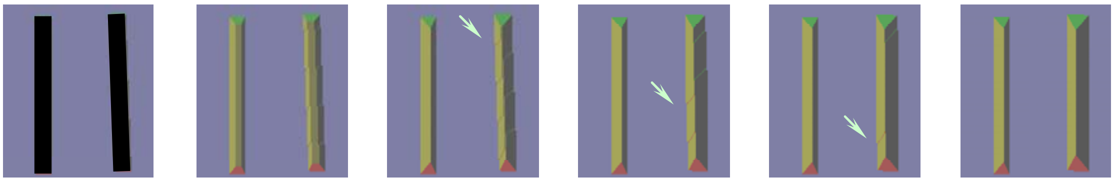
mask t_1 t_3 t_4 t_5 t_6

Figure 45. Simulation of the anisotropic etching of silicon, depending on the etching time, comparing the result for an aligned and not aligned line, acting as masks. In t1, the lines are not etched to completion yet, and in the not aligned line "steps" can be observed, corresponding to $\{111\}$ planes. In t2, both lines are etched to completion (for longer etching times, depth will not change). For longer etching times, steps can be observed to advance along the line, following the right crystal direction (t2, t3, t4), until they achieve the opposite extreme of the line (t5).

■ mask; 🟪 top (100) planes; 🟫 bottom (100) planes; 🟩 🟥 🟨 ▨ (111) planes of Silicon ;

[††] Developed by the Micro Actuators, Sensors and Systems Group (MASS), at the Center of Compound Semiconductor Microelectronics, University of Illinois at Urbana-Champaign. http://galaxy.micro.uiuc.edu

[‡‡] This is not accurate. The etching continues, but the rate for the $\{111\}$ planes is very slow (0.015 µm/min). Thus, for normal etching times, the etching of these planes is negligible.

2.2-2:c.- Pattern design and E-Beam Lithography

To define the lines mask, e-beam was performed using a negative resist (SAL601), to avoid the inclusion of other fabrication steps to inverse the mask.

The pattern design consisted on arrays of lines, 300 nm wide, with a pitch of 900 nm, covering areas of 100 µm x 100 µm.

As shown in the simulated images (Figure 45), long etching give as a result trenches with wider lateral dimensions than those patterned. This change in the width of the structures is not important for the final goal of the application, as the slope remains constant. However, the broadening of the lines had to be taken into account because of a possible overetching if adjacent lines get in contact. For a misalignment of 1º, a 100 µm long line becomes 1.7 µm broader. Dividing the length by a factor of 4, the broadness is also decreased down to 400 nm (Figure 46). Figure 46 shows the tolerance for the misalignment angle for these geometrical specifications.

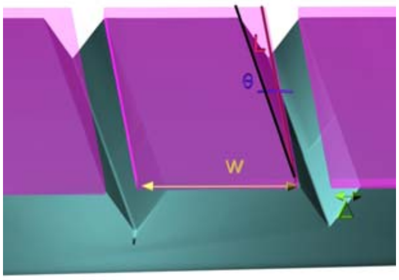

$$\Delta = L \cdot \tan(\theta) \approx L \cdot \theta$$

$$\Delta \le w \Rightarrow \theta \le \frac{w}{L}$$

$$L = 25\mu m \quad w = 600nm$$

$$\boxed{\theta \le 1.37^{\circ}}$$

Figure 46. . Scheme and calculations of the misalignment angle (θ) tolerable for 25 µm long (L) lines, 300 nm wide, separated 600 nm (w). If the broadening, Δ, equals w, adjacent lines will get in contact and the pattern will be etched away.

The pattern design was conveniently modified to maintain a total area of 100 x 100 µm^2 and take these specifications into account, by substituting long continuous lines with 4 shorter lines, 25 µm long.

Other aspects of the pattern design had to take into account the long etching step. A frame had to be added to EBL pattern, acting as "etching stoppers", at the extremes, avoiding the shortening of the lines, as it is shown in Figure 47.

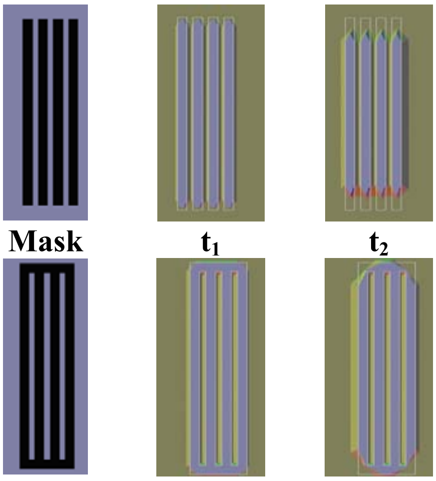

Figure 47. Simulation of anisotropic etching of silicon, comparing a mask made of lines, and a similar one, but with a frame, for different etching times. Underetching along the mask is observed.

■ *Mask;*
🟪 *top (100) planes;* 🟫 *bottom (100) planes;*
🟩 🟥
🟨 🟫 *(111) planes of silicon.*

This effect was even worse at the corners, as can be seen in the top row of Figure 48, where the mask design is shown ((a) and (d)), together with SEM images of silicon structures obtained before ((b) and (e)) and after removing the mask ((c) and (f)). A large line (length > 25 µm) was added in the corners of each square (Figure 48(d)), that effectively avoided the overetching at the corners, as can be seen in (e) and (f).

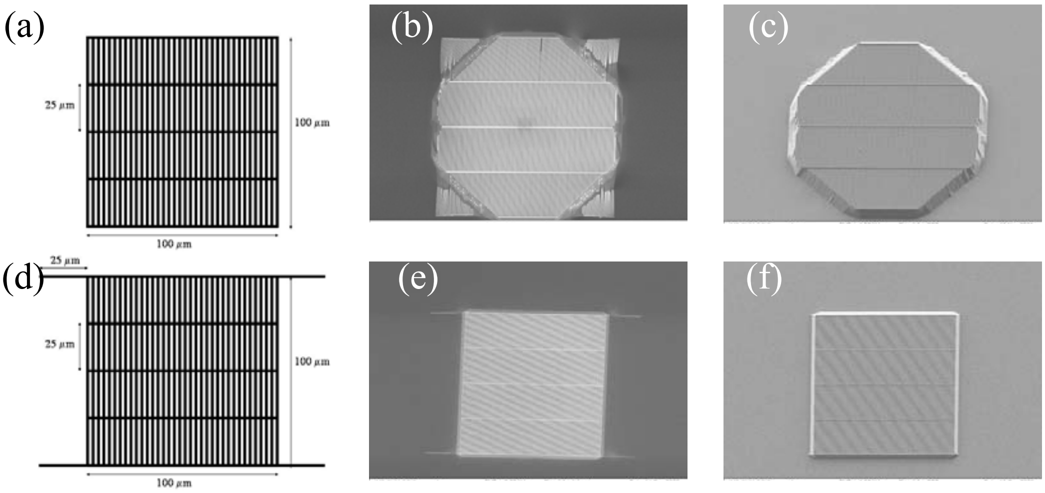

Figure 48. Figure 9. Mask drawing ((a) and (d)) and SEM images of the etching results with the oxide mask ((b) and (e)) and the resulting pattern without it ((c) and (f)) for a mask without long corners (first row) and with them.

The combination of patterning a negative resist (where only the patterned lines remain covered by the resist after developing) and longer etching times (than those necessary for etching to completion of the pattern lines), gives as a result an interesting structure: the triangular shape etched lines lye in the top of a mesa, several microns high (see Figure 49). This configuration is very attractive for NIL stamps, as LISA structures [23] are avoided during the imprinting process.

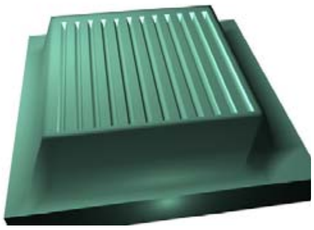

Figure 49. Drawing of the geometry of a pattern (100 x 100 µm^2) of the stamp: small triangular lines (some hundreds of nanometers wide and depth), on the top of a high mesa (some microns in height).

2.2-2:d.- Final design, detailed process and fabricated stamps

The final design shown above (first image in the bottom row of Figure 49) was repeated several times, with a separation between them of 100 µm, completing a 20 x 20 array, in the middle of a 4 inch wafer, as schematized in Figure 50.

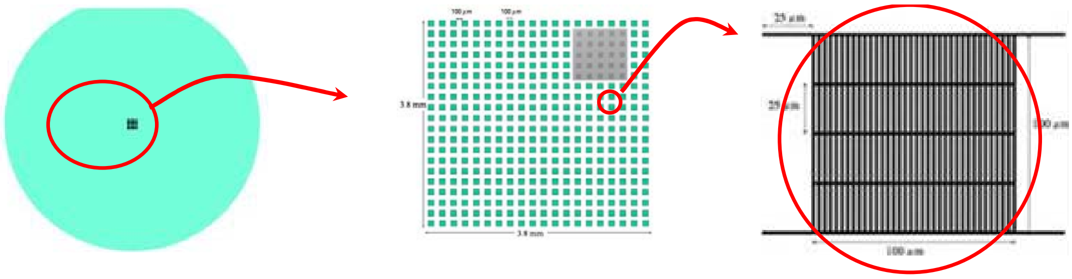

Figure 50. Drawings of the pattern distribution in the centre of a 4 inch wafer (left), scheme of the 20 x 20 array (middle) and design for each EBL pattern (right).

Few minutes of etching were sufficient for defining the triangular shape of the channels (1 min 30 seconds for a 600 nm wide line). However, the etching time was increased up to 15 minutes, to ensure the complete etching of the steps that may appear as a consequence of the misalignment. The resist used for EBL did not sustain such long wet etching, so a thin thermal oxide layer was grown on the silicon surface, prior spin coating of the negative resist. After the EBL exposure and resist development, a reactive ion etching (RIE) was needed, to open the windows to the silicon substrate.

The whole final process and SEM images corresponding to each step are shown in Figure 52. The process recipes and the place of the equipment used are also listed.

Several similar stamps were fabricated. SEM images of the results are shown in Figure 51, where the typical dimensions have been marked.

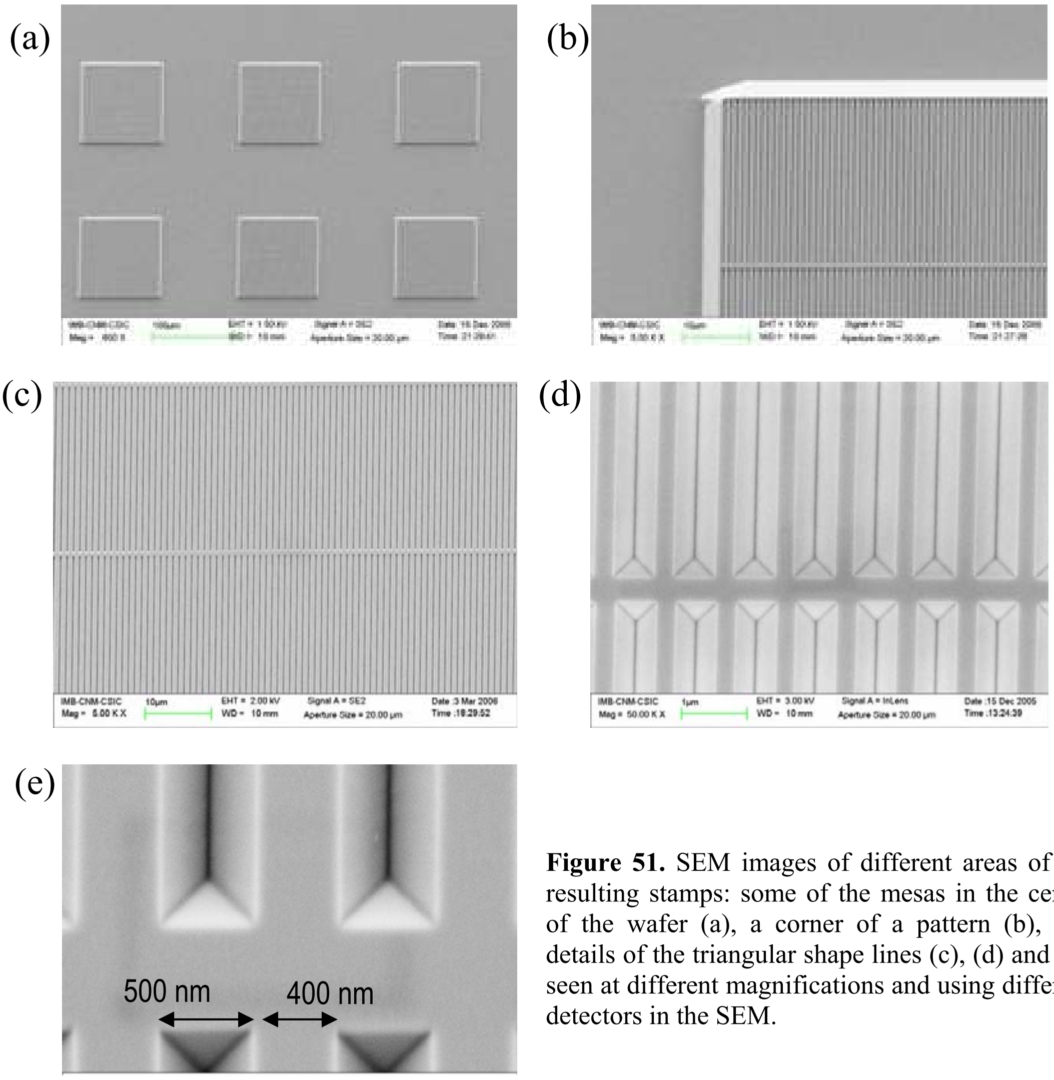

Figure 51. SEM images of different areas of the resulting stamps: some of the mesas in the center of the wafer (a), a corner of a pattern (b), and details of the triangular shape lines (c), (d) and (e), seen at different magnifications and using different detectors in the SEM.

These stamps were used to measure the residual stress that is induced in the polymeric structures during the NIL process. The details of this task will be described in Chapter 3.

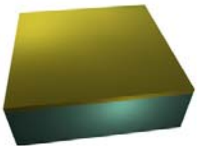

212 nm of **thermal oxide**, on a 4 inch **silicon wafer**.
(MIC)

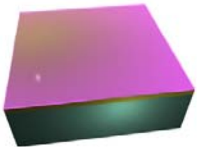

Spin-coat the **negative resist**: 240 nm of SAL 601.
(MIC)

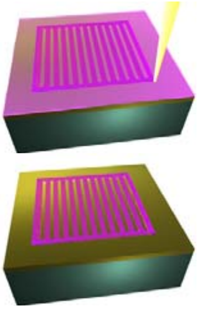

EBL exposure:
V_{acc}:100 kV, I: 6 nA,
Dose: 16 μC/cm^2.

Development of the resist:
8 min. in MF322 developer.
(MIC)

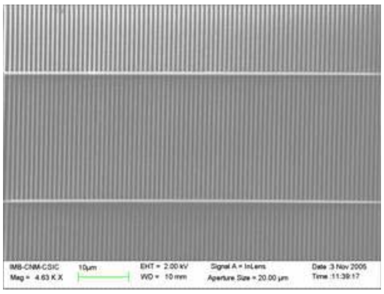

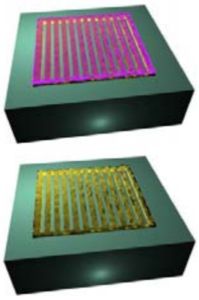

RIE of **SiO$_2$**: Alcatel GIR 160 equipment, 400W, 0.05mbar, 25 sccm of CHF$_3$, 16sccm of CF$_4$; 3 minutes.

O$_2$ plasma (15 minutes) to remove residual CHF$_3$ and the remaining resist.
(CNM)

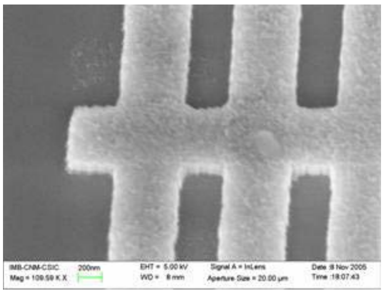

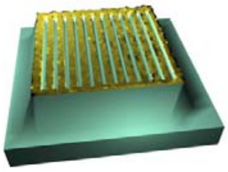

DIP in ***Sioetch*** (1 second) to remove native oxide.

TMAH (25%, 80ºC) etching for 15 minutes.
(CNM)

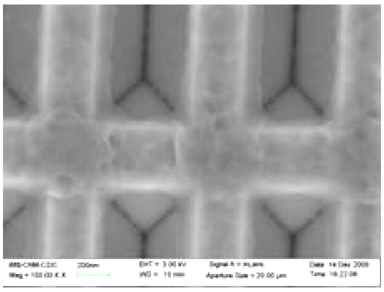

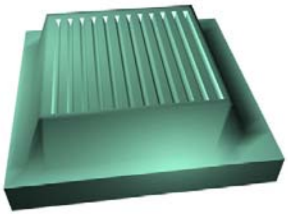

Sioetch for 2 minutes to remove the oxide.
(CNM)

Lines width ≈ 600nm
Lines depth ≈ 400nm

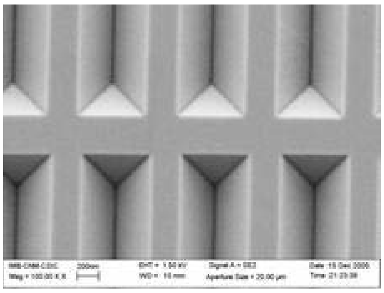

Figure 52. Drawings (left), experimental process (description, parameters and cleanroom where the step was processed) (middle) and SEM images (right) of the fabrication steps.

▭ *Resist;* ▭ *Exposed resist;* ▭ *SiO$_2$;* ▭ *Silicon.*

2.2-3. AFM-based fabrication of stamps

As already described above, LAO-based fabrication presents the main advantage of robustness and simplicity, needing very short time for the fabrication of stamps.

This method is interesting, as a stamp can be rapidly obtained [24]. The patterning may take only some minutes (depending on the pattern density and extension), and there is no need of resist spin-coating. Working at ambiend conditions avoids using vacuum chambers, that need conditioning or pumping steps. Focusing or defining the write-field are also unnecessary. Afterwards, no development is needed (it is not an additive/subtractive method, but the nature of the substrate is chemically changed) and the sample can be directly immersed in the appropriate solvents to selectively remove the mask or the un-patterned area, and to etch the features into the substrate. The wet etching takes few seconds (from 10 to 120 s, depending on the desired depth). For the materials commonly used/obtained within this process, the used solvents present a very good selectivity, as already shown in Table 2.

Figure 53 shows the complete fabrication process of a stamp by AFM LAO of Si_3N_4 thin films onto silicon substrates (a). After the definition of the pattern (b), the oxide is removed (c), and the lines transferred into the silicon substrate by a wet etching in TMAH (d). 30 seconds result in a depth of 180 nm.

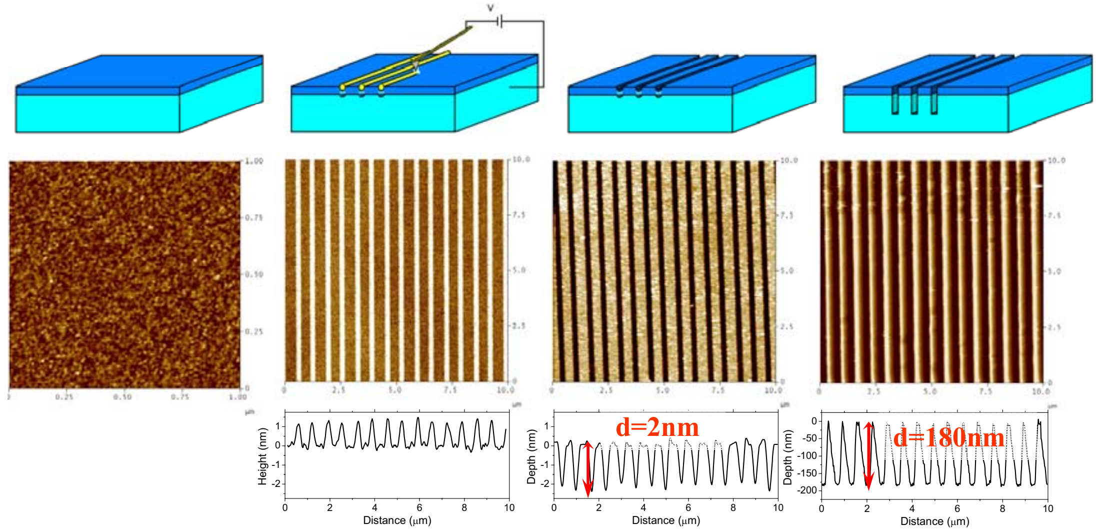

(a) LPCVD Si_3N_4 (b) Local oxidation (c) Oxide etching (d) Silicon etching

Figure 53. Fabrication process based on LAO. The silicon nitride thin film is deposited onto a silicon substrate by LPCVD (a). LAO is performed (b), and the oxide removed with sioetch (c). A TMAH etching is done, to finally transfer the pattern into the silicon substrate (d).

In order to find a trade-off between resolution and fast writting of the patterns, several lines were defined following the procedure shown in Figure 53, varying the LAO conditions (tip velocity and applied voltage). The LAO patterns were transferred to the silicon substrate by dipping the sample 6 seconds in *Sioetch* and 10 seconds in TMAH. This resulted in an approximate depth of the trenches of 60 nm. As we used Si(100), the slope of the sidewalls was 54º. This can be avoided by using Si(110) wafers, provided that the pattern is properly oriented. Figure 54 shows SEM images of the lines obtained after TMAH etching for different prototyping conditions

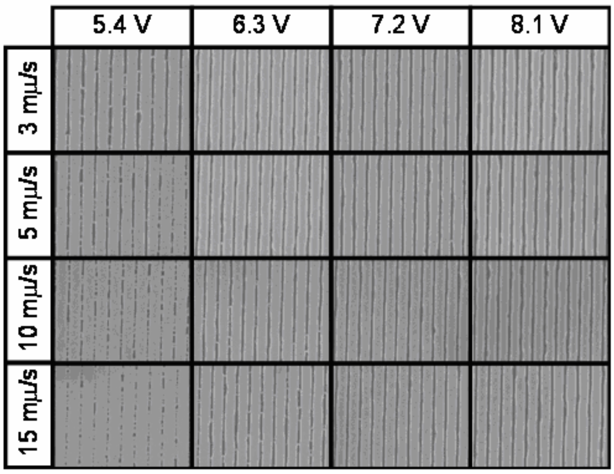

Figure 54. SEM images of 300 nm pitch lines patterned at different LAO conditions (applied voltage and tip velocity), after dipping the sample 6 s in Sioetch and 10 s in TMAH. It can be observed that for low voltages the lines are not continuous. For fast oxidation velocities, lines are straight and resolution increases.

For low voltages (~ 5V), discontinuities appear in the lines, even for low tip velocities. The number of defects is significantly reduced by increasing the voltage in less than one volt, and none is observed for voltages higher than 7V. It can be also observed that straighter lines are achieved for faster tip velocities, together with a better resolution.

As an example of the versatility of this fabrication process, suitable for stamps fabrication, we present the fabrication of stamps that can be used for the realization of sensors based on interdigitated arrays of nanoelectrodes (details of these devices will be reported in Section 3).

Figure 55 are SEM images of structures patterned with non optimized (a) and optimized (b), (c) LAO conditions. The patterns of Figure 55 (b) and (c) were obtained by applying a voltage of 6.3 V between the tip and the sample (scanning velocity: 15 μm/s), which was successfully transferred to the silicon by dipping the sample 6 seconds in Sioetch and 20 seconds in TMAH.

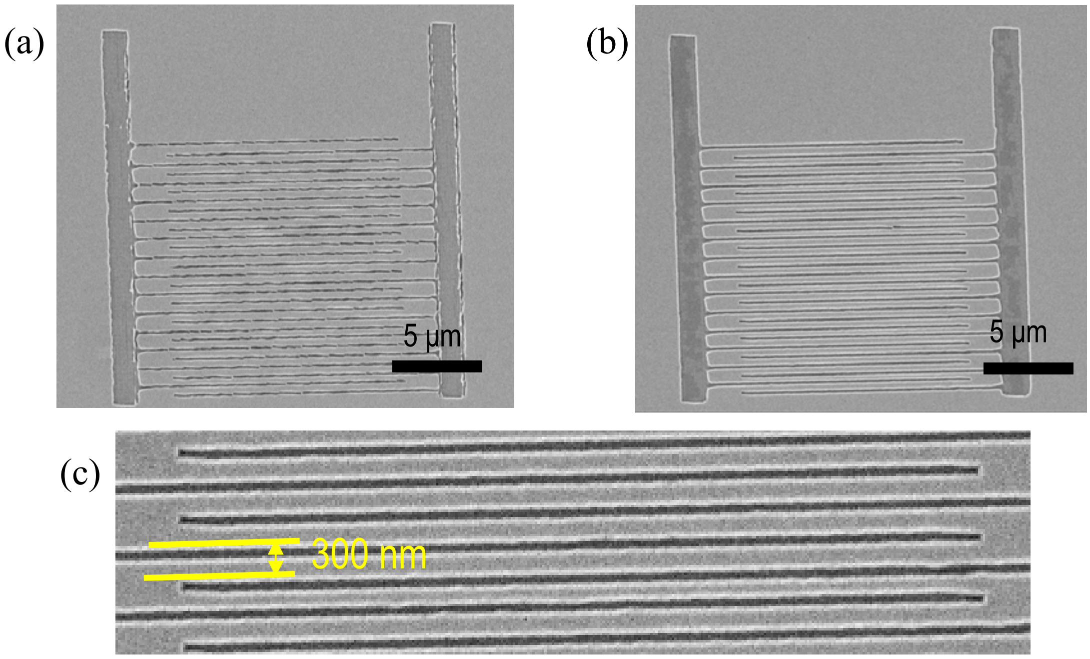

Figure 55. SEM images of a pattern defined with oxidation conditions non aggressive. As a result, the lines are not continuous (a). When the conditions are optimized, the lines appear nicer and more homogeneous, as shown in (b), and in the closer look of (c).

We used these samples as stamps for nanoimprint lithography. The stamp and the resulting imprint are shown in the SEM images of Figure 56 (a) and (b) respectively. The height of the lines was measured with AFM, resulting in an average height of 120 nm, which corresponded to the depth of the lines in the stamp.

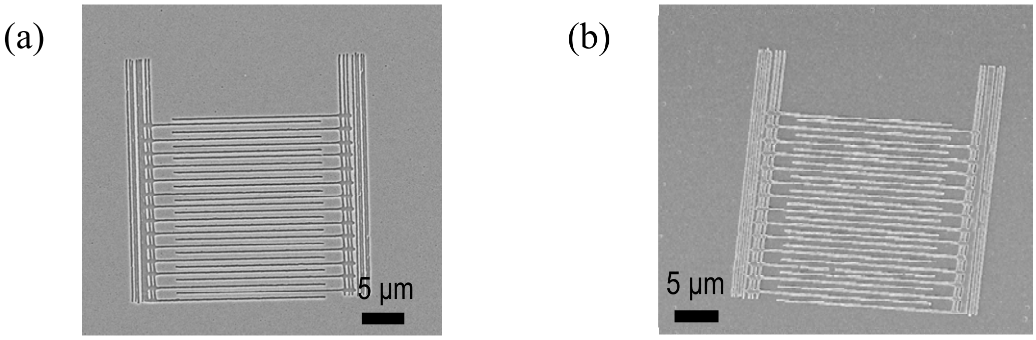

Figure 56. Stamp fabricated by AFM LAO and wet etching (a) and the resulting imprint in PMMA (b).

2.3.- FUNCTIONALIZATION OF THE STAMPS

One of the peculiarities of NIL compared to other lithographies (photon-beam, electron beam, LAO, etc) is that it is based on the full direct contact of the stamp with the polymer. This sandwiched-like method leads to adhesion problems, as the stamp and the substrate are generally made of the same material (silicon, or silicon oxide). The effective area of the stamp is larger, as it has structures. Thus, the adhesion of the polymer to the stamp will be stronger, compared to the substrate, which can cause deformations, cracking of the structures, or even peeling of the polymer film (Figure 57 (a)). Several solutions have been proposed to overcome this problem, like modified polymers, nonsticking stamp materials, etc. The most common one is the functionalization of the stamp with an antiadhesive layer, that effectively avoids the adhesion of the polymer to the stamp (Figure 57 (b)).

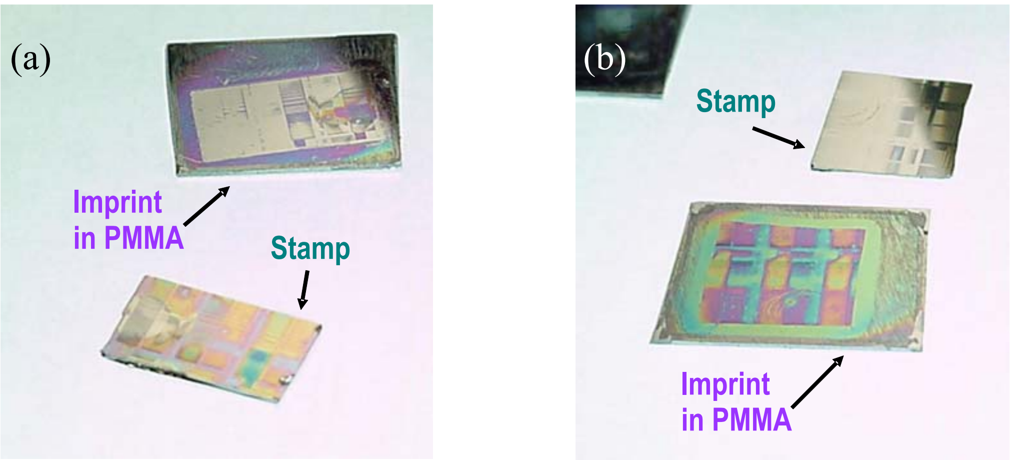

Figure 57. Comparison of the results o fan imprint with a non-functionalized stamp (a), and with a functionalized one (b). In the first case, the resist is mainly stuck to the stamp, as the total surface is larger compared to the substrate. After functionalization, the resist is structured, and remains onto the substrate, so the coating effectively avoids stiction problems.

2.3-1. Antisticking coating

Fluorinated silanes are the most interesting molecules for this application, specially those with long chains. In concrete, in this work, commercial tri-chloro silanes (F_{13}-TCS) (Figure 58 (a)), were used. These molecules have several peculiarities that make them suitable for antisticking functionalization:

- During the silanization process, the silicon atoms covalently bond to the substrate, as shown in the reaction of Figure 58 (b). The chemical nature of the link makes it strong and stable for the typical temperatures needed for NIL.
- These molecules have a strong tendency to form self-assembled monolayers, due to their asymmetric shape.
- The Fluor atoms of the chain confer the antisticking properties, due to their strong electronegativity, which makes the resulting layers highly hydrophobic.
- Silanes with longest chains have better antisticking properties, and form easier the monolayer.

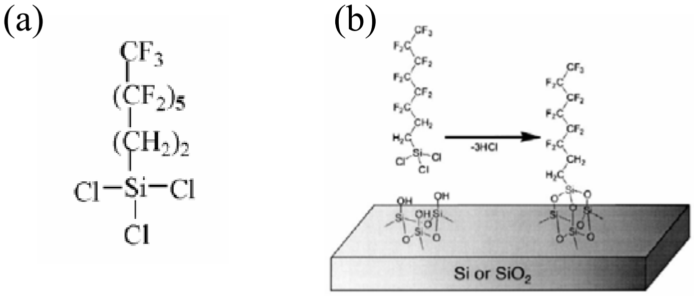

Figure 58. (a) Silane molecule (F_{13}-TCS) used to create the antiadherent functionalization. (b) Silanization reaction: the silicon atom bonds covalently to the Silicon atoms of the substrate. [25].

Even thought, not always a perfect monolayer is formed. Several defects, like molecules not bounded to the substrate, multi layers, and others appear after the deposition. This problem is solved by doing some (two or three) dummy imprints, so the contamination particles and weakly bounded molecules stick to the imprinting polymer, and only the monolayer formed by the covalently bonded silanes remains onto the stamp surface.

The formation of this monolayer can be done by liquid deposition. But, for stamps with nanometer features, non-wetting may occur, so it is better done in gas phase. This is schematized in Figure 59 [25]..

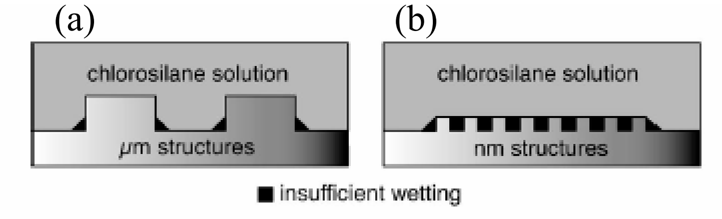

Figure 59. Liquid phase deposition for micro (a) and nano (b) structures. When the features are in the nanometric range, de-wetting effects impede the homogeneous coverage with the liquid. [25].

A robust method to deposit the F_{13}-TCS monolayer in gas phase was developed by Beck et al, [25]. The process is performed in an inert atmosphere, to avoid polymerization of the silanes in contact with humidity, according to the following steps:

a. The stamp is put inside a Petri capsule and it is heated above 250 ºC (i.e., above the vaporization temperature of the silanes) (Figure 60 (a)).

b. A drop of silanes is introduced in the Petri capsule (because of the high temperature, the liquid evaporates immediately and the silanes fill the whole volume of the capsule.

c. Then, the system is left for 2 hours to react, and the silanes form a monolayer on top of the surface.

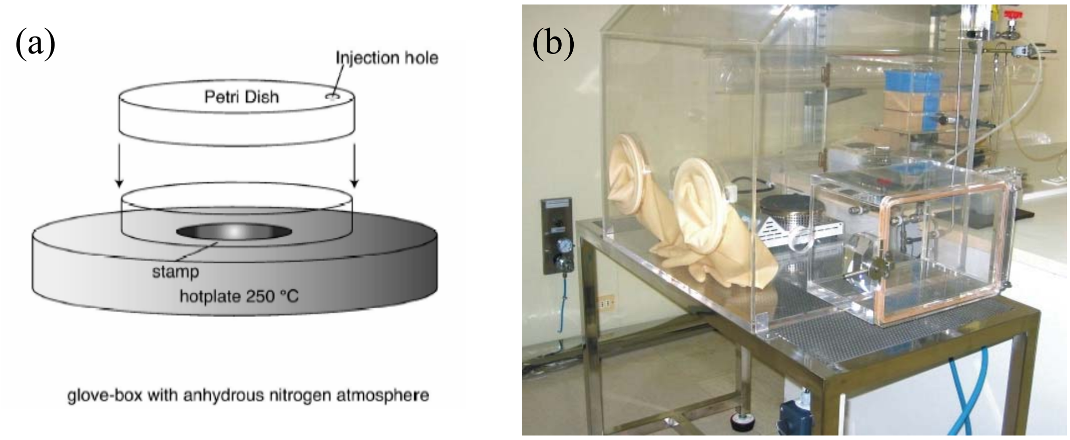

Figure 60. Scheme of a Petri capsule onto a hot plate (a), as placed inside the chamber. Glove box with nitrogen atmosphere used during this work (b).

This procedure was used at the begging of this thesis work, performed inside the glove box with N_2 shown in Figure 60 (b). This process is slow, and the result is not always as desired (burned particles may appear on the surface, and other phases are formed, resulting sometimes in non-homogeneous coating).

2.3-2. Fast functionalization

During this work we developed a simpler and faster method to deposit the F_{13}-TCS monolayer, performed at room temperature (RT) and that can also be used for deposition of other type of silanes [26]. This method takes profit of the high volatility of these chemicals, increased when the pressure is lowered, allowing a chemical vapour deposition from a liquid droplet of silanes, even at room temperature.

For this, a droplet of silanes is deposited near the sample, (Figure 61(a)) placed inside a Petri capsule (inside the glove box shown in Figure 60 (b)). Low pressure (slightly lower than ambient pressure) facilitates the evaporation of the silanes, that volatilize and react with the silicon surface of the sample (Figure 61(b)) in the same way that they do when the system is at 250ºC and bind to the sample surface, assembling into a monolayer (Figure 61(c)).

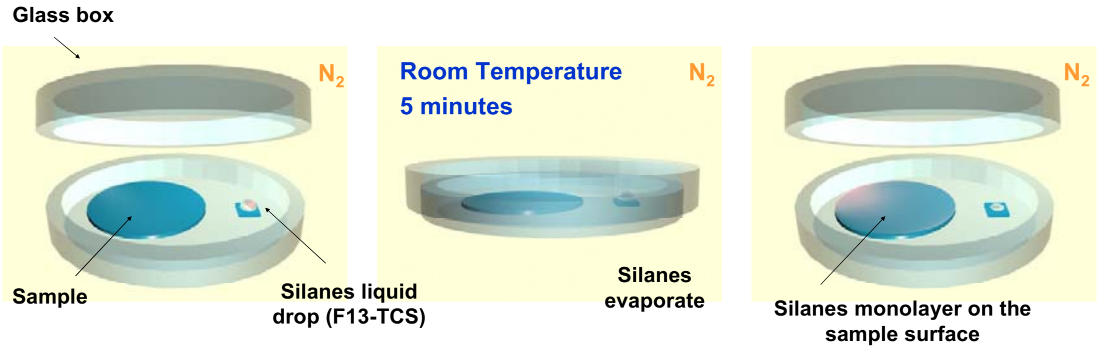

(a) Dropping the liquid in the box

(b) Silanization, at RT, few minutes

(c) The monolayer is created

Figure 61. Ambient temperature silanization: scheme of the process. A drop of the liquid silanes is deposited next to the sample, and both placed inside a glass box inside a nitrogen atmosphere chamber (a). The sample is left for several minutes to react. The silanes are volatile, so evaporate rapidly, especially when the pressure is lowered. The athmosphere inside the glass box is saturated, and the monolayer is created onto the sample surface (c).

Figure 62 shows images showing the contact angle for a water drop onto a silicon surface (a), and after different silanization times: 1 minute (b) and 5 minutes (c). It was observed that few minutes were enough to achieve a contact angle of 107º (Figure 62 (c)), which is similar to the contact angle usually reported for monolayers created by other methods [27], and the final homogeneity of the layer in the samples surface appeared to be good.

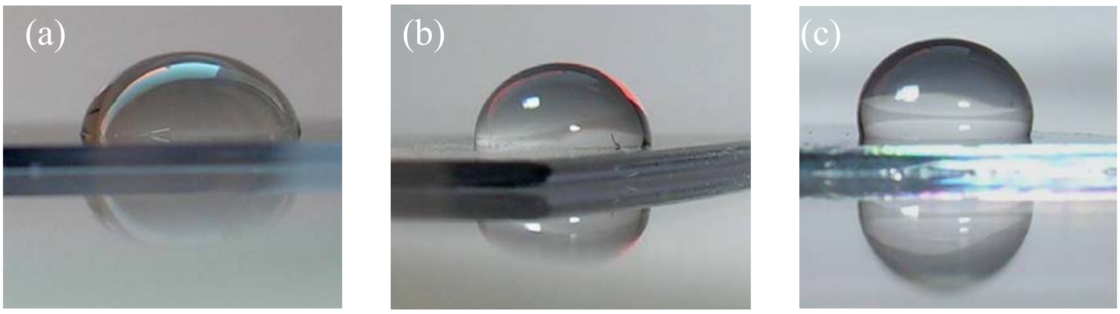

Figure 62. Images of a water droplet on top of an untreated silicon surface (a), on a sample that was submitted to 1 minutes of silanization at room temperature (b) and after 5 minutes of silanization (c). The contact angle increases 25º-30º. After 5 minutes, an angle of 107º is achieved.

To check the improvement of the hydrophobicity of the surface after the treatment, force curves were done with the AFM. Figure 63 show the results obtained in various points of the stamp topography before (blue lines) and after (red lines) silanization.

The difference recorded for the approaching and separation routes is related to the adhesion of the tip to the surface by capillarity forces. Thus, its decrease (comparison between red and blue lines) can be related to the increment in the hidrophobicity of the surface. This probes the successful improvement in the antisticking properties.

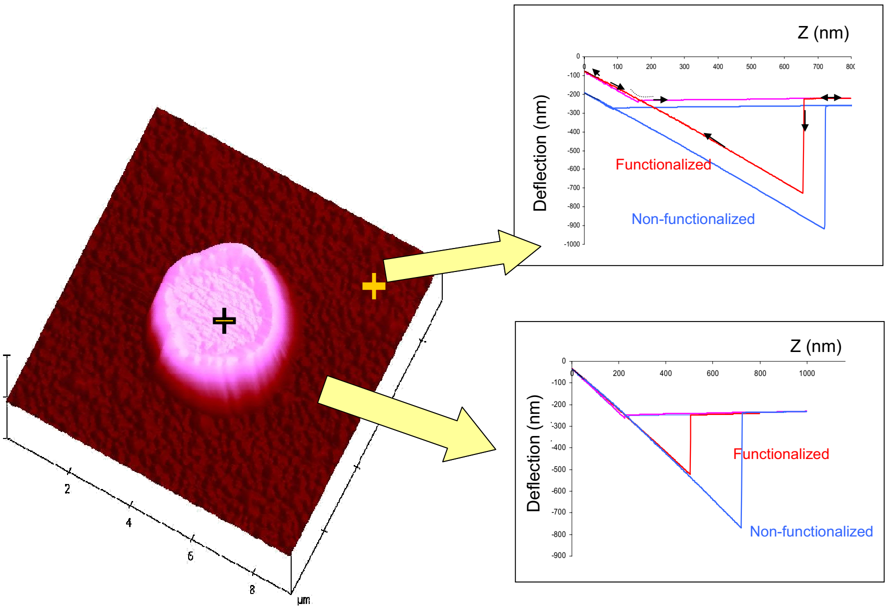

Figure 63. Force curves in a treated and non-treated stamp, obtained in several different points of the stamp surface. The blue line curves were obtained before antisticking coating, and the red ones afterwards.

Finally, the best way of testing the antisticktion coating is by imprinting the stamp. Figure 64 shows several examples. Even further, most of the imprints shown in this thesis were obtained by using stamps that were functionalized with this RT method.

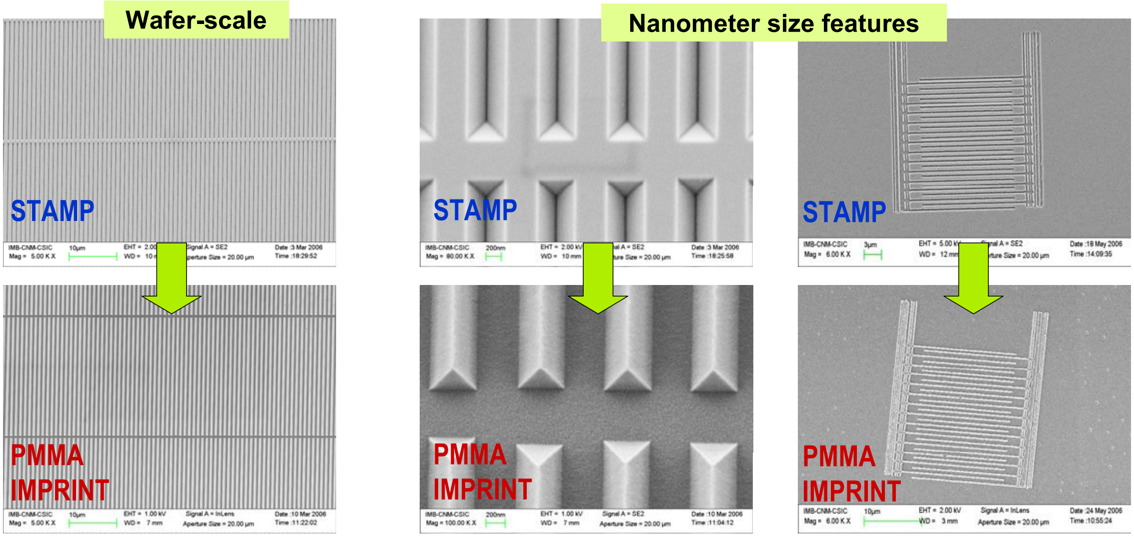

Figure 64. Imprinting examples obtained by using stamps functionalized with the fast method. The silicon stamps are shown in the top, and the corresponding imprints in PMMA in the bottom.

No degradation of the coating was observed along the lifetime of the stamps used during this work: they maintained the antiadhesive properties even after several imprints.

2.3-3. Local silanization

Another advantage of the method for fast functionalization described previously, that enables to deposit silane monolayers without heating up the sample (apart from being faster than conventional methods) is that it can be used for local deposition of silanes, using the PMMA as a mask, since no solvents or high temperatures are needed [28].

Silanes are very interesting, as they are very small molecules that strongly bond to the silicon surfaces, and that can change the surface properties of the sample. Changing the atoms linked to the carbonated chain, their properties can be conveniently chosen.

In consequence, we can modify the chemical (or physical) properties of a surface, without altering its topography. The possibility of local chemical modification of surfaces has attracted the interest of many research groups in the last years because it allows a selective surface functionalization for a wide range of applications. Hydrophilic and hydrophobic surfaces, as well as areas reactive to a specific entity, can be patterned in the same sample. Locally modified surfaces can be applied to define a fairly large range of structures and devices, covering a wide field of applications, like biomedical, biological or microelectronic devices (controlled cell growth, DNA biosensors, molecular devices, etc).

Also, as a complementary work to the previous section (1.3.2), local modification with F13-TCS allows comparing directly the properties of surfaces of bare silicon to those with the silanes monolayer.

This versatile, simple, robust and fast method of local functionalization by lithography and vapour-phase deposition is shown in Figure 65:

a. First, the sample, coated with a 100 nm film of PMMA, is patterned by EBL or NIL.

b. Then, the sample is introduced into the glove box, in a Petri Capsule and kept under nitrogen atmosphere. A small liquid droplet of silanes is dropped inside the recipient. After few minutes (the required time depends on the silanes nature), the silanes evaporate, saturating the atmosphere, and a layer of silane molecules is created onto the non-protected areas of the sample.

c. The last step is a conventional lift-off process: the sample is rinsed for 5 minutes in acetone at 50ºC, and 5 more minutes in RT acetone with ultrasounds agitation, to remove the resist.

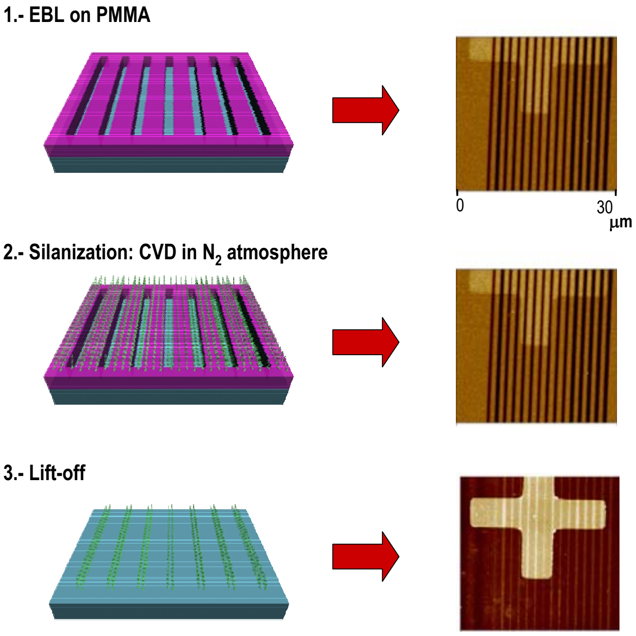

Figure 65. Scheme of the selective functionalization process (drawings in the left) and AFM images of the resulting patterns for an amino-silane deposition (right). First step: EBL patterning of the PMMA and exposed resist development. Second step: Deposition of silanes [(3-Aminopropyl)TriMethoxySilane] in gas phase, in a controlled nitrogen atmosphere, at room temperature, for 24 hours. Last step: lift-off to remove the remaining resist, with a hot acetone (50ºC) bath during 5 minutes, and ultrasounds, for 5 minutes. Resulting silane lines have a pitch of 1.5 µm and a height of 7 nm (not a monolayer, due to the long CVD time).

It should be noticed that, prior to the steps described above, metallic marks were patterned in the substrate, to localize the silanized areas that are not visible by naked eye nor with an optical microscope. Part of one of these marks can be observed in the AFM images of Figure 65.

AFM characterization was used to study the local properties of the surfaces. When silanes formed a self assembled monolayer, topographical images were complemented with lateral force/friction images, as shown in Figure 66 (top), that corresponds to a fluorinated silane (F_{13}-TCS) pattern, 250 nm wide, 1 µm pitch. Topographical images show that the mean height of the lines was 1 nm, and friction images revealed that in the functionalized areas, friction decreased significantly, as expected, owing to their highly hydrophobic nature.

Figure 66 (bottom) shows AFM curves of deflection vs. distance (force curves) for both, covered and non covered areas. The decrease in the adhesion area, once again, meaned an increment of the hydrophobicity of the surface.

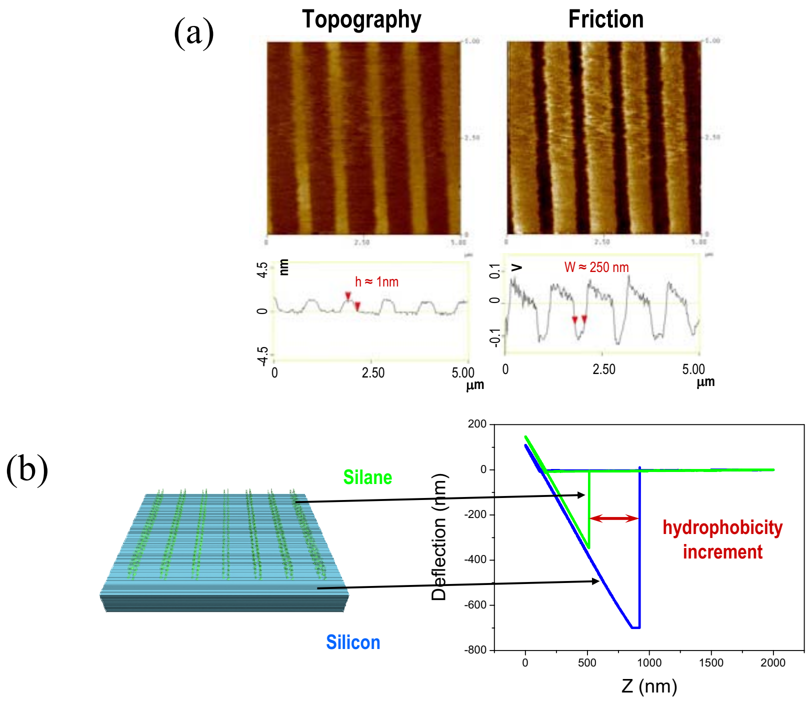

Figure 66. (a), AFM images of topography in contact mode (left) and lateral friction (right) of a lines pattern (1 µm in pitch) of fluorinated silane, deposited during 5 minutes. Lines height is less than 1nm. A high contrast can be observed in the friction image: silicon surface shows a higher value than the silane-covered one. (b) AFM Curves of Force/Deflection vs Distance in silicon and in a functionalized area. The difference in the traces is an evidence of the high hydrophobic nature of the fluorinated silanes. (b) Deflection vs. z distance curves, performed on bare silicon, and on the functionalized lines. The decrease in the adhesion area is due to an increment in the hidrophobicity of the surface.

Figure 67 shows examples of nanometer scale patterns defined by 3 different types of silanes: an amine-silane (a), an acrilate-silane (b), and fluorinated-silane (c). The first type is interesting because its high reactivity to DNA, the second one because of its high hydrophilicity, and the third one because of its high hidrophobicity.

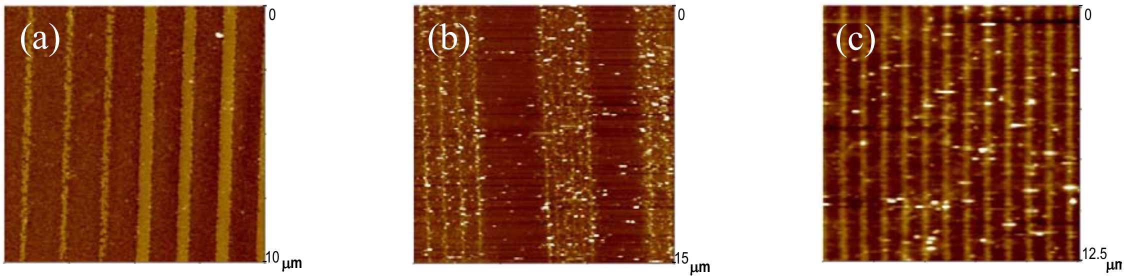

Figure 67. Examples of patterned surfaces with different types of silanes: (a) Patterns of (3-Aminopropyl)TriMethoxySilane, deposited as described above. The average width is 220 nm for the lines in the left, and 450 nm for the lines in the right. (b) Arrays of lines with different pitch of 3-(Trimethoxysilyl)PropylMethacrylate: 1µm, on the left, 500 nm in the middle, and 1.2 µm on the right. Average line with is 200 nm and measured height is less than 1 nm, corresponding to a monolayer, achieved for a CVD time of 24 hours. (c) Lines of 1µm pitch and 200 nm wide of TridecaFluoruro-(1,1,2,2)-tetrahydrooctyl-triChlorosilane (F13-TCS). Deposition time is 5 minutes, resulting in a monolayer of 0.7 nm in height.

These images demonstrate the **versatility of this method for the local modification of the chemical properties of surfaces.**

.

2.4.- REFERENCES

[1] McCord, M.A. and Rooks, M.J.,
Microlithography,
in *SPIE Handbook of Microlithography, Micromachining and Microfabrication*, P. Ralchoudhury, Editor. 2000: Cornell University.

[2] Dagata, J.A.,
Device Fabrication by Scanned Probe Oxidation.
Science, 1995. **270**(5242): p. 1625-1626.

[3] Matsumoto, K.,
STM/AFM nano-oxidation process to room-temperature-operated single-electron transistor and other devices.
Proceedings of the Ieee, 1997. **85**(4): p. 612-628.

[4] Villarroya, M., Perez-Murano, F., Martin, C., Davis, Z., Boisen, A., et al.,
AFM lithography for the definition of nanometre scale gaps: application to the fabrication of a cantilever-based sensor with electrochemical current detection.
Nanotechnology, 2004. **15**(7): p. 771-776.

[5] Held, R., Luscher, S., Heinzel, T., Ensslin, K. and Wegscheider, W.,
Fabricating tunable semiconductor devices with an atomic force microscope.
Applied Physics Letters, 1999. **75**(8): p. 1134-1136.

[6] Maoz, R., Frydman, E., Cohen, S.R. and Sagiv, J.,
Constructive nanolithography: Site-defined silver self-assembly on nanoelectrochemically patterned monolayer templates.
Advanced Materials, 2000. **12**(6): p. 424-+.

[7] Dagata, J.A., Perez-Murano, F., Abadal, G., Morimoto, K., Inoue, T., et al.,
Predictive model for scanned probe oxidation kinetics.
Applied Physics Letters, 2000. **76**(19): p. 2710-2712.

[8] Calleja, M., Anguita, J., Garcia, R., Birkelund, K., Perez-Murano, F., and Dagata, J.A.,
Nanometre-scale oxidation of silicon surfaces by dynamic force microscopy: reproducibility, kinetics and nanofabrication.
Nanotechnology, 1999. **10**(1): p. 34-38.

[9] Fernandez-Cuesta, I., Borrise, X. and Perez-Murano, F.,
Atomic force microscopy local oxidation of silicon nitride thin films for mask fabrication.
Nanotechnology, 2005. **16**(11): p. 2731-2737.

[10] Hwang, J.S., You, Z.Y., Lin, S.Y., Hu, Z.S., Wu, C.T., et al.,
Effect of gold coating on local oxidation using an atomic force microscope.
Applied Physics Letters, 2005. **86**(16).

[11] Martin, C., Rius, G., Borrise, X. and Perez-Murano, F.,
Nanolithography on thin layers of PMMA using atomic force microscopy.
Nanotechnology, 2005. **16**(8): p. 1016-1022.

[12] Gwo, S., Yeh, C.L., Chen, P.F., Chou, Y.C., Chen, T.T., et al.,
Local electric-field-induced oxidation of titanium nitride films.
Applied Physics Letters, 1999. **74**(8): p. 1090-1092.

[13] Gwo, S.,
Scanning probe oxidation of Si3N4 masks for nanoscale lithography, micromachining, and selective epitaxial growth on silicon.
Journal of Physics and Chemistry of Solids, 2001. **62**(9-10): p. 1673-1687.

[14] Farkas, N., Comer, J.R., Zhang, G., Evans, E.A., Ramsier, R.D., and Dagata, J.A.,
SPM oxidation and parallel writing on zirconium nitride thin films.

Journal of Vacuum Science & Technology A, 2005. **23**(4): p. 846-850.

[15] Ruskell, T.G., Pyle, J.L., Workman, R.K., Yao, X. and Sarid, D.,
Current-dependent silicon oxide growth during scanned probe lithography.
Electronics Letters, 1996. **32**(15): p. 1411-1412.

[16] Avouris, P., Hertel, T. and Martel, R.,
Atomic force microscope tip-induced local oxidation of silicon: Kinetics, mechanism, and nanofabrication.
Applied Physics Letters, 1997. **71**(2): p. 285-287.

[17] Kuramochi, H., Perez-Murano, F., Dagata, J.A. and Yokoyama, H.,
Faradaic current detection during anodic oxidation of the H-passivated p-Si(001) surface with controlled relative humidity.
Nanotechnology, 2004. **15**(3): p. 297-302.

[18] Dagata, J.A., Perez-Murano, F., Martin, C., Kuramochi, H. and Yokoyama, H.,
Current, charge, and capacitance during scanning probe oxidation of silicon. I. Maximum charge density and lateral diffusion.
Journal of Applied Physics, 2004. **96**(4): p. 2386-2392.

[19] Kuramochi, H., Ando, K. and Yokoyama, H.,
Minute current detection during anodic oxidation by atomic force microscope at high humidity.
Japanese Journal of Applied Physics Part 1-Regular Papers Short Notes & Review Papers, 2003. **42**(9A): p. 5892-5895.

[20] Klauser, R., Hong, I.H., Su, H.J., Chen, T.T., Gwo, S., et al.,
Oxidation states in scanning-probe-induced Si3N4 to SiOx conversion studied by scanning photoemission microscopy.
Applied Physics Letters, 2001. **79**(19): p. 3143-3145.

[21] Gritsenko, V.A., Svitasheva, S.N., Petrenko, I.P., Wong, H., Xu, J.B., and Wilson, I.H.,
Study of excess silicon at Si3N4 thermal SiO2 interface using ellipsometric measurements.
Journal of the Electrochemical Society, 1999. **146**(2): p. 780-785.

[22] Dagata, J.A., Inoue, T., Itoh, J., Matsumoto, K. and Yokoyama, H.,
Role of space charge in scanned probe oxidation.
Journal of Applied Physics, 1998. **84**(12): p. 6891-6900.

[23] Schift, H., Heyderman, L.J., Maur, M.A.D. and Gobrecht, J.,
Pattern formation in hot embossing of thin polymer films.
Nanotechnology, 2001. **12**(2): p. 173-177.

[24] Fernandez-Cuesta, I., Borrise, X. and Perez-Murano, F.,
Atomic force microscopy local anodic oxidation of thin Si3N4 ayers for robust prototyping of nanostructures.
Journal of Vacuum Science & Technology B, 2006. **24**(6): p. 2988-2992.

[25] Beck, M., Graczyk, M., Maximov, I., Sarwe, E.L., Ling, T.G.I., et al.,
Improving stamps for 10 nm level wafer scale nanoimprint lithography.
Microelectronic Engineering, 2002. **61-2**: p. 441-448.

[26] Fernandez-Cuesta, I., Borrisé, X. and Pérez-Murano, F.
Fast antisticking coating at room temperature: process and characterization. in *International Conference on NanoImprint and NanoPrint Technology (NNT)*. 2006. San Francisco, CA (USA): Poster.

[27] Schift, H., Saxer, S., Park, S., Padeste, C., Pieles, U., and Gobrecht, J.,
Controlled co-evaporation of silanes for nanoimprint stamps.
Nanotechnology, 2005. **16**(5): p. S171-S175.

[28] Fernandez-Cuesta, I., de la Rica, R., Borrisé, X. and Pérez-Murano, F.
Local Functionalization of Surfaces by EBL and CVD and AFM characterization. in *NanoSpain*. 2006. Pamplona (Spain): Poster.

Chapter 3

Polymer Rheology

In the thermal nanoimprint process, a thermoplastic material is used to replicate the stamp geometry by heating it up above its glass transition temperature, T_g, (entering the viscous regime) and by forcing it to flow by applying a pressure. Thus, it is important to know the behaviour of these materials under these especial conditions, to optimize the imprinting time, avoid defect formation and improve the quality of the obtained structures.

During this work, we investigated on the stress accumulation in the polymer structures during the imprinting process, and, more precisely, in the cooling step.

The results obtained by collaboration of several different groups all around Europe towards benchmarking of thermal-NIL will be also detailed at the end of the chapter.

3.1.- INTRODUCTION

3.1-1. Mechanical properties of thermoplastics

The general mechanical behaviour of thermoplastics as a function of the temperature is shown in Figure 68 [2]. The key point is that their properties strongly depend on the temperature: they are rigid for a certain range of temperatures, but start to flow when they are heated-up above the “**glass transition temperature (T_g)**”, different for each one. T_g is below their melting point (T_f), and it does not depend on the molecular weight. Meanwhile the melting point does. This is important, as the mechanical behaviour and the flow of the polymer depend on the viscous regime, that is determined by these two temperatures (T_g and T_f).

The thermoplastic behaviour is explained attending to the internal structure of these polymers. They are formed by individual long molecules. Monomers are chemically linked to form these long chains, which length depends on the molecular weight. These chains interact between them by electrostatic and Van der Waals forces. When $T<T_g$, the forces that maintain the chains bonded are higher than their thermal energy. When $T>T_g$, the energy is enough to break these links, and the chains can move one respect to the others when an external force is applied: the polymer flows. This is the viscous (or viscoelastic) regime. When flowing, the chains do not stop interacting between them (the links are broken and re-built continuously), which accounts for the viscosity of the material. When the pressure is released, the new shape is maintained. Even further, the polymer can be re-melted and the process repeated as many times as needed, as the process is reversible.

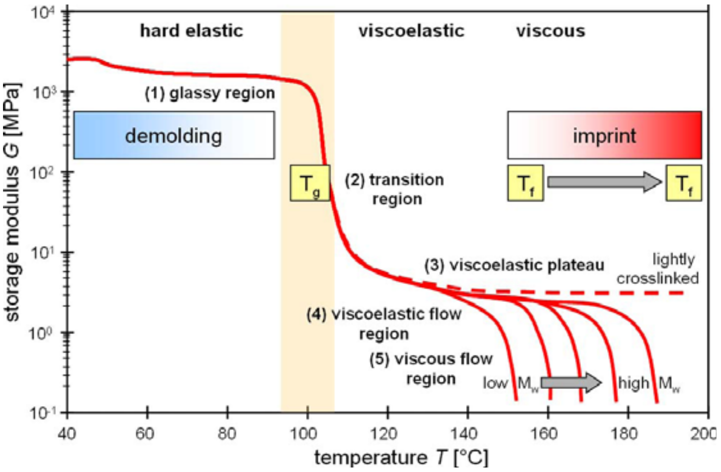

Figure 68. Mechanical properties of polymers dependent on temperature, molecular weight, and cross-linking. Schematic for a polymer with a T_g around 100 °C. Particularly important for thermal NIL are the large drops of the storage modulus, G[*], at two temperatures, T_g and T_f. At T_g the thermomechanical properties between stamp and polymer become sufficiently different for repeated molding. T_f characterizes a point at which viscosity drops. [2]

3.1-2. Rheology during the imprinting process

During the imprinting process, the polymer is heated above T_g, so the chains have enough energy to move ones respect to the others. When the pressure (P) is applied, the material is forced to flow and it is deformed with the shape of the stamp.

Nevertheless, as can be observed also in the graph of Figure 68, there are two regimes above T_g: the **visco-elastic** and the **viscous**. In the purely viscous regime, G drops sharply, all the polymer chains

---

[*] G: (shear) storage modulus: is a measure of the energy stored during a cycle, representing the elastic properties. The elastic deformation is accompanied by storage of elastic energy within the structure of the material.

flow and renew the links in their current positions. But, for lower temperatures (visco-elastic regime) not all of them are broken, and some of the movements are due to *strain of the chains*. This means that, when the stress is released, part of the shape is recovered.

Thus, the chose of imprinting parameters has to take into account the behaviour of the polymer, so the temperature (T) has to be high enough to allow flowing of the polymer, but not too high, to avoid melting, and the imprinting time (t) has to be long enough to prevent the shape recovery (among other effects).

Therefore, for each case, there are several parameters that have to be studied and optimized. There is not a standard recipe or procedure, and it varies depending on the equipment, the stamp geometry, the imprinting polymer, etc.

The geometry of the stamp influences the conditions needed to obtain a good replication in the polymer, and, in contrast to other nano-fabrication processes, the micro rather than the nanodimensions play the main role for process optimization. Longer imprinting times are needed for larger amounts of polymer that have to flow and/or when they have to move larger distances. In thermal NIL, the mold filling depends on the structures size and on the filling factor. The filling factor is the relation between the protusions (w) and buried (g) areas width (w/g), as shown in Figure 69. The polymer flow is governed by viscoelastic properties of the material, which are dependent on the temperature, and by the strain induced by the application of the force. On the other hand, trade-offs between the parameters are possible (e.g., lower P can be compensated with a longer t, or a higher T), so, in general, they can be varied to a large extent.

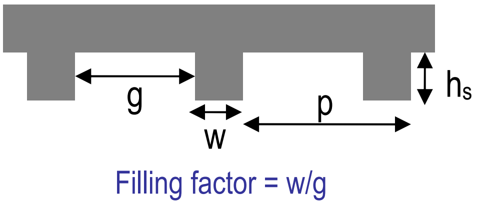

Figure 69. Definition of the parameters of the stamp geometry: pitch of the patterns in the array (p), width of the protrusions (w), buried gap between them (g), height (h_s) and filling factor, that is generally defined as w/g.

Apart from the imprinting conditions, the properties of the polymers themselves play an important role, and can be chosen to optimize the application. And, for each polymer, the properties change as a function of **its molecular weight**, so the viscosity (ability to flow) can vary for a fix temperature [5]. Figure 70 shows the dependence of the viscosity on the temperature for various polymers commonly used for NIL in (a), and a detail of this dependence for three different molecular weights of PMMA (b). There exists a wide variety of materials [6] that can be used for NIL (such as *Poly(methyl methacrylate)* - **PMMA** or *Polystyrene* - **PS**) or even further, that have been specifically designed for this process [7], taking into account the needs of the application for which the sample is being developed (such as low T_g, high resistance to RIEs, higher thermal stability, lower viscosity, etc).

The molecular weight (M_w) is expressed in g/mol. In the case of the polymers used for NIL, the typical values for M_w are in the range of 10^4 to 10^5 g/mol, in order to achieve a trade-off in the mechanical properties. Generally, they are named in a shortened, way, expressed in *k* (e.g., PMMA with a molecuar weigh of 50^4 g/mol would be named PMMA 50k).

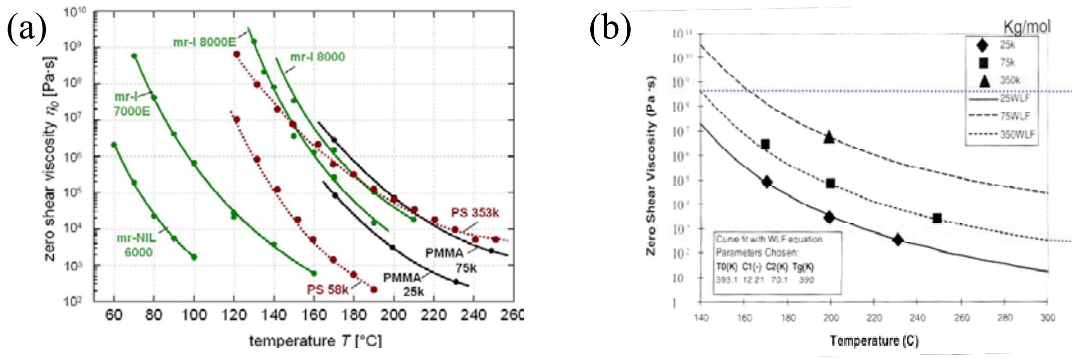

Figure 70. (a) Zero shear viscosity[†] for some standard resists for thermal NIL for different polymers, taken from different sources: PMMA with Mw of 25 and 75 kg/mol,14 PS with Mw of 58 and 353 kg/mol;PS 58kg/mol and PS 353kg/mol, and the commercial resists mr-I 7000E, 8000, 8000E, and mr-NIL6000. These curves are presented for the temperature range characterizes above the viscous T_g. A process window for imprint is limited by high viscosity where unwanted viscoelastic effects become dominant and molding slow. Lower viscosities than 103 Pa s are often not useful because it is often achieved with too low Mw or too high Timprint. (b) shows a similar plot, related only to PMMA with different molecular weights (25k, 75k and 350k).

3.1-3. Imprinting parameters

In this work, PMMA with low molecular weights (35k, 50k) was mainly used. Its glass transition temperature is T_g = 105 ºC. Other polymers, such as various commercial mrI, from Microresist Technology [8] were eventually used, to improve the mechanical stability of the structures or for benchmarking tasks.

For imprinting PMMA, the temperature was chosen between ~ 60 ºC and 80 ºC above T_g, and the demolding temperature ~15 – 40 ºC below T_g. Pressures between 20 and 40 bars were commonly applied. Figure 71 shows a typical graph of the imprinting parameters (P, T) acquired during a conventional imprinting process in PMMA 50k. The recipe used during this imprint is also shown in the table, including the total imprinting time (t_{TOT}) and the demolding temperature (T_D).

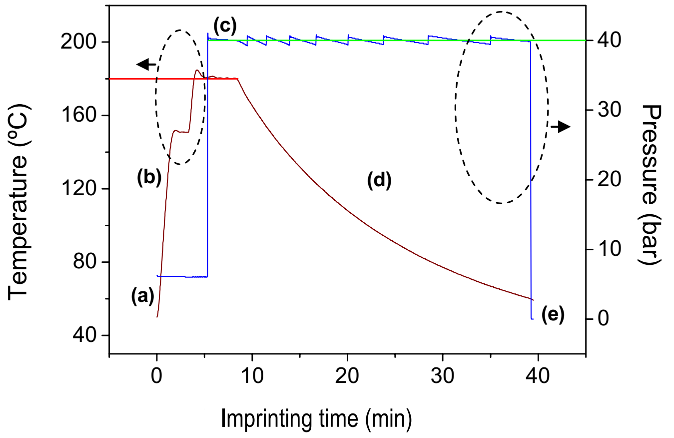

P = 40 bar
T = 180 ºC
t = 5 minutes
t_{TOT} = 40 minutes
T_D = 50 ºC

Figure 71. Graph showing the imprinting conditions during the process. Temperature (red lines, left axes) and pressure (blue and green lines, right axes), are recorded as a function of time.

[†] Zero shear viscosity: the resistance to flow of a fluid (strictly speaking, the resistance to shearing) is defined as *viscosity*. The asymptotic viscosity value at zero shear rate (i.e., the maximum value) is the so-called *zero shear viscosity*. As the shear rate increases, the viscosity decreases due to alignments of molecular chains in the direction of flow and molecular chain disentanglements. The zero shear viscosity is proportional to the 3.4 power of the average molecular weight (M_w) (i.e. η_0 = constant * $M_w^{3.4}$ for most common polymers). Obviously it is extremely difficult to extrude polymers having very high molecular weight.

Our main contribution to the rheology of polymers during the NIL process was a detailed study of the stress built up in the polymeric structures during the cooling step, in the framework of the NaPa project. The determination and quantification of the residual stress in the structures is important, as it will affect their final shape and dimensions and the long term stability of the imprinted features.

On the other hand, we were involved in a task, together with other research labs, that studied the polymer flow below the protruded areas of the stamp (this is, the remaining residual layer) for different equipments, processes, and stamp sizes.

3.2.- FROZEN-IN STRESS

3.2-1. Introduction, motivation and state of the art

The polymers used for NIL, in general, do not present a pure viscous behaviour for the normal imprinting parameters, but **viscoelastic** properties appear. This means that they can flow and change their shape when a load is applied (viscosity), but, part of the deformation is recovered when the load is released (elasticity), as already described above. Thus, it is important to know in which range of temperatures is better to work (according to Figure 68) and to know the typical time constants for each polymer [9]. Figure 72 shows two examples of shape recovery effects, probably caused by a short imprinting time, and/or low temperature. Thus, it is well known that, when applying a pressure, an internal stress is being induced in the polymer. This stress may have an impact in the long term recovery of the shapes, and stability and reproducibility of the dimensions.

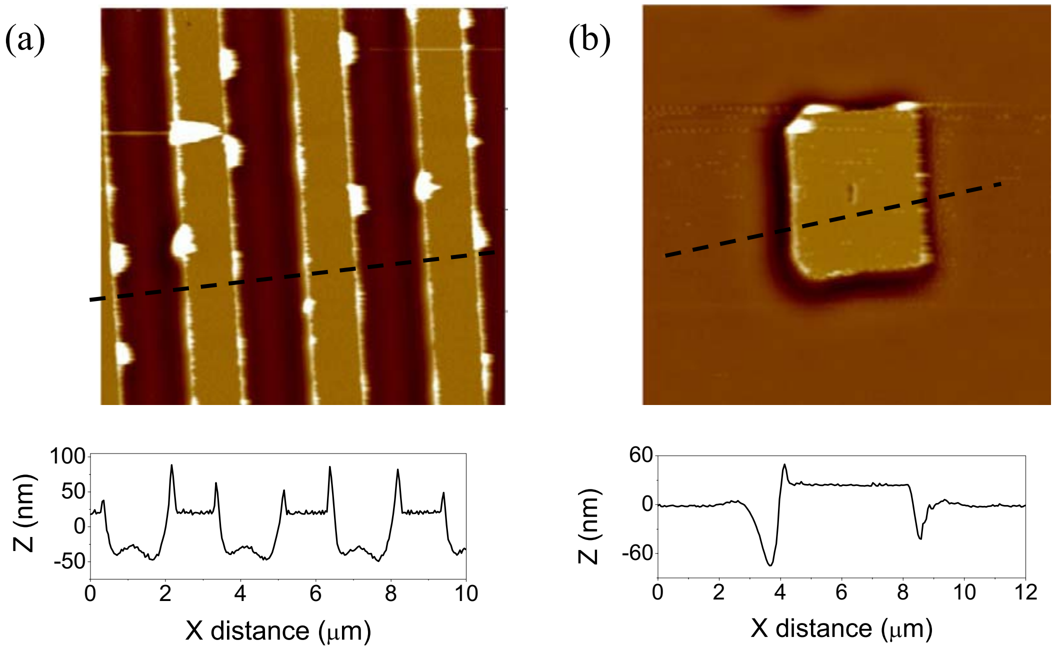

Figure 72. AFM images of two examples of deformations in the imprinted structures due to internal stress, that leads to a shape recovery. (a), micrometric lines, where the buried (pressed) areas show protrusions, due to internal stress. In (b), a similar effect is shown in a micrometric squared area.

Stress building up during the imprinting process has been considered from various approaches.

Hirai et al. [10] estimated internal stress build-up in a complete imprinting sequence: hot embossing, cooling-down and stamp releasing (Figure 73). They concluded that the stress was mainly generated during the cooling step, and that the most affected locations were the bottom corners of the lines (Figure 73 (a)). As a consequence of the stress accumulation, they also reported on cracking of high aspect ratio lines (Figure 74(a) and (b)) when demolding at low temperatures, a problem that could be solved by releasing the stamp at temperatures close to T_g. We have also observed similar cracks for high aspect ratio structures, as shown in Figure 74(c).

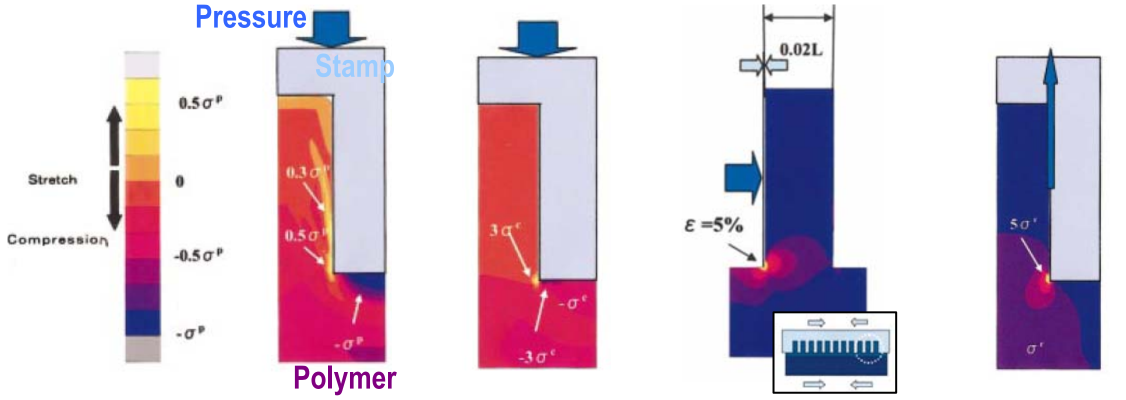

(a) Initial pressing step (b) Pressing step (c) Cooling step (d) Releasing step

Figure 73. Simulations of the stress in the polymer for the imprinting steps, modelled by Hirai et al. [10] in a complete imprinting cycle: initial applied pressure, forcing the polymer to flow (a), pressing step during the imprinting duration (b), cooling step, taking into account possible differences in the thermal expansion coeficients for the stamp and substrate (c), and releasing step (d). The main stress accumulation occurs in the cooling step, in the bottom corners of the lines.

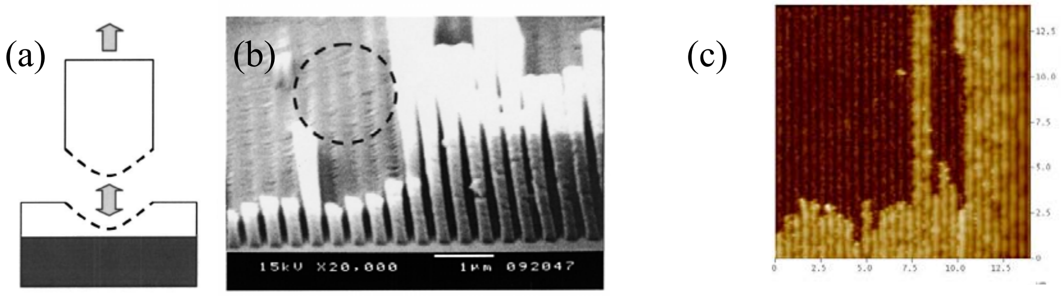

Figure 74. Scheme of a typical fracture defect in thermal nanoimprint lithography (a), and SEM image of cracked lines (b), reported by Hirai et al. [10]. Similar defects were observed during this thesis work, as shown in the AFM image in (c).

Ro et al. [11, 12] evidenced the existence of residual stresses by real-time measurement of anisotropic relaxation processes of lines imprinted in different polymers, heated back on a hot plate. They observed that, if the structures were previously relaxed, the shape obtained afterwards was different compared to non-relaxed structures (Figure 75 (a)).

Bogdanski et al., [13] studied the shape recovery of the flat areas between imprinted lines in the micron range (Figure 75 (b)), that are similar to those shown in Figure 72. It results from the release of internal stress accumulated during the process, and can hamper the post-processing, due to the resulting inhomogeneous height of the residual layer.

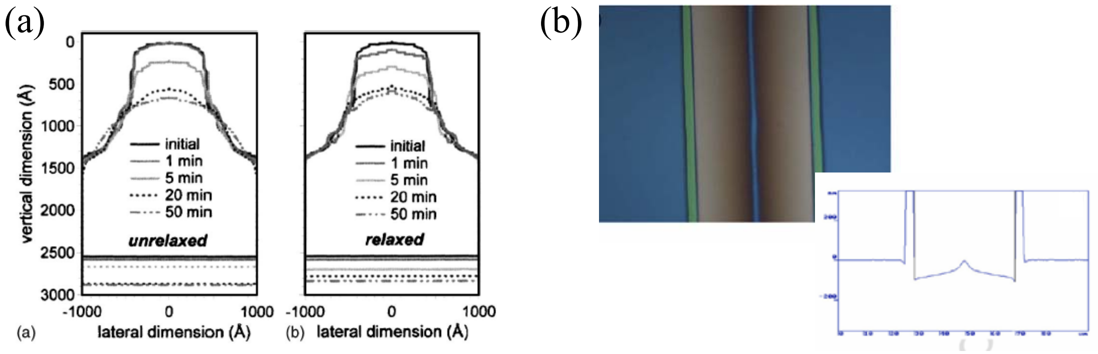

Ro et al.

Bogdanski et al.

Figure 75. (a): evolution of the profile of imprinted lines when heated on a hot plate: the relaxation process is different when a previous backing of the samples inside the stamp is done (to relax the internal stresses), reported by Ro et al [11, 12]. (b) shape recovery defects in micrometric size lines, due to internal stress acumulation, as reported by Bogdanski et al. [13].

In this work, we focused the rheological studies to characterize the stress built-up in the structures during the **cooling step** [14]. A method was developed that allows the direct measurement of residual stresses based on high resolution atomic force microscopy (AFM) characterization of triangular shaped polymer lines. The method was demonstrated for imprints in PMMA 50k.

3.2-2. Experimental procedure

The test platform chosen to study the internal stress effects were Λ-shaped lines imprinted in PMMA 50k, as shown schematically in Figure 76(a), using the triangular shaped stamps described in Chapter 2. The triangular shape of the cross-section allows univocal measurement of the profiles by AFM, thanks to the minimization of tip convolution. Thus, the sidewalls can be studied, unlike the case of squared lines. Furthermore, the slope and exact geometry of the stamp are compared to that of the replicated PMMA structures, so that any difference is effectively related to internal stress effects.

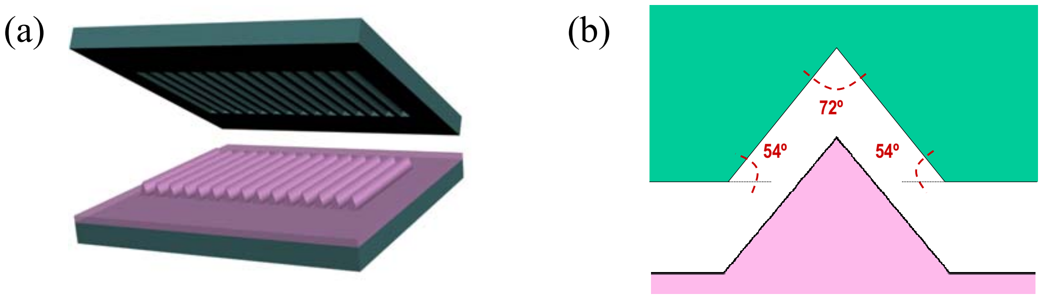

Figure 76. (a) Drawing of the silicon stamp, containing the triangular shape lines, and the resulting imprint in PMMA 50k. (b) Scheme of the geometry of the triangles, where the slope and the angles are fixed by the {111} crystalline planes of (100) oriented silicon.

Typical deformations should be in the range of few nanometers, thus, a precise characterization of the topography of both, stamp and imprinted pattern was required. AFM, using supersharp tips was the most suitable tool for this purpose. AFM resolution can be better than 0.1 nm, but is limited by material softness and surface roughness. PMMA roughness after imprinting was measured to be 0.6 rms. The characteristic dimensions of the fabricated structures were in the order of 500 nm, so a deformation of 1 nm corresponds to a 0.2%, which sets the minimum stress that can be detected.

$$\frac{\partial u}{\partial x} \approx \frac{1nm}{500nm} \approx 0.002 \tag{6}$$

Deformations were expected to appear at the sidewalls (due to compressive or relaxation stress) or, according to Hirai simulations [10], in the bottom corners, as it is shown in Figure 77.

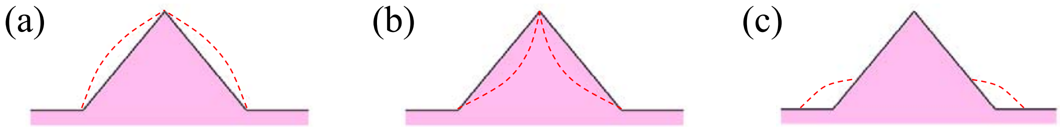

Figure 77. Scheme of the deformations expected to appear due frozen-in strain. (a) and (b): deformations changing the triangles slope due to compressive or relaxations stress, respectively; (c): topographic deformation in the corners, according to Hirai et al. [10] results.

As already described previously, the V-shaped lines in the stamp were defined by electron beam lithography and anisotropic wet etching of (100) oriented silicon, as already described in the previous chapter. This fabrication method presents several advantages for the development of the work: (i) the geometry and the slope of the lines are fixed and well-known from the crystallographic orientation, as depicted in Figure 76(b); (ii) after optimization of the method, lines with very smooth sidewalls were fabricated, enabling the AFM characterization and facilitating interpretation of the results.

3.2-3. FE simulations

This task was developed in the framework of the European project NaPa, so part of the work was done in collaborations with other institutes, both for experimental development, and for theoretical studies.

Finite Elements (FE) simulations were done in collaboration with David Mendels, from NPL[‡]. A complete study of the full imprint of triangular shaped structures process was done by FE simulations, using a "**spring-back model**" [15]. Here, the PMMA was modelled as a hyperelastic-viscoelastic solid with time-temperature (WLF) superposition, to account for thermal and rate dependence [16]. Figure 78 shows the mesh used for the simulations. The number of points was increased in the areas where the deformations were expected to appear: sidewalls and corners.

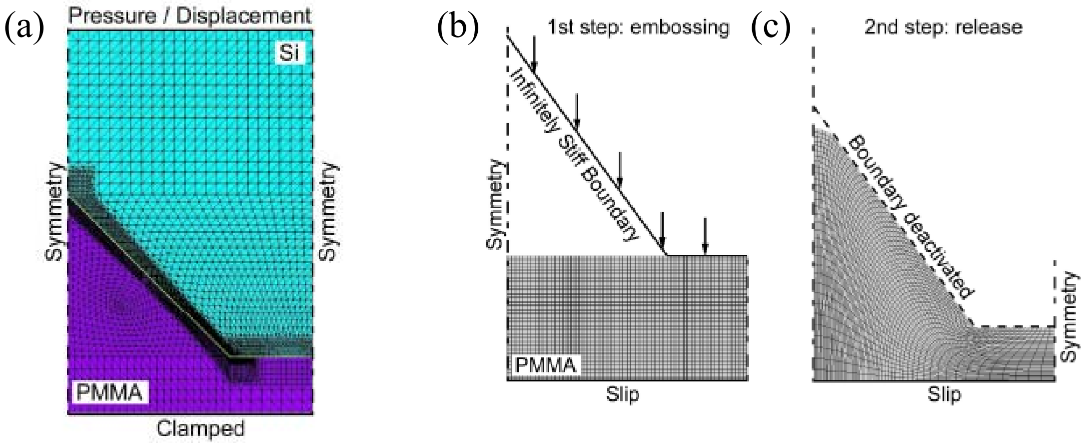

Figure 78. Finite element mesh and boundary conditions for the internal stress build-up determination, and examples for the embossing and releasing steps simulations.

[‡] NPL – National Physical Laboratory – Teddington Middlesex TW11 0LW (UK)

The results obtained for the frozen-in stress were thus compared with the experimental ones, and a model was proposed, that allows a physical interpretation of the filling process and the stress built up.

3.2-4. Results

Figure 79 (top row) shows SEM images of the fabricated stamps: a view of one of the areas (a), a general view of the lines (b), and a detail in (c), where the triangular shape can be seen. The smoothness of the sidewalls is noteworthy and apparent. In Figure 79 (bottom row), the resulting imprints in PMMA 50k can be seen. These structures are extremely smooth as well, as confirmed by AFM characterization.

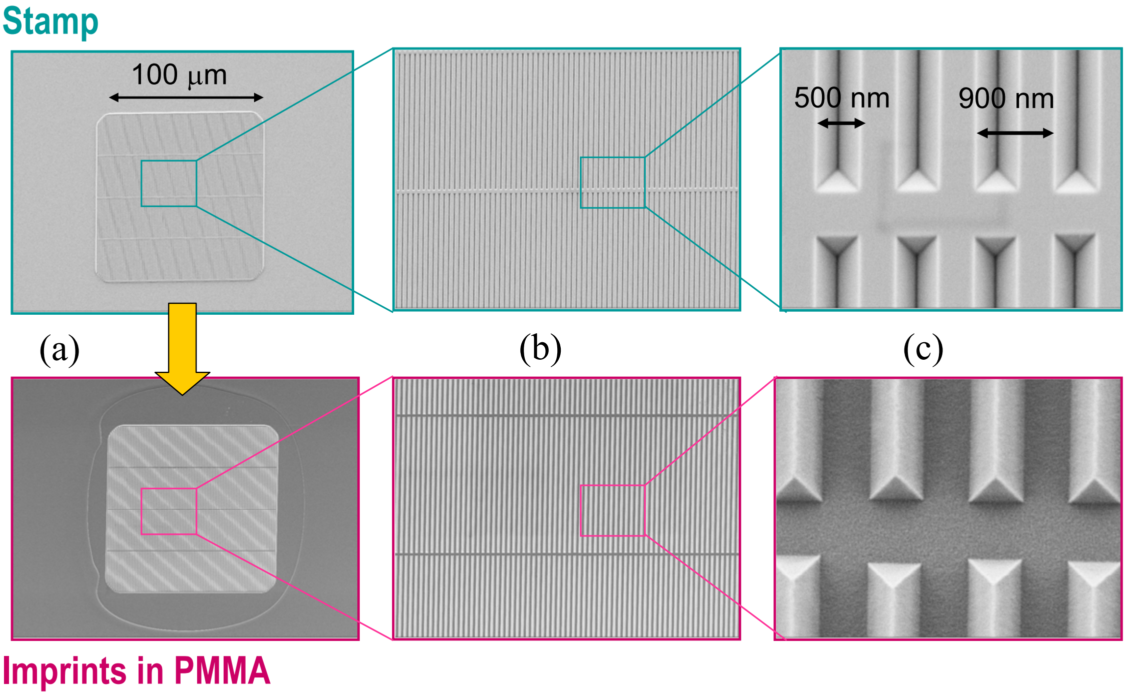

Figure 79. SEM images of the silicon stamp (top row), and an imprint in PMMA (bottom row), where a general view of one of the areas is presented (left), the lines (middle), and a detail (right), where the triangular shape can be observed. The smoothness of the sidewalls is remarkable.

The triangles were imprinted several times at different imprinting conditions, and subsequently characterized by AFM using super-sharp tips. The expected deformations to be measured were in the order of 1 nm or below. Surface roughness was around 0.5 nm thanks to the optimized fabrication process as it has been described above. In order to reduce the noise induced by the AFM image acquisition itself (thermal noise of the cantilever and external vibrations) most of the data were obtained while disabling the slow scan axis, and then *averaged over 256 scans*

In order to facilitate the localization of the minute deformations, the **derivative** of the profiles was calculated. Figure 80 shows a drawing of the profiles and the corresponding derivatives for a perfect triangle (dark blue), and for two different types of relaxed shapes (yellow and red) (the deviations have been magnified for visual aid). The differences on the derivative shapes are clear, and facilitate the data interpretation, as the differences in the profiles are minute.

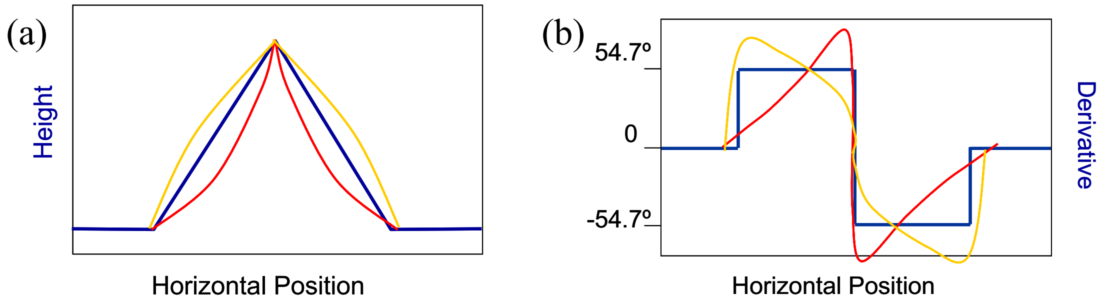

Figure 80. Schemes of the profiles and the corresponding derivatives for different types of strains (a), and their corresponding derivatives (b), from where the slope angle can be calculated (left axes in (b)). The deformations have been exagerated, for visual aid.

Figure 81 (a) shows a typical profile of a strained structure and its derivative (dotted line in the graph). Three zones of interest appear: the bottom corners appear protruded (A), the slope changes (B), and the peak of the triangle is rounded and its height is smaller than the theoretical one (C).

To get a deeper understanding of the polymer flowing and stress build-up, the finite elements (FE) simulations were compared to the results [15]. A typical result is shown in Figure 81 (b). Note that the representation of the displacements in Figure 81 has been enhanced in a factor of 15 for visual aid.

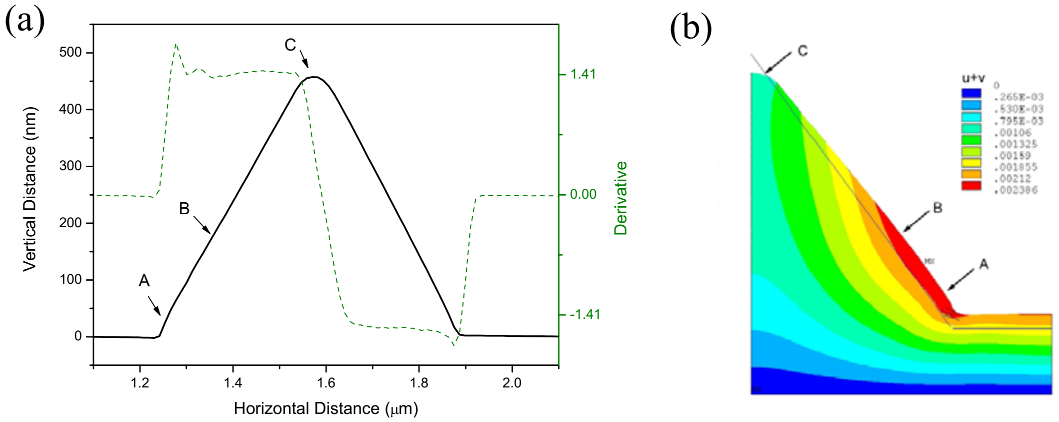

Figure 81. Experimental results of AFM characterizations (a) and FE simulations (b) of a strained profile. For easier visualization, the derivative of the experimental profile has been calculated (dashed line in (a)), so three mainly strained areas appear: bottom corners (A), the middle of the sidewall, where a change in the slope trend appears (B), and the top peak of the triangle, that is rounded and which height is lower than the theoretical one (C).

This model allows to directly relate the observed residual deformation to internal stress build up due to **two competing contributions**:

(i) The flow of the **polymer forced to fill the cavities**, which tends to **produce a convex shape**.

(ii) A **concave shape**, due to the **cool-down through the glass transition** of the polymer **while maintaining the pressure**, and the **difference in the thermal expansion coefficients**, that leads to a compressive pressure in the polymer.

Simulations varying the parameters related to the stamp-polymer *adhesion* (high and low adhesion) showed that although important for the dynamics of the stamp release, it did not change the final shape of the polymer after release.

3.2-5. Systematic study

A systematic experimental study was carried out, varying all the imprinting parameters in the ranges that are listed in Table 4: imprinting time, pressure and temperature; cooling conditions (cooling rate and demolding temperature); imprinting equipment, demolding procedure (manual vs. automatic), and initial polymer thickness. It is remarkable that three different equipments were used and compared.

Table 4. List of the parameters that have been varied in the systematic study, and their range of values.

Parameter	Values
Imprinting Machines	Jenoptik, Obducat, EVG
Cooling ratio (CR)	18ºC/min, 2ºC/min, 1ºC/min
Demolding Temperature (TD)	120ºC, 100ºC, 70ºC and 40ºC
Demolding	Automatic and Manual
Temperature (Ti)	From 100ºC to 190ºC
Imprinting time (ti)	From 1 to 10 min
Imprinting Pressure (Pi)	From 10 to 60 bars
PMMA layer thickness	500 nm, 700 nm, 5 μm, 3 mm.

The first conclusion drawn from all the obtained data is that the residual deformations are minute. Essentially, no dependence on the imprinting conditions (temperature, time and pressure) was observed. However, a trend was obtained depending on the **cooling conditions**. The predominance of the cooling conditions on the level of stress built up was not unexpected: while the polymer is in its viscous regime ($T>T_g$), being the imprinting time longer than the typical relaxation times for PMMA [17], that in the order of few seconds, the imprinting stress is supposed to relax almost completely. Only the unrelaxed portion, due to non-linear viscoelastic phenomena, is frozen during cool-down and can be measured, together with the stresses accumulated during the cooling step, after releasing the stamp.

This result agrees with the conclusions obtained by modelization by Hirai et al., as already mentioned, and reported in [10], where it was shown that the stress is mainly built up during the cooling step.

To get a deeper insight in the effect of the cooling step on the structures, some samples were imprinted in the same conditions (180 ºC, 40 bar, 5 min), changing only the demolding temperature, and then heated up on a hot plate for 4 hours at 100ºC (this is, 5 ºC below T_g), to accelerate the relaxation processes.

Figure 82 shows the resulting AFM profiles (a) and the spatial derivatives (b) of the samples after post-baking on the hot plate. The sample demolded at high temperature (100ºC) shows that the initial strains (like shown in Figure 81) are relaxed, and that the slope maintains a constant value, similar to the theoretical one (54.7º); i.e., an isotropic relaxation has occurred. For the other two samples, the trend is different, and an anisotropic relaxation is obtained. These results agree with those reported in [11], where it was shown that the residual stress leads to an anisotropic recovery of the shape.

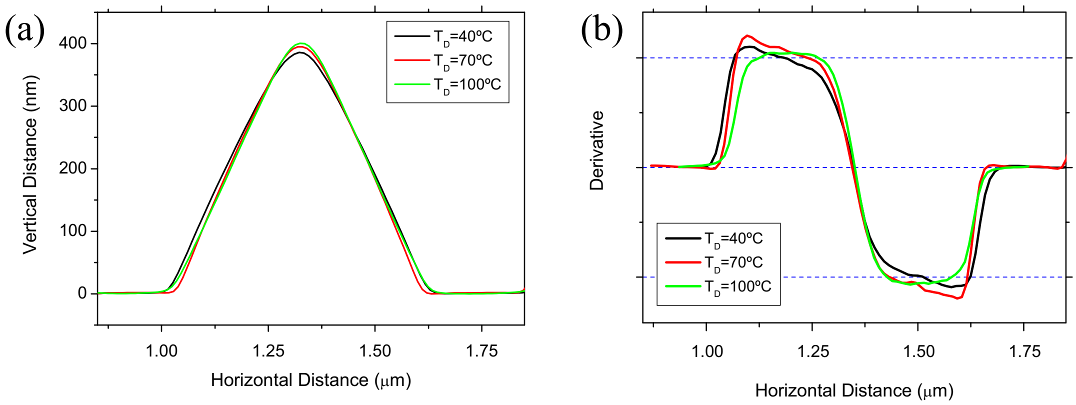

Figure 82. Profiles (a) and derivatives (b) obtained for three different samples, imprinted in the same conditions, but changing only the demolding temperature (TD) after 4 hours in a hot plate at 100ºC. Note that the relaxation is more anisotropic for low values of TD.

Demolding at high temperatures is the main recommendation following the present measurements, in order to reduce the residual stress and improve the long term stability of the structures. In all cases, the residual deformations due to stress build up appear to be minute, compared to the typical dimensions of the features, across the range of parameters studied. However, the high stress concentrations in the bottom corners may lead to pattern cracking when scaling down dimensions, particularly if the stressed area inside the structure is longer than half the width of the structure.

It is worth noting that the temperature for releasing the stamp should be below Tg. Fatal defects related to air escaping from the polymer while it is still in the viscous regime have been observed in some of the equipments, because the vacuum inside the chamber is not enough to avoid air trapping during the imprinting process.

3.2-6. Influence of T_D on the quality of different size lines

To study how much the imprinting temperature can be raised, -which is a very convenient to reduce the total imprinting time- and to study how much this stress affects to other kind of structures, a stamp consisting on squared-shape lines with different aspect ratio (from 2 to 0.1) was fabricated. Then, different imprints were done in PMMA 50 k, changing only the demolding temperature: 40ºC, 70ºC, 100ºC and 120ºC.

SEM images of the imprinted lines corresponding to T_D = 40 ºC can be seen in Figure 83. No damage was observed in any of the wider lines (w > 200 nm), but the smaller ones appear pulled-off for T_D = 40ºC. The narrowest lines (w ≈ 100 nm) are pulled-off from the base, and for w ≈ 150 nm, the crack appears in the lower part of the lines, but does not remove material from the base.

These cracks do not appear for T_D = 70ºC, which means that the stress accumulation in the base corners is not so high to cause the cracks.

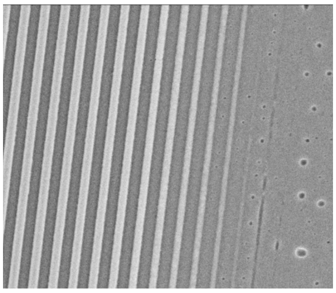
T_D = 40 ºC

Figure 83. Lines with different aspect ratios (from 0.1 to 2) imprinted in PMMA 50k, at 180º and 40 b during 5 minutes, and varying the demolding temperature: 40ºC (a) and 70ºC (b).

When demolding at higher temperatures, close to T_g, the defects appearing were different. Figure 84 shows two areas corresponding to a sample demolded at 100ºC. Here, some of the areas presented nice imprinted lines (Figure 84, left), but some others showed fatal defects (Figure 84, right), probably due to the dettraping of air.

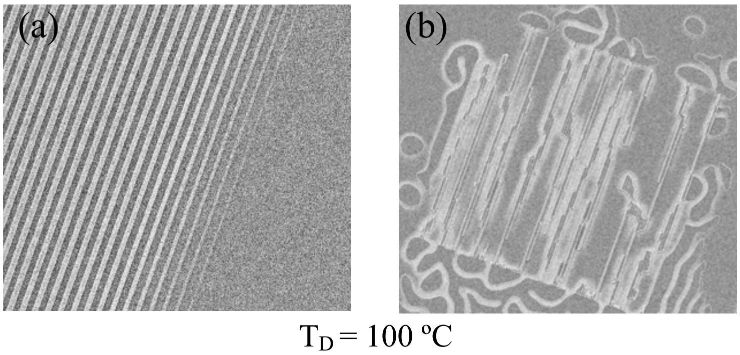

Figure 84. Two areas in a sample imprinted in PMMA 50k, at 180º and 40 bars during 5 minutes, demolded at 100ºC. The area shown in the left is nicely replicated, unlike the area shown in the right. We attribute these defects to the air escaping from the polymer, while it is still in its viscous regime.

When the demolding temperature is risen up to 120 ºC, which is above the T_g of the polymer, none of the areas was successfully imprinted, and the magnitude and number of these fatal defects related to air detrapping drastically increases, as it is shown in Figure 85 (a).

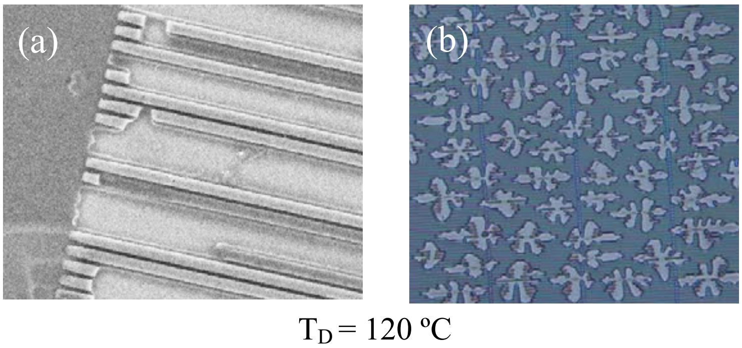

Figure 85. (a): defects in a sample imprinted in PMMA 50k, at 180º and 40 bars during 5 minutes, demolded at 120ºC. None of the areas is successfully replicated in the polymer. Similar defects are shown in (b), corresponding to the triangular shaped lines, imprinted at similar conditions, with no vacuum in the chamber.

We think that these defects can be related **to the presence of air dissolved in the polymer**, because we have observed that if the vacuum was increased inside the chamber, the number of defects was significantly reduced. These structures did never occur in the imprints done with the EVG equipment from MIC, that always pumps the imprinting chamber. In contrast, for the Obducat equipment at CNM, they occurred when demolding at high temperatures. And their number varied in the imprints obtained in Tekniker, as the Jenoptik equipment allowed to make optionally vacuum in the chamber.

When the air is compressed inside the cavities of the stamp, it can be dissolved in the polymer, that is above T_g. When cooling the polymer, the solubility gets lower, and if it is too fast or the polymer is still in the viscous regime, the air forms bubbles, leading to these kind of defects. Another example is shown in Figure 85 (b), corresponding to a more general view of the polymeric triangular-shaped lines, demolded above T_g, where the traces of the air can be observed.

Thus, the **demolding temperature should be risen up to 20 or 30ºC below T_g, to reduce the stress accumulation in the polymer structure** (so the long-term stability is improved), but **not higher, to avoid air de-trapping deffects**, that may result in fatal defects in the imprinted structures, when the vacuum system of the imprinting equipment is not very good.

3.3.- RESIDUAL LAYER MEASUREMENT AND BENCHMARKING WITHIN NAPA

The polymer squeezed below the protrusions, that flows to fill the cavities, depends not only to the stamp design, but also on the applied pressure and its homogeneity at wafer scale. Thus, the study of the residual layer, its concordance with the calculated value, and its distribution in all along the sample can give an idea of the quality of the processing, related to the equipment, compilance layer and imprinting parameters used.

The wafer scale homogeneity of the residual layer is a key parameter for NIL, as it limits the pattern transfer fidelity. Tasks towards benchmarking and comparison of processes and equipments were done, taking advantage of the large number of partners working in the NaPa project and the diversity of equipments and recipes used for NIL,

As the rheology, recipes and results are different for micro and nanometric features, two different benchmarking tasks were proposed by the project coordinators: one, for micrometric size structures, leaded by MIC, and another for nanometric structures, leaded by CEA-LETI-MINATEC.

3.3-1. Micrometric size structures

In the first benchmarking task, leaded by MIC (A. Kristensen), the wafer scale residual layer homogeneity was assessed for different 4-inch wafer-scale NIL setups, available in the NaPa consortium, for imprints of large areas of micrometric size structures [18]. The silicon stamps and substrates to be imprinted were all fabricated in the same laboratory (at MIC). The imprint results were compared afterwards, only deviating between them due to the different NIL setups. 7 partners (having 7 different equipments) were involved in this task: Tyndall, CNRS/LETI, PSI, TEKNIKER, TASC, CNM and MIC. The research centres and the NIL equipments used are listed in Table 5.

Table 5 – List of the institutes involved in the benchmarking tasks, the country where they are placed, and the NIL equipment used for the experiments.

Institute	Country	NIL Equipment
Tyndall	(Ireland)	Jenoptik HEX03 hot embosser
CNMS/LETI	(France)	EVG
PSI	(Switzerland)	SPECAL - Hydraulic Press
TEKNIKER	(Spain)	Jenoptik Hex03
TASC	(Italy)	Weber Hydrolic Press
CNM	(Spain)	Obducat
MIC	(Denmark)	EVG

The silicon stamp consisted on micrometric size lines (25 µm wide, 125 µm pitch, 1 mm long, 300 nm high), in arrays of 1 mm x 1 mm, placed in the top of a mesa, as shown in the scheme (a) and in the SEM images ((b), (d) and (d)) of Figure 86.

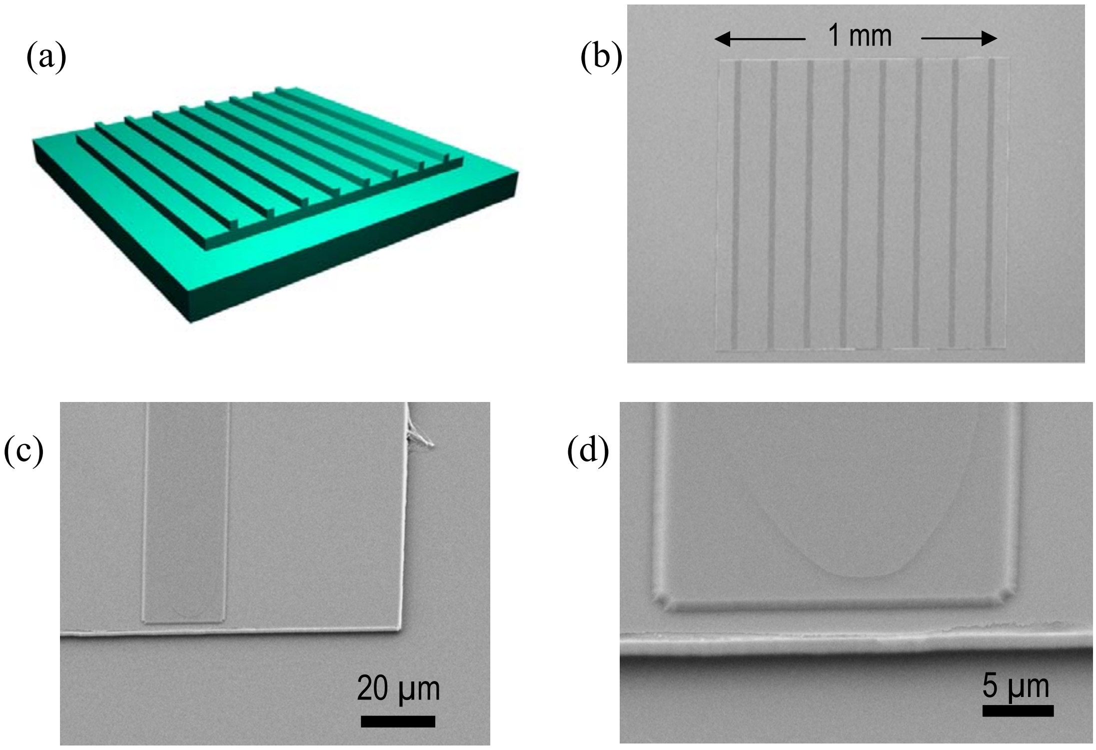

Figure 86. Stamp for residual layer benchmarking: scheme (a) and SEM images of one of the arrays (b), and two details of the lines ((c) and (d)), where the mesa can be observed.

Two different types of imprinting were planned: with full-cavity-filling, and with non-complete-cavity-filling.

The volume of PMMA before (V_0) and after (V_f) imprint (equations (7) and (8) , and schemes in Figure 87 (a) and (b) respectively) owes to volume conservation laws (10), so, for the geometry of this stamp (w = 25µm; g = 100 µm; h_s = 300 nm), the minimum thickness of PMMA (that corresponding to minimum residual layer, i.e., $h_R = 0$) should be h_0 = 240 nm (10).

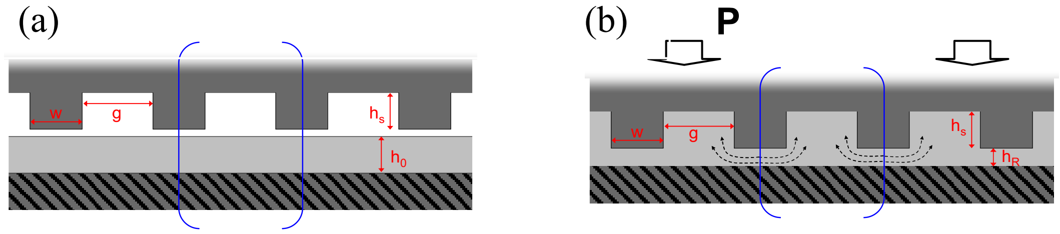

Figure 87. Scheme to illustrate the volume conservation before (left) and during imprinting (right).

$$V_0 = h_0(w+g) \qquad (7) \qquad\qquad V_f = h_R w + g(h_R + h_s) \qquad (8)$$

$$V_0 = V_f \qquad (10) \qquad \longrightarrow \qquad h_0 \geq \frac{g \cdot h_s}{w+g} = 240 \text{ nm} \qquad (9)$$

So, for **complete cavity filling**, the substrates were coated with a **320 nm** thick PMMA film, and, for **incomplete cavity filling**, with **210 nm**.

Each partner could choose the imprinting conditions. At CNM, the imprints were obtained at 180 ºC and 40 bar, and demolded at 60 ºC. The imprinting time was varied from 220 s to 600 s.

Figure 88 shows optical images of the stamp (a) and of three different imprints: with complete cavity filling (b), and non complete cavity filling ((c) and (d)). The last two images were obtained in similar conditions, just changing the imprinting time (from 220 s in (c) up to 600 s in (d)), so the polymer was able to flow, and did not to stay stuck to the sidewalls of the protrusions. Even though, some self-assembled structures can be still observed in (d).

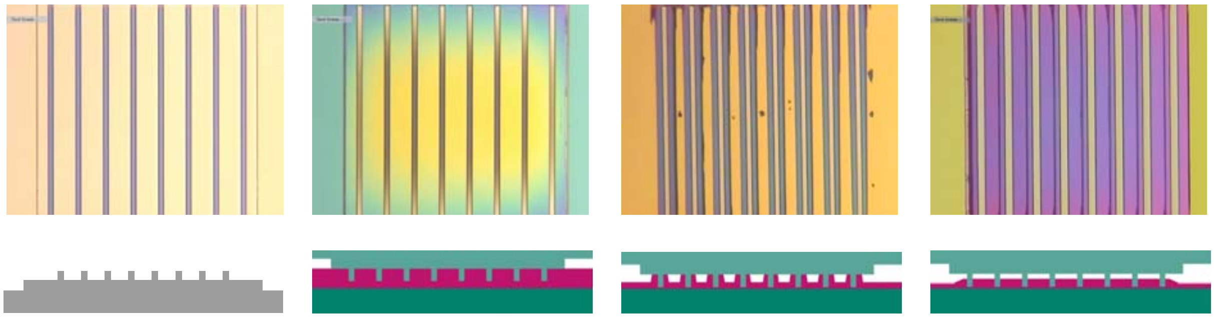

(a) Stamp

(b) Complete cavity filling

(c) Incomplete cavity filling (t_i = 220 s)

(d) Incomplete cavity filling (t_i = 220 s)

Figure 88. Optical image of one of the arrays of the stamp (a), and imprints obtained at CNM, for different conditions: complete cavity filling (b), and incomplete cavity filling (c) and (d). The imprinting time was enlarged from (c) to (d). The corresponding profiles have been schematized below each image.

The measuring technique implied measuring the PMMA height under the protrusions with respect to some reference points, and was done by A.K. et al at MIC [18]. The reference points were made mechanically by removing the PMMA with a scalpel, to get in contact with the underlying silicon substrate. Two reference points were scratched on each side of each protrusion array using a profilometer (Dektak 8 stylus profiler), so a total of 191 points were measured in each sample. Whit this, a residual layer map was obtained, like the ones shown in Figure 89, corresponding to two of the imprints obtained at CNM with the Obducat equipment. The black dots in the figure indicate the measuring points. The mean residual layer, h_R, and the corresponding standard deviation, σ_{hR}, were calculated from the residual layer maps.

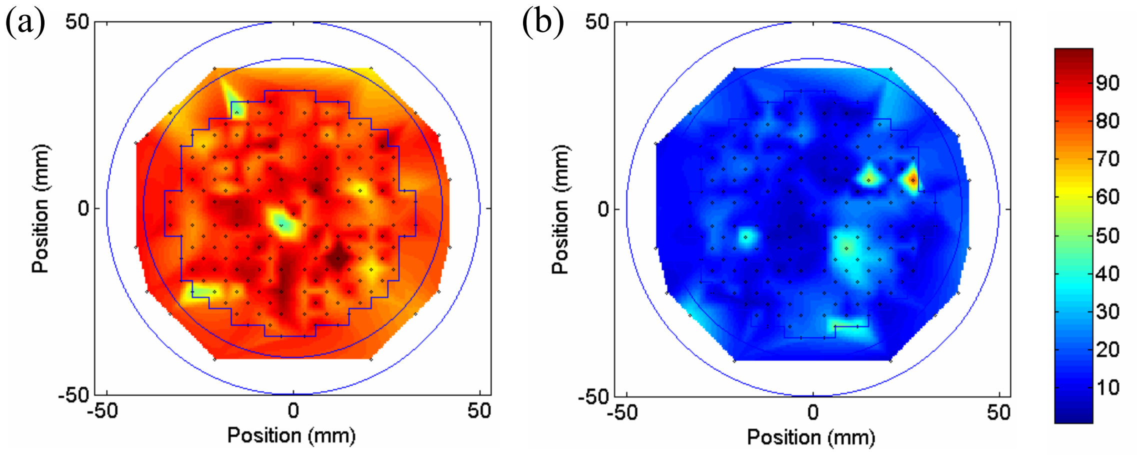

Complete cavity filling

Incomplete cavity filling

Figure 89. Residual layer thickness. The residual layer was measured at 191 different point distributed all over the wafer. The black dots indicate the measuring points. The images corresponds to the imprints obtained for complete (a) and incomplete (b) cavity filling. The colour scalebar ranges from 0 (dark blue) to 100 nm (dark red). Courtesy of A.K. [18]

The characterizations were repeated for all the 14 different imprints obtained with the 7 different equipments. When these residual layer values were plot, interesting results were obtained. The residual layer is plotted in Figure 90 as a function of imprint temperature, T, and imprint pressure, P, both for complete and incomplete filling conditions. The black dashed lines in Figure 90 indicate the theoretical residual layer under complete filling conditions calculated by combining (7), (8) and (10), that corresponded to the volume conservation laws:

$$V_0 = V_f \quad \rightarrow \quad h_r = \frac{h_0(w+g) - gh_s}{w+g} \qquad (11)$$

Due to variations in the measured initial PMMA layer, h_0, and the stamp protrusion height, h_S, the theoretical residual layer thickness lied between the upper (93.8 nm) and lower (71 nm) dashed black line. The value in between is the mean (82.4 nm).

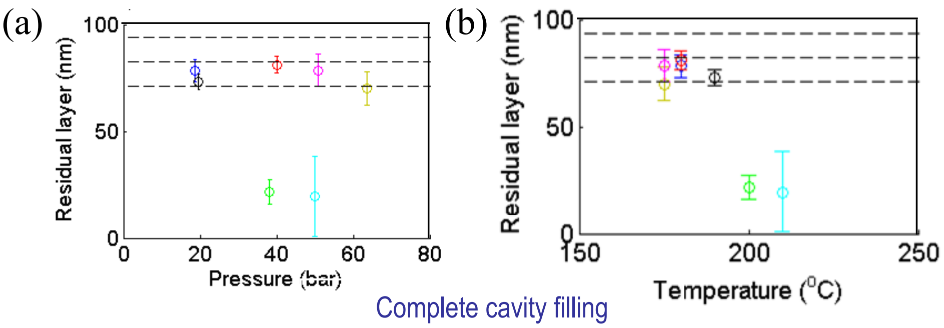

Figure 90. Complete cavity filling conditions. Residual layer (h_r) as a function of the imprint pressure at complete filling conditions (a), and as a function of the imprint temperature (b). The bars in the plots have a length of two times the standard deviation belonging to the individual residual layers. The black dashed lines indicate the theoretical hr for complete filling conditions. The upper line is the upper limit, the middle is mean value and the lower is the lower limit. Courtesy of A. K. [18]

For **complete filling**, h_r was found to be independent of both imprint temperature and pressure, and the theoretical and experimentally measured residual layer thickness agreed, for the used imprint times. Only two imprints deviate from this characteristic. As seen from the plots, the only parameter at which these imprints differ from the others is the imprint temperature. This deviation can probably be explained from the viscosity of the PMMA and the geometry of the stamp. The stamp protrusions are placed on top of mesas elevated from the wafer level. And, on the other hand, the viscosity is strongly depending on temperature (increasing temperature → decreasing viscosity). For low molecular weight PMMA, at temperatures above 200 ºC the polymer melts, so the viscosity drastically drops. Thus, the PMMA flows in-between the mesas. Thus, the polymer thickness in the protrusions is not the initial h_0, but thinner. So, at this point the complete filling description collapse, and the incomplete takes over. The two situations are plotted in Figure 91. The size of the residual layers obtained for the deviating imprints, and the residual layers of the imprints under incomplete filling, with the same imprint parameters, are similar. This indicates that the conclusion is valid.

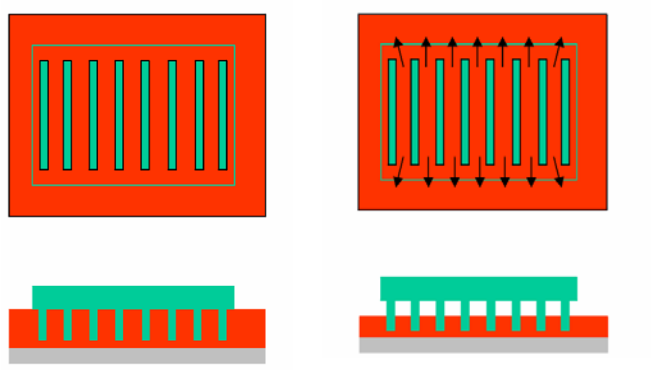

Complete cavity filling   Melting and collapse

Figure 91. Both drawings shows one of the protrusion array imprinted. The left image corresponds to an imprint under complete filling conditions, and the right image is also complete filling, but with imprint temperature above 190°C - 200°C, at which the complete filling conditions collapse, as the polymer melts so the total thickness is reduced. Courtesy of A. K. [18]

The best homogeneity corresponds to the smallest standard deviation, that is 4 nm, obtained with an imprint temperature of 180°C - 190°C and imprint pressure of 20 - 40 bars.

The residual layer thickness measured for the imprints obtained with incomplete cavity filling conditions are shown in Figure 92 as a function of the imprinting temperature. It can be seen that the residual layer thickness decreases with increasing temperature.

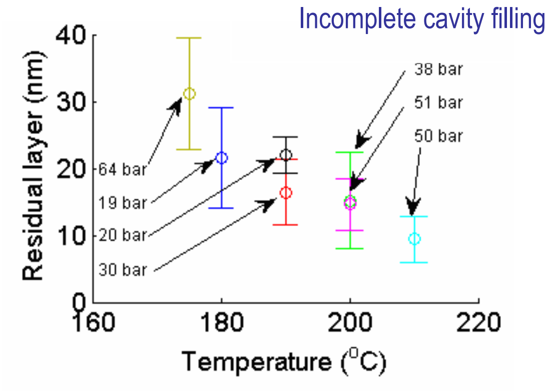

Figure 92. Residual layer thickness (h_r) as a function of the imprinting temperature, for incomplete cavity filling conditions. The measured values decrease with increasing temperature, as predicted by Stefan equation.

The theoretical description of the PMMA flow is given by the Stefan equation:

$$\frac{1}{h(t)^2} = \frac{1}{h_0^{\,2}} + \frac{2P}{\eta_0 w^2} t \qquad (12)$$

Here, h(t) is the residual layer thickness as function of time, and η_0 is the zero shear viscosity, which is decreasing logarithmic with temperature, and w is the width of the protrusions. The Stefan equation predicts that the residual layer thickness will decrease with increasing temperature, and is in agreement with the observation, plotted in Figure 90 (d).

In this case, the smallest residual layer obtained was 9 nm, for an imprint temperature of 210 °C and imprint pressure of 50 bars. The smallest obtained standard deviation is 3 nm, with an imprint temperature of 190 °C and imprint pressure of 20 bars.

This work leads to the conclusion that **all the NIL machines used through the project perform homogeneous imprinting**, with standard deviation in the order of 3 nm to 8 nm. The standard deviation does not seem to change very much, whether the imprint is preformed under incomplete or complete filling conditions. Thus, the wafer-scale homogeneity seems to be more related to the equipment itself than to the imprinting conditions.

3.3-2. Nanostructures benchmarking

A similar task was proposed for nanometric size structures [19]. In this case, the task was leaded by CEA-LETI-Minatec and LTM-CNRS[§] (C. Gourgon) where the stamps were fabricated and the residual layer thickness measured. The method chosen for measuring the residual layer thickness was scatterometry, so non destructive characterizations could be performed.

The partners (and so, the equipments) involved were the same as in the previous task. Only one thickness of PMMA (100 nm) was used for imprinting, and some different types of resists were used for imprinting (PMMA and various mrI).

Once again, to ensure maximum reproducibility, the molds were fabricated in a single batch at CEA-LETI, and one of these molds sent to each laboratory. They were fabricated by electron-beam/deep UV lithography. The patterns were gratings consisting of dense lines with various sizes such as 100/100 and 50/50 nm, defined in several areas with different surfaces: 1 mm^2, 400 x 400 µm^2, and 60 x 60 µm^2. The area outside from that patterned with the features under study was filled with 350 nm wide dots, defined by deep UV lithography in order to homogenize the pressure distribution. The pattern height was ~ 110 nm, as can be seen in Figure 93.

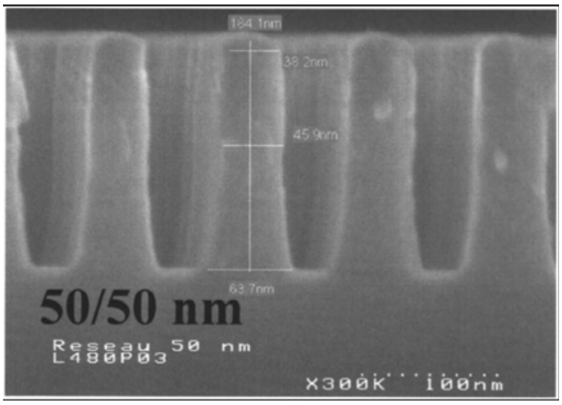

Figure 93. SEM micrograph of 50 nm dense lines on the Si mold used for the benchmarking at the nanoscale [19].

Even though, during the development of the study, several problems were encountered, as imprinting large areas of lines 50 nm wide, 100 nm pitch was not as trivial as expected. Only a couple of partners could successfully imprint the 50 nm wide lines.

During the analysis of the defected structures obtained for the lines array by almost all the partners, some important observations were drawn, that can apply for the optimization of the NIL process when imprinting sub-100 nm size structures, covering large areas.

(i) A very good **antisticking coating** is very important. The antisticking coating was done together with the stamp fabrication, with a commercial tool, and in liquid phase. One of the partners (PSI[**]) that could manage to replicate the lines, performed its own treatment, in gas phase.

(ii) **Pressure** plays an important role. The lines printed at 40 bars were completely pulled off. This was not due to sticking problems, as the appearance of the cracks would have been different. As an example, Figure 94 shows two of the structures imprinted at CNM. In (a), high pressure (40 bars) was used, and in (b), it was reduced to contact pressure (10 bars). In some other labs, for reduced pressures down to 15 or 10 bars, the lines were well printed, in larger areas. Furthermore, even at 1.5 bars it was shown that the mold cavities were filled. The behaviour obtained at 40 bars is attributed to a mold bending [20] during the printing step or to an excessive stress at the bottom of the patterns [10].

[§] CNRS-LTM and CEA-LETI-Minatec- F-38054, Grenoble Cedex 9 (France)

[**] Paul Scherrer Institute (PSI) Villigen 5232 (Switzerland).

(iii) The **chemical composition of the polymer** is also important. Sticking effects to the mold and deformation of the lines due to the high pressure depended on the polymer nature, since the results were better when using the mr-I17010E polymer. This difference is still under investigation.

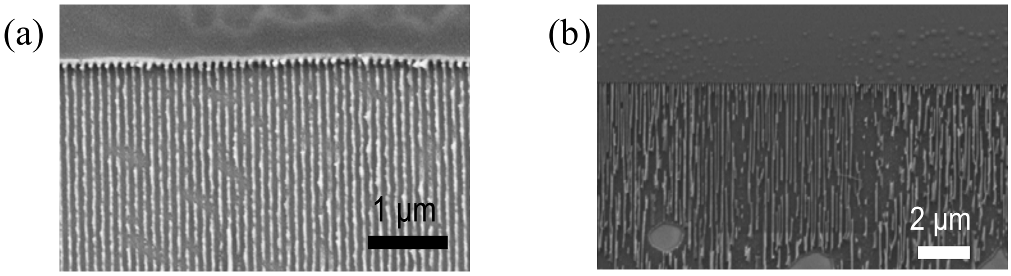

Figure 94. Defected lines (50 nm wide, 100 nm pitch), obtained by imprinting at 40 bars (a) and at 10 bars (b). In the first case, the defects may be related to high applied pressure. In the second, as the appearance is different, the defects could be due to sticking problems.

With some of the imprints made by the partners that could manage to get nice lines, scaterometry showed that the residual layer thickness was in good agreement with the calculated by the material conservation law (11), as shown in Figure 95. Unfortunately, the number of partners and imprints was not enough to get a tendency or a statistic like that obtained for the micrometric size structures.

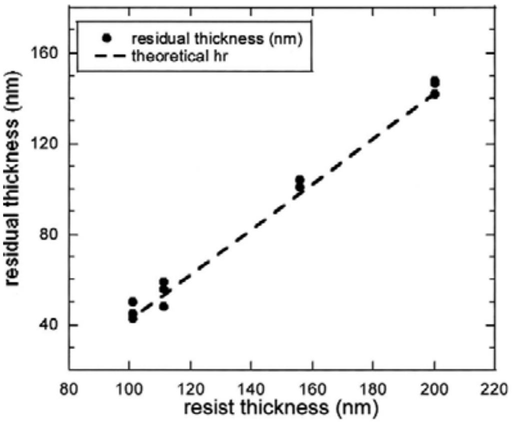

Figure 95. Residual layer thickness as a function of the initial resist thickness: experimental measurements (a) and calculations (b). [21]

At CNM, we obtained cracked lines, like the ones shown in Figure 94. A dependence on the pressure was also observed, as already mentioned and shown above. The quality was improved as a function of the imprinting parameters, and some of the areas seemed nice. But we didn't obtain a complete area nicely imprinted. Some of the defects may be due to stamp bending, and/or related to the applied pressure. Nevertheless, we attribute the cracks to sticking problems or stamp design, as also some of the areas containing patterns with larger lateral sizes appeared often defectuous.

This benchmarking demonstrates that the printing of nanostructures needs special rules and precautions.

3.4.- REFERENCES

[1] Schift, H., Heyderman, L.J. and Gobrecht, J.,
Efficient replication of nanostructured surfaces.
Chimia, 2002. **56**(10): p. 543-546.

[2] Schift, H.,
Nanoimprint lithography: An old story in modern times? A review.
Journal of vacuum science & technology. B, Microelectronics and nanometer structures, 2008. **26**(2): p. 458-480.

[3] Merino, S., Retolaza, A., Juarros, A., Schift, H., Sirotkin, V., et al.
Refined coarse-grain modeling of stamp deformation in nanoimprint lithography. in *Technical Proceedings of the 2008 NSTI Nanotechnology Conference and Trade Show, NSTI-Nanotech, Nanotechnology 2008*. 2008.

[4] Merino, S., Retolaza, A., Juarros, A. and Schift, H.,
The influence of stamp deformation on residual layer homogeneity in thermal nanoimprint lithography.
Microelectronic Engineering, 2008. **85**(9): p. 1892-1896.

[5] Schulz, H., Wissen, M., Bogdanski, N., Scheer, H.C., Mattes, K., and Friedrich, C.,
Impact of molecular weight of polymers and shear rate effects for nanoimprint lithography.
Microelectronic Engineering, 2006. **83**(2): p. 259-280.

[6] Schulz, H., Scheer, H.C., Hoffmann, T., Torres, C.M.S., Pfeiffer, K., et al.,
New polymer materials for nanoimprinting.
Journal of Vacuum Science & Technology B, 2000. **18**(4): p. 1861-1865.

[7] Tour, J.M. and He, T.,
Electronics: The fourth element.
Nature, 2008. **453**(7191): p. 42-43.

[8] *microresist technology, GmbH (Berlin).* www.microresist.de.

[9] Scheer, H.-C., Bogdanski, N., Wissen, M., Konishi, T. and Hirai, Y.,
Polymer time constants during low temperature nanoimprint lithography.
Journal of Vacuum Science & Technology B, 2005. **23**(6): p. 2963-2966.

[10] Hirai, Y., Yoshida, S. and Takagi, N.,
Defect analysis in thermal nanoimprint lithography.
Journal of Vacuum Science & Technology B, 2003. **21**(6): p. 2765-2770.

[11] Ro, H.W., Ding, Y.F., Lee, H.J., Hines, D.R., Jones, R.L., et al.,
Evidence for internal stresses induced by nanoimprint lithography.
Journal of Vacuum Science & Technology B, 2006. **24**(6): p. 2973-2978.

[12] Ding, Y.F., Ro, H.W., Douglas, J.F., Jones, R.L., Hine, D.R., et al.,
Polymer viscoelasticity and residual stress effects on nanoimprint lithography.
Advanced Materials, 2007. **19**(10): p. 1377-+.

[13] Bogdanski, N., Wissen, M., Mollenbeck, S. and Scheer, H.C.,
Structure size dependent recovery of thin polystyrene layers in thermal imprint lithography.
Microelectronic Engineering, 2007. **84**(5-8): p. 860-863.

[14] Fernandez-Cuesta, I., Borrise, X., Retolaza, A., Merino, S., Mendels, D.A., et al.,
Determination of stress build-up during nanoimprint process in triangular Polymer structures.
Microelectronic Engineering, 2008. **85**(5-6): p. 838-841.

[15] Mendels, D.A., Fernandez-Cuesta, I., Borrise, X., Retolaza, A., Merino, S., et al.,
A finite element mesh tailored to full NIL process modelling: hot embossing, cool-down and stamp release, in *Microprocesses and Nanotechnology 2007, Digest of Papers*. 2007, JAPAN SOCIETY APPLIED PHYSICS: Tokyo. p. 278-279.

[16] Mendels, D., Fernández-Cuesta, I., Borrisé, X., Retolaza, A., Merino, S., et al.
-. in *NNT*. October 2007. Paris (France).

[17] Scheer, H.C., Bogdanski, N., Wissen, M., Konishi, T. and Hirai, Y.,
Polymer time constants during low temperature nanoimprint lithography.
Journal of Vacuum Science & Technology B, 2005. **23**(6): p. 2963-2966.

[18] Kristensen, A.,
NaPa Residual layer thickness benchmarking. 2005, MIC: Copenhagen. p. 67.

[19] Gourgon, C., Chaix, N., Schift, H., Tormen, M., Landis, S., et al.,
Benchmarking of 50 nm features in thermal nanoimprint.
Journal of Vacuum Science and Technology B, 2007. **25**(6): p. 2373-2378.

[20] Merino, S., Retolaza, A., Schift, H. and Trabadelo, V.,
Stamp deformation and its influence on residual layer homogeneity in thermal nanoimprint lithography.
Microelectronic Engineering, 2008. **85**(5-6): p. 877-880.

[21] Gourgon, C., Chaix, N., Schift, H., Tormen, M., Landis, S., et al.,
Benchmarking of 50 nm features in thermal nanoimprint.
Journal of Vacuum Science & Technology B, 2007. **25**(6): p. 2373-2378.

Chapter 4

Explorative fields for NIL applications

Besides the study of the polymer rheology to minimize the internal stress accumulation and the residual layers benchmarking, an important goal of this work was the use of NIL technology **to fabricate devices**, designed and devoted for different **applications** and **projects**. In the next sections of this thesis memory (Section 2 and Section 3), two applications will be described in depth, starting from the design of the devices, describing the fabrication process and ending with their characterizations. Nevertheless, we have also collaborated in other projects where nanostructures were needed, and NIL was the most suitable fabrication process. In this chapter we will have a general overview of some of these projects, to give an idea of the versatility of NIL, and the different fields of possible applications.

4.1.- FABRICATION OF STO NANOPILLARS

The first application was developed in collaboration with N. Mestres and T. Puig, from ICMAB[*], within a National Project CANNAMUS[†], focused in the assisted growth of complex oxides with templates.

Magnetic oxide perovskites are particularly interesting materials, especially in the superconductive field, due to the wide range of electronic and magnetic properties available within the same crystal structure. However, the fabrication of structures from epitaxial perovskites with lateral dimensions of less than few hundreds of nanometers, (the relevant scale for future electronic and spintronic applications), remains a challenge [1]. Problems inherent to the top-down fabrication route include the low etching rate of the materials, damage to the crystal structure from ion milling, and redeposition of amorphous material on the substrate [2].

4.1-1. Fabrication process

An assisted bottom-up method, based in nanoimprint lithography, was considered to achieve the fabrication of arrays of nanodots of the magnetic perovskite $La_{0.7}Sr_{0.3}MnO_3$ (LSMO) over large areas (diameter and pitch below 1 µm) [3] that are supposed to maintain the crystallinity of the substrate, its epitaxial structure and ferromagnetic properties after the fabrication process. An imprinted polymer template was used to assist the chemical solution synthesis. Since magnetic perovskites can also be combined epitaxially with ferroelectrics and high temperature superconductors, this technique opened the possibility of fabricating novel nanoscale multifunctional heterostructures.

A scheme of the whole fabrication process is depicted in Figure 96:

a. The **stamp**, containing the dot array is designed (diameter, pitch, aspect ratio) and fabricated by EBL and RIE; a 200 nm thick layer of PMMA is spun onto a $SrTiO_3$ (STO) substrate. Then, the stamp is imprinted at 180ºC and 40 bars, during 20 minutes. The imprinting time needs to be enlarged, compared to the time set when a silicon substrate is used for the same stamp, as the thermalization of the system is slower when using such an insulating substrate.
b. After removing the residual layer with an oxygen plasma[‡] for 4 minutes, **chemical precursor solutions** (prepared from lanthanum, strontium and manganese nitrates in water, mixed with ethylene glycol) are used to fill the PMMA holes by capillarity.
c. Then, the samples are **heated up** to high temperatures (800-1000 ºC, 5 hours) for oxide formation and phase crystallization.
d. During the high temperature treatment the PMMA template is eliminated by combustion, and the as-synthesized **nanodots are grown** onto the STO substrate.

---

[*] ICMAB – Instituto de Ciencia de Materiales de Barcelona (ICMAB, CSIC). Campus de la UAB. 08193 – Bellaterra (Spain)

[†] CANNAMUS - *Crecimiento asistido por nanoplantillas de nanoestructuras multifuncionales a partir de soluciones químicas* – Intramurales CSIC (2005-2007).

[‡] Residual layer removal with an oxygen plasma: Oxford Plasmalab 80+: 10 sccm, 20 W, 75 mtorr. Etching rate: 40 nm/s.

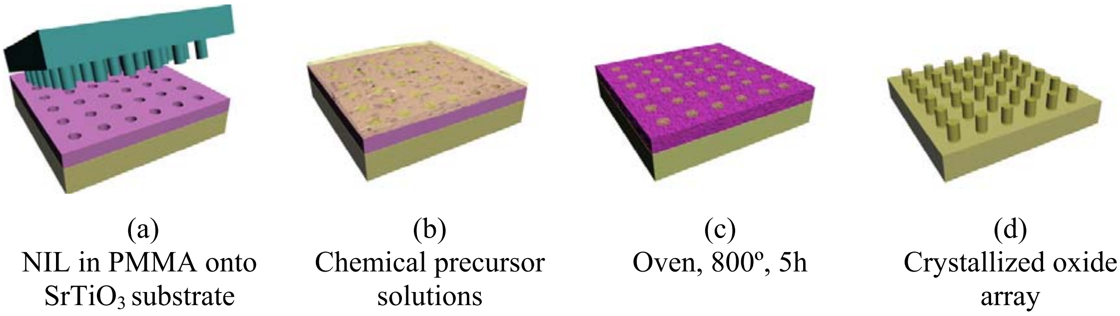

Figure 96. Description of the fabrication process. (a) the array of dots of the silicon stamp is imprinted in layer of PMMA, spun onto a SrTiO3 (STO) substrate. (b) chemical precursor solutions (lanthanum, strontium and manganese nitrates in water, mixed with ethylene glycol), that fill the PMMA holes. (c) the sample is heated in an oven. PMMA is burned during the process, and the oxide crystallizes. (d), resulting perovskite nanodots arrays.

4.1-2. Results

Figure 97 shows images of the results of the process. Figure 97 (a) corresponds to a stamp, made in silicon, consisting of 1μm pitch dots, 200 nm high. After imprinting and removing the residual layer, the holes showed a diameter of 400 nm, as can be seen in Figure 97 (b). The non-rounded shape of the imprinted holes (compared to that of the stamp) is probably due to thermalization effects, related to the different thermal expansion coefficients of the silicon stamp and the STO substrate. Figure 97 (c) shows the perovskite pillar array, 400 nm diameter, resulting from the synthesis process, that demonstrates that $La_{0.7}Sr_{0.3}MnO_3$ nanodots arrays could be successfully grown on lattice matched STO substrates by chemical solution deposition using PMMA templates fabricated by NIL. Figure 97 (d) corresponds to a similar sample, processed with a different PMMA template height.

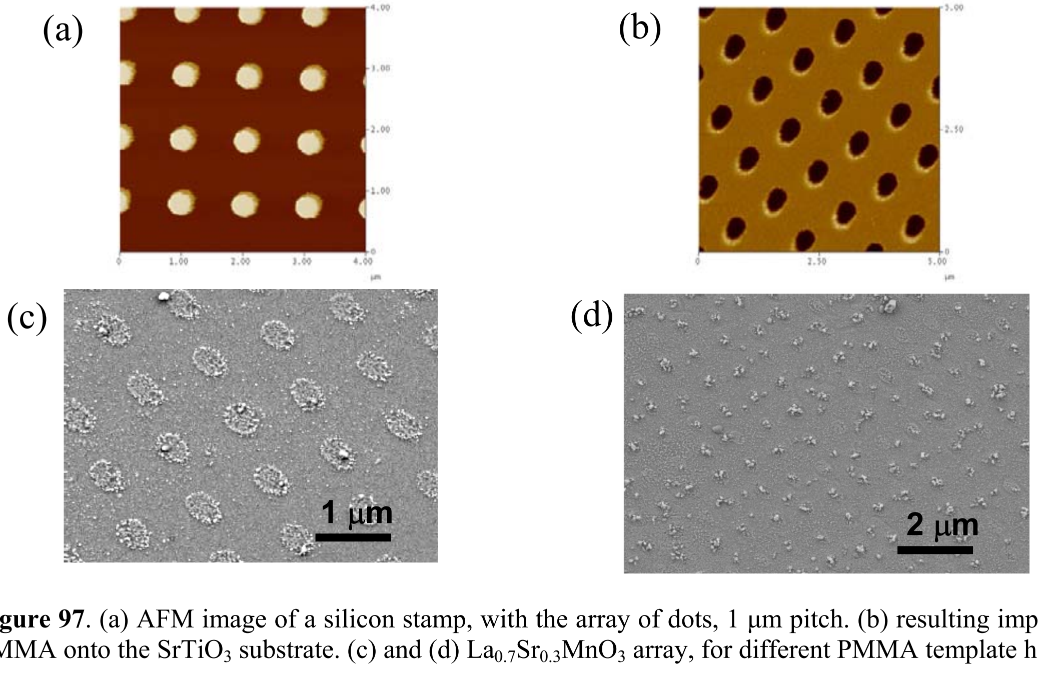

Figure 97. (a) AFM image of a silicon stamp, with the array of dots, 1 μm pitch. (b) resulting imprint in PMMA onto the $SrTiO_3$ substrate. (c) and (d) $La_{0.7}Sr_{0.3}MnO_3$ array, for different PMMA template height.

Further experiments are currently being performed, in order to optimize the process conditions: pillars aspect ratio, and synthesis time and temperature.

Figure 98 shows a silicon stamp (a) and the resulting imprint in PMMA (b) of an array of dots, with a diameter of 100 nm, and a pitch of 200 nm that is being used to reduce the pitch and diameter of the pillars. The possibility of oxidation of the pillars of the stamp as described in previous chapters is also being explored as a possibility to reduce the lateral dimensions.

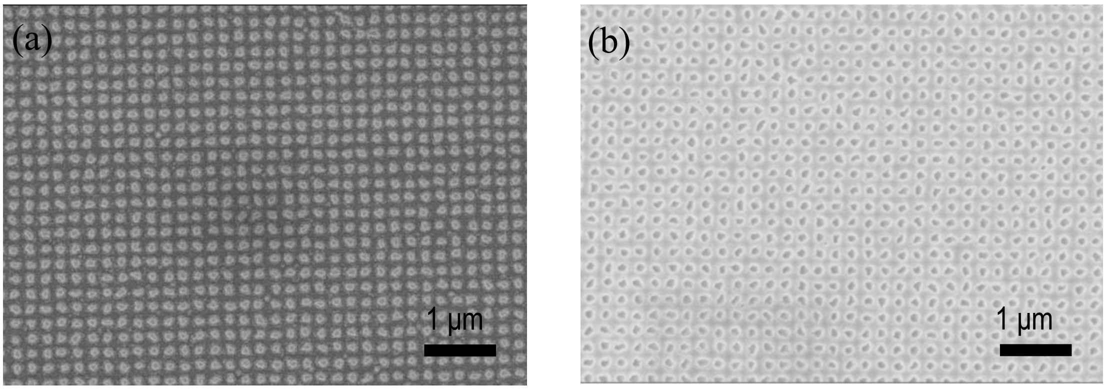

Figure 98. (a) Silicon stamp, with smaller dimensions (100 nm diameter, 200 nm pitch). (b) imprinted PMMA holes onto the STO substrate.

This work leaves an open line for research, as several aspects remain un-optimized. Apart from the shrinkage of the lateral dimensions of the pillars, the aspect ratio of the imprinted holes needs to be increased. The growth process based on a liquid precursor leads to a reduction in the final vertical dimensions, so, to obtain pillars with a certain height, the depth of the holes in the matrix should be increased. The results obtained up to now consist on nano-clusters, probably not connected between them, that do not cover the whole imprinted area, as can be seen in Figure 97 (c) and (d), as a consequence of the low aspect ratio of the used stamp. The increase in the aspect ratio of the pillars would allow having more liquid material available for the growth of epitaxial pillars.

This constitutes a very interesting application of nanoimprint lithography, as it is very difficult to nano-structure insulating substrates, especially in the case of complex oxides, where the crystallographic net should not be affected by the fabrication process. It's remarkable also the novelty of the work, as there are very few NIL applications related to the **superconductive materials** field.

4.2.- LARGE SCALE AREAS FOR PROTEIN PATTERNING

Another application of NIL is based on the possibility of direct nanostructuration of functional polymers. This work has been done in collaboration with S. Merino and A. Retolaza, from Tekniker and A. Cruz, from Gaiker[§] in the frame of a national project, NILSIS, that aims to explode the advantages of NIL technology to fabricate devices in different fields, such us biology, electrochemistry, metrology and/or sensors.

Selective localization of active proteins on patterns or specific places is important for the development of biosensors, bioMEMS, tissue engineering, and basic proteomic research. Nanopatterning by NIL of a polymer that has functional properties is a flexible technique for selectively patterning bioactive proteins with nanoscale resolution. This, together with fluoropolymer surface passivation allows exploiting the specificity of certain recognition events. Taking advantage of NIL-based nanofabrication, high throughput reproducible nanoscale protein patterns with high selectivity and retained biofunctionality can be obtained.

Many applications of patterned biomolecules can be enhanced by improving the resolution of the protein features. Smaller feature sizes enable, for example, the fabrication of high density protein

---

[§] Gaiker. Parque Tecnológico – Zamudio 48170, Vizcaya (Spain).

arrays for biosensors or proteomic screening, or facilitate studies of cellular interactions with small precisely located clusters of extracellular matrix proteins.

In this work, we were in charge of the fabrication of stamps with nanometric features, Tekniker of imprints, process development and optimization and characterization, and Gaiker of the functionalization protocol.

4.2-1. Fabrication process

NIL has been used in previous works for protein patterning combining high resolution and high density of proteins [4-6]. Hoff et al [4] developed a technique based on NIL and fluoropolymer surface passivation (to avoid protein adsorption) and an aminosilane passivation to form a covalent layer with biotin, exploiting later the specificity of the biotin/streptavidin linkage (Figure 99 (a)). Falconnet et al. [5] developed a technique for protein patterning combining NIL and molecular assembly patterning by lift-off (Figure 99 (b)). Park et al [6] used NIL and aminosilane deposition followed by lift-off of the sacrificial printable polymer to get streptavidin patterning at the nanoscale (Figure 99 (c)). However all these three processes require the use of a sacrificial printable polymer and vapour deposition of aminosilane, which leads to a complex process.

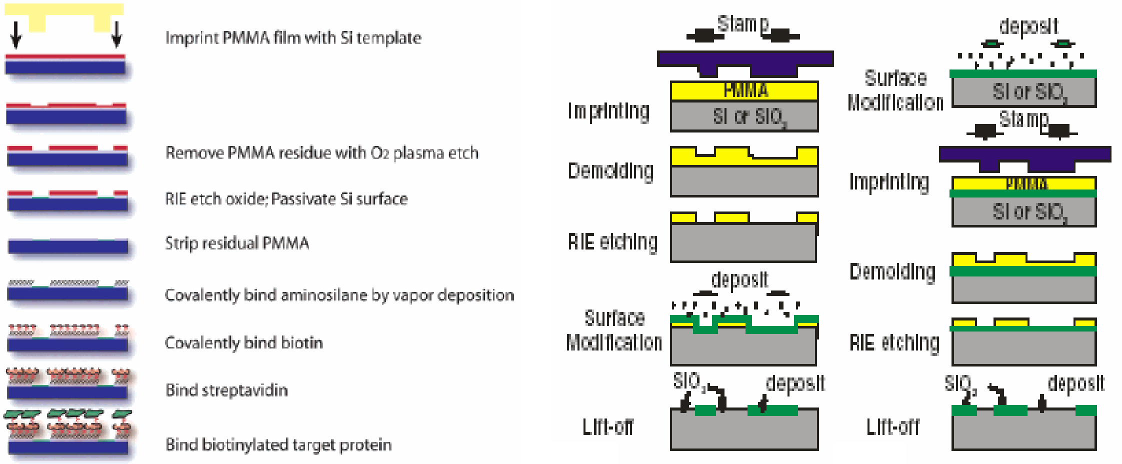

(a) (b) (c)

Figure 99. Process approaches reported in previous works for protein pattern. In (a), a method proposed by Hoff et al. [4] is shown, that is based in local functionalization with different types of silanes, selective for specific binding. In (b), the methods reported by Park et al. [6] are schematized. In both of them, the pattern is created by NIL, and the protein pattern by deposition and lift-off (b) or a layer, that is already deposited below the PMMA, selectively etched after NIL (c).

In this work, we overcame a new approach [7]. A new bio-functionalized copolymer[**] developed at CIDETEC[††] was used as a printable material, following the procedure shown in Figure 100. It has a great affinity to streptavidin protein, so it can be used to immobilize any biotinylated protein and an enzymatic immunoassay. As an example, it was proposed to detect the presence of the immunoglobulin G (IgG) protein on a rabbit serum sample.

[**] Functionalized co-polymer: 80% benzyl methacrylate and 20% succinimydil methacrylate

[††] CIDETEC - Parque Tecnológico de San Sebastián. 20009 - San Sebatian (Spain)

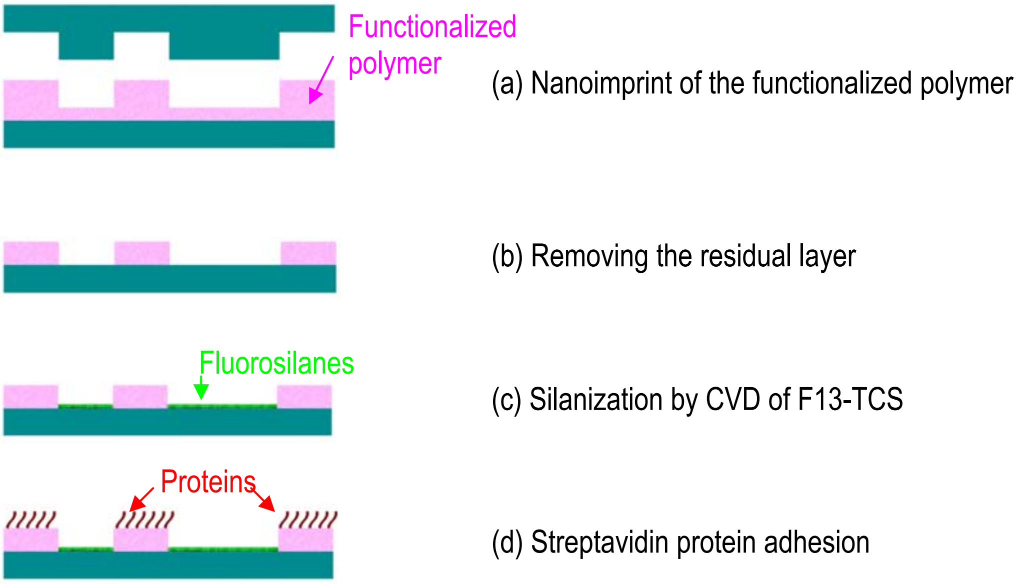

Figure 100. Process flow for protein patterning. The functionalized co-polymer is structured by NIL (a), and the residual layer removed with an oxygen plasma (b). In the un-covered areas, a fluorosilane is deposited (c), to minimize the non-specific adhesion of the proteins. The proteins are selectively adhered to the functionalized polymer, due to the biotin-streptavidin affinity.

4.2-2. Stamp design and fabrication

Two different types of silicon stamps were fabricated. The first consisted on **microscale patterns**, with five different gratings (ranging from 3.3 µm to 11.3 µm periods and equal line width and space), that were fabricated in Tekniker, by UV-Lithography and RIE (SF_6/C_4F_8 plasma) to reach 270 nm in depth.

The second type consisted on **nanometric features**, fabricated by e-beam lithography at CNM. As the lines would have to be observed with a fluorescent microscope, the lines were patterned with long spacing between them, and covering large areas. Squared arrays of 200 nm wide lines, spaced 20 µm, 1 mm long, were defined by stitching of smaller fields (200 µm x 200 µm) by using a SEM with lithographic capabilities. The GDS design is shown in Figure 101 (a). Such small lines, with such a large distance between them, patterned in a 4 inch wafer, are very difficult to locate. Thus, some marks, such as crosses in the corners and additional arrays of lines, wider and closer (to scatter the light) were added in order to facilitate the location of the arrays. Figure 101 (b) shows one of the patterned areas in a 4 inch silicon wafer, defined in PMMA after e-beam exposure and development. Here, the stitching fields can be seen. The reactive ion etching resulted again in features 270 nm deep.

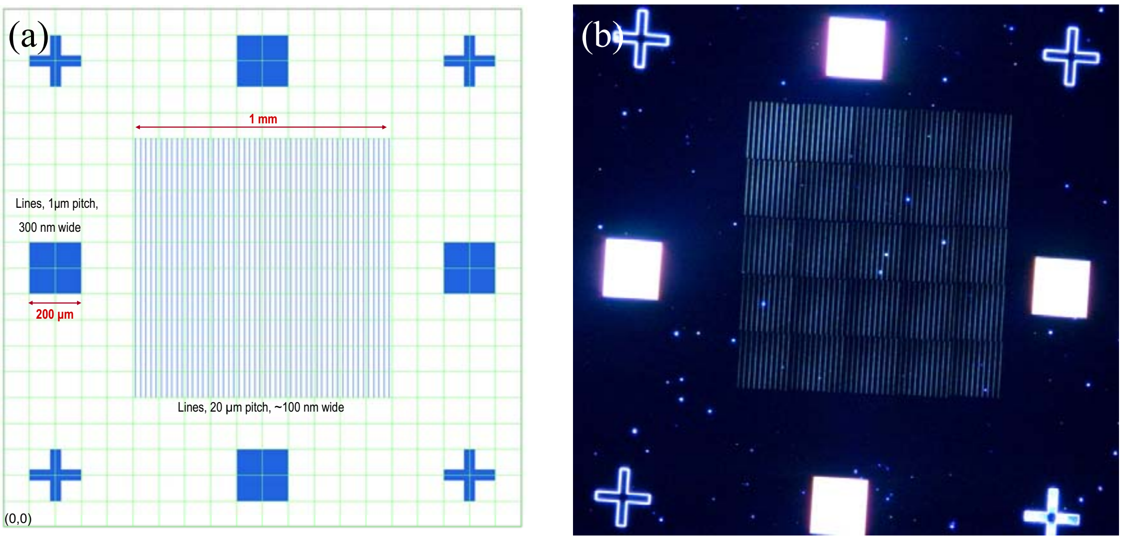

(a) Design

(b) Optical image of the pattern in PMMA

Figure 101. GDS design (a) and optical image (dark field) of the pattern in PMMA (b). An area covering 1mm x 1mm was patterned with lines 100 nm wide, 20 µm pitch, by stitching of small fields. The structures around this area serve to locate the area of interest, as it cannot be easily seen by naked eye. This structure was repeated several times in the wafer.

4.2-3. Results

The stamps were imprinted on silicon substrates coated with a 270 nm thick film of the functionalized polymer at 160 ºC (glass transition temperature of 86 ºC) and the residual layer was etched by an O_2 plasma. To avoid the adsorption of proteins on the silicon areas, **fluorinated silanes** were deposited. These substrates were soaked in a solution of streptavidin (small concentrations of BSA[‡‡] protein were added to avoid non-specific binding) containing the enzyme HRP[§§] and streptavidin marked with a fluorescent label[***] for ELISA type tests and fluorescence detection respectively. Figure 102 shows fluorescence images of the streptavidin protein patterning on the micro (a) and nanoscale (b), compared to the low fluorescence signal of the background.

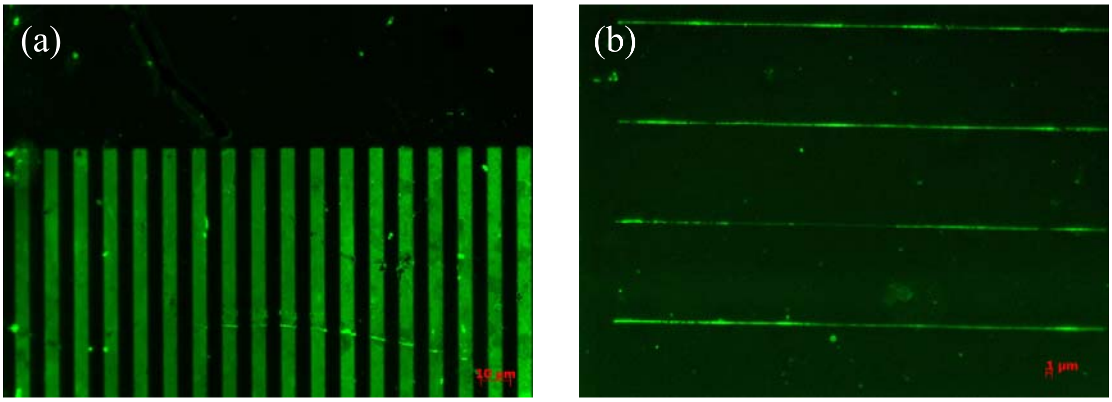

Figure 102. Fluorescence images of patterned samples for a streptavidin concentration of 20 µg/ml containing 0,05 µg/ml of BSA protein. Grating with 10 µm period and equal lines and spaces (a), and 200 nm width lines (b).

[‡‡] BSA - bovine serum albumin.

[§§] HRP - horseradish peroxidase

[***] Fluorescent label: Alexa Fluor 488

With the aim of showing the biological functionality of the streptavidin protein once it is bound to the polymer, the substrates were incubated with a biotinylated antibody (Goat pAb[†††] to rabbit IgG) adding later a rabbit serum sample and finally a secondary antibody specific for IgG (Goat anti-rabbit IgG) conjugated to a colour development enzyme (HRP).

Figure 103 shows the colour development measured as absorbance at 450 nm in the sandwich-ELISA test for the complete system as well as the negative controls showing the specificity of the immunoassay for IgG detection and the biological functionality of streptavidin bounded to the polymer. Different dilutions of serum were prepared aiming to establish a correlation between IgG concentration and light absorbance (ELISA type tests) and fluorescence signal (fluorescent detection).

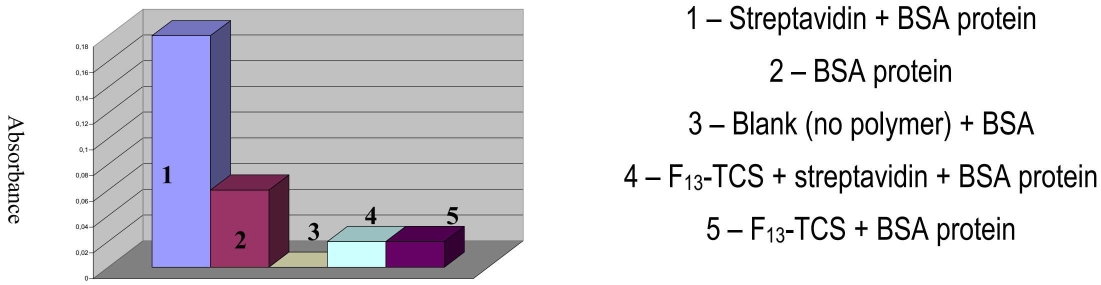

Figure 103. Absorbance of light at 450 nm for the immunoassay proposed for the IgG detection as the whole of the sequence (Goat pAb to rabbit IgG+ rabbit serum plasma+ Goat anti-rabbit IgG-HRP) is cultivated on the polymer with: (1) streptavidin and BSA protein, (2) BSA protein, (4) F13-TCS+streptavidin + BSA protein, (5) F13-TCS+ BSA protein. (3) Absorbance of light at 450 nm for the same immunoassay cultivated on Silicon + BSA protein (without polymer). Streptavidin concentration 20 µg/ml and BSA concentration 0, 05 µg/ml for all the enzymatic reactions.

This work shows the potential of this simple process, which can be used with different immunoassays for the detection of the presence of other proteins from the detection of a threshold showing its presence in a biological sample.

In order to check the advantages of reducing the dimensions down to the nanoscale, additional tests are currently being developed. For this, stamps with lines of different widths and pitch are being fabricated. The design is similar to that shown in Figure 102, but the number of lines is varied, so the total amount of polymer that is structured is the same for all the dimensions. An optical image of the overall patterned area of the wafer is shown in Figure 104. Here, the insets show a zoom of the lines under study. The ones of the upper patter are wider, meanwhile those in the bottom are narrower. Thus, the total patterned area with lines is the same in all of them.

[†††] PAB - polyclonal antibody

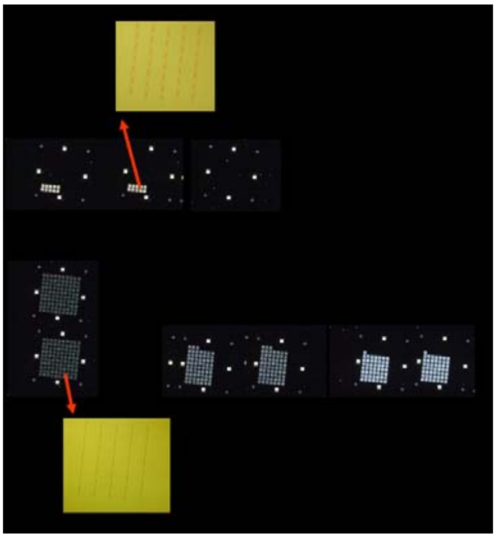

Figure 104. Optical (dark field) image of the new stamp. The areas having different number of lines, with different widths, but maintaining the total structured area can be seen. The two insets show optical images of the lines in two different areas.

One of the aims of this work is to compare the optical results obtained for the ELISA tests for all the chips, in order to see if the adhesion and selectivity is improved for smaller dimensions, and/or to find an optimal width/pitch ratio.

This explorative field is still under study, as it has many possibilities for applications. The basics are also being studied, by using new chemicals and the new stamps.

4.3.- FABRICATION OF SURFACES WITH CHEMICAL CONTRAST

The last application that will be described in this chapter was developed in the framework of the NaPa project, in collaboration with A. Meister, from CSEM[‡‡‡], as a mix-and-match task, to combine the MEMS and NIL sub-projects. Surfaces with chemical contrast were fabricated by NIL. The purpose of the samples is to be used to control, study (and reduce) the lateral dimensions of droplets of a liquid locally deposited onto them. For this, a tool, that was developed at CSEM within the NaPa project would be used (NanoDispensing - NADIS [8]).

Two different kinds of samples were fabricated.

The first ones consisted on holes made in a PMMA film, which thickness was reduced after NIL with an oxygen plasma, so the final topographical contrast was very small. This allows studying the difference between the chemical nature of PMMA and the silicon substrate, as the topographical contrast can be neglected (Figure 105 (a)).

In the second one, the surfaces (Si or SiO_2) were locally silanized, using the imprinted PMMA features as a mask. As described in previously in chapter 2, the silanes form a monolayer (height ~ 1 nm), that is highly hydrophobic (fluorinated silanes). After removal of the remaining PMMA, the contrast between silanized and bare substrate can also be studied (Figure 105 (b))

[‡‡‡] CSEM - Centre Suisse d'Electronique et de Microtechnique SA - CH-2002 Neuchâtel (switzerland)

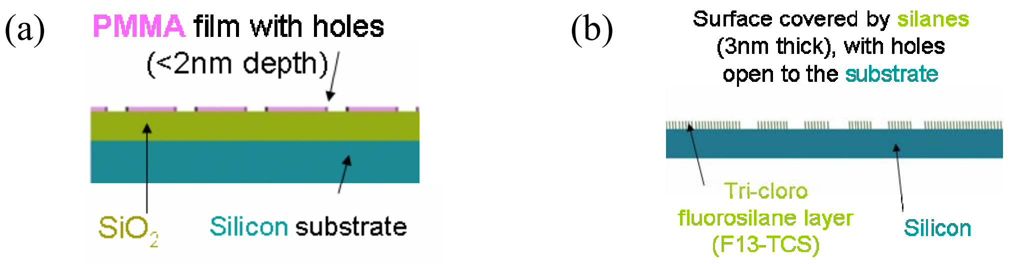

Figure 105. Schemes of the two types of samples having surface chemical contrast fabricated by NIL. SiO2 holes, defined in a matrix of very thin PMMA (a), and silicon holes, in an hydrophobic matrix (fluorosilanes) (b).

One of the problems of dealing with this kind of samples is that the final patterns could not be seen with an optical microscope, which made further post-processing or location of the NADIS tip arduous. In order to facilitate the location of the modified areas, micrometric metal structures were first defined in both types of samples, by EBL or NIL, metallization (~ 20 nm of aluminium) and lift-off.

4.3-1. SiO_2 holes in a PMMA matrix

4.3-1:a.- Fabrication process

A scheme of the steps of the fabrication process to define **holes** in a very **thin PMMA film onto a SiO_2** substrate by NIL is shown in Figure 106:

a. Aluminum marks were first defined onto the silica substrate by NIL, metallization and lift-off.
b. Then, a 200 nm thick film of PMMA 35k was spun onto the sample and imprinted using a silicon stamp with pillars (100 nm high, 300 nm diameter, 1 µm pitch), at 180 ºC and 40 bars, during 10 minutes. The stamp used had very large areas patterned with pillars (larger than the area of the substrate itself), so no alignment was needed prior to NIL, in order to coincide the imprinted structures inside (or close to) the metal marks.
c. In order to minimize the topographical contrast, the samples were treated in an anisotropic oxygen plasma for 5 minutes. Controlling the etching time only a very thin layer of PMMA (below 10 nm) was left, with holes open to the SiO_2 substrate.

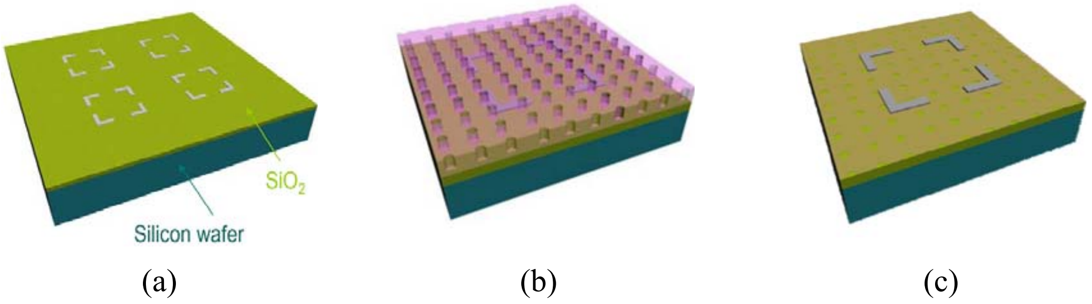

Figure 106. Sketch of the process to create a structured very thin PMMA layer with holes. Aluminum aligning marks are patterned onto the SiO_2/Si substrate (a). Then, it is covered with PMMA, and patterned by NIL (b). An oxygen plasma is finally done, to reduce the thickness of the layer down to few nanometers (c).

4.3-1:b.- Results

Figure 107 (a) shows optical images of a sample before the oxygen plasma. Here, the aluminium marks can be seen, inside which, by zooming up, the patterned dots can be observed (b).

Figure 107 (c) shows an AFM image of the patterned dots in PMMA, after the oxygen plasma. The remaining thickness of PMMA was ~ 2 nm, as evaluated from the AFM image. This thickness is low enough, so for the NADIS dispensing and control of the droplets, **the chemical contrast will be dominant over the topographical** one.

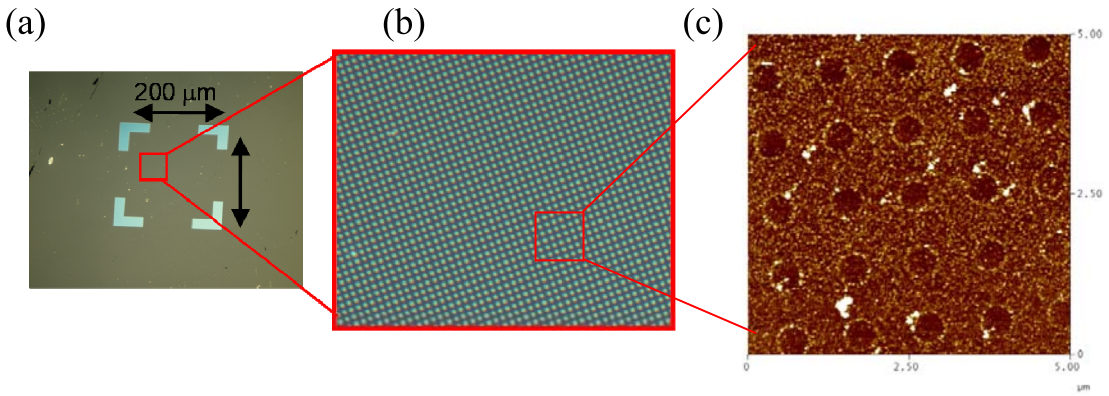

Figure 107. Optical images of a patterned area (a). The chip is covered with holes imprinted in a PMMA film, and only those that lye inside the aligning marks were studied. AFM image holes PMMA layer (b). The residual PMMA layer inside the holes after nanoimprint was removed using oxygen plasma. The thickness of the remaining PMMA layer outside the holes is below 2 nm, as measured from the topographical AFM image (c).

Different samples were fabricated, varying the SiO_2 thickness of the substrate (from 35 nm to 1.5 µm), in order to check its influence on the chemical contrast. No difference was found during the AFM characterizations.

4.3-2. Silicon holes in a Fluorinated surface

4.3-2:a.- Fabrication

In Figure 108 the fabrication process to fabricate the second type of samples is shown. Here, **hydrophilic holes** (silicon) were opened in a highly **hydrophobic matrix** (silicon substrate treated with a fluorinated silane).

a. First of all, aluminium marks were fabricated by NIL, metallization and lift-off. A stamp was specifically fabricated, with the crosses in a well-known positions respect to the edges.

b. A 100 nm thick film of PMMA 35k was spun onto the sample and imprinted with a silicon stamp at 180 ºC and 40 bars during 2 minutes (Figure 108(b)). This stamp was also designed specifically for this application. It contains matrixes of holes with different diameter and pitch, agreed to ensure an optimal deposition of the liquid and a good separation of the droplets when doing the local dispensing (NADIS).

c. An oxygen plasma was performed to remove the residual layer, so only the PMMA pillars were left onto the surface.

d. Then, the sample was put inside a Petri capsule into a nitrogen chamber during 5 minutes at room temperature, with a drop of fluorosilanes (F_{13}-TCS), so the silanes are bounded to the silicon surface, but not where the PMMA pillars are (process described in Chapter 2).

e. The sample was finally cleaned, and the PMMA removed in acetone with ultrasound agitation for 5 minutes, leaving the holes open to the untreated silicon in a hydrophobic surface.

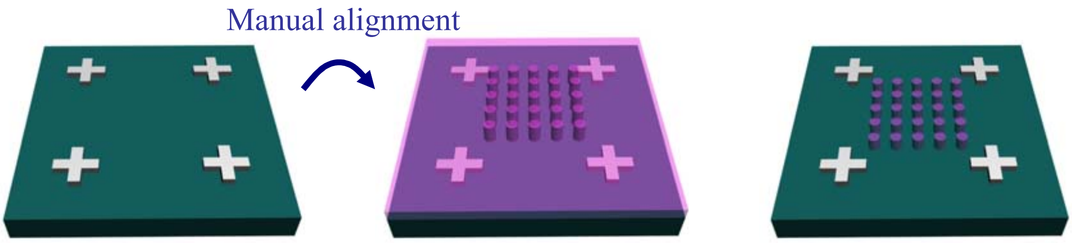

(a) Aligning Marks (b) PMMA and NIL (c) Residual layer removal

(d) Silanization (e) Mask (PMMA) stripping

Figure 108. Scheme of the fabrication process to define silicon holes open in an hydrophobic surface (fluorinated silicon) by nanoimprint lithography. NIL is performed with manual aligning, with respect to a previous design, needed to define the aluminium marks (a and b). The residual layer is removed (c) to leave only pillars covered, that act as a mask for a silanization process (d). After removing the remaining PMMA, the surface with chemical contrast is defined.

4.3-2:b.- Alignment issues

As it has already been commented during the description of the fabrication process, two complementary stamps were designed and fabricated for this application. The first one contained several micrometric crosses, devoted to define the aluminium marks in a given position respect to the edges or corners of the chip. The second stamp consisted on several matrixes of holes with different pitch and diameter, which positions were chosen so, by aligning the edges of the first substrate (with the aluminium crosses) and the edges of this second stamp, the PMMA columns would lie inside (or close to) the marks. Figure 109 shows images of the results. In (a), the area with the aligning crosses are shown, and in the dark field optical image in (b), the imprinted dots in PMMA can be seen. As expected from this manual aligning method, the accuracy is in the order of tens of microns, which is good enough for the final goal of these samples

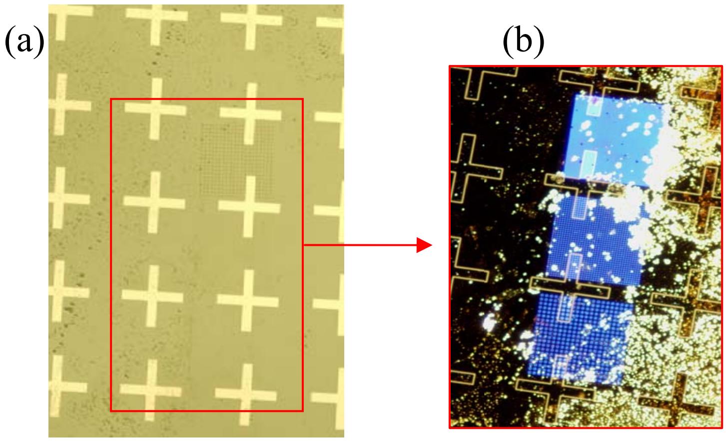

Figure 109. Optical images of pillar arrays with different diameters and pitch, fabricated inside a matrix of aluminium marks (a), by manual alignment. In the dark field image (b), the position of the dots with respect to the marks can be seen.

. Another example to prove the reliability of the manual alignment method is shown in Figure 110. This corresponds to a SEM image of another pattern fabricated following the same procedure, where an aligning accuracy ≈ 20 µm was achieved for areas of 100 x 100 µm^2.

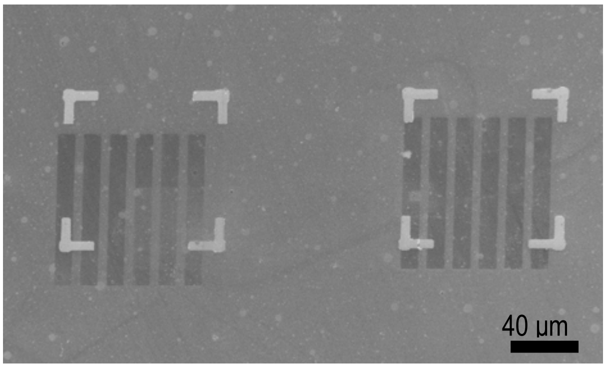

Figure 110. SEM images of silanized lines onto a silicon surface, fabricated by two NIL steps with manual alignment.

4.3-2:c.- Results

Figure 111 shows contact mode AFM images of some of the patterned areas: a matrix of dots, 2 µm pitch in Figure 111 (a), 5 µm pitch in (b), and 10 µm pitch in (c). The images in the top row are topographical images of the sample, and those in the bottom row, the corresponding friction mode maps. The depth of the holes was below 3nm. The chemical contrast between the fluorinated and non-fluorinated surfaces is evidenced from the friction images, revealing a clear difference in the nature of the surface inside and outside the holes.

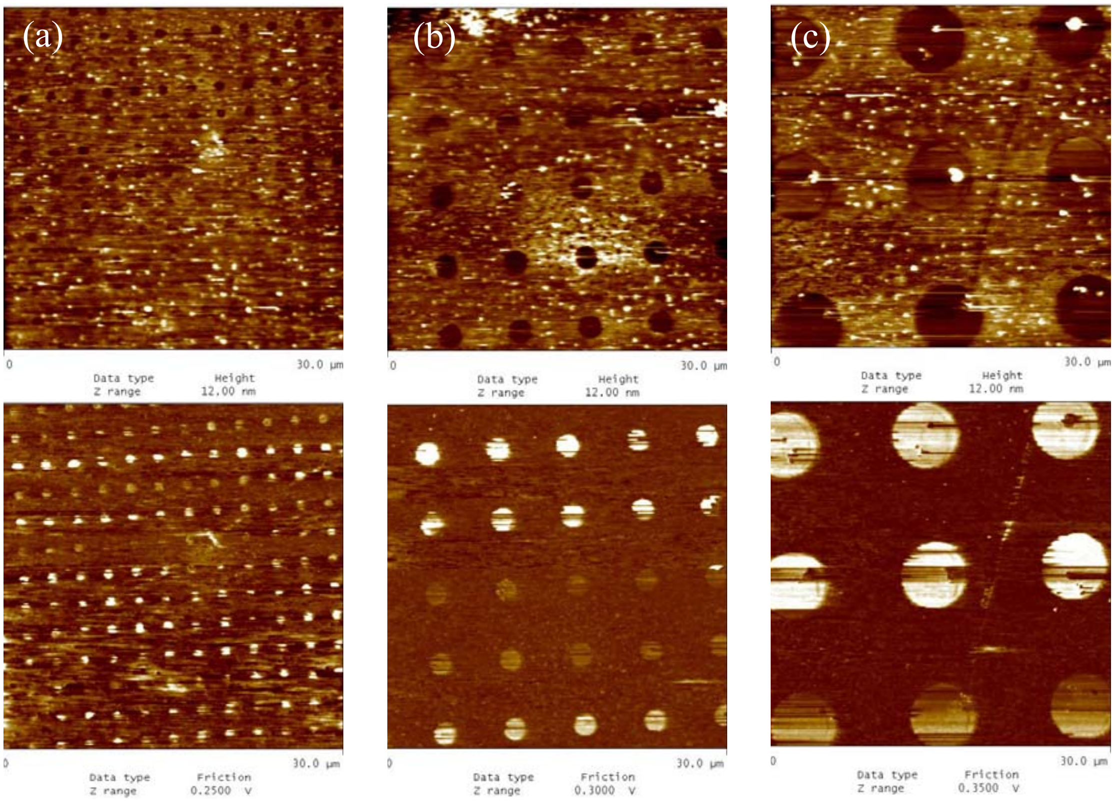

Figure 111. Contact mode AFM images (topography in the left and friction in the right) showing three matrixes of chemically patterned arrays of hydrophilic dots on a hydrophobic matrix, with different diameters and pitch (2 µm pitch in (a), 5 µm in (b) and 10 µm in (c)).

Also in this type of samples, the topographical contrast can be neglected, compared to the chemical one.

4.3-3. Future: NADIS deposition

The goal of these samples with surfaces having local chemical contrast is to enhance the resolution that can be achieved by local deposition of liquid (NADIS). This tool consists on an AFM, properly modified to deposit liquid droplets: the tip is hollow, and has an aperture in the apex, and the cantilever is hollow as well. The cantilever is connected to a deposit, for liquid supplier [8].

The samples fabricated during this work would allow in future works to study the effect of the chemical/topographical contrast on the dimensions of the droplets deposited by NADIS for different liquids, as it is depicted in Figure 112.

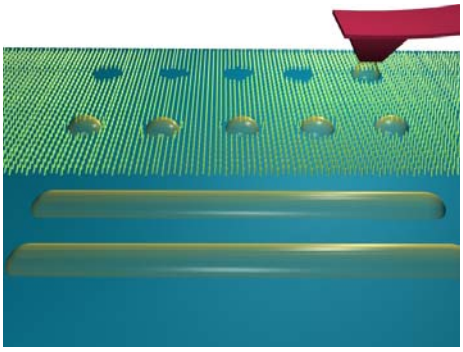

Figure 112. Scheme of the deposition of liquid onto the fabricated surfaces with chemical contrast with the NADIS tool. The diameter of the holes would determine the diameter of the drops.

The results of NADIS deposition in the structures is still under study, and leave a research deal open, for future works.

4.4.- REFERENCES

[1] A. M. Haghiri-Gosnet, T.A., R. Soulimane, M. Koubaa, J. P. Renard,,
Spintronics: perspectives for the half-metallic oxides.
physica status solidi (a), 2004. **201**(7): p. 1392-1397.

[2] Wu, Y., Matsushita, Y. and Suzuki, Y.,
Nanoscale magnetic-domain structure in colossal magnetoresistance islands.
Physical Review B, 2001. **64**(22): p. 220404.

[3] Fernandez-Cuesta, I., Zabaleta, J., Borrisé, X., Puig, T., Mestres, N., et al.
Fabrication of ordered lattices of nanopillars of magnetic perovskite. in *International Conference on NanoImprint and NanoPrint Technology (NNT)*. 2007. Paris (France): Poster.

[4] Hoff, J.D., Cheng, L.-J., Meyhofer, E., Guo, L.J. and Hunt, A.J.,
Nanoscale Protein Patterning by Imprint Lithography.
Nano Letters, 2004. **4**(5): p. 853-857.

[5] Falconnet, D., Pasqui, D., Park, S., Eckert, R., Schift, H., et al.,
A Novel Approach to Produce Protein Nanopatterns by Combining Nanoimprint Lithography and Molecular Self-Assembly.
Nano Letters, 2004. **4**(10): p. 1909-1914.

[6] Park, S., Saxer, S., Padeste, C., Solak, H.H., Gobrecht, J., and Schift, H.,
Chemical patterning of sub-50-nm half pitches via nanoimprint lithography.
Microelectronic Engineering, 2005. **78**: p. 682-688

[7] Merino, S., Retolaza, A., Trabadelo, V., Cruz, A., Heredia, P., et al.
Protein patterning on the micro and nanoscale by thermal nanoimprint lithography on a new functionalized copolymer. in *International Conference on Micro- and Nano-Engineering (MNE)*. 2008. Athens (Greece): Poster.

[8] Meister, A., Jeney, S., Liley, M., Akiyama, T., Staufer, U., et al.,
Nanoscale dispensing of liquids through cantilevered probes.
Microelectronic Engineering, 2003. **67-68**: p. 644-650.

Section 2

Plasmon confinement in V-grooves fabricated by NIL

"Metals are not just shinny to visible light…they have fascinating new properties, arising from the combined motion of their surface electrons and the electric field of the light."

E. Moreno

Universidad de Zaragoza, 2008

The backbone of the world's communication system is a network of optical fibres that carry information in the form of light pulses. Large volumes of data can be transmitted very efficiently down these fibres but bottlenecks in the system occur when the light pulses are converted into electrical signals at various "junction boxes" that ensure information reaches its correct destination. The telecommunications industry, among others, is therefore extremely interested in microphotonic circuits that can manipulate light pulses directly and therefore increase data rates.

Plasmon confinement and propagation is sub-λ structures

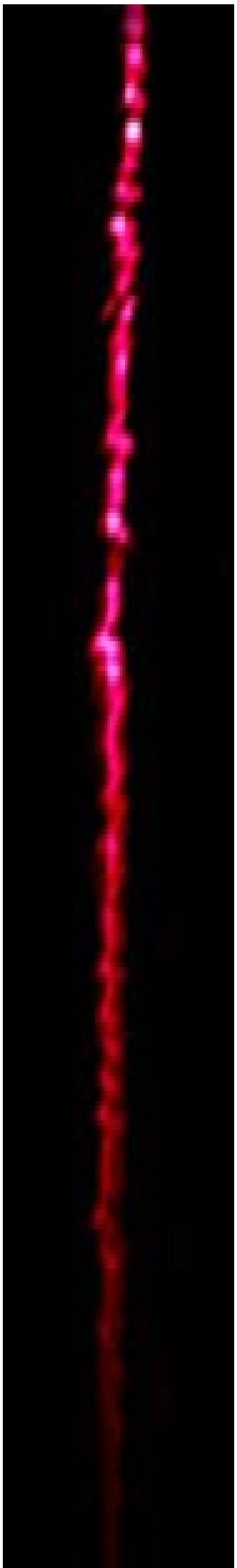

Metals, apart from being reflective for visible light, have an optical characteristic that is not so well known: at certain conditions, light can travel bounded to metal surfaces without moving away from them. This is a very particular property, as light usually travels along the three dimensions of the space and it is very difficult to confine. Actually, these waves bounded to a surface are more complex than free light, as not only electromagnetic fields are involved, but also electron oscillations on the metal surface. These waves are the so-called surface plasmons or surface plasmon-polaritons.

One of the most interesting properties of surface-plasmons is that they can be coupled and confined into channels, so light can be squeezed and propagate in structures with sub-λ lateral dimensions.

In this section, the basic notions needed to understand the optical properties of metals, and hence, plasmons, surface plasmons and confined modes will be first detailed, in Chapter 5. Then, the design and process flow to fabricate integrated devices based on gold V-grooves by means of NIL will be explained in Chapter 6. The corresponding optical characterization, both in the near and far fields will be reported in Chapter 7, to probe light confinement and propagation into the imprinted V-grooves. Finally, the results obtained when filling the V-grooves with fluorescent beads will be also detailed in this chapter.

This part of the work was done in close collaboration with DTU·Nanotech, during a stay of four months long. Other laboratories with large expertise in the plasmonics and photonics fields were also involved in the optical characterization of the samples.

The image in the right corresponds to a near optical field image (SNOM), obtained by launching light (λ_0 = 1500 nm) into one of the imprinted V-groove based plasmonic devices.

Index of Section 2:

Plasmon confinement in V-grooves fabricated by NIL

Chapter 5

Plasmons, Surface Plasmon-Polaritons and Channel Plasmon-Polaritons

In this chapter, after presenting a general introduction to plasmons, surface plasmons-polaritons and channel plasmon-polaritons, the parameters that describe the propagation of these quasi-particles on different surfaces and geometries will be explained, and, more precisely, those concerned to confinement and propagation in V-grooves will be detailed.

5.1.- PLASMONS. DRUDE'S MODEL.

In physics, a **plasmon** is the quasi-particle resulting from the quantization of the oscillations of plasma. In this work, we will use this term referred to the oscillations of the plasma formed by the electrons in the conductive band of a metal.

Plasmons are explained in the classical picture using the **Drude's model**: the metal is treated as a three dimensional crystal of positively charged ions, and a delocalized electron gas is moving in the periodic potential of this ion grid.

The optical properties of metals are complex, as the electron motion (and hence, the optical constants) depends on the frequency of the applied field. In Drude's model the relative permittivity is given by (13),

$$\varepsilon_m(\omega) = 1 - \frac{\omega_p^2}{\omega^2 - i\Gamma\omega} \qquad (13)$$

where ω_p is the *plasma frequency*[*] of the electrons in the given metal (frequency at which the charge density oscillates if the electrons are slightly displaced with respect to the ions as the Coulomb force pulls back as a restoring force) and Γ is the *scattering rate* or *frequency of collision*[†], used to account for dissipation through scattering of the electron motion [1].

For the most commonly studied metals (gold and silver) these constants have the following values:

Gold	**Silver**
$\omega_p = 9.056$ eV/ħ	$\omega_p = 7.9$ eV/ ħ
$\Gamma = 0.027$ eV/ ħ	$\Gamma = 0.06$ eV/ ħ

The dielectric constant (13) can be split in real (15) and imaginary (16) parts:

$$\varepsilon_m(\omega) = \varepsilon' + i\varepsilon'' \quad (14) \longrightarrow \quad \varepsilon'(\omega) = 1 - \frac{\omega_p^2}{\omega^2 + \Gamma^2} \quad (15) \qquad \varepsilon''(\omega) = \frac{\omega_p^2\Gamma}{\omega^3 + \Gamma^2\omega} \quad (16)$$

The real part (ε') is negative, and the imaginary part (ε") is small and positive, accounting for absorption and scattering losses in the metal. Figure 113 shows the representation of the real (a) and the imaginary (b) parts of the dielectric constant for gold and silver in the ultraviolet-infrared range.

---

[*] Plasma Frequency: $\omega_p{}^2 = n_e e^2 / m\varepsilon_0$, where n_e is the density of electrons, e is the electron charge, m the electron mass and ε_0 the dielectric constant of vacuum.

[†] Frequency of collision: $\Gamma = (2\pi c\tau)^{-1}$, where c is the velocity of light, and the electron lifetime.

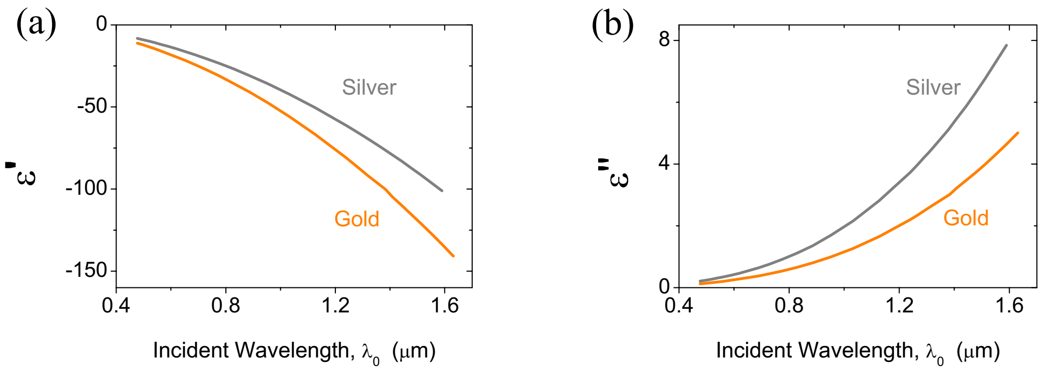

Figure 113. Real (a) and imaginary (b) parts of the dielectric constants of gold (—) and silver (—), as a function of the wavelength λ_0.

Plasmons play a large role in the optical properties of metals. For light of frequency below the plasma frequency the electrons precisely follow the incident field and the dielectric constant is negative. Thus, the wave is reflected with a 180º phase shift. Light of frequency above the plasma frequency is transmitted because the electrons cannot respond fast enough to screen it. In most of the metals the plasma frequency lies in the ultraviolet part of the spectrum, so, for visible wavelengths they behave as mirrors. Some metals, such as copper and gold, have electronic interband transitions in the visible range, whereby specific light energies are absorbed, yielding to their distinct colours. In semiconductors, the valence electron plasma frequency is usually in the deep ultraviolet, so that is why they are reflective too.

5.2.- SURFACE PLASMONS

5.2-1. Introduction to SPPs

A **surface plasmon** is an evanescent wave resulting from the quantization of the oscillation of the electrons in the conduction band on a metal surface, excited by an external force. The term surface plasmon-polariton (SPP) is used to describe **optically induced oscillations** [2]. SPPs are bounded to and propagate along a dielectric/metal interface (i.e., they occur at the interface of a vacuum or material with a positive dielectric constant with that of a negative dielectric constant, usually a metal). The SPPs field components decay exponentially into both neighbouring media, as it is shown in the scheme of Figure 114 [3].

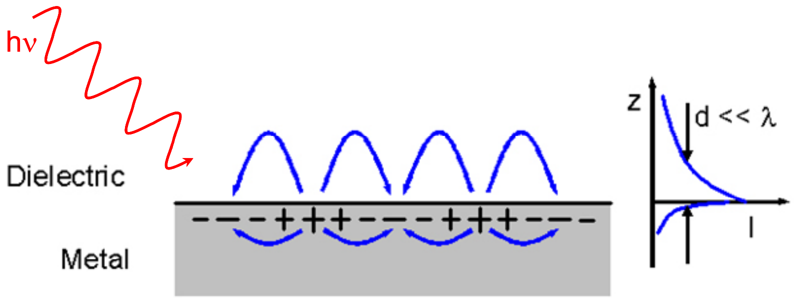

Figure 114. Scheme of surface plasmon-polaritons. The incident (optical) field induces an oscillation in the charge density on the metal surface, resulting in an evanescent wave, called surface plasmon-polariton. These waves have the amplitude of the field components exponentially decaying into both medias.

The topic of surface plasmon–polaritons has a history going back more than fifty years [4], albeit at the beginning they were considered as a drawback for the use of metals as optical components, because the energy was "lost" via SPPs excitation. Recently, they have retrieved the interest. One of the main reasons is that there are now a variety of routine nanoscale fabrication technologies that allow suitable sized structures to be made and explored as a way of harnessing SPPs. Surface plasmon–polaritons are being developed for their use in bio-molecule sensors [5], they can help us to characterize the optical properties of complex structures such as liquid crystals [6], and they are seen as a promising route in the development of subwavelength optics [7].

5.2-2. Propagation of SPPs. General parameters.

The parameters that describe a surface-plasmon-polariton can be deduced from the **dispersion relationship** between the frequency and the in-plane wavevector. This dispersion relation can be found by looking for surface mode solutions of Maxwell's equations under appropriate boundary conditions. The details of the calculation can be found in [8] and the obtained expression is given by (17). Here, the dielectric constant of the metal, ε_m, is complex, and given by Drude's model as described above, and ε_d is the dielectric constant of the dielectric media.

$$k_{SPP} = \frac{\omega}{c}\sqrt{\frac{\varepsilon_d \varepsilon_m}{\varepsilon_d + \varepsilon_m}} \qquad (17)$$

From this expression, the physical parameters necessary to understand and study SPPs propagation can be calculated for a given λ_0. Three of these are schematized in Figure 115: **wavelength** of the oscillation (λ_{SPP}), **penetration depth** into the **dielectric** (δ_d) and into the **metal** (δ_m). A fourth parameter that is also important is the **propagation length** (δ_{SPP}). Next, their analytic expressions will be presented and the properties deduced from them commented.

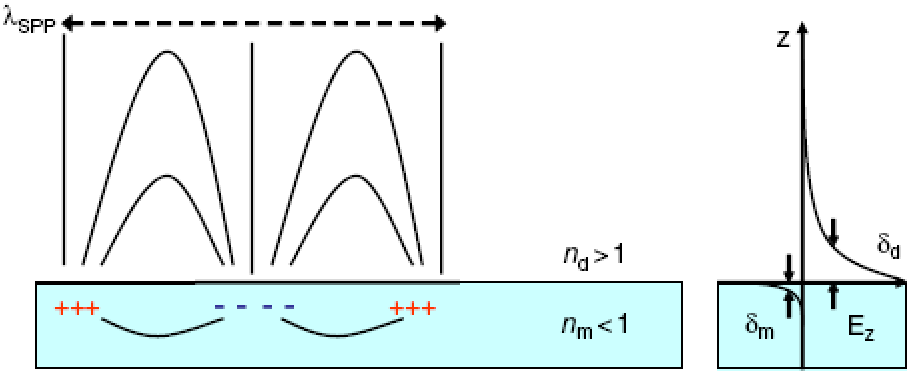

Figure 115. Scheme of some general parameters that describe a SPPs: wavelength (λ_{SPP}), penetration depth into the dielectric (δ_d), penetration depth into the metal (δ_m).[3].

One of the consequences arising from the hybrid nature of SPPs (photon/electron coupling) is that the **wavelength** of the resulting oscillation (**λ_{SPP}**) is shorter than that of the incident electromagnetic field (λ_0). It depends on the properties of the interface, i.e. on the dielectric constants of the two medias (18), accounting for how fast electrons move.

$$\lambda_{SPP} = \lambda_0\sqrt{\frac{\varepsilon_d + \varepsilon'_m}{\varepsilon_d \varepsilon'_m}} \qquad (18)$$

Figure 116 (a) shows the variation of the normalized surface plasmon-polariton wavelength (λ_{SPP} relative to free space wavelength, λ_0) for the UV-IR range for gold and silver abut vacuum (i.e. fix ε_d, varying ε_m). The line corresponding to the free space wavelength has been also plotted. The most important point is that λ_{SPP} is similar to but always less than λ_0. When the overlying dielectric is not air but some other medium, then the SPP wavelength is reduced in proportion to the refractive index. Figure 116 (b) shows the normalized wavelength for SPPs propagating in gold abut two different dielectrics: air, $\varepsilon_d = 1$, and a dielectric media with $\varepsilon_d = 2.2$. The election of this value is not arbitrary, and corresponds to a material (made by a combination of latex and air) that was used and studied during the development of this work, that will be described in Chapter 7.

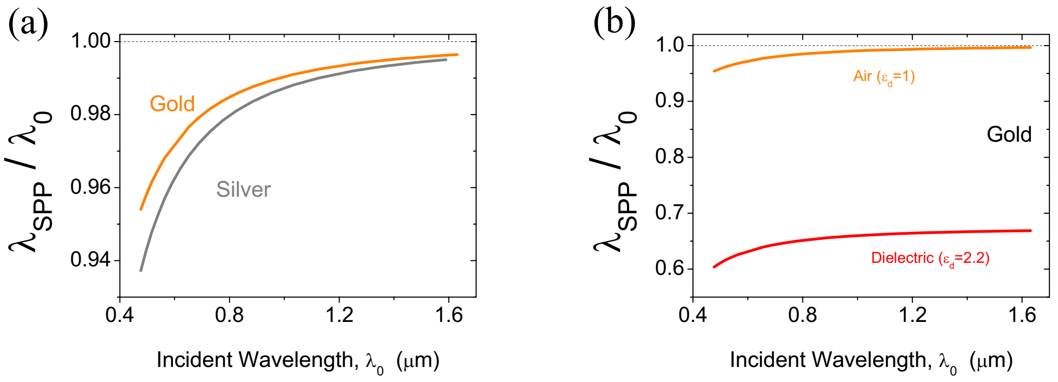

Figure 116. Normalized wavelength of the surface plasmon polaritons, λ_{SPP}, as a function of the incident wavelength λ_0. In (a), a gold/air interface (—) and a silver/air interface (—) are compared to the free space propagation (—). In (b), the effect of increasing the dielectric constant of the media abut a gold surface (—) is shown.

As it has been mentioned above, SPPs arise from the combined motion of electrons and the optical field in the dielectric. An evanescent wave results from this interaction, having the amplitude of the fields decaying exponentially (19) with the distance to the excitation point in the horizontal plane.

$$I = I_0 e^{(-x/\delta_{SPP})} \tag{19}$$

Thus, a very important parameter to describe SPPs is the **propagation length** (**δ_{SPP}**), that also depends on ε_d and ε_m. The propagation length is defined as the distance that the SPP propagates before loosing 1/e of its energy, and is given by (20) [3]. The imaginary part of ε_m appears in the denominator, indicating that the attenuation comes from dissipation of energy by the electron gas of the metal.

$$\delta_{SPP} = \lambda_0 \frac{(\varepsilon'_m)^2}{2\pi\varepsilon''_m} \left(\frac{\varepsilon'_m + \varepsilon_d}{\varepsilon'_m \varepsilon_d} \right)^{3/2} \tag{20}$$

Figure 117 (a) shows the dependence of the propagation length on the incident wavelength for gold and silver/air interfaces. As could be deduced from the higher values of ε” (higher Γ) in silver, the propagation length for a given λ_0 is shorter than that in a gold surface. When the air at the gold interface is substituted for a material with a higher dielectric constant, the propagation length is significantly reduced, as it is shown in Figure 117 (b), again for a dielectric constant $\varepsilon_d = 2.2$.

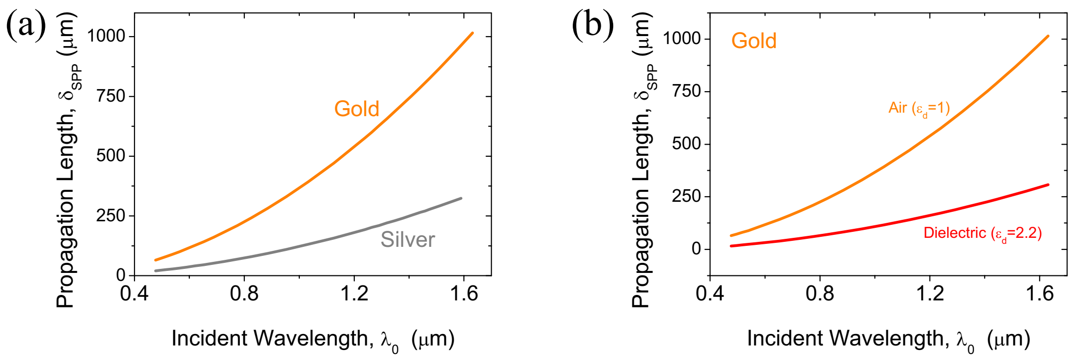

Figure 117. Propagation length of the surface plasmon polaritons, δ_{SPP}, as a function of the incident wavelength λ_0. In (a), a gold/air interface (—) and a silver/air interface (—) are compared. In (b), the effect of increasing the dielectric constant of the media abut a gold surface is shown for a material with a dielectric constant of 2.2 (—).

Another two important parameters that characterize SPPs bound to a metal/dielectric interface is the **penetration depth** of the fields into both medias, that are given by (21) and (22) for the dielectric (**δ_d**) and the metal (**δ_m**) respectively. Their dependence on λ_0 is plotted in Figure 118.

$$\delta_d = \frac{\lambda_0}{2\pi}\left|\frac{\varepsilon'_m + \varepsilon_d}{\varepsilon_d^{\,2}}\right|^{1/2} \qquad (21) \qquad\qquad \delta_m = \frac{\lambda_0}{2\pi}\left|\frac{\varepsilon'_m + \varepsilon_d}{\varepsilon'^{\,2}_m}\right|^{1/2} \qquad (22)$$

The **penetration depth into the dielectric** increases with the wavelength (becomes more similar to free light), as can be seen in Figure 118(a), and, consequently, the SPP is less confined to the surface. This parameter is important, as it gives us a measure of the length scale over which the SPP is sensitive to the presence of changes in the refractive index at the interface, which is important for the use of SPP-based *(bio)sensors*. Although the sensitivity of the SPPs to changes in the dielectric medium falls off exponentially, the distance over which the fall off takes place is large on a molecular scale. δ_d in air for gold and silver abut air are very similar, and is reduced when the dielectric constant of the cladding is increased (the confinement to the surface increases in this case).

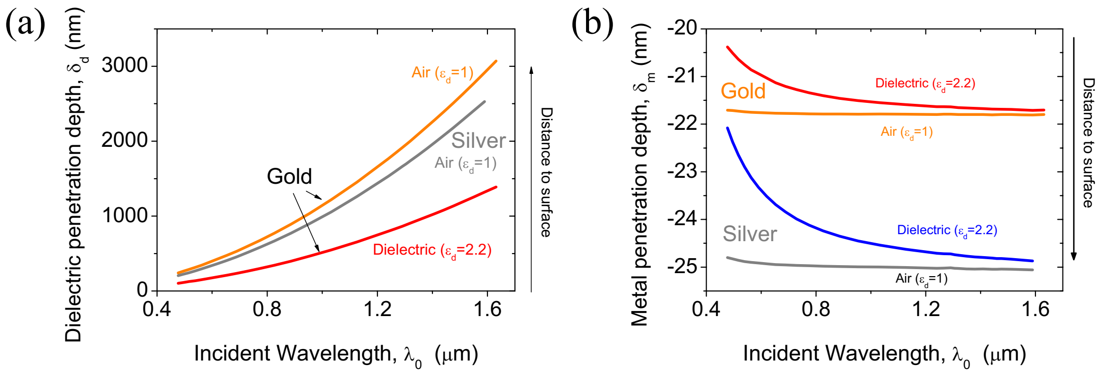

Figure 118. Penetration depths of the surface plasmon polaritons into the dielectric media, δ_d (a) and into the metal, δ_m (b). Various different interfaces have been considered: gold/air (—), silver/air (—), gold/ ε_d=2.2 (—) and silver/ε_d=2.2 (—).

On the other hand, the **penetration depth of the field into the metal** is in the range of few tens of nm (20-30 nm, depending on the metal), and almost independent on λ_0. When the dielectric constant, ε_d, is increased (Figure 118(b), red and blue lines), the SPP is more confined into the metal for high frequencies (electrons do not respond fast enough to screen the electric field), but it reaches the same constant value for low frequencies. For metals with high conductivity, the attenuation coefficient is large, meaning that the field penetrates only a short distance. This distance is called the *skin depth* (d_m) (23), and the values for gold and silver are 21.8 nm and 25 nm respectively.

$$d_m = \frac{\lambda_p}{2\pi} \left\{ \begin{array}{l} \text{Gold: 21.8 nm} \\ \text{Silver: 25 nm} \end{array} \right. \qquad (23)$$

5.3.- CHANNEL PLASMON POLARITONS

Channel plasmon-polaritons (CPPs) [9] are SPPs that are bounded to a micro/nano structure.

For two close metal surfaces, the SPPs associated to each one can become coupled. When the surfaces are close enough together the fields associated with the SPPs overlap and interact: *a coupled mode is produced.*

The dispersion relation for metal channels with an arbitrary shape (not necessarily straight) was analytically calculated and numerically solved by Novikov et al. [9]. The description of these coupled waves is not trivial and becomes very arduous thorough the analytical expressions, that are very complex and require advanced calculation methods to be solved and/or plotted.

The **effective-index method** (EIM) [10, 11] is a simulation method that allows quantitative and qualitative analysis of CPPs channelling, propagation and field distribution in different types of structures in a more visual way. The EIM has been extensively used to simulate and to analyze numerically the light propagation in a large variety of structures [12, 13]. This method converts the original three-dimension channel waveguide into effective two-dimension planar waveguides. Each part of the effective waveguide is described with an effective refraction index, numerically calculated by the software as a function of the number of layers, their thickness and dielectric constant.

5.3-1. Slits

Figure 119, reproduced from [14], shows the effective index (N_{eff}) for a CPP guided in-between the air gap between two metal surfaces, as a function of their separation, w. For sufficiently close surfaces, N_{eff} significantly increases, meaning a higher confinement of the light in the channel. Meanwhile, the propagation length decreases as a consequence of the confinement.

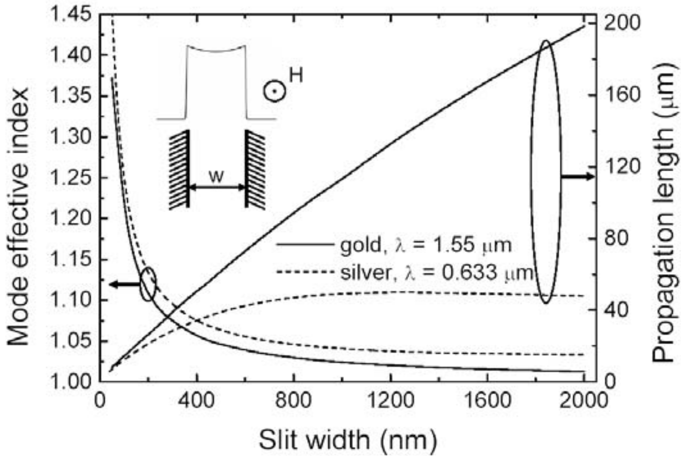

Figure 119. SPP coupled mode effective index and its propagation length as a function of slit width, w, for gold (at the light wavelength λ_0= 1.55 μm) and silver (λ_0= 0.633 μm). The inset shows the slit configuration and coupled SPP magnetic field orientation along with the example of the field distribution across a 1 μm-wide gold slit (λ_0= 1.55 μm). [14]

5.3-2. V-grooves: confinement and propagation

5.3-2:a.- Description

The devices developed and studied in the experimental work of this thesis were **V-groove based plasmon waveguides**. The geometry of these structures is shown in the schemes of Figure 120(a) and (b), in 2 and 3 dimensions. The most representative geometrical parameters are marked: width (w), depth (d), apex angle (θ) and length (L).

For the study of CPPs bounded to a V-shaped channel the idea for the EIM calculations is the same as before: one should analyze the SPP guiding in the air gap between two metal surfaces, but being the gap width variable with the depth.

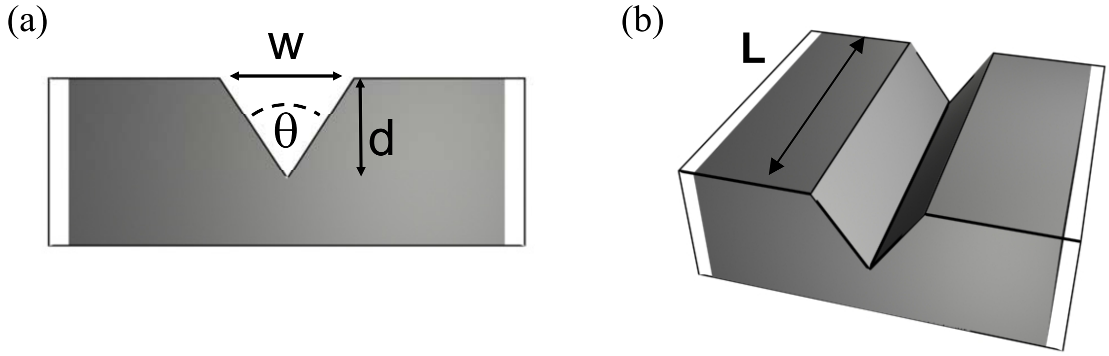

Figure 120. Profile of the V-grooves in 2D (a) and 3D (b). The geometrical parameters have been marked: groove width (w), depth (d), apex angle (θ) and length (L).

Figure 121 shows N_{eff} and the propagation length as a function of the groove depth for two different apex angles (16º and 25º) as reported by Bozhevolnyi et al. in [14]. The effective index experienced by the CPP decreases with increasing the distance from the tip of the groove (i.e., with increasing gap width), which results in a waveguiding structure.

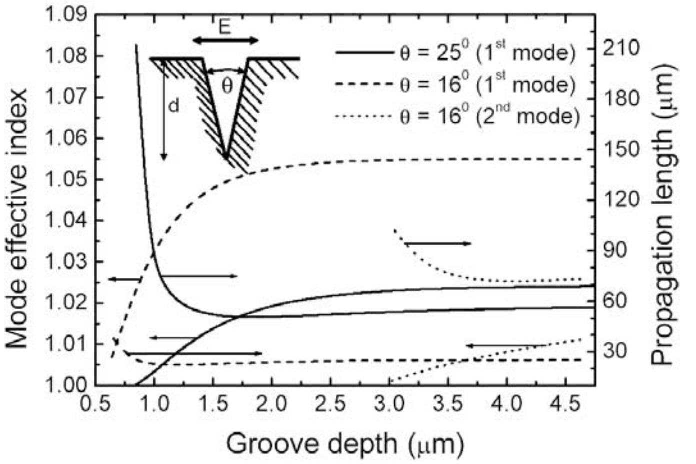

Figure 121. The effective indexes of CPP modes and their propagation lengths as a function of groove depth d for different groove angles θ .The inset shows the groove configuration and dominant orientation of CPP electric field [14, 15].

5.3-2:b.- Modes

The dispersion relation for CPPs from where the expressions for the electric and magnetic fields (E and H) inside the grooves can be obtained has an infinite number of branches. This means that there are several modes that may be sustained for a certain groove (not necessarily with straight sidewalls, as reported by Novikov et al. [9]). Figure 122 shows the electric field distribution inside a Gaussian-shaped channel[‡], excited at different λ_0.

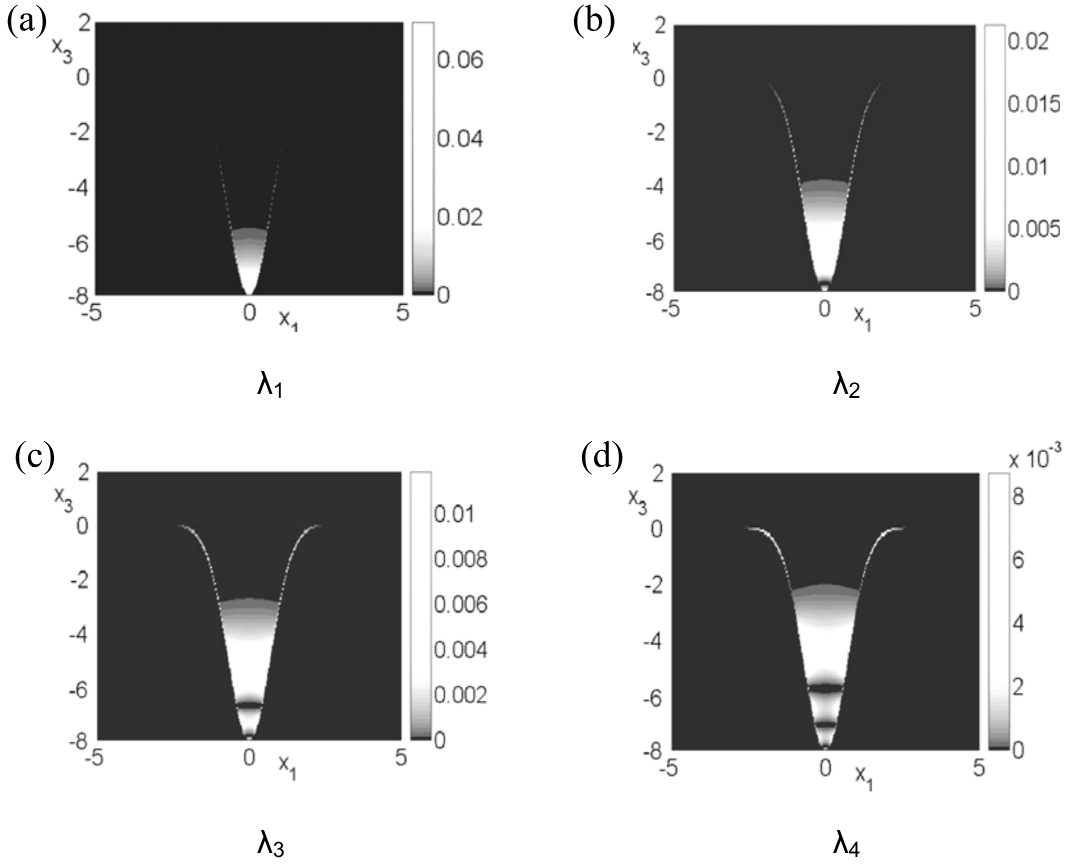

λ_1 λ_2

λ_3 λ_4

Figure 122. Plot of the squared modulus of the second component of the electric field in a channel defined by a Gaussian profile, for different excitation wavelengths, where $\lambda_1 < \lambda_2 < \lambda_3 < \lambda_4$. [9]

5.3-2:c.- Experimental variables

The characteristics and properties of CPPs confinement and propagation depend mainly on three issues: incident wavelength (λ_0), geometrical parameters (w, d, θ), and interface properties (metal and dielectric materials forming the interface).

As it has already been shown, the EIM is a powerful method to study the characteristics accounting for confinement and propagation of CPPs in V-grooves. Further, relevant results found in the literature related to these experimental variables will be described, that will be interesting and useful for the experimental results obtained during this thesis.

Incident wavelength

The modal shape of CPPs in gold V-grooves with a fix geometry (600 nm wide, 1.2 μm deep, 25º of apex angle) was modelled by Moreno et al. and reported in [16] for different λ_0. Figure 123 (a), (b) and

---

[‡] Gaussian-shaped channel: $y(x) = -Ae^{-x^2/R^2}$

(c) show the averaged electric field distribution of the fundamental mode excited at three different wavelengths: 0.6 μm, 1 μm and 1.4 μm respectively. As λ_0 increases, the field is pushed out of the groove and, after a certain threshold value, it can no longer be confined by the structure and is radiated out in the form of a SPP along the horizontal metal surface. It is important to realize that, before being squeezed out of the groove as SPPs, modes propagating in the wedges (wedge plasmon polaritons, WPP [17]) are excited.

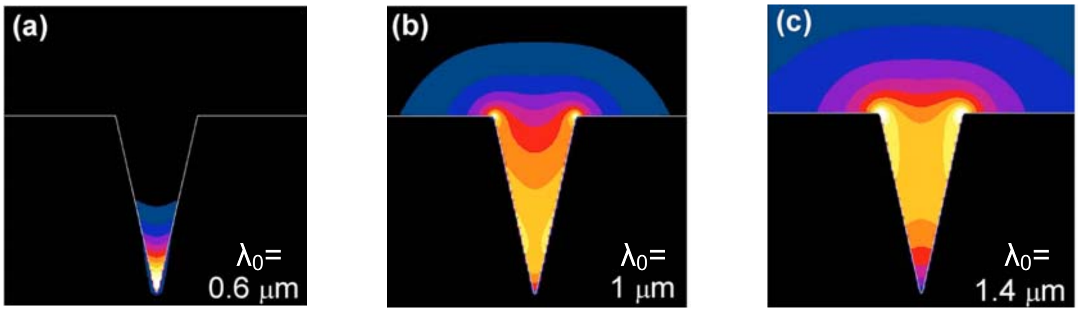

Figure 123. Modal shape (time averaged electric field) of the CPP fundamental mode for increasing wavelength λ_0. (a) λ_0=0.6 μm, (b) λ_0=1 μm, (c) λ_0=1.4 μm (close to cutoff). The colours represent the intensity of the fields: from yellow (maximum) to dark blue (minimum). [16]

Figure 124 (a) shows the propagation length of different plasmon-polariton modes as a function of λ_0. Non-coupled (*surface*) modes (SPPs) propagate longer distances than coupled ones (WPPs and SPPs). WPPs (Figure 124 (b)) are less confined than CPPs (Figure 124 (c)), thus, having a larger typicall propagation length.

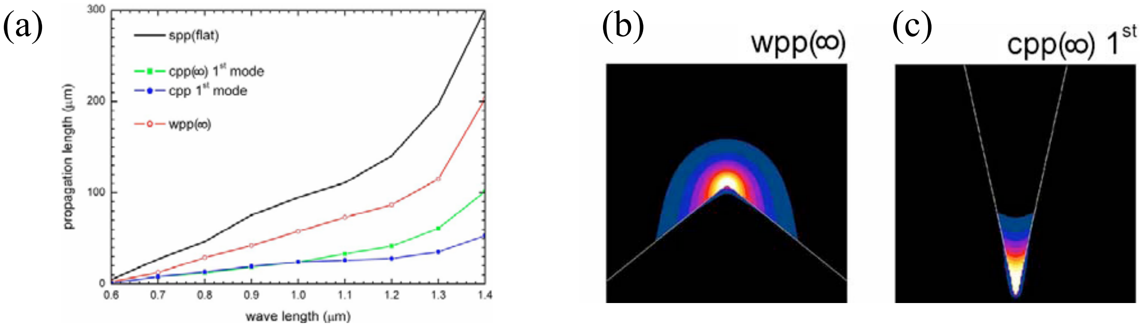

Figure 124. (a) Propagation length versus wavelength for various modes. SPP mode on a flat surface (—); CPP fundamental mode for a groove of height 1.172 μm (—); CPP(∞) fundamental mode for an infinitely deep groove (—); WPP(∞) mode for an infinitely deep wedge (—). (b) and (c), time averaged electric field of a WPP in a wedge, and for the fundamental mode on an infinitely deep V-groove respectively. The colours represent the intensity of the fields: from yellow (maximum) to dark blue (minimum). [16]

From the point of view of design and fabrication of devices, it has to be kept in mind that CPPs excited at visible wavelengths will be more sensitive to the characteristics of the groove tip (roundness, defects) than those excited at larger wavelengths (IR), that travel at higher distance from the bottom.

Geometrical parameters

The size-dependent parameters (w, d, θ) have to be carefully studied, as their right combination for a given range of λ_0 will determine whether the structure support CPPs or not. Also, the structural parameters can be changed and optimized with the fabrication process in order to find a trade-off between confinement and sufficiently low propagation losses. Even more, multimode waveguiding can be efficiently avoided.

Apex angle, θ.

The effective index experienced by the plasmons in the groove decreases with increasing distance from the bottom of the groove. The light experiences successive reflections, what leads to the confinement and propagation phenomena. If the groove angle θ is too small, then the change in N_{eff} is not high enough, and the CPPs won't be reflected back and no propagation will take place. This **lower critical angle**, θ_{c2}**,** is given by (24):

$$\theta_{c2} = -\frac{2\varepsilon_d}{\varepsilon'_m} \tag{24}$$

This critical angle strongly depends on the materials forming the interface: it is proportional to the dielectric constant of the cladding, ε_d, and increases when decreasing the real part of ε_m. This means that it also depends on the incident wavelength, as it is plotted in Figure 125 for three combinations (silver/air, gold/air and gold/dielectric with ε_d=2.2).

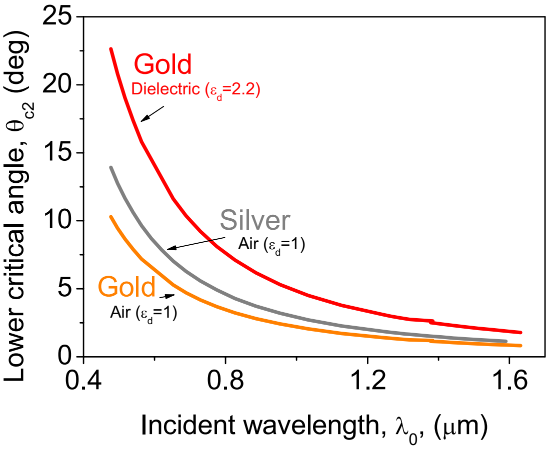

Figure 125. Lower critical angle as a function of the incident wavelength, , for V-grooves made in different interfaces: gold/air (—), gold/ε_d=2.2 (—) and silver/air (—).

There is also an **upper critical groove angle**, θ_{c1}, above which the confinement is not possible. The values of this upper critical angle are significantly different for the different CPP modes: θ_{c1} decreases with increasing the order. This means that the number of higher modes increases with decreasing θ. At the upper critical groove angle, the wave number of the respective CPP mode becomes equal to the wave number of surface plasmons on the sides of the groove. Therefore, if $\theta > \theta_{c1}$, the respective CPP mode leaks into surface plasmons on the side of the groove, and thus it stops being a structural eigenmode.

No analytical equation for the upper critical angle has been obtained so far. This cut-off angle can be visualized also in a simple model: if the sides of the grooves are far enough, the plasmons bounded to each side will not interact or couple. Thus, the angle is expected to depend on the penetration depth in the dielectric (i.e., on the incident wavelength and properties of the metal/dielectric interface).

The apex angle also affects the confinement of the mode in the groove, and, in consequence, to the corresponding propagation length. Figure 126 shows the effective index and propagation lengths for grooves with three different angles: 30º, 25º and 16º. It is seen that the CPP effective index increases while the propagation length decreases with the decrease of the groove angle. This is due to the better mode confinement (note that the index N_{eff} determines the confinement because the penetration depth, d_{pen}, in air is given by (25).

$$d_{pen} = \frac{\lambda}{2\pi}(N_{eff}^2 - 1)^{-0.5} \tag{25}$$

Therefore, a larger N_{eff} corresponds to a smaller penetration and a better field confinement in depth. In this respect, CPP guiding is better for narrower grooves, but it is achieved at the expense of larger damping (shorter propagation length).

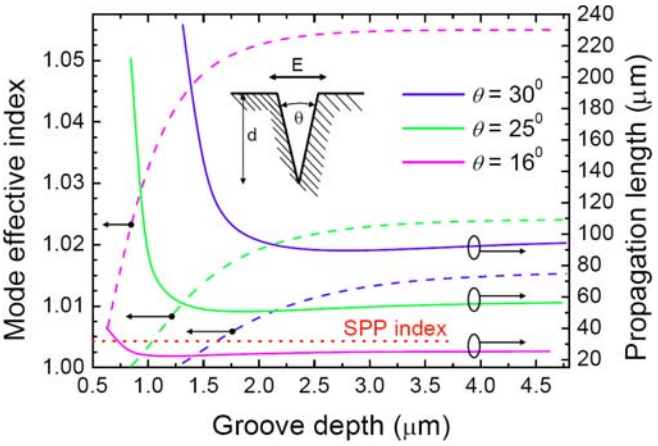

Figure 126. Effective indexes of fundamental CPP modes at λ_0=1.55 μm and their propagation lengths as a function of the groove depth, d, for different groove angles, θ. The insert shows the groove configuration and dominant orientation of the CPP electric field. The plane SPP effective index is also indicated. [10]

Groove depth, d.

The conditions for the existence of CPPs related to the depth of the groove, d, are less strict than those for θ. There is only one restriction concerning the minimum value so the groove can hold at least the fundamental mode. For this is, d has to be comparable to the penetration depth of the fundamental mode. Even further, the optimal configuration is when both values are in a similar range, as that avoids higher order modes, which may result in additional losses.

As it has already been mentioned above, several modes can be supported by infinitely deep grooves. Multi-mode guiding constitutes an impediment for the performance of effective plasmonic waveguides, as the propagation losses increase, the modes may interact one with the others, and for practical applications (such as information guiding) this becomes a handicap.

As it has been shown in the literature, single-mode waveguiding can be performed by choosing the right depth for the V-grooves [18].

An infinitely deep groove can support several CPP modes.

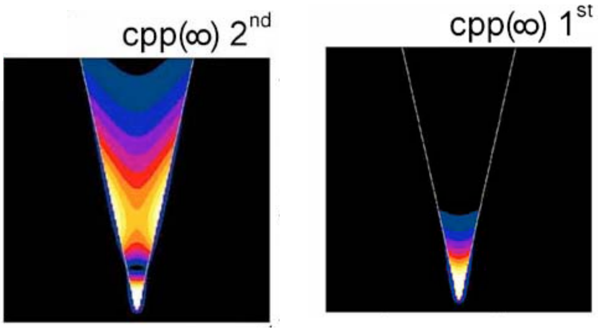

Figure 127. Time averaged electric field distribution for an infinitely deep groove for the fundamental mode (left) and 2nd mode (right). The colours represent the intensity of the fields: from yellow (maximum) to dark blue (minimum). [16]

Groove width, w.

For obvious reasons, for a given angle and depth, the width of the grove is fixed. Narrower grooves (smaller cross-section) are better for the confinement of the modes, as the lateral confinement just depends on the width of the air gap where the CPP is propagating. As always, at the expense of larger damping.

Interface properties

Very recently, Vernon et al. [19] have used numerical simulations to determine the impact of filling the V-grooves with a dielectric material different from air ($\varepsilon_d>1$).

The effect of increasing ε_d inside the groove results in a higher confinement of the CPP modes to the V-groove, with all the consequences mentioned before. This effect is illustrated in Figure 128, where the amplitude of the electric field (a) and the localization region (b) are plotted for various ε_d and apex angles.

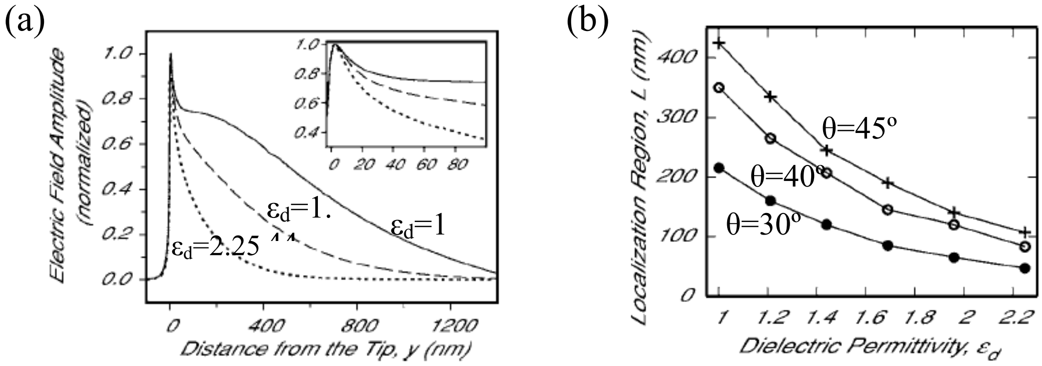

Figure 128. The dependencies of the magnitude of the electric field amplitude in the fundamental CPP modes in the middle of the groove on distance from the tip for a silver groove with θ=45°, λ_0=632.8 nm and three different values of the dielectric permittivity (1, 1.44 and 2.25). All the three curves are normalized to the maximum of the field in the mode. (b) Dependencies of the localization region L along the depth of the fundamental CPP mode in the V groove for different apex angles: θ =45° (+), θ =40° (o), and θ =30° (•). [19]

One of the most relevant consequences that affects the fabrication process is an increase in the dimensions of the grooves, due to a higher confinement of the mode for increasing ε_d, thus allowing more flexibility for choosing the apex angle. Figure 129 (a) and (b) [19] show the dependence of the lower (θ_{c2}) and upper (θ_{c1}) critical angles on the dielectric permittivity of the material in the groove (ε_d) for gold and silver, showing in both cases, an increase in the angles value. For example, for air, 15º < θ < 60º, and for a dielectric with ε_d = 2.2, 30º < θ < 70º.

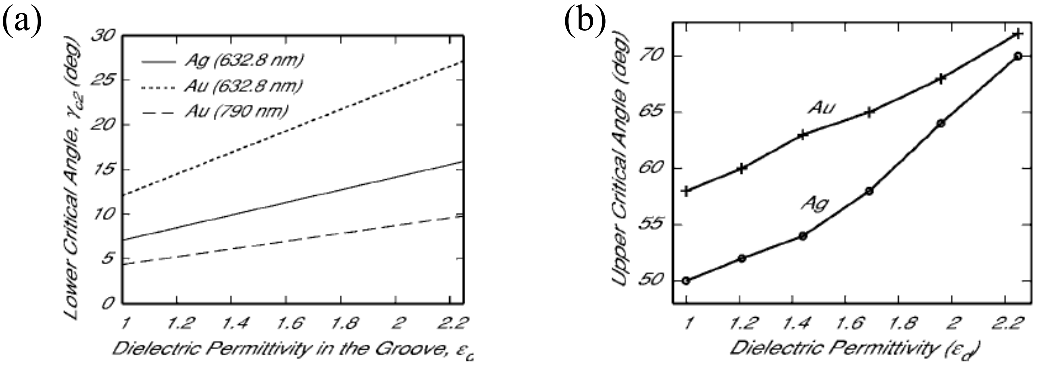

Figure 129. Dependence of the lower (a) and upper (b) critical angles on the dielectric permittivity in the grooves. The structural parameters are the same as for Figure 128. [19]

The better confinement of the mode results in a shorter propagation length, as can be seen in the plot of Figure 130 [19].

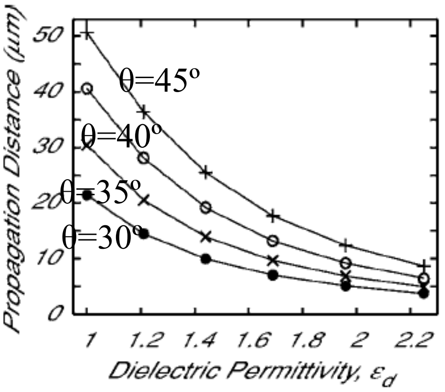

Figure 130. Dependence of the propagation length for the fundamental CPP mode on the dielectric permittivity for different groove angles: θ=30° (•), θ=35° (x), θ=40° (o), and θ =45° (+). [19]

5.3-2:d.- Attenuation

The evanescence of SPPs and CPPs is due to the hybrid nature of the oscillations: coupling between light and electrons leads to a fast decaying of the intensity of the fields along the surface due to energy dissipation (as heat) in the metal due to **electrons damping**. **Multimode propagation** can also lead to additional losses, due to the fields coupling and interaction.

These two sources of losses were modelled by Gramotnev et al. in [18]. Figure 131 (a) shows a scheme the studied structure: a silver V-groove, with an apex angle of 30º.

Figure 131(b, c, d) show the distribution of the magnitude of the instantaneous electric field along the propagation axes, resulting from the excitation of CPP modes at λ_0 = 633nm for three different cases. In the first one (Figure 131(b)), an *infinitly deep* groove was considered. A clear periodic modulation of the field distribution occurs in the groove due to interference beats between two modes. Figure 131(c) shows how this interference can be avoided by considering a *finite depth* of the groove, lower than the penetration depth of the field in the dielectric, so the second CPP mode is eliminated. An ideal metal (ε_m''=0) (non dissipating) was considered again in this case. No attenuation is observed in the figure. When introducing *dissipation*, the exponential decay of the intensity along the groove is clearly seen (Figure 131(d)).

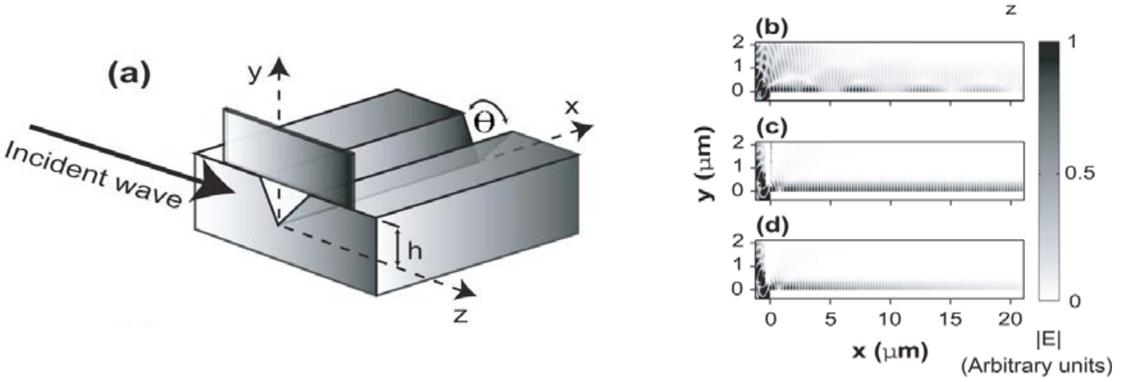

Figure 131. (a) Metal V-groove of finite depth, h, abut vacuum (ε_d=1). (b) Distribution of the magnitude of the instantaneous electric field in an infinitely deep (h= +∞) groove in silver, with a free charge density ρ≈−7.68 C/m^{-3} and damping frequency Γ=1.4 Hz. (c) Same as in (b), but with a finite depth of the groove (h =316.4 nm) and Γ = 0 (no dissipation in the metal). (d) Same as in (b) and (c), but with h=316.4 nm and Γ =1.4 Hz. [18]

Filling the V-groove with a dielectric -different from air or vacuum- (i.e., increasing ε_d) results in additional propagation losses, according to the results reported in [19] and to the experimental observations during this thesis [ref artículo bolas]. This is usually explained attending to the increase in the penetration depth into the metal, (22), what leads to a faster attenuation of the fields intensity. On the other hand, an imperfect (real) dielectric material interacts with the electromagnetic fields that propagate inside it. Thus, it results in energy losses due to the absorption and/or scattering by the atoms/molecules of the material.

5.4.- REFERENCES

[1] Ordal, M.A., L.L. Long, R.J. Bell, S.E. Bell, R.R. Bell, et al.,
Optical properties of the metals Al, Co, Cu, Au, Fe, Pb, Ni, Pd, Pt, Ag, Ti, and W in the infrared and far infrared.
Applied Optics, 1983. **22**(7): p. 1099-1119.

[2] Raether, H.,
Surface Plasmons, ed. Springer. 1988, Berlin.

[3] Barnes, W.L.,
Surface plasmon-polariton length scales: a route to sub-wavelength optics.
Journal of Optics a-Pure and Applied Optics, 2006. **8**(4): p. S87-S93.

[4] Ritchie, R.H.,
Plasma Losses by Fast Electrons in Thin Films.
Physical Review, 1957. **1**(5): p. 874-881.

[5] Homola, J.,
Present and future of surface plasmon resonance biosensors.
Analytical and Bioanalytical Chemistry, 2003. **377**(3): p. 528-539.

[6] Welford, K.,
Surface-Plasmon Polaritons and Their Uses.
Optical and Quantum Electronics, 1991. **23**(1): p. 1-27.

[7] Barnes, W.L., A. Dereux and T.W. Ebbesen,
Surface plasmon subwavelength optics.
Nature, 2003. **424**(6950): p. 824-830.

[8] Lakowicz, J.R.,
Radiative decay engineering 5: metal-enhanced fluorescence and plasmon emission.
Analytical Biochemistry, 2005. **337**(2): p. 171-194.

[9] Novikov, I.V. and A.A. Maradudin,
Channel polaritons.
Physical Review B, 2002. **66**(3).

[10] Bozhevolnyi, S.I., V.S. Volkov, E. Devaux, J.Y. Laluet and T.W. Ebbesen,
Channelling surface plasmons.
Applied Physics a-Materials Science & Processing, 2007. **89**(2): p. 225-231.

[11] Bozhevolnyi, S.I.,
Effective-index modeling of channel plasmon polaritons.
Optics Express, 2006. **14**(20): p. 9467-9476.

[12] Kogelnik, H.,
Guided-wave Optoelectronics,
in *Theory of dielectric waveguides*, Springer-Verlag, Editor. 1988, Tamir, T: Berlin. p. 69-74.

[13] Lim, T.K.,
Effective index method for generalised waveguide dispersion characteristics analysis of optical channel waveguides, in *Electronics letters*. 1991. p. 917-918.

[14] Bozhevolnyi, S.I., V.S. Volkov, E. Devaux and T.W. Ebbesen,
Channel plasmon-polariton guiding by subwavelength metal grooves.
Physical Review Letters, 2005. **95**(4).

[15] Bozhevolnyi, S.I., V.S. Volkov, T. Sondergaard, A. Boltasseva, P.I. Borel, and M. Kristensen,
Near-field imaging of light propagation in photonic crystal waveguides: Explicit role of Bloch harmonics.
Physical Review B, 2002. **66**(23).

[16] Moreno, E., F.J. Garcia-Vidal, S.G. Rodrigo, L. Martin-Moreno and S.I. Bozhevolnyi,
Channel plasmon-polaritons: modal shape, dispersion, and losses.
Optics Letters, 2006. **31**(23): p. 3447-3449.

[17] Boltasseva, A., V.S. Volkov, R.B. Nielsen, E. Moreno, S.G. Rodrigo, and S.I. Bozhevolnyi,
Triangular metal wedges for subwavelength plasmon-polariton guiding at telecom wavelengths.
Optics Express, 2008. **16**(8): p. 5252-5260.

[18] Gramotnev, D.K. and D.F.P. Pile,
Single-mode subwavelength waveguide with channel plasmon-polaritons in triangular grooves on a metal surface.
Applied Physics Letters, 2004. **85**(26): p. 6323-6325.

[19] Vernon, K.C., D.K. Gramotnev and D.F.P. Pile,
Channel plasmon-polariton modes in V grooves filled with dielectric.
Journal of Applied Physics, 2008. **103**(3).

Chapter 6

Fabrication of V-groove plasmonic waveguide devices by NIL

The increasing interest of the use CPPs to confine light in micro/nanometric structures lead in the last years to a large activity regarding theoretical studies and modellization, as has been described and summarized in the previous chapter. In 2006 the group leaded by S. Bohzevolnyi published two landmark papers [1, 2], **demonstrating experimentally** that it was possible to confine and guide light in sub-wavelength metallic V-grooves. Albeit the relevance of these results, the samples used were just prototypes for a proof-of-concept, and couldn't be exploited for further applications, due to the time consuming and poor reliability of the fabrication process.

In this chapter, the experimental results obtained by this group on CPPs confinement propagation in metal V-grooves will be summarized. Next, a novel method for the fabrication of integrated devices for plasmon confinement, based on nanoimprint lithography, will be presented. Its main advantage is that is a reliable and low cost approach for the massive fabrication of integrated devices based on gold V-grooves.

6.1.- PREVIOUS EXPERIMENTAL RESULTS

Up to date, the most relevant experimental characterizations to probe the possibility of squeezing light in sub-λ structures and to study the CPPs propagation and confinement issues in metallic V-grooves have been performed by S. Bohzevolnyi et al. [1-3].

They utilized home made samples, fabricated by **direct milling of the metal** by using a focused ion beam (FIB) [1]. Figure 132 (a) and (b) show SEM images of two of the grooves milled in a gold layer, that have two different apex angles: 16º and 25º respectively. It can be observed that this fabrication method leads to rough sidewalls. As it can also be seen in the images, after milling the groove, a large area had to be carved as well in one of the ends, so the light could be launched into the grooves for the optical characterizations.

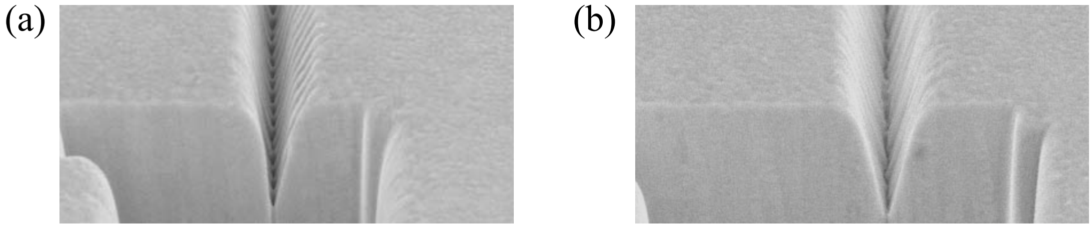

Figure 132. Two grooves fabricated by direct milling of the metal (gold) by FIB, as reported in [1]. Two different apex angles were obtained: 15º (a) and 30º (b).

Different wave-guiding devices with sub-λ lateral dimensions were fabricated and light confinement and propagation was demonstrated by near optical field characterizations (SNOM). The results reported *for different optical components*, such as Y splitters and Mach-Zehnder interferometers, are shown in Figure 133 [2]. It is noticeable that the light bend in very small distances, without noticeable loss of intensity, which is a very important result.

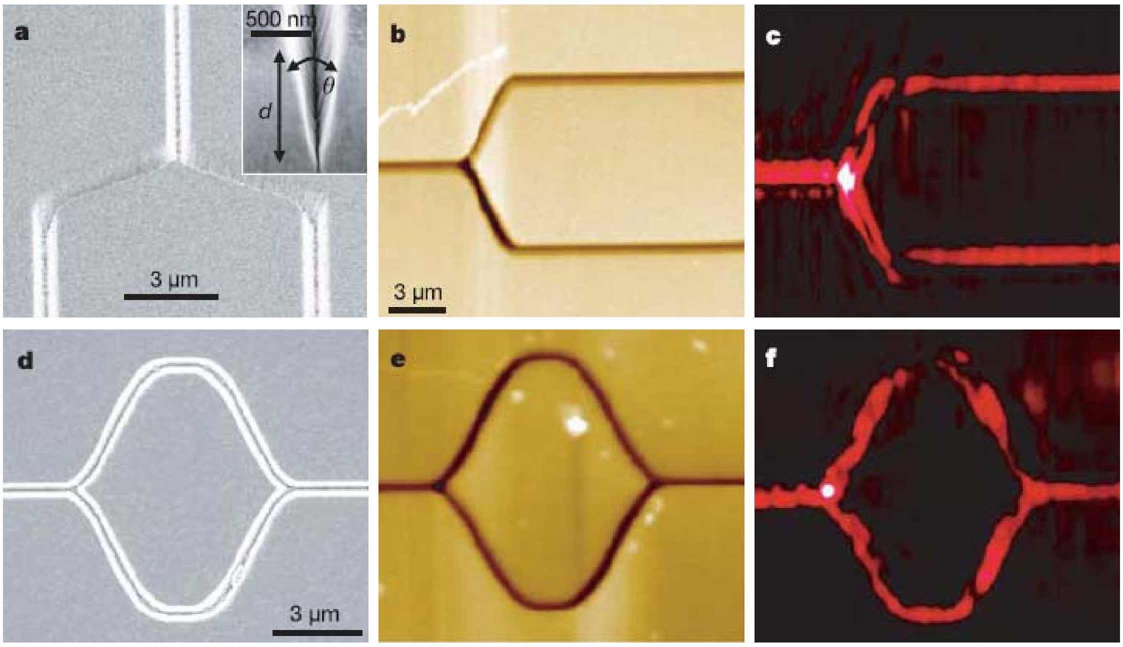

Figure 133. Plasmonic Y-splitter and Mach–Zehnder interferometer. SEM (a) and AFM (b), topographical images and its corresponding near-field optical (λ_0= 1600 nm) SNOM images of the Y-splitter; inset in (a), SEM image showing typical groove profile. (d), (e) and (f), same as (a–c) but for the Mach-Zehnder interferometer. Reproduced from [2].

They measured the **confinement and propagation parameters** in *straight* V-grooves. Figure 134 (a) shows the SNOM image corresponding to the CPPs inside a groove (light propagates from left to right). The graphs in Figure 134 (b) correspond to a transversal profile (bottom coordinates) and to the averaged optical intensity along the groove (top coordinates). In the first, the full width at half maximum (FWHM) of the optical intensity was measured, which gave the **confinement of the mode**. This was 1.13 μm, and remained almost constant for the range of wavelengths used in the work (1425-1620 nm). A **propagation length** of 90 μm was obtained from the exponential fit of the optical intensity along the groove. They found that it was varying between 90 and 250 μm depending on the wavelength used and on the coupling arrangement.

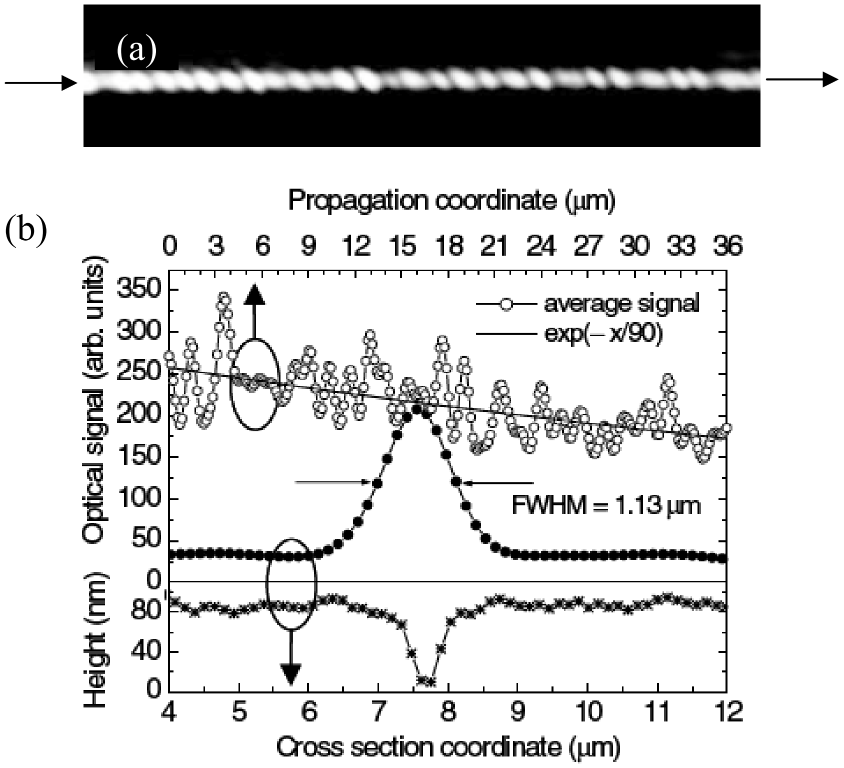

Figure 134. Near-field optical image (36 x 9 μm^2) of a V-groove with an apex angle of 30º, excited at λ_0= 1.44 μm. The CPP propagation is from left to right. (b) Cross sections of the topographical (stars) and nearfield optical (filled and open circles), averaged from (a). The exponential dependence fitted by the least-square method to the signal dependence along the propagation direction is also shown. [1]

These results confirmed the possibility of squeezing light inside channels with sub-λ lateral dimensions. The chosen structures (metallic V-grooves) exhibited superior features compared to other configurations, such as slits, metal gaps [4], or nanoparticle-chains [5]. V-grooves have shown a strong subwavelength localization of the CPP modes, relatively low losses even thorough sharp bends, low sensitivity to surface roughness or defects and broadband transmission.

6.2.- DESIGN OF THE DEVICES

Direct individual milling of each groove leaded to poor reliability and throughput. The goal of the work described in this chapter is to fabricate integrated devices based on V-groove waveguides by means of nanoimprint lithography (NIL) [6], overcoming the difficulties of the fabrication methods used in the previous works, and that can be used in forthcoming applications. A NIL-based technology allows strongly improving the simplicity and robustness of the process. Also, the smoothness of the sidewalls is better. And, as it is a parallel method, multiple designs and geometries can be included in one single wafer, processing several devices (~200) at the time.

First, a detailed design of the devices will be presented.

The good performance of the devices for CPP confinement was proven by various characterization techniques [7], as will be described in Chapter 7. Even further, fluorescent nanoparticles deposited inside the grooves showed CPPs propagation with no need of near field microscopes, being also the first step for the possible use of these devices as (bio)sensors.

Figure 135 shows a drawing of one of the structures. Each device consisted of one V-groove integrated with two deep channels, where input and output fibers could be placed for optical characterizations. The channels had a width of 200 µm and were 300 µm deep. These dimensions were chosen so the optical fibers (which typical diameter is 150 µm) fit laterally into the channel. The core of the optical fiber lied approximately in front of the V-groove, which, even if it didn't result in a self-aligned configuration, facilitated the coupling of the light into the waveguide. The channels were deep enough to allow vertical displacements of the fibers, in order to be able to light up the groove at different depths.

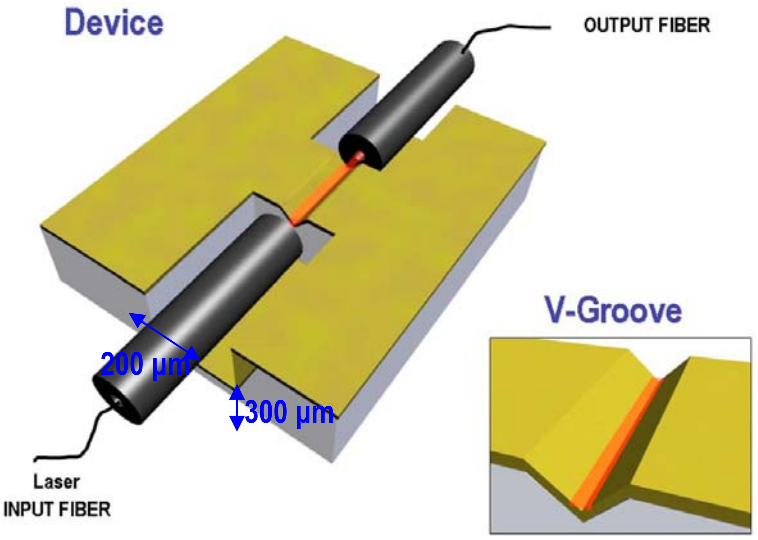

Figure 135. Schematic drawing of a single device, containing the V-groove where the channel plasmon polaritons are confined and guided, and two deep channels, where the input and output fibers fit, to facilitate the coupling of the light into the waveguide.

In this work, the apex angle of the grooves was wider than that of the grooves reported in the literature [1, 2], which implied an increase in the propagation length. According to the calculations in [8], a larger angle (50° in our case, compared to 30° in the previous works) results in a weaker coupling of the light to the groove, thus, reducing the losses, and leading to a longer propagation length, closer to the one of SPPs propagating on a non-patterned surface, as has been described in the theory in the previous chapter.

Multiple waveguides with the V-grooves length varying from 100 µm to 500 µm were designed and fabricated. The V-groove (top)width was varied from 2 µm to 12 µm. As the angle of the V-groove is fixed by the fabrication technology in 70.6 °, the depth was determined by the width. Thus, it goes from 1.4 µm up to 8.5 µm.

The grooves were fabricated in gold, which is more stable than silver, allows robust fabrication process and shows better adhesion properties to the materials used as substrates. SPP penetration depth in gold is around some tens of nm (~21 nm for IR-UV range, as described in the previous chapter), so a thicker layer of the metal (200 nm) was preferred in order to avoid coupling between the SPPs on upper and lower gold/dielectric interfaces.

6.3.- NIL-BASED FABRICATION PROCESS

The fabrication process was started and developed at the Technical University of Denmark. It took the advantages of a NIL-based fabrication process, such as simplicity, high throughput, and reliability. It also allowed multilevel fabrication: the deep channels and the V-grooves could be imprinted simultaneously.

The **process flow** is shown in the schemes of Figure 136:

a. A silicon stamp is first fabricated with the desired structures.

b. The stamp is imprinted in a PMMA sheet (5 mm thick), at 180 ºC and 20 kN, for 10 minutes using an EVG 520HE parallel press nanoimprint tool.

c. A 200 nm thick layer of gold is deposited onto the PMMA structures by e-beam evaporation.

d. A viscous transparent pre-polymer (Ormocomp*) is cast onto the sample and left several minutes to completely fill all the channels by viscous flow. Then, it is cured using UV light (2 minutes, at 350 W) so it polymerizes and becomes hard.

e. The PMMA is afterwards dissolved in acetone for several hours, leading to the final structures. The curing step and PMMA striping was optimized (pre and post backing, N_2 cleaning) so the adhesion of the gold to the cured Ormocomp was improved with respect to the PMMA.

f. The resulting geometry of the final structures (f) is the same as those of the silicon stamp (a), but replicated in gold onto Ormocomp. The CPPs propagation takes place at the gold/air interface and the Ormocer plays the role of supporting the thin gold layer. A transparent substrate was preferred, as opens the possibility of launching the light from below the sample, using it as a prism.

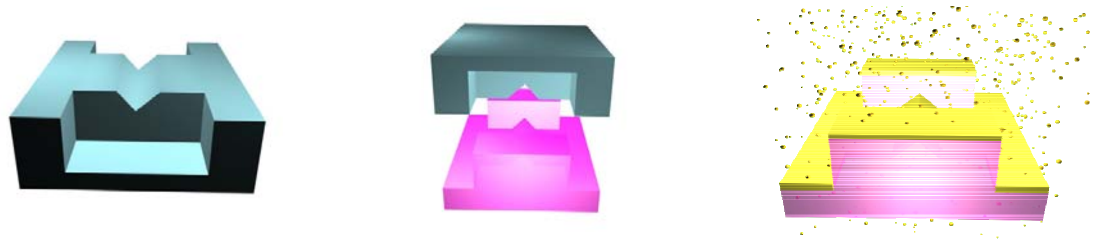

a. Silicon Stamp b. Nanoimprint c. Gold deposition

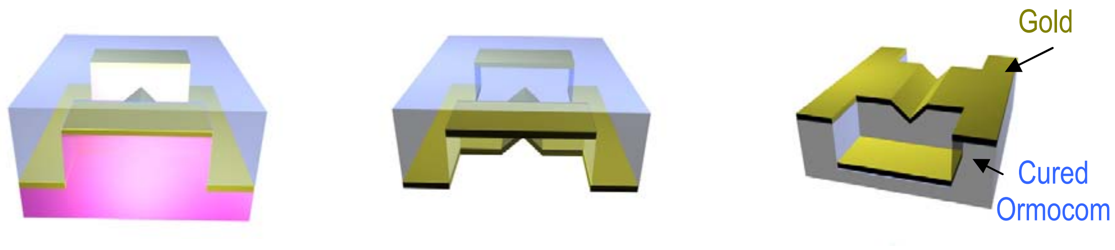

d. Ormocomp Cast and curing e. Dissolving PMMA f. Final samples

Figure 136. Scheme of the fabrication process: (a) silicon stamp, containing the v-grooves. (b) nanoimprint process, to transfer the features to PMMA. (c) a 200 nm thick film of gold was deposited on the PMMA structures. (d) casting of a UV curable polymer (Ormocomp) on the structures, and UV curing. (d) PMMA was then dissolved in acetone. (f) scheme of the final structures, showing the same geometry of the initial stamp, but made in gold on top of Ormocomp.

---

[*] Ormocomp (ORMOCER®s), hybrid photocurable polymer, from *MicroResist Technology, GmbH,* Berlin. www.microresist.de

There are some reasons for performing a double-replication process and not to deposit gold directly on the imprinted structures. One is that the process to fabricate stamps with triangular grooves was very well known and optimized, as has been already described in Chapter 2. The fabrication of triangular protrusions is not so easy and reliable, though. The second reason is related to loose of sharpness during the metallization step. Figure 137 (a) shows a scheme of a metallization performed directly in a sharp triangular channel: the anisotropic deposition leads to a rounded shape. Even thought, if the metal is deposited in a protruded triangle, that will be removed further, the sharpness and smoothness of the groove is maintained, as depicted in Figure 137 (b).

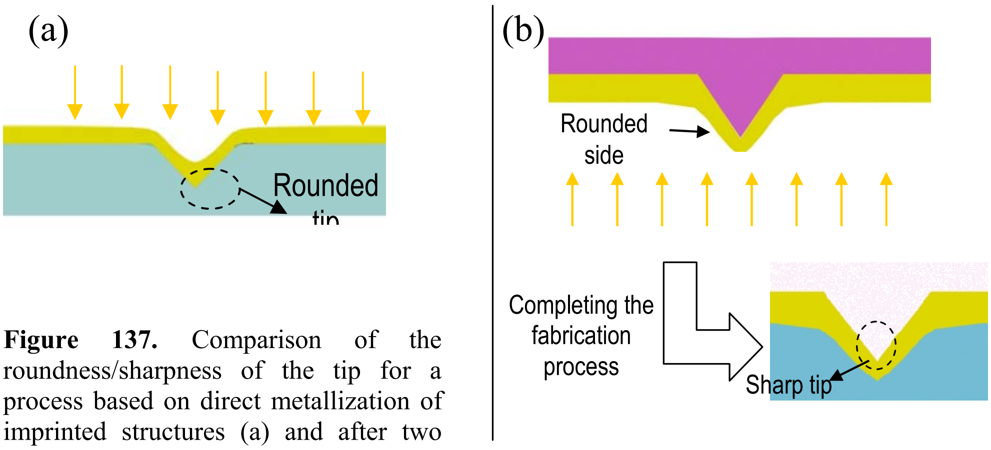

Figure 137. Comparison of the roundness/sharpness of the tip for a process based on direct metallization of imprinted structures (a) and after two replications in different materials as proposed in our fabrication method (b).

6.3-1. Stamp

The silicon stamps were fabricated in 4 inch silicon (100) wafers. The stamp played a critical role, not only because it determined the resolution of the patterns and the overall quality of the structures, but also to enable a wafer scale processing.

6.3-1:a.- Stamp design

An example of the distribution of the devices is depicted in Figure 138 (a): 36 chips were defined in each wafer, each chip containing 5 grooves with different lengths (100 μm, 200 μm, 300 μm, 400 μm and 500 μm). Twelve of the chips had 5 μm wide grooves, other twelve 7 μm wide grooves, and the other twelve 12 μm wide grooves.

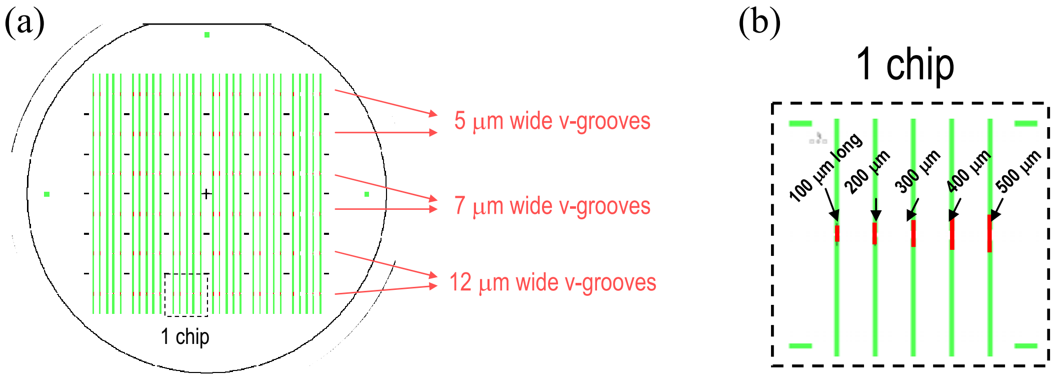

Figure 138. Scheme of the distribution of the devices in a 4 inch wafer. 36 chips, containing 5 v-grooves each one, were included in each wafer. Several widths and lengths were designed and fabricated simultaneously in each processed wafer.

6.3-1:b.- Stamp fabrication

The stamp fabrication process is outlined in Figure 139.

I. **V-shaped grooves.** The grooves were fabricated by anisotropic wet etching of silicon in KOH, using a silicon oxide layer as a mask, which was previously patterned by standard photolithography (steps a, b, c and d in Figure 139).

II. **Deep channels.** A second photolithography step was performed to define the channels just next to the grooves, and the resist was used as a mask for a deep reactive ion etching to transfer the pattern into the silicon. After resist stripping and antisticking coating with F13-TCS, the stamp was ready to be used for nanoimprint lithography (steps e, f, g and h of Figure 139).

Once the stamp was fabricated, multiple wafers could be processed to obtain the devices without the need of any additional optical lithography process.

It is important to remark that the v-grooves were defined by anisotropic wet etching of silicon, what results in very smooth sidewalls. Several etching tests were done in order to improve the smoothness of the sidewalls, as has been described in chapter 2 to fabricate triangular grooves. We checked that, after imprinting, the resulting polymeric features were also extremely smooth.

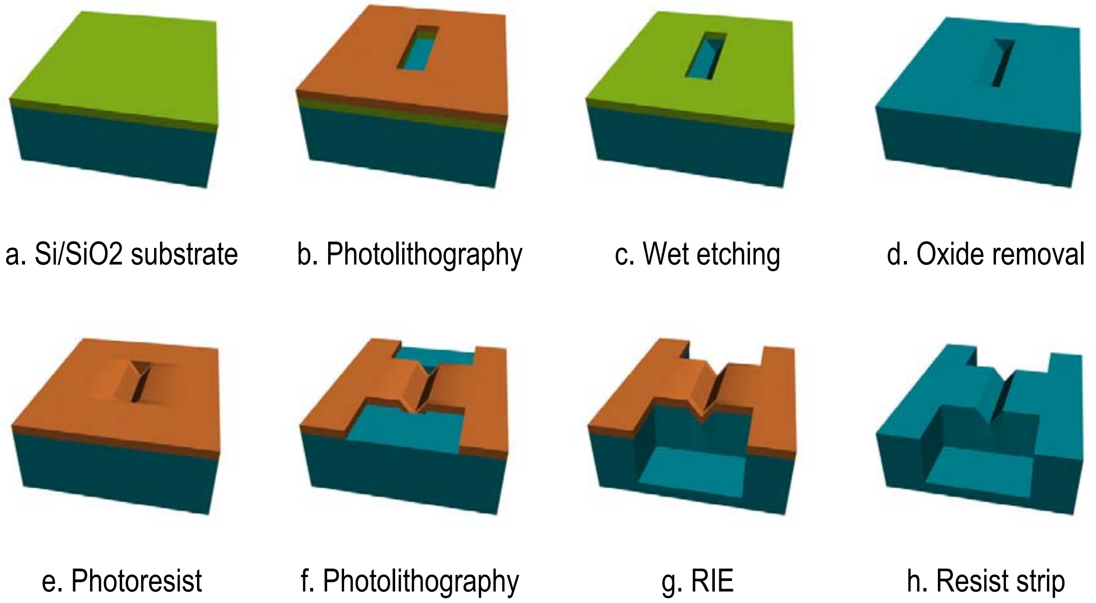

Figure 139. Scheme of the fabrication process: the v-grooves are fabricated first, by anisotropic wet etching in KOH, using SiO_2 as a mask, previously patterned by photolithography. The deep channels are fabricated by Deep RIE, using a second photolithography step to define the mask.

V-grooves in the stamp were fabricated in different sizes and lengths in a 4 inch silicon wafer, following the distribution of Figure 138. Figure 140 (a) shows an example of one of the devices in the stamp, where both, the groove and the channels, can be observed. Figure 140 (b) corresponds to a detail of one v-groove.

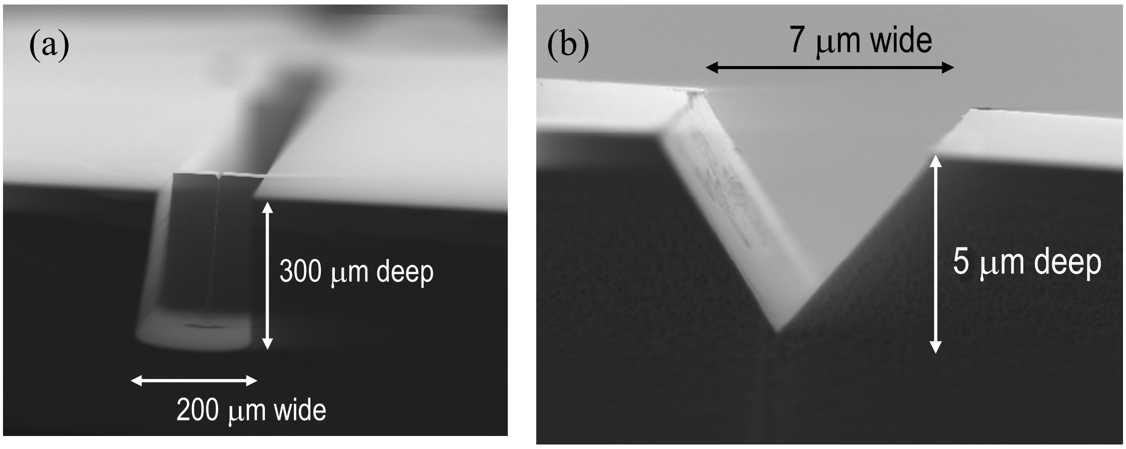

Figure 140. SEM images of the stamp: (a), general view of one of the devices, where the v-groove and the deep channels can be observed. (b), a detail of the v-groove, showing the smooth sidewalls that can be fabricated with wet etching in KOH.

In order to obtain smooth sidewalls, the lines in the mask should be parallel to a <100> crystallographic direction of the substrate, as was already shown in the studies of chapter 2. Here, as previously done, to avoid the inclusion of additional steps to achieve a precise alignment, the etching time was enlarged, so that any roughness that appears in the sidewalls due to misaligning effects was etched away, leading to flat sidewalls, as can be observed in Figure 140 (b). The resulting increase in the width of the grooves was not relevant for the final aim of this work.

6.3-1:c.- Oxidation

Anisotropic wet etching of silicon determinates that the groove angle is ~70º, which is just in the limit where plasmons can be confined in v-grooves. To improve the sharpness of the grooves, an additional wet oxidation step could be included at the end of the stamp fabrication process. In order to find the optimal conditions to achieve a shape where the angle in the bottom is as small as possible, simulations were performed using SILVACO[†]. Temperature, time, and groove size were varied. The best conditions were found to be 6 hours at 1150 ºC, for a 5 µm wide groove.

Figure 141 shows the simulation (top row) and a cross section SEM image of the grooves (bottom row) before (a and d) and after wet oxidation at 1150 ºC during 6 h, for two different sizes: 12 µm wide groove (b and e) and 5 µm wide (c and f). In the last case the angle is effectively reduced from 70º to 50º.

[†] *Part of ATHENA simulation package, Silvaco International, www.silvaco.com*

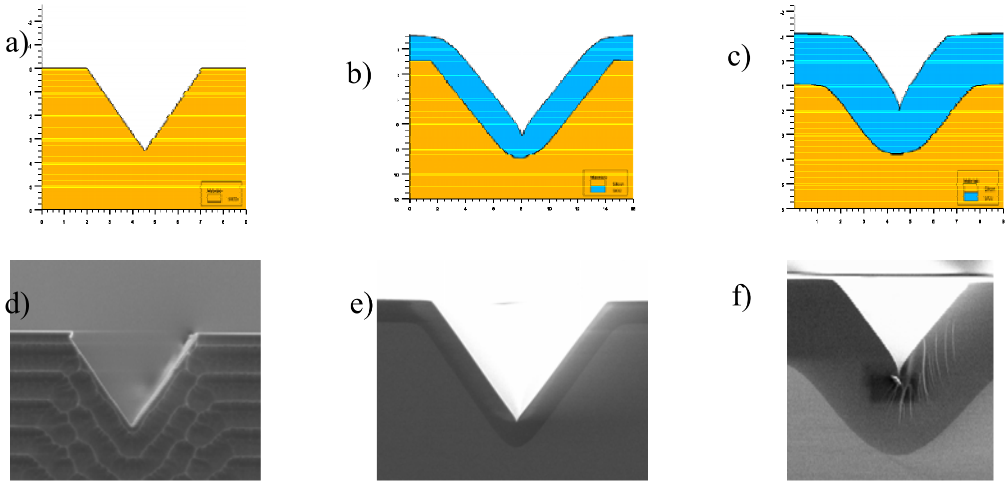

Figure 141. Results of simulations (top row) and SEM images of the results (bottom row) of wet oxidation of the silicon v-grooves at 1150 ºC during 6 h. (a,d), non-oxidized silicon groove; (b,e), 12 µm wide oxidized groove; and (c,f), 5 µm wide groove. Agreement between simulation and oxidized sample is shown. The shape of the 5 µm wide grooves is the most interesting for plasmon confinement. The angle in the bottom of the groove is improved from 70º to 50º.

6.3-2. Samples

Three major difficulties had to be solved before achieving a successful fabrication of the devices.

First, the stamps were very fragile due to the presence of the channels, so they often broke during the nanoimprint process. To make them more robust, they were anodically bounded to another silicon wafer.

Second, the imprinting process itself had to be optimized, as the area of channels that needs to be filled is very large. Thus, a PMMA thick sheet (1mm) was used, instead of a layer spin-coated onto a substrate. And the imprinting time was enlarged, compared to a normal process, up to 20 min, so the replication of the big structures was ensured.

Third, gold deposition in a PMMA sheet was not homogeneous at 4 inch scale, and bubbles, wrinkles or cracks appeared in the gold layer. To reduce these effects, the PMMA sheets were dehydrated in an oven at 80 ºC for 10 hours before the nanoimprint process. To minimize local thermal effects during evaporation, a silicon wafer was attached to the back of the sheets during the process.

Finally, successful fabrication of the devices was achieved, as can be seen from the SEM images of Figure 142. Figure 142 (a) corresponds to a general view of a structure of one of the chips, where the channels and the groove can be observed. Figure 142 (b and c) shows a detail of the grooves. Some delamination of the gold is observed outside the grooves, however inside the grooves we found that the gold layer was very uniform, smooth and continuous, ensuring a good optical performance.

Figure 142 (d) shows a groove imprinted with a stamp subjected to the additional oxidation step at 1150 ºC during 6 h. The angle of the v-groove was clearly reduced as can be observed by comparing the images of Figure 142 (c) and Figure 142 (d).

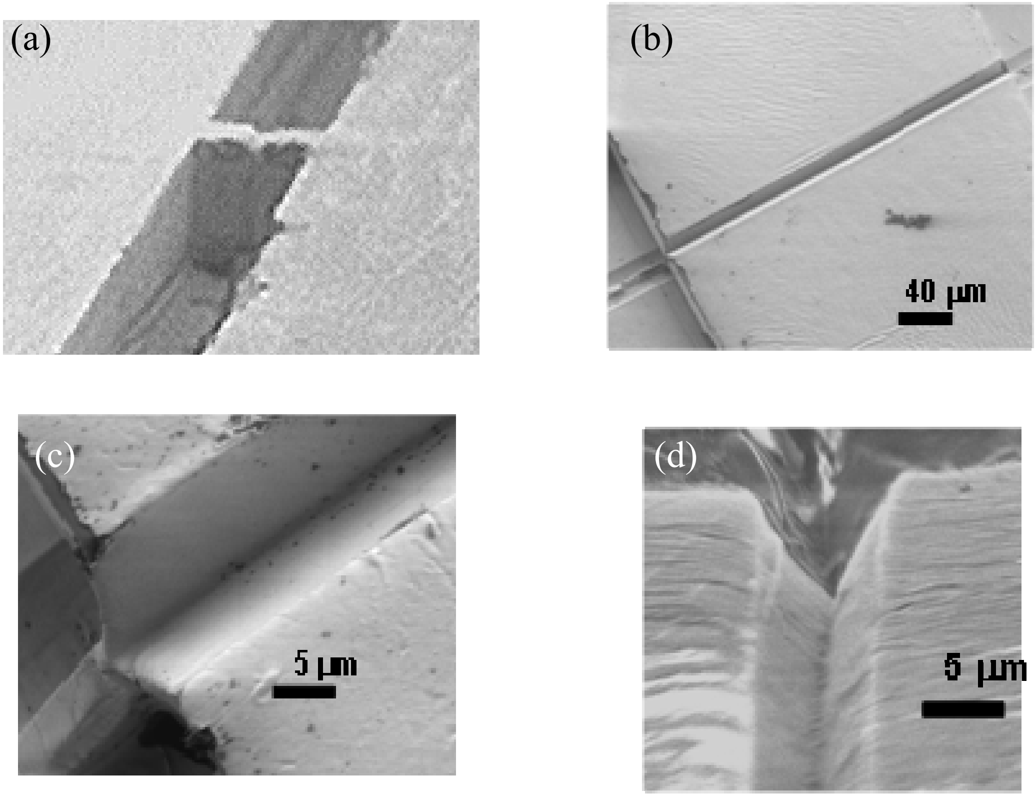

Figure 142. SEM images of the fabricated samples (gold onto Ormocer): (a), general view of a device, and (b), a detail of a single v-groove, that is 100 µm long, and 7 µm wide. (c) shows a zoomed area of the V-groove, where the smoothness inside the channel can be observed. SEM image of the final gold structure fabricated using an oxidized stamp. It can be seen that this groove is narrower in the bottom, what improves the plasmon confinement.

After dissolving the PMMA, the wafer is cut in individual chips (Figure 143 (a)) of 1cm^2 approximately. Each chip contains 5 V-grooves (Figure 143 (b)), with a fix angle and width and varying length.

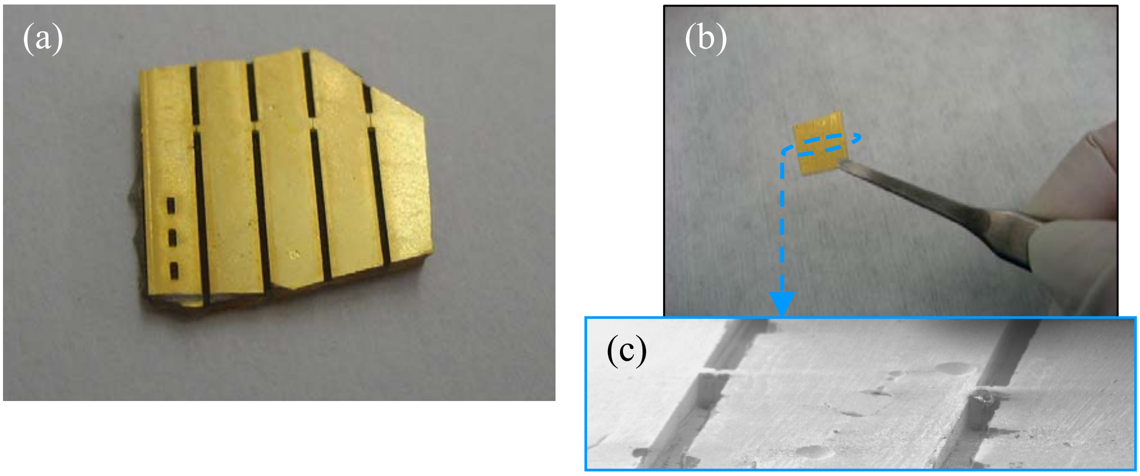

Figure 143. Photography of one of the chips, cut from the wafer (a). Each chip contains 5 v-grooves (b) with a fix width and 5 different lengths.

6.3-3. Fabrication process improvement

After the development of this first fabrication flow, the process was changed and improved, making it more robust at the expense of simplicity.

One of the main challenges of the first fabrication process was the demolding. The RIE process used to define the deep channels in the stamp, lead often to rough sidewalls and/or to non-straight angles (zipper-shape trenches). As it has already been mentioned above, wafers used to fabricate the stamps were 500 µm thick. Thus, below the channels (300 µm deep) only 200 µm of silicon remained. This, together with the typical stiction problems of NIL, made the demolding process hazardous (for the stamp) and tricky. Anodic bounding of a wafer below the stamp improved its life-time, but after few imprints, it broke anyway.

Thus, the stamp geometry was re-designed, so it only had the V-grooves (with sharpened angle, by oxidation, as described before). The new configuration of the stamp made the imprinting step much simpler and faster (there was no need to fill the big channels anymore). The whole fabrication process (Figure 144) was slightly changed, as outlined below:

a. The stamp with only V-grooves is imprinted in a thin layer of PMMA.
b. The gold layer is then evaporated covering the PMMA.
c. The Ormocomp is poured onto the structures.
d. The Ormocomp is locally cured by UV exposure by using a mask, where the device geometry (“H” shape) has previously been designed.
e. The non-exposed material is dissolved in Ormodev, a especial developer for this Ormocers.
f. The PMMA is removed in an acetone bath, acting as a sacrificial layer. This releases the samples from the silicon substrate.
g. The gold layer remains adhered to the cured Ormocomp, and that part that was onto the non-cured material breaks during the ultrasound stripping bath.
h. Finally, the gold layer is left only onto the hard cured Ormocomp substrate, as can be seen in the scheme of the final device in Figure 144.

The fabricated structures showed good replication of stamp features, as can be seen in the SEM images of Figure 146. The quality of the gold surface was generally good (Figure 146 (a) and (b)) with a roughness of around 2 nm as determined by atomic force microscopy (AFM) measurements, and few defects or dust particles were present after proper cleaning of the samples. However the gold edges at the V-grooves extremes were slightly ragged due to breaks from ultrasound agitation (Figure 146 (b))., which may influence the in-coupling of the light and losses, leading to variation between grooves under similar conditions.

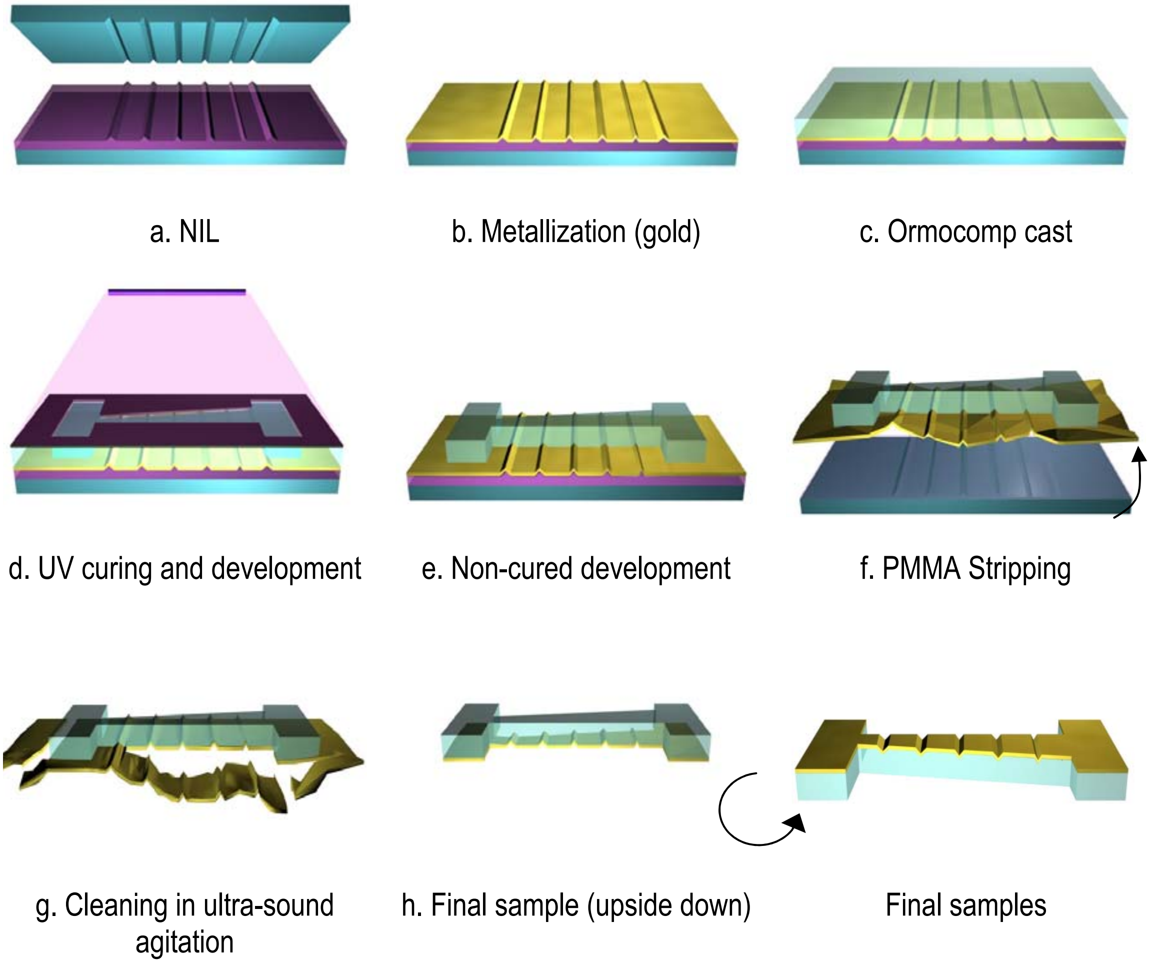

a. NIL

b. Metallization (gold)

c. Ormocomp cast

d. UV curing and development

e. Non-cured development

f. PMMA Stripping

g. Cleaning in ultra-sound agitation

h. Final sample (upside down)

Final samples

Figure 144. Improved process flow. The stamp geometry was simplified (only the v-grooves are imprinted) (a). The gold is deposited onto the structures (b) and the Ormocomp casted onto the sample (c). Then, it is locally cured by using a mask, where the device geometry has already been defined (d). After developing the un-cured Ormocomp (e), and stripping the PMMA (f), the samples are released, the non-adhered thin layer of gold breaks (g) and the structures are finally fabricated in gold onto Ormocomp (h).

Figure 145 shows two photographs of the samples. After developing the Ormocomp and stripping the PMMA, all the devices patterned in the wafer are released (Figure 145 (a)), so they can be manipulated individually (Figure 145 (b)).

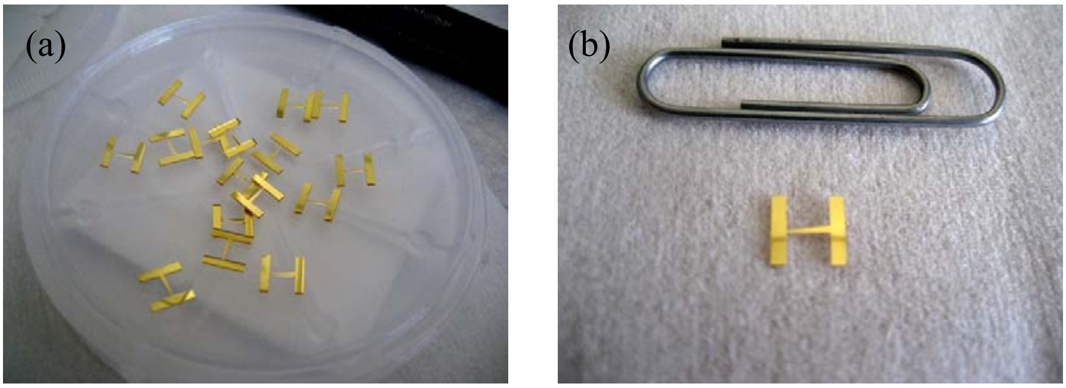

Figure 145. Photographs of the samples. Multiple device fabrication was achieve with the NIL-based methods, so, after removing the substrates, the individual chips were released (a). The samples were small (b), but could be easily handled, thanks to the lapels of the sides.

In this new design, the resulting samples were different from those presented in the previous section, as can be seen in Figure 146 (c). Each individual chip has 29 V-grooves, which length varies from 100 µm to 400 µm. Figure 146 (d) shows the distribution of V-grooves, which length increases from left to right. The big areas in both sides of the area are useful to handle the samples.

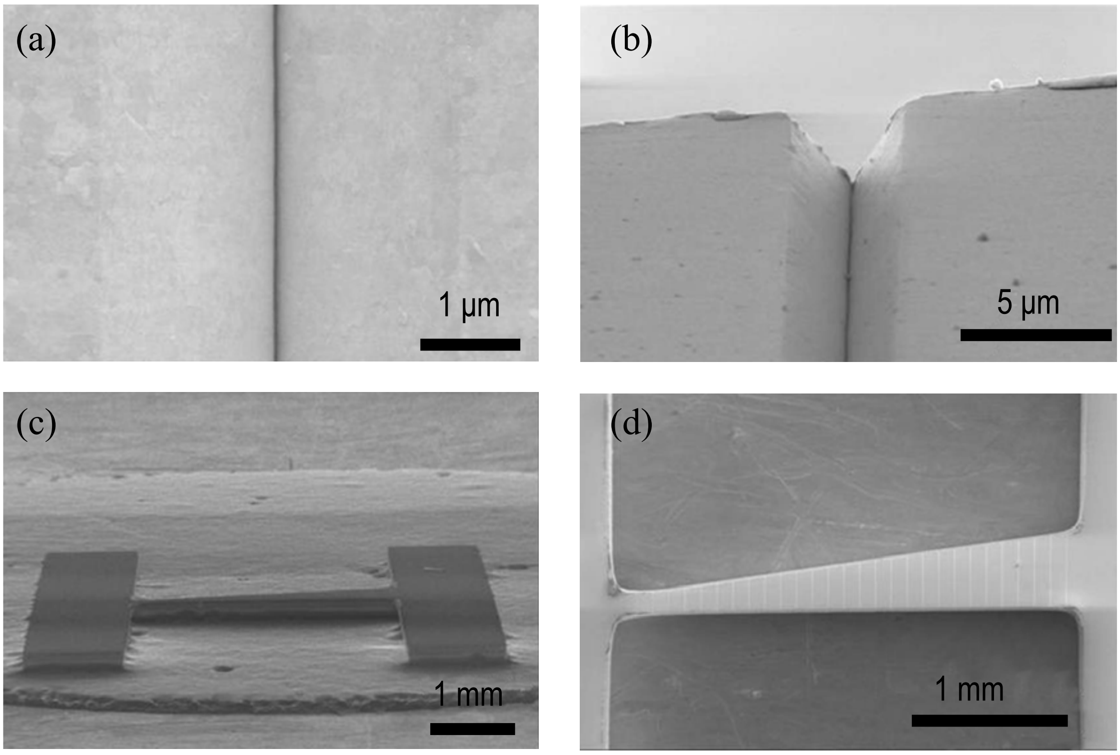

Figure 146. SEM images of the structure. (a) and (b) shows details of the grooves, where the smooth sidewalls and the profile with the sharpened angle can be observed, respectively. A tilted view of the device is shown in (c), and all the grooves with different lengths fabricated in each device in (d).

The images of Figure 142 - Figure 143 and Figure 146 - Figure 145 prove the robustness and reliability of both processes to fabricate devices consisting on gold V-grooves, with free extremes, so they can be easily reached with input lasers or optical fibers. In the next chapter, the performance of the waveguides to confine light will be shown, and the main characteristics of CPPs propagation will be measured.

6.4.- REFERENCES

[1] Bozhevolnyi, S.I., Volkov, V.S., Devaux, E. and Ebbesen, T.W.,
Channel plasmon-polariton guiding by subwavelength metal grooves.
Physical Review Letters, 2005. **95**(4).

[2] Bozhevolnyi, S.I., Volkov, V.S., Devaux, E., Laluet, J.Y. and Ebbesen, T.W.,
Channel plasmon subwavelength waveguide components including interferometers and ring resonators.
Nature, 2006. **440**(7083): p. 508-511.

[3] Bozhevolnyi, S.I., Volkov, V.S., Devaux, E., Laluet, J.Y. and Ebbesen, T.W.,
Channelling surface plasmons.
Applied Physics a-Materials Science & Processing, 2007. **89**(2): p. 225-231.

[4] Pile, D.F.P., Ogawa, T., Gramotnev, D.K., Matsuzaki, Y., Vernon, K.C., et al.,
Two-dimensionally localized modes of a nanoscale gap plasmon waveguide.
Applied Physics Letters, 2005. **87**(26).

[5] Wei, Q.H., Su, K.H., Durant, S. and Zhang, X.,
Plasmon resonance of finite one-dimensional Au nanoparticle chains.
Nano Letters, 2004. **4**(6): p. 1067-1071.

[6] Fernandez-Cuesta, I., Nielsen, R.B., Boltasseva, A., Borrise, X., Perez-Murano, F., and Kristensen, A.,
V-groove plasmonic waveguides fabricated by nanoimprint lithography.
Journal of Vacuum Science & Technology B, 2007. **25**(6): p. 2649-2653.

[7] Nielsen, R.B., Fernandez-Cuesta, I., Boltasseva, A., Volkov, V.S., Bozhevolnyi, S.I., et al.,
Channel plasmon polariton propagation in nanoimprinted V-groove waveguides.
Opt. Lett., 2008. **33**(23): p. 2800-2802.

[8] Bozhevolnyi, S.I.,
Effective-index modeling of channel plasmon polaritons.
Optics Express, 2006. **14**(20): p. 9467-9476.

Chapter 7

Optical characterization of V-groove plasmonic waveguides fabricated by NIL

CPPs propagation and characteristic parameters (propagation length, depth cut-off, etc) in the V-grooves fabricated by NIL were studied by various optical techniques.

Far field images show the modal shapes and light distribution inside the grooves in a qualitative way. SNOM characterizations confirm the CPPs confinement, and serve for a quantitative analysis of the propagation parameters. Filling the V-grooves with fluorescent nanoparticles allow to visualize the near field with an optical microscope, and makes the first step for the use of these devices for sensing..

7.1.- NEAR FIELD CHARACTERIZATION

7.1-1. Scanning Near Optical Field Microscopy (SNOM)

Scanning Near Field Optical Microscope (SNOM) is a form of scanning probe microscopy (SPM) that breaks the far field resolution limit by detecting the optical near field. The probe (that is a sharpened optical fiber, often coated with a metal) is placed very close (<< λ) to the sample surface (Figure 147(a)). By surface mapping (Figure 147(b)), the near optical field propagation with spatial, spectral and temporal [1] resolution can be studied. With this technique, the resolution of the image is limited by the size of the fiber aperture and not by the wavelength of the light. A shear-force feed-back system is generally used to maintain the fiber-surface distance, and to plot the surface topography. It can be used in several configurations (not only scanning mode) to perform different types of measurements, spectroscopic analysis [2], or even local excitation [3].

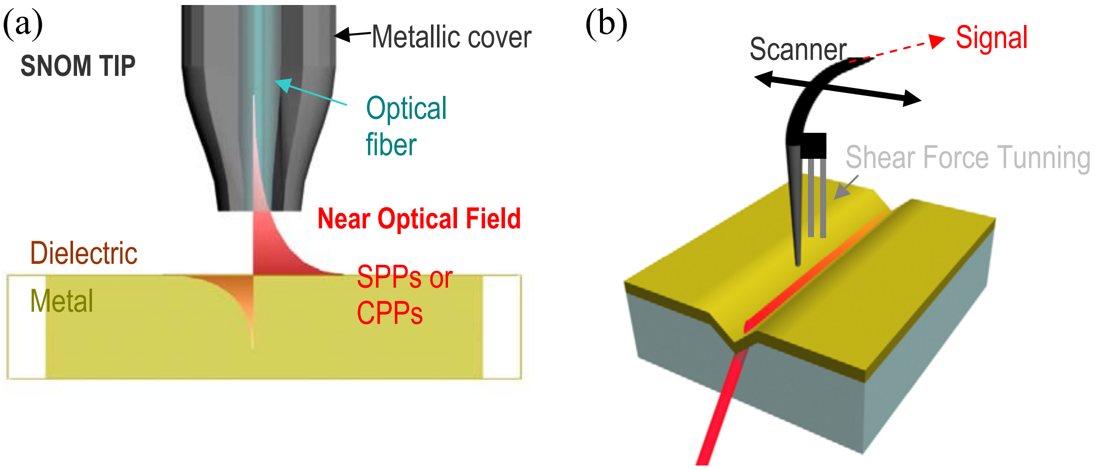

Figure 147. Scheme of the Scanning Near Field Optical Microscope (SNOM). A sharpened optical fiber (usually coated with a metal) is used as a probe, and, by placing it very close to the sample surface (<< λ) the near optical field can be collected (a). The tip can be scanned all along the sample surface, for local mapping of the optical intensity (b). The tip-sample surface is kept constant by using a feed-back method (often, shear-force). The signal is analyzed with the suitable electronic equipments.

7.1-1:a.- In-coupling of the light

Surface or Channel plasmon-polaritons on a metal/dielectric interface cannot be excited directly by light beams since β > k, where k is the wave vector of light on the dielectric side of the interface. Therefore, the projection along the interface of the momentum

$$k_x = k \sin \theta \qquad (26)$$

of photons impinging under an angle θ to the surface normal is always smaller than the SPP propagation constant β, even at grazing incidence, prohibiting phase-matching [4]. The wavevector matching at the interface is not possible. The wave cannot penetrate the metal and is reflected.

There are mainly three different configurations (Figure 148) to confer the necessary momentum on the incident photons: by using a prism (a), a grating (b), or the edge of the structure (“end-fire”) (c).

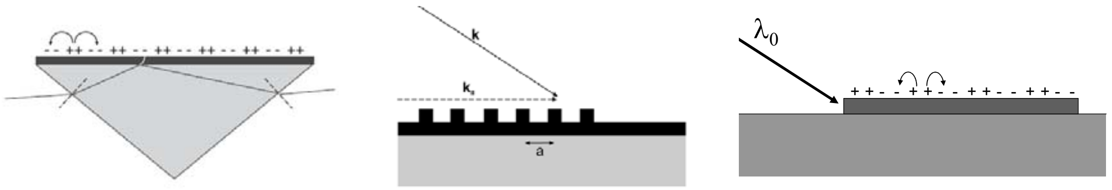

(a) Prism (b) Grating (c) End fire

Figure 148. In-coupling configurations. SPPs and/or CPPs cannot be directly excited just by lighting up the metal surface, as there is a momentum miss-matching. To “give” the incident light the necessary k, a prism with a higher refractive index can be used (a) or a grating (b). Also, by focusing the beam in the edge of the structures (c), the matching can be achieved.

Prism. In the first configuration, as schematized in Figure 148(a), the plasmons can be excited by launching the light through a high refractive index prism. The prism shortens the wavelength of light incident on the metal film (Figure 148(a)).

Grating. The second case is similar to the prism, but in this one, the momentum is obtained by exciting the plasmons thorough a grating (Figure 148(b)).

End-fire configuration. A free-space optical beam is focused on the end-facet of the desired waveguide. Rather than relying on phase-matching, this scheme operates via matching the spatial field distribution of the waveguide as much as possible by adjusting the beam width. This configuration allows the excitation of truly bound modes that do not radiate into the substrate (Figure 148(c)).

In this work, end-fire excitation was mainly used. For some of the characterizations, we also used the Ormocomp substrate as a prism for the in-coupling of the light into the V-grooves, as it has a refractive index n = 1.518.

7.1-2. Results on the Near Field Characterizations

Two different equipments, placed in two different institutes, were used for the near field measurements.

One belongs to the group leaded by Professor S. Bozhevolnyi, and was placed in Aalborg University[*]. This group has global expertise in SNOM characterizations in plasmonic waveguides, and has studied in detail CPPs propagation in V-grooves and channels. The equipment and set-up utilized were the same as those that they used in the previous works to study CPPs propagation in milled V-grooves [5, 6].

The second equipment used was placed at ICFO[†], and the characterizations were done in collaboration with Professor Niek van Hulst and Dr. Dominique Heinis. This group has also a wide knowledge about SNOM characterizations and have home-made equipment, which had an interferometric branch, making it a unique tool.

The quality of the topographical and near field images obtained in Aalborg was very good, which allowed measuring quantitatively the confinement and propagation characteristics of the CPPs in the imprinted V-grooves. By using the same system as in the previous works, the obtained values could be compared to those obtained for the propagation of CPPs in the milled grooves. Complementary data were obtained at ICFO, as the interferometric branch allowed obtaining phase maps of the light coupled and propagating in the samples surfaces, that are the first report on these kind of characterizations.

---

[*] Department of Physics and Nanotechnology, Aalborg University, DK-9220 Aalborg Øst (Denmark)

[†] Nano Photonics Group. Institut de Ciencies Fotoniques (ICFO) -08860 Castelldefels –Barcelona (Spain)

7.1-2:a.- Propagation and confinement

The first batch of SNOM images were obtained in Aalborg, using an uncoated fiber tip, and in the end-fire coupling configuration. Light with a tunnable λ_0 in the range 1425–1550 nm, TE-polarized, was used to excite the CPPs in end-fire configuration. It was launched into the groove by positioning a tapered-lensed polarization maintaining single-mode fiber (Figure 149 (a)). The adjustment of the in-coupling fiber was accomplished by visualization of the scattered light along the surface with a conventional optical microscope. The track of the propagating radiation was clearly distinguishable for distances up to 300 µm from the in-coupling point at the groove edge (Figure 149 (b)). After alignment and signal maximization, the whole fiber-sample arrangement was moved under the SNOM head. The optical intensity distribution near the surface of the groove was mapped being the fast scan direction perpendicular to the groove at a constant distance of a few nanometers, maintained by shear-force feedback. The optical signal collected by the fiber was detected with a femtowatt InGaAs photo receiver.

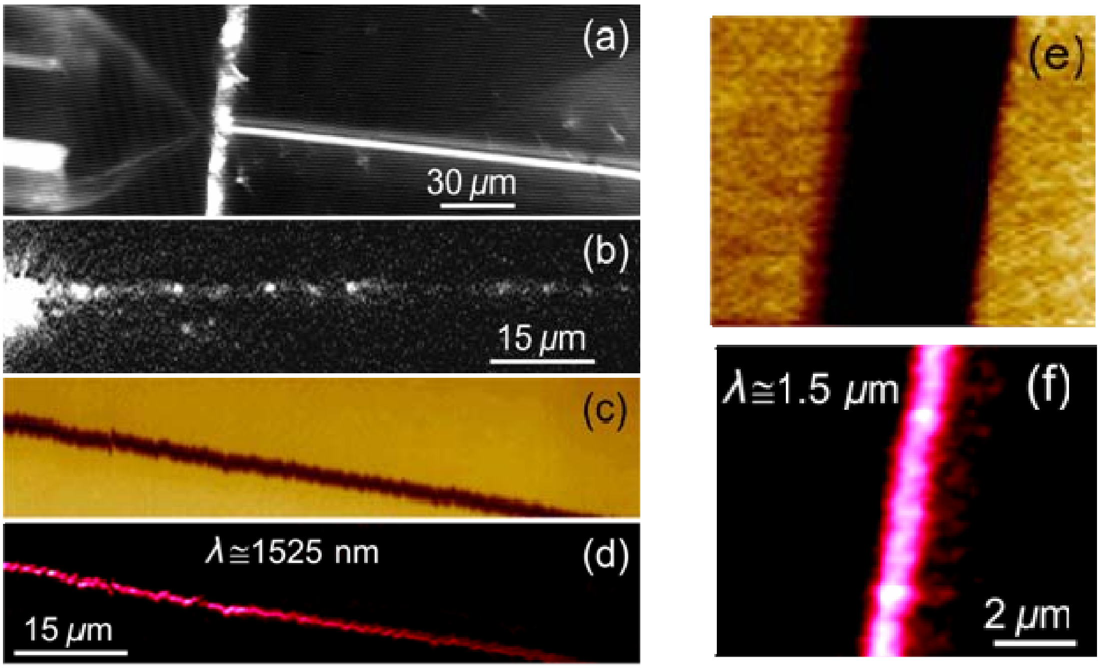

Figure 149. Optical microscope images of (a) the coupling arrangement (the tapered fiber is seen at the left and the illuminated groove at the right) and (b) the track of radiation propagating ($\lambda \cong 1525$ nm) along 3.8-µm-wide and 400-µm-long V-groove. (c, e) topographical and (d, f) near-field optical images obtained in the V-grooves at $\lambda_0 =$ 1525 nm in (d) (the CPP propagates rightwards), and $\lambda_0 = 1500$ nm in (f) (the CPP propagates upwards). Published in [7].

SNOM images were recorded at different wavelengths together with the corresponding topographical images. Figure 149 (d) and (f) show the near-field images obtained at λ_0=1525 nm, and Figure 149 (c) and (e) the corresponding topography, for a groove with an apex angle ~50°, a width of 3.8 µm, and 4 µm deep. They demonstrate efficient and well-confined CPP propagation. The non-uniform structure of the groove edge (see Figure 149 (c,d)) is due to scanning instability when scanning large areas. It is reduced when reducing the area (e.g. Figure 149 (e-f)).

The confinement of the mode was given by the average full-width-at-half-maximum (FWHM) of the optical intensity profile, perpendicular to the propagation direction (Figure 150, bottom edge). For the used wavelength range (1425–1550 nm), the FWHM was almost constant, and equal to **1.33 ± 0.1 µm**.

The propagation length was determined from SNOM images (Figure 150, upper edges). It varied between ~ **90 and 140 µm**, increasing gradually with λ and slightly depending on the coupling arrangement.

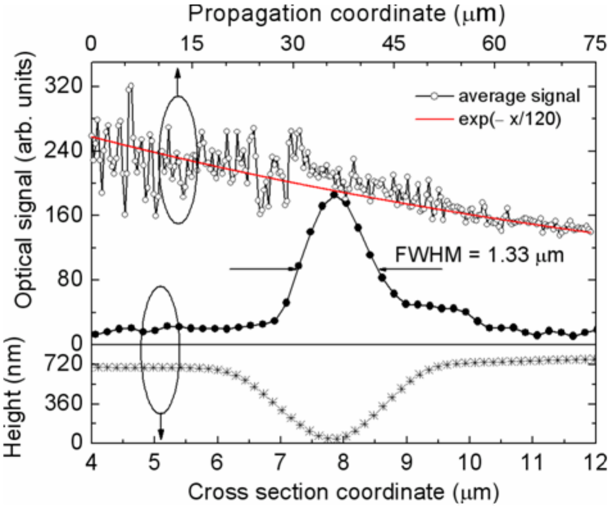

Figure 150. Cross sections of the topographical (stars) and near-field optical (filled and open circles) images of Figure 149 (d, e and f, respectively) averaged along the propagation direction or perpendicular to it. The exponential fit along the propagation direction is also shown.

It was also found from the SNOM images that the CPP mode distribution (in lateral cross-section) was not varying noticeably for different adjustments of the in-coupling fiber with respect to the position of the investigated V-groove (being very close to a Gaussian distribution shape). This can be attributed to single-mode waveguiding, at least, over the used wavelength range and the studied geometries.

Note also that the experimental observations reported above are consistent with the main properties of CPP modes (as well as with the experimental findings on CPP guiding reported previously [5, 6, 8, 9]). Thus, considering the dimensions of the studied V-groove (width ~ 3.8 µm, depth ~ 4 µm, apex angle ~50°), it was expected that the fundamental CPP mode was weakly confined (in lateral cross-section). This means that its propagation length should be closer to 150 µm than to 90 µm (or even longer) at the used wavelengths [5].

7.1-2:b.- Interferometric images

The second batch of near field measurements was performed in collaboration with Professor Niek van Hulst, at ICFO[‡]. Here, a home-made SNOM with an interferometric branch was used [10], which is a unique capability. Samples fabricated following the first process described in the previous chapter were used.

Figure 151 (a) shows a scheme of the experimental set-up. The light was launched into the grooves at one of the ends. An aluminium coated fiber tip with an aperture of ~ 90 nm was used to scan the surface and pick-up the near optical field. The fiber probe was kept at a constant distance (~10 nm) of the surface by a feedback mechanism (shear force).

Characterizations with this SNOM were particularly interesting, as it allowed interferometric measurements. To retrieve direct information on light propagation and interaction with the surface, the collected light was mixed with a reference beam in a *heterodyne*[§] interferometric arrangement. This way, the interference between the two branches was obtained yielding to amplitude and phase mapping of the local field (Figure 151 (b) and (c), respectively).

[‡] Nano Photonics Group. Institut de Ciencies Fotoniques (ICFO) - 08860 Castelldefels (Barcelona), Spain.

[§] Heterodyne detection: non-linear mixing with radiation of a reference frequency.

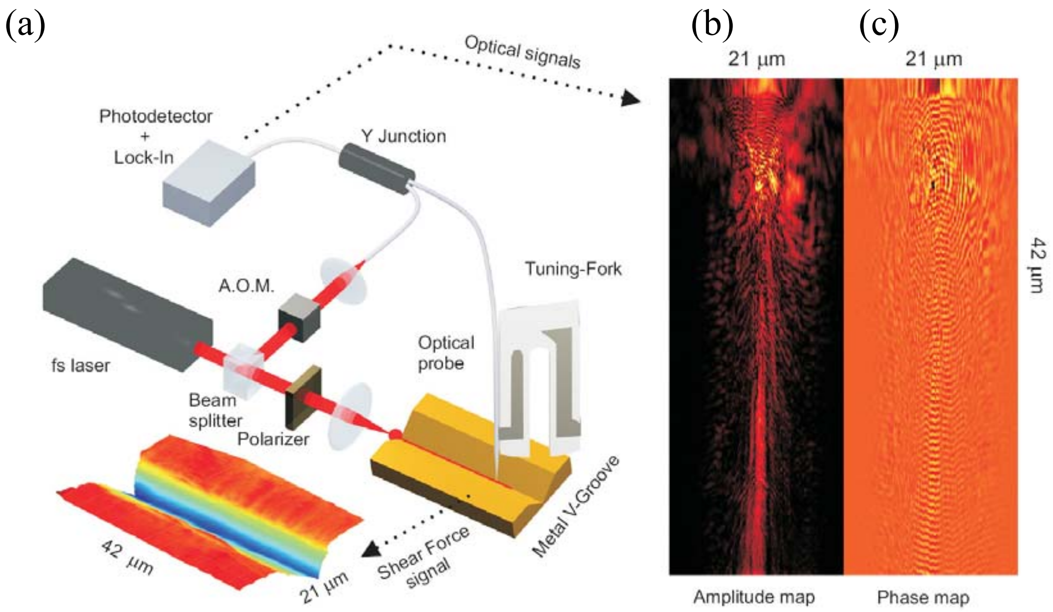

Figure 151. (a) Configuration of the SNOM used at ICFO. The incident fs pulse is divided in two parts. One part is coupled into the guiding V-groove with an end-fire configuration to launch the SPP. The other part is shifted in frequency and forms the reference branch. The two signals are coupled together and the resulting interference signal detected by a photodiode and demodulated by a Lock-In Amplifier, reveals both amplitude (b) and phase (c) of the light inside the structures. [11]

Figure 152 shows an example of the topographical image: top view in (a), 3D view in (b). The corresponding optical intensity is shown in (c), obtained for one of the samples, 4 µm wide, 2.8 µm deep, with an apex angle of 70º, by exciting the V-groove with a red laser. By overlapping both profiles (Figure 152(d)), it can be seen that the optical intensity was confined mainly inside the V-groove. The grooves width and depth were in the micron range, what made difficult the shear-force feedback system to follow fast and precisely the topography inside the groove. This was one of the major difficulties encountered for characterization.

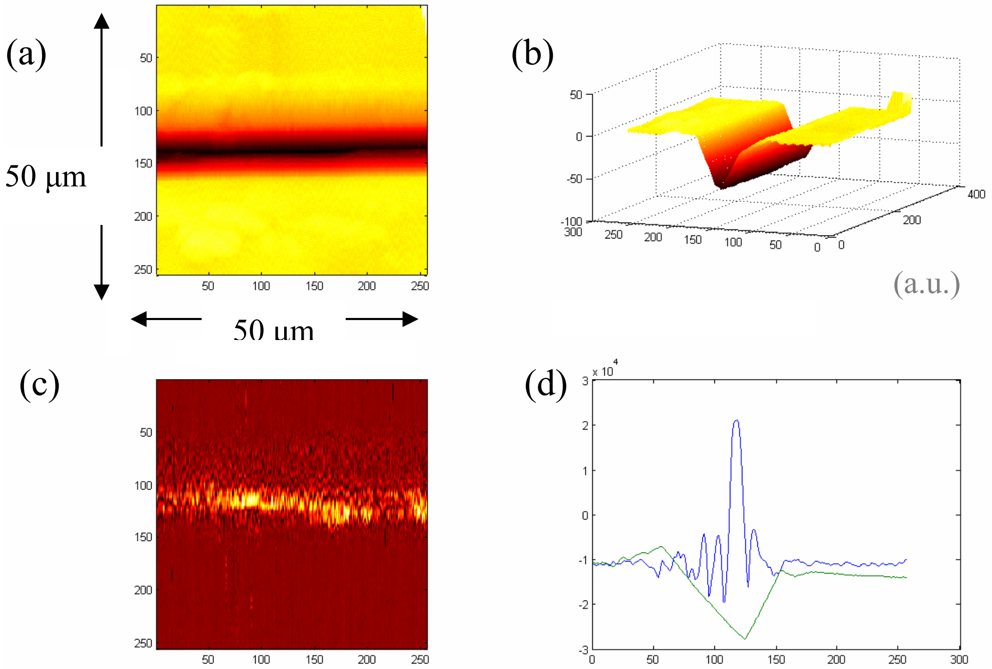

Figure 152. Results of the SNOM characterizations: (a) and (b) correspond to the topography of the V-groove, obtained by the shear-force signal. (c) corresponds to the optical amplitude, that propagates inside the groove, as can be deduced by comparing the profiles of the topography and the optical intensities (d).

The second challenge encountered was controlling the in-coupling of the light into the grooves. Two different arrangements were used for the in-coupling of the light: by end-fire configuration and through a prism (Figure 153) placed below the sample.

For the second experimental set up, an index matching oil was used to fill the possible discontinuities or air gaps between the bottom of the sample and the prism surface, as shown in the drawing of Figure 153. By focusing the laser beam below the sample, plasmon-polaritons in the Ormocomp/gold interface would be excited, and these, would excite the CPPs in the opposite side of the metal layer (in the gold/air interface). The problem in this case was that the gold layer was too thick, hindering the excitation of the CPPs on the gold/air interface (the samples were specifically designed to prevent this effects, as described in the previous chapter).

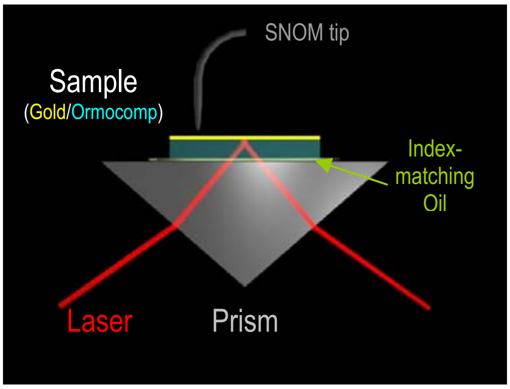

Figure 153. In-coupling of the light thorough a prism. An index-matching oil is used in-between the sample and the prism surface.

Nevertheless, the samples used were those obtained with the first process flow and the punctual defects or small cracks in the gold layer were enough to allow the excitation of the CPPs inside the V-grooves at the gold-air interface.

Figure 154 shows the phase maps images, with the profiles of the shear force (blue) and the optical intensity (red) for a sample, 8 µm wide, 5.7 µm deep. Two different wavelengths were used: 633nm (a) and 580nm (b). For shorter wavelengths, it seems that more than one mode appears to propagate and interfere inside the V-groove.

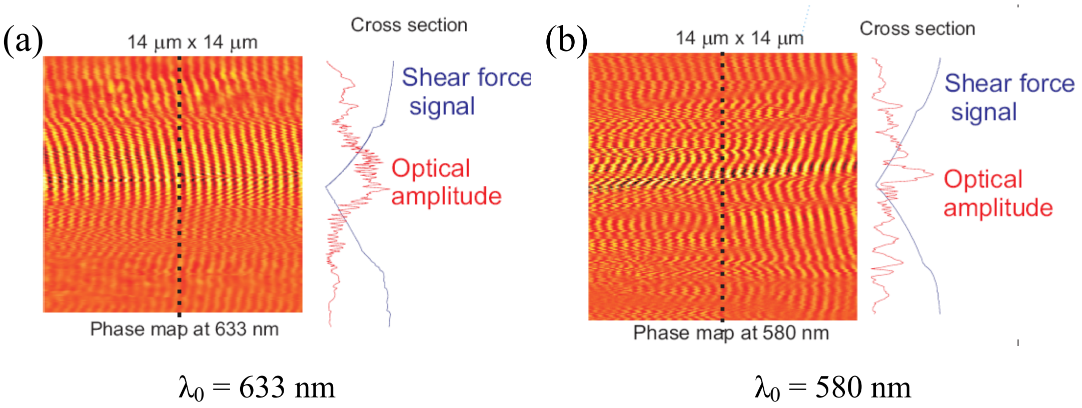

Figure 154. Phase SNOM images obtained for two different wavelengths in the same V-groove: 633nm in (a) and 580nm in (b). The shear force signal and the optical amplitude are also shown for each one.

By tunning the wavelength of the incident light and by measuring the phase propagation in the different regions of the sample (flat surface, wedges, and inside the V-groove), the dispersion relation can be obtained. Figure 155 (a) and (b) shows the preliminary results of the dispersion relation for SPPs and CPPs. In (b), a representation of what could be called the "effective index" (λ_0/λ) is plotted as a function of the incident wavelength. The line corresponding to air ($\lambda_0/\lambda=1$) is, as expected, below those obtained from the dispersion curve obtained in the flat gold surface outside the V-groove, and inside the V-groove. This last one is slightly higher, which means a higher confinement of the light compared to light couplet to the flat surface.

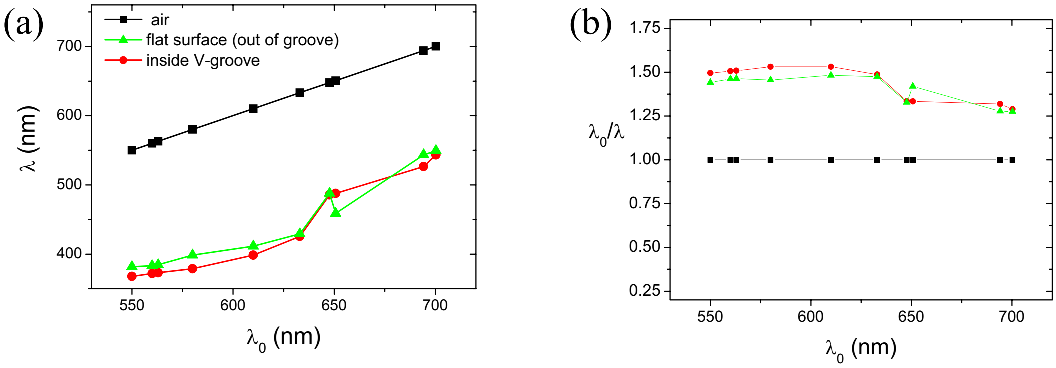

Figure 155. Dispersion relation (a) for light travelling at free-space (black line), bounded to the flat surface outside the channel (green line) and inside the V-groove (red line). In (b), λ_0/λ has been plotted as a function of λ_0, what could be a measure of the effective index for the light coupled in the different situations: free surface, flat surface and V-groove.

Again, SNOM characterizations demonstrated that the near optical field was bounded to the V-grooves. It exhibited propagation characteristics different from the SPPs, leading to the conclusion that CPP modes were effectively confined and propagated along the V-grooves.

7.2.- FAR FIELD

Far field studies are much simpler than SNOM characterizations, as a conventional optical bench is enough. Qualitative complementary information to the near field images can be obtained.

7.2-1. Experimental Set up

The experimental set up used to obtain far field images was located at COM[**] (DTU). It is shown in the scheme in Figure 156 and in the photographs of Figure 157 (a). The light (coming from different sources, e.g. an infrared laser, or a broad band source) is polarized and launched into a polarization-maintaining fiber. The sample is mounted into a holder below an optical microscope, that facilitated the coupling of the light into the V-grooves (Figure 157 (b) and (c)). To observe the front output images, an objective is placed at the other side of the sample, to focus the images to a camera, connected to a computer to records them. The input fiber, the sample and the objective are all mounted onto independent stages with micromanipulators, so they can be moved and focused individually.

[**] COM - *now* DTU-Fotonik. 2800 Kogens Lyngby (Denmark).

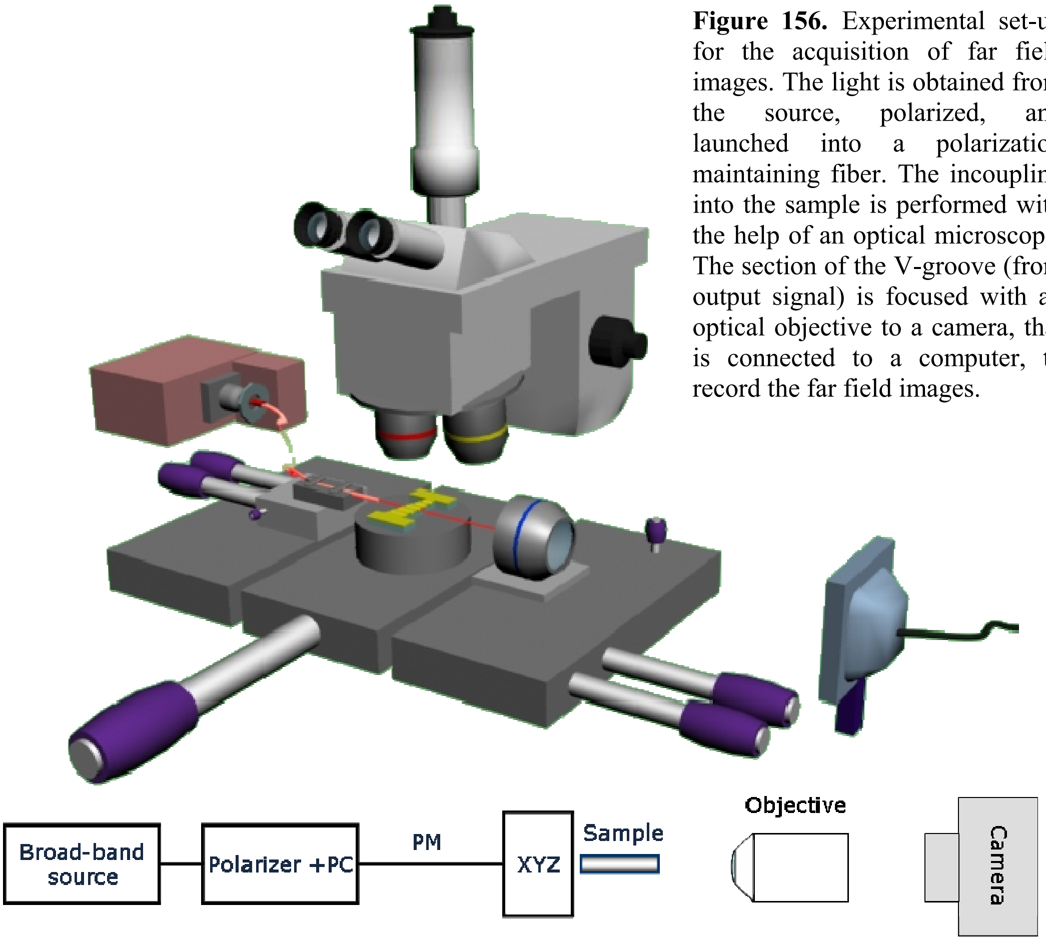

Figure 156. Experimental set-up for the acquisition of far field images. The light is obtained from the source, polarized, and launched into a polarization maintaining fiber. The incoupling into the sample is performed with the help of an optical microscope. The section of the V-groove (front output signal) is focused with an optical objective to a camera, that is connected to a computer, to record the far field images.

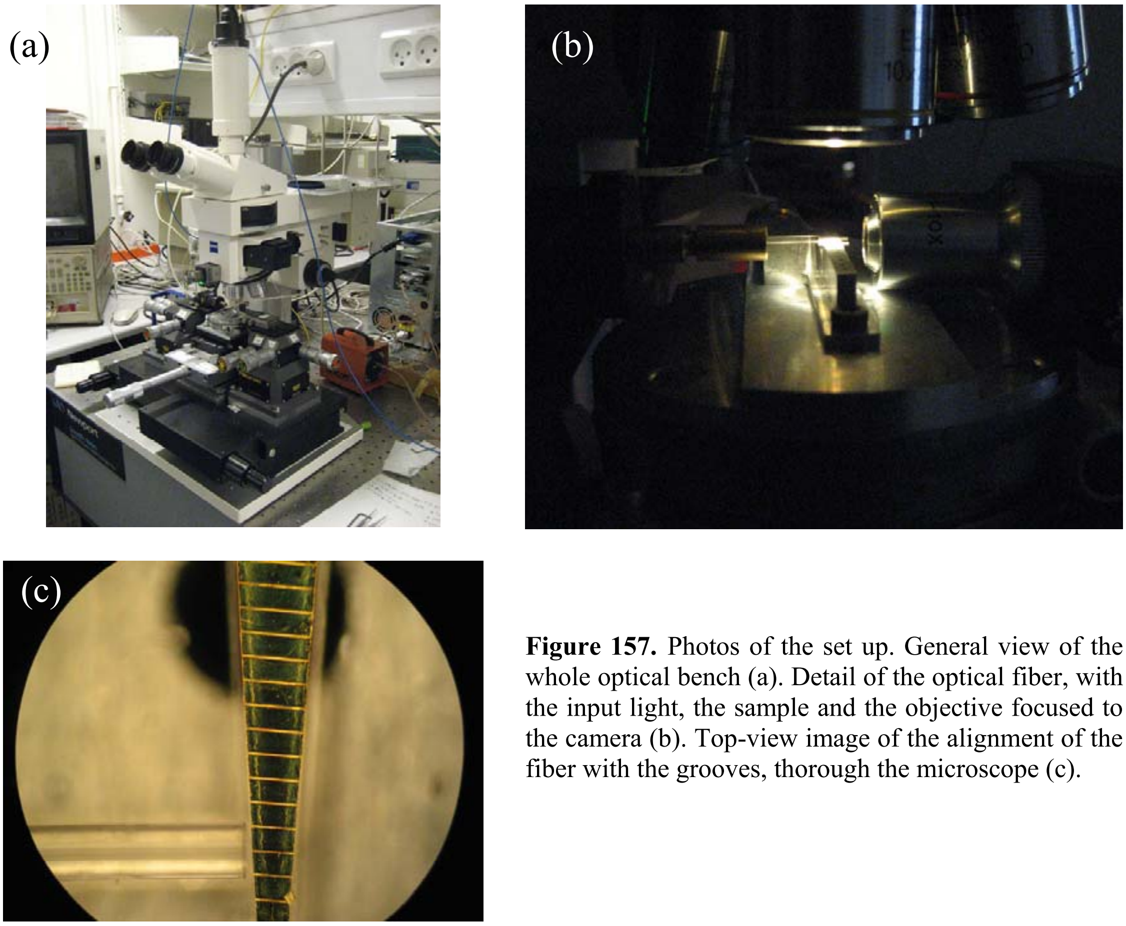

Figure 157. Photos of the set up. General view of the whole optical bench (a). Detail of the optical fiber, with the input light, the sample and the objective focused to the camera (b). Top-view image of the alignment of the fiber with the grooves, thorough the microscope (c).

7.2-2. *Front* Far field images

Figure 158 (right column) shows *front* far field images, as recorded with the camera. Drawings of the different experimental configurations are shown in the left column of the figure, to facilitate the visualization and the description of the set-ups.

Figure 158 (a) corresponds to the light coming out directly from the **fiber at air** (i.e., with no sample in the stage). Its approximate diameter was 5 µm.

Figure 158 (b) and (c) show the scattering of the light by a **flat surface**. The top area corresponds to air, the bottom to the Ormocomp substrate, and the flat part in the middle of the images, to the gold layer. In the small inset, the sample surface has been outlined with a dashed yellow line. These images were obtained by placing the fiber in-between two grooves (schematic drawing on the left). In this case, when the polarization of the incident light was changed, no difference was observed between the images: (b) for TM and (c) for TE polarization.

Figure 158 (d) and (e) shows the output images when the light was launched **into a V-groove**. In this case, the interaction of the light with the structures is more complex. SPPs and CPPs do not radiate free light expontaneously, in the same way that they cannot be excited just by focusing the photon-beam to the metal surface (there is a momentum miss-matching, as has already been described previously). Nevertheless, at the edge of the V-grooves they can become radiative (same case as the end-fire for the in-coupling configuration). Thus, in the experimental set-up that we used, the propagation distance (δ_{CPP}) and the length of the groove played an important role. If the CPP mode propagated long enough so the fields arrived to the other side of the groove, then the far field images picked up the radiated free-light. Figure 158 (d) shows an example: a bright spot appears inside the groove. If the groove was too long compared to the corresponding δ_{CPP}, the mode vanished completely along the groove, so it appeared as a dark area in the images. In the case that they did not sustain CPPs confinement (under certain conditions), then there was no difference in the far field signal between the air onto the flat surface and the air in the groove, as shown in Figure 158 (e): no confinement can be observed. The small insets in the figures (d) and (e) show the same images, with the V-groove profile marked with a yellow dashed line, to facilitate the interpretation.

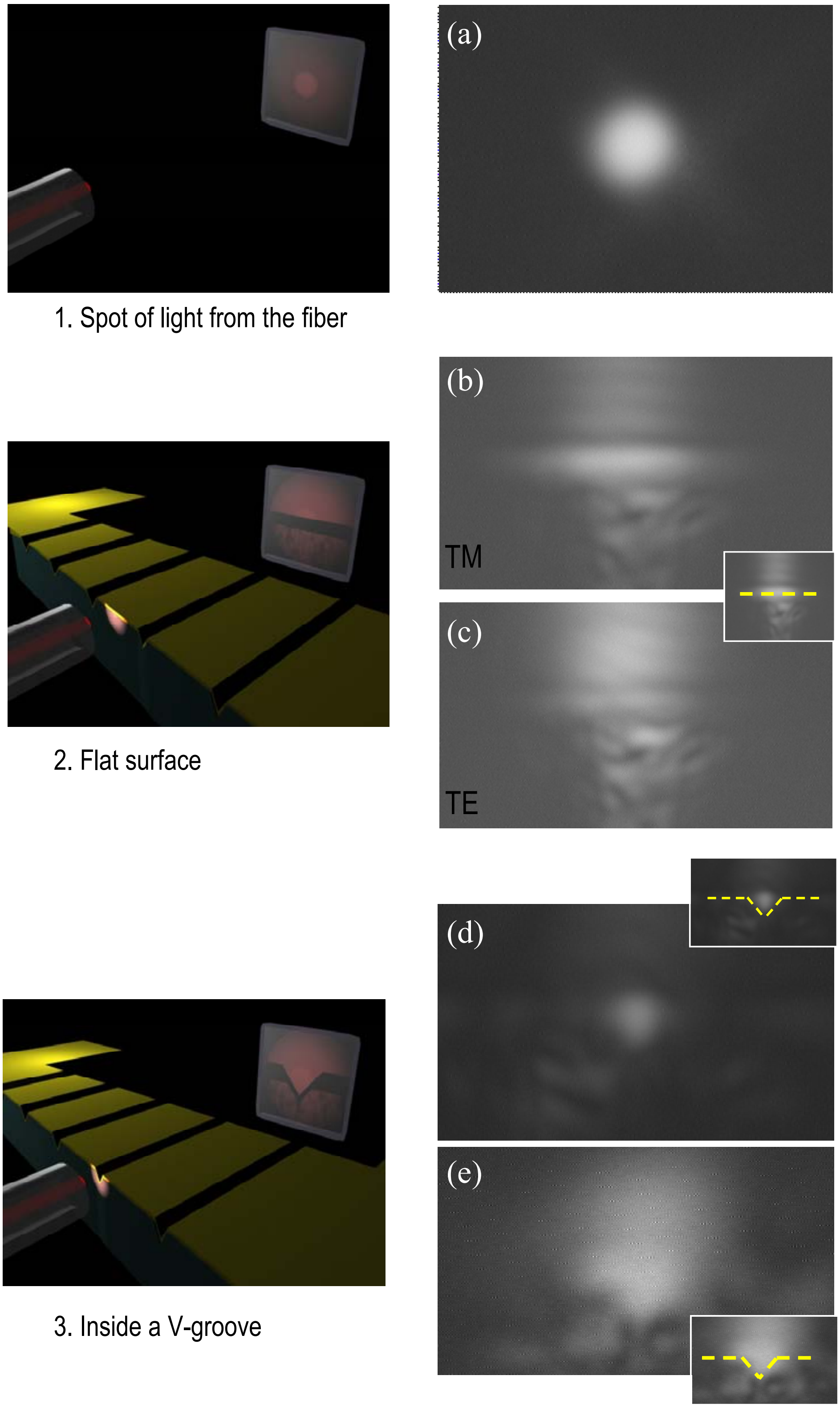

1. Spot of light from the fiber

2. Flat surface

3. Inside a V-groove

Figure 158. Front Far field images: drawings of the experimental configurations (left) and front far field images (right). (a), corresponds to the output of the fiber (no sample). (b) and (c) corresponds to the illumination of a flat surface, for two different polarizations. (d) and (e) corresponds to the light launched into a V-groove, for two cases: when a CPP mode is excited and when it is not in (d) and (e) respectively. The insets show the same images, with the surface or the groove profile marked with a yellow dashed line.

The excitation (or not) of CPPs in the groove could be also sustained by the **dependence** (or not) **on the polarization** of the incident light.

Figure 159 shows the excitation of different modes depending on the polarization for a groove 6 μm wide, with an apex angle of 50º. For a monochromatic IR laser (λ_0 = 1.5 μm), well confined CPPs were excited with TE polarization (Figure 159(a)). For the perpendicular polarization (TM), the light was squeezed out of the groove, and travelled near the wedges, as WPP modes (Figure 159(b)). The propagation distance of WPPs, δ_{WPP}, is longer than δ_{CPP}, as the confinement in the wedges is weaker, as was illustrated in Chapter 5. Thus, for sufficiently long grooves, the CPPs were not observed anymore, and only WPPs appeared in the far field images. This "critical" length was ~ 180 μm, which is in good concordance with the propagation length, δ_{CPP}, calculated from the SNOM images (δ_{CPP} =140 μm).

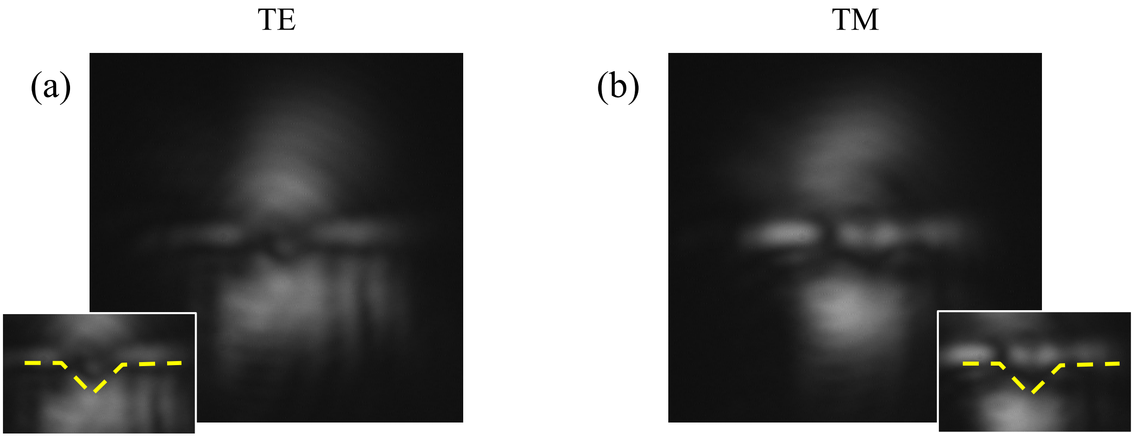

Figure 159. Dependence of the modes excitation on the polarization. For TE polarization (a), CPPs are excited and propagate inside the V-grooves. For TM polarization (b) the modes are squeezed out and WPP are excited. The insets show the same images, with the groove profile marked with a yellow dashed line.

For a visible broadband source, the propagation appeared to be mainly in the wedges. The **WPP modes** could be observed even for the longest grooves (~ 350 μm long). Figure 160 shows how, by varying the polarization, the WPPs coupled to the left and the right wedges were excited.

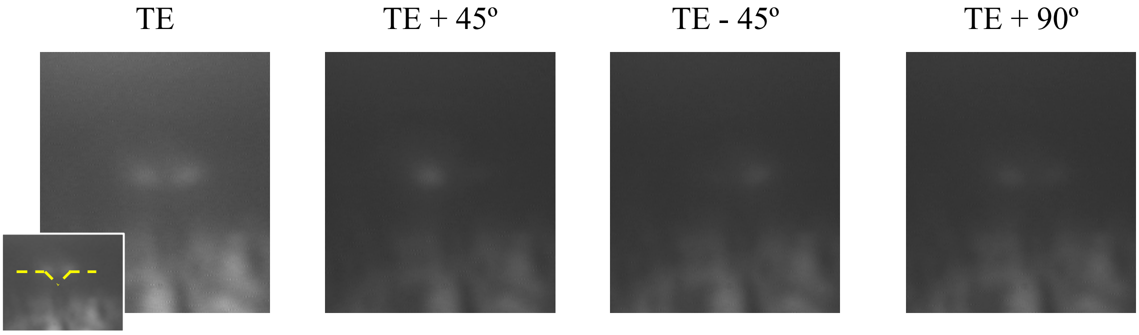

Sample 4 (beads) - Groove 24 (detailed) -> Broadband source (d1)

Figure 160. Polarization dependence for the WPPs. As the polarization of the light is twisted, the light is bounded to one or to the other wedge of the V-groove.

No propagation of bounded modes (CPPs or WPPs) was observed for the smallest grooves (~ 2 µm deep) or for the largest ones (~ 8 µm deep) for IR wavelengths. In the grooves with a larger apex angle (70º) only the WPPs appeared to be excited.

Thus, *front* far field images were useful to make an estimation of the optimal conditions for CPP confinement and propagation (geometry, λ_0, polarization), and to observe the modes and their shapes appearing under different excitation conditions.

The modal shapes are important, with a view to the possible applications of the devices. For their use in bio-sensing, and/or as micro-fluidic channels based devices, the propagation inside the V-grooves is much more interesting than WPPs excitation. In the first case, the bio-elements placed inside the grooves change CPPs propagation properties, and the differences in the excitation/absorption could be measured. In the last case, further considerations should be taken into account, as the refractive index inside the V-groove, due to the liquid filling, would change with respect to air.

7.3.- FLUORESCENT BEADS

We used fluorescent beads to see whether the excitation of fluorescent nanoparticles with confined near field was possible, and to characterize the propagation in V-grooves filled with a dielectric material different from air. For this purpose, two different approaches were considered: (i) filling the grooves with very small beads with a diameter ϕ = 100 nm ($\phi << \lambda_0$), and (ii) with micrometric size beads (ϕ = 1 – 3 µm).

By filling the grooves with a fluorescent material, the propagation can be studied with a conventional optical microscope, as it converts the near field into far field. This is the first experimental report on filled V-grooves, as SNOM measurements are complex or even not possible if the groove is not empty. On the other hand, micrometric size beads can be individually illuminated and observed, what opens a way to use these devices for sensing or biosensing.

7.3-1. Nanometric size beads: propagation in a gold/dielectric V-groove

Fluorescent polystyrene nanometric size (ϕ = 100 nm) beads[††] were deposited inside the V-grooves. For this, the liquid with the suspended nanoparticles was dropped onto the surface (Figure 161 (a)). Then, the droplet was directionally dried, and the beads filled the V-grooves by capillarity, as can be seen in the schemes of Figure 161 and in the SEM images of Figure 162 (b).

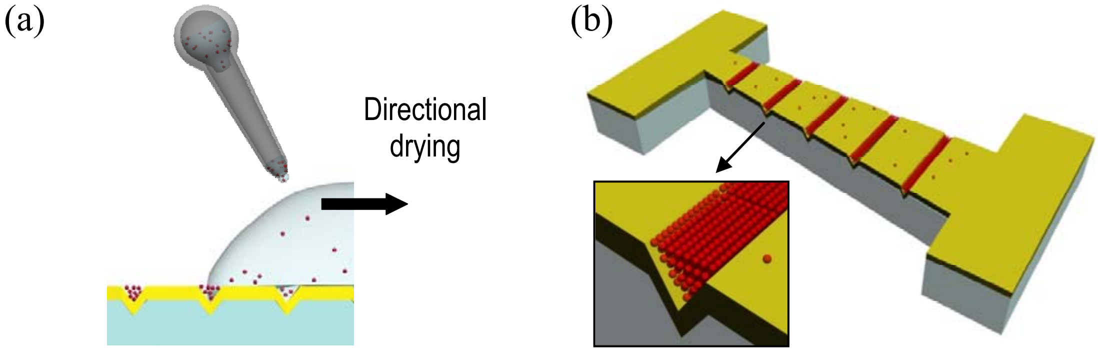

Figure 161. (a) Deposition scheme. A drop of the suspension containing the nanoparticles is deposited onto the surface, and directionally dried, so the beads fill the grooves by capillarity. (b) Drawing of the result: for high concentrations of the solution, the beads completely fill the V-grooves.

[††] Polystyrene spheres (n=1.55), 100nm diameter. Excitation maxima: 542 nm (green). Emission maxima: 612 nm (red). From Duke Scientific.

Fluorescence images (overall illumination), like those shown in Figure 162 (a) and Figure 163 (b) revealed a uniform distribution of the beads along some of the grooves.

Some particles remained onto the surface of the sample, outside the grooves, as can be also observed in the images. This did not affect the experiments, as the studies were performed by local excitation, and the propagation of the channel modes took place inside the V-grooves.

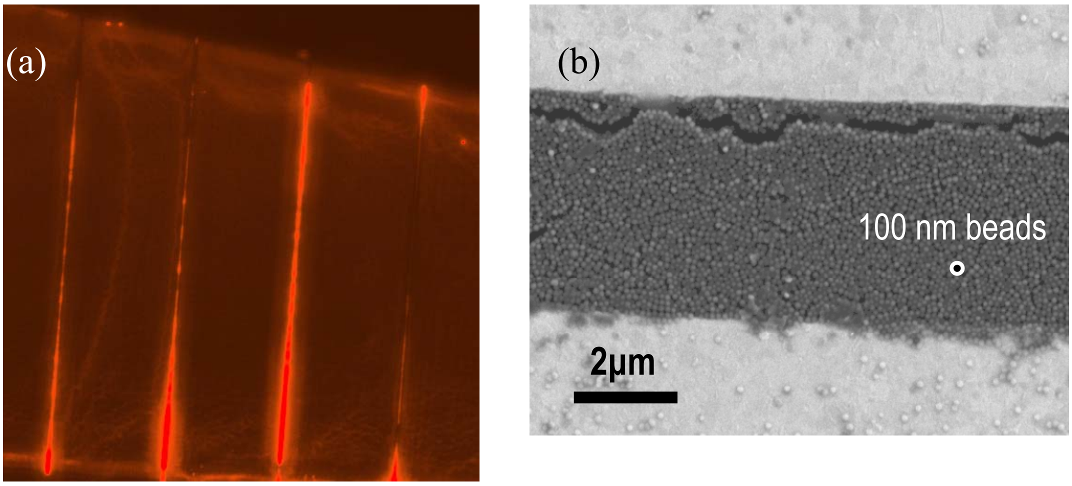

Figure 162. (a), Fluorescence image (over-all illumination) of a sample, where most of the V-grooves are filled with the red nanometric fluorescent beads. (b) High magnification SEM image where the nanometric beads filling the groove can be observed.

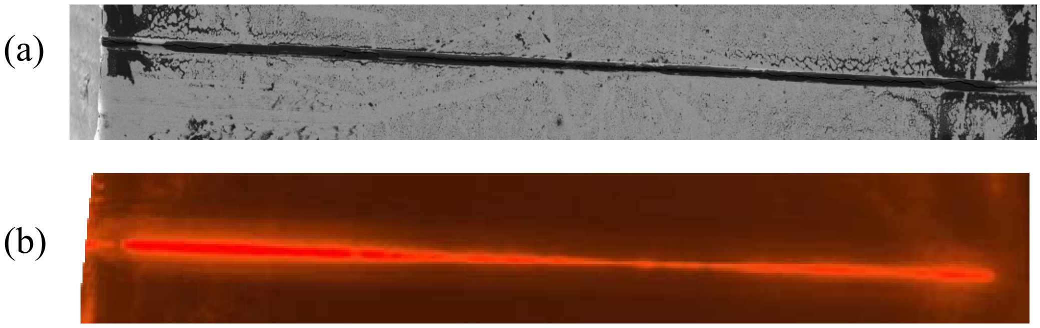

Figure 163. SEM (a) and fluorescence (overall illumination).(b) images of a groove, filled with beads. The homogeneous distribution of the beads can be deduced from both images.

As the diameter of the beads was smaller than the optical wavelengths used ($\lambda_0 >> \phi$), for our practical purposes it could be considered that the grooves were filled with a continuous dielectric media. To calculate the volume occupied by the nanoparticles, we considered a squared volume full-filled with spheres. This simple calculation leaded to an 80% of the volume occupied by latex nanospheres. Thus, the media experienced by the light inside the filled channels could be treated as a continuum, approximated as a ponderated mix of air (20 %) and polystyrene (80%). The dielectric constant resulting to describe this hybrid material is **$\varepsilon_d = 2.2$.**

After filling the V-grooves, the excitation of CPPs was done by locally illuminating one end of the V-grooves, with the fiber tilted with respect to the sample (to minimize the direct lightening of the beads) as it is shown in the drawings of Figure 164(a). The *top* view images were obtained with a camera coupled to a conventional optical microscope using adequate filters, so only the red (fluorescent) light was recorded.

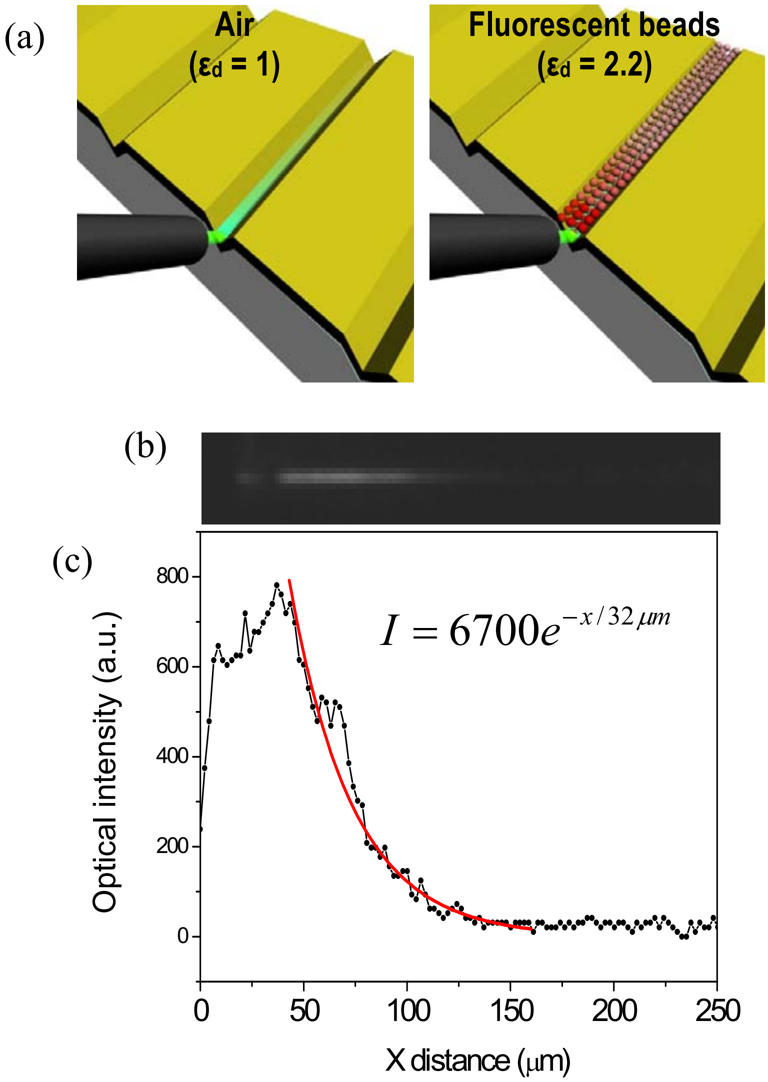

Figure 164. (a) schematic view of the experimental set-up: green light is launched in one end, with the sample tilted respect to the fiber. The beads convert the near field of the excited CPPs to far field, by luminescence. The beads form a compact structure, so the material can be described by εd= 2.2. (b), far field image of CPPs propagating a V-groove filled with beads. (c), optical intensity profile and exponential fit of (b), from where a propagation length of 32 μm is calculated.

Figure 164(b) shows the fluorescence image of a V-groove illuminated with a green laser (λ_0 = 532 nm) on the left side (light propagates rightwards). The graph in Figure 164(c) corresponds to the optical intensity profile along the V-groove averaged from (b), and its exponential fit. A propagation length **δ_{CPP} ≈ 32 μm** is obtained.

$$I = I_0 \cdot e^{-x/\delta_{CPP}} \longrightarrow I = 6700 \cdot e^{-x/32\mu m} \qquad (27)$$

The dependence on the polarization was studied using a broadband source in the visible range (Figure 165). A strong dependence was observed, and the maximum confinement occurred for TE polarization, as can be seen in Figure 165 (d). Unexpectedly, a propagation length of **δ_{CPP} ≈ 33 μm** was measured also for this white source, by fitting the optical intensities.

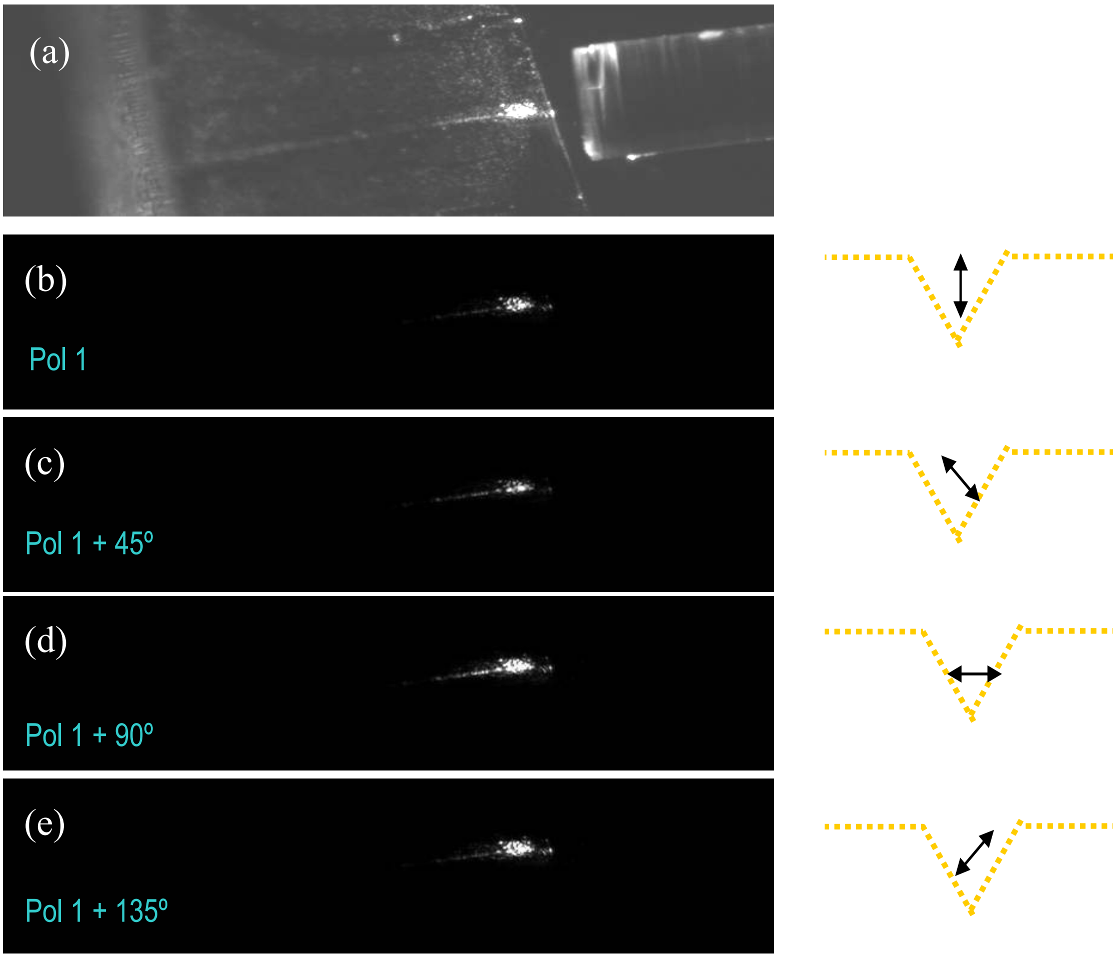

Figure 165. Dependence on the polarization. Ambient illumination image (a), where the fiber, the groove and the light spot can be seen. (b), (c), (d) and (e) correspond to the same area, with local illumination (light outcoming only from the optical fiber), for different polarizations, as schematized on the drawings of the right.

A significant decrease of δ_{SPP} when increasing ε_d was expected and already predicted as a consequence of a stronger confinement in [12], where the properties of CPPs in a V-groove filled with a dielectric were modelled. But, during the analysis of the results obtained during this work, there were two observations that points to a complex mechanism of CPP propagation in this system.

The first one is that the δ_{CPP} observed for the CPPs excited with the green laser was longer than the calculated for surface plasmon polaritons excited in similar conditions: green laser (λ_0 = 532 nm), gold/beads interface (ε_d = 2.2, and ε_m = 23 - 2i) [13], that is **δ_{SPP} =23 µm** (green line in Figure 166 (a)).

$$\delta_{SPP} = \lambda_0 \frac{(\varepsilon'_m)^2}{2\pi\varepsilon''_m} \left(\frac{\varepsilon'_m + \varepsilon_d}{\varepsilon'_m \varepsilon_d} \right)^{3/2} \tag{28}$$

The second one is that the propagation length was the same for the visible broadband source and for the green laser, which is counterintuitive, as the propagation length strongly depends on the incident λ_0.

The light re-emitted by the beads has a wavelength of 612 nm, what is below the minimum needed to directly excite other beads, but that can create new CPPs in the V-grooves. Surface Plasmon Polaritons (SPPs) excited at conditions identical to those in our experiments (red light, gold/beads interface) have a theoretical wavelength of λ_{SPP} = 417 nm, that can be absorbed by the spheres, and that propagate along a theoretical distance of **δ_{SPP} =38 µm** (red line in Figure 166 (a)).

$$\lambda_{SPP} = \lambda_0 \sqrt{\frac{\varepsilon_d + \varepsilon'_m}{\varepsilon_d \varepsilon'_m}} \tag{29}$$

This value is not in disagreement with the experimental observations, and explains the fact that the propagation length is similar for different sources. Thus, the fluorescent beads are acting as a frequency converser for the CPPs propagating in the grooves. Hakala et. al. [14] have very recently reported a high conversion ratio of SPPs by organic molecules on a silver surface. Figure 166 (b) shows a scheme that summarizes our vision of the mechanism of propagation of CPPs in V-grooves filled with nanometric latex red beads: The green laser excites CPPs. These CPPs excite the fluorescent beads, that radiate red light. This red light is also exciting CPPs, that propagate along the V-groove, with a propagation length ~ **δ_{SPP} =30 µm,** as determined from far field characterizations.

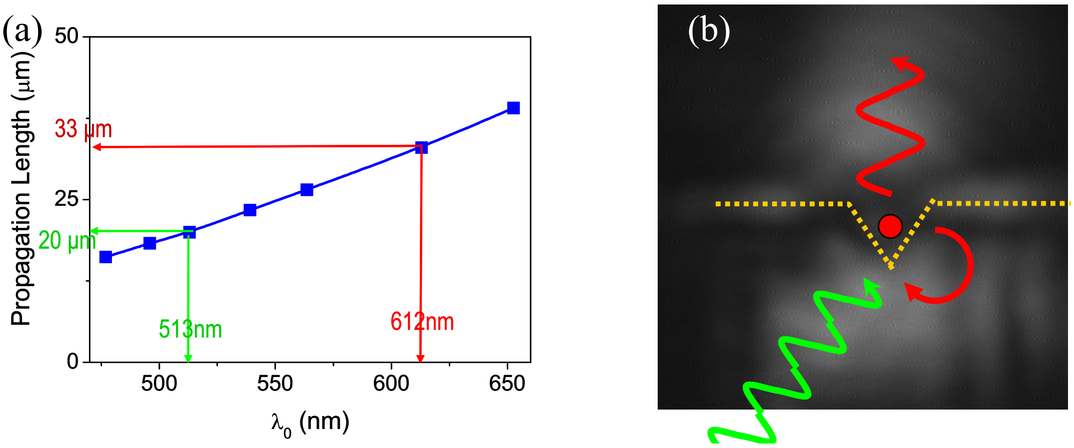

Figure 166. (a) Propagation lengths for SPPs, as already described in chapter 5, for a gold/ε_d=2.2 interface, where those corresponding to red and green excitations have been outlined. (b) Porpagation mechanism: the green laser excites CPPs. These, excite the beads, that radiate red light. This red light excites new CPPs, that can also excite the fluorescent beads. The radiated light can also be seen with a conventional optical microscope.

7.3-2. Micrometric size beads: individual visualization

Micrometer size beads (1–3 µm diameter, red fluorescence) were also deposited inside the grooves, following the same procedure as described above. When deposited in low concentrations, they could be individually observed.

The use of micrometric size beads for individual visualization, and not of nanometric ones, attends to two main reasons:

1. The microscope used in this work has only two optical objectives, corresponding to big magnifications (2x, 5x), as it is commonly used to visualize wide working areas. So, one individual fluorescent bead, 100nm diameter, would hardly be observed. But, if needed, more objectives that allow higher magnifications could be installed.
2. The second reason is the nanoparticles deposition. Diluted solutions of the liquid containing the micrometric beads allow obtaining low concentrations, and individual placing, as shown in the images. This is more difficult for the nanometric spheres, as they tend to agglomerate. Nevertheless, if needed, the deposition conditions could be optimized, so the beads would be deposited far enough one to the others, for individual excitation and visualization.

Figure 167 shows a fluorescence (overall illumination) of the beads deposited in one of the samples (a), a SEM image of them (b), and an optical image (ambient illumination) of the beads lying in the bottom of the groove (c), where their red colour is observed.

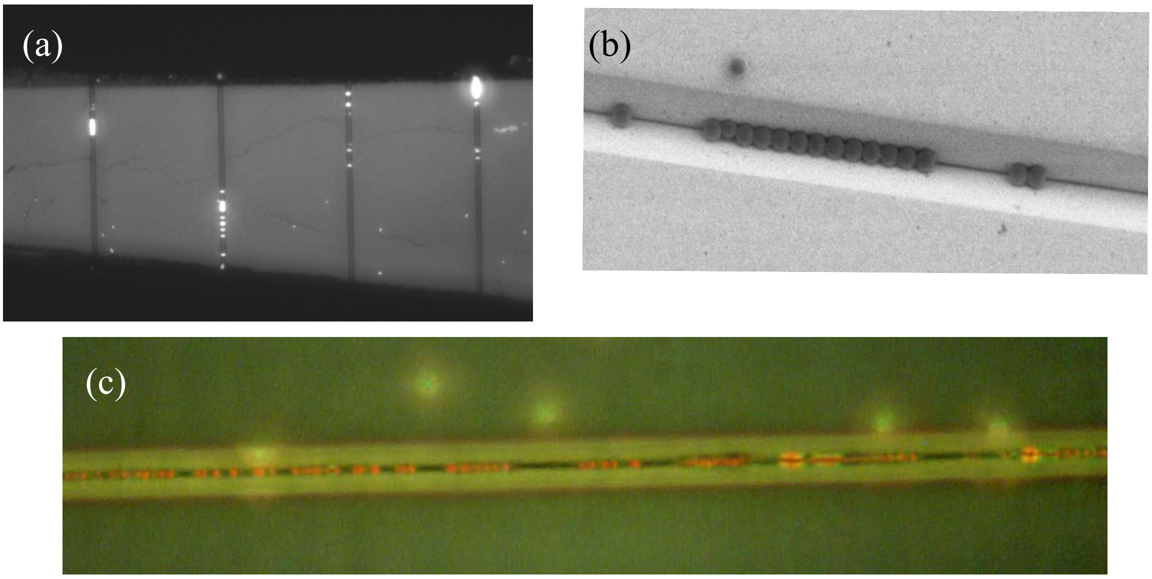

Figure 167. Fluorescent image (overall illumination) (a), SEM image (b) and optical image (c) of the micrometric beads (1µm diameter) lying in the bottom of the V-groove.

Figure 168 shows an image with ambient illumination (a), and the corresponding fluorescence non-filtered images (b) and (c), showing the possibility of individual lightening. The beads were ~95 µm far from the incident spot which was just in the limit of the propagation length (δ_{SPP} = 140 µm, as determined for these samples by SNOM measurements). At these conditions, just by changing the intensity of input signal, the number of beads that were lighted up could be controlled, as it can be seen by comparing in Figure 168 (b) and (c). If the intensity was increased (the illuminated area, corresponding to the incident spot was larger), one or two beads were lighted-up.

This is the first step for the use of the V-groove-based waveguides for (bio)sensing applications.

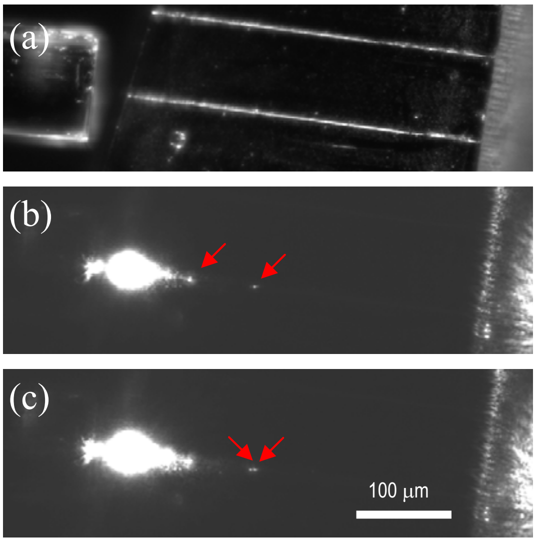

Figure 168. (a), topography of a sample, where the fiber and the waveguides can be seen. Micrometric red fluorescent beads have been deposited inside the V-grooves (SEM image in the inset). (b), (c), fluorescence images (non filtered), with individually lighted beads.

Thus, manipulation, excitation and observation of individual nanometric size beads leaves an open work, very interesting for future applications.

By using fluorescent beads, we were able to demonstrate and characterize the propagation of CPPs in V-grooves, with no need of a SNOM. The possibility of individual illumination of the beads by means of the light confined in the grooves opens the possibility of using these devices for sensing.

7.4.- FUTURE WORK: BIOSENSING

The ability of local excitation of CPPs and of light propagation inside sub-μ channels opens new possibilities that can be exploited for biosensing. Surface Plasmon Resonance (SPR) is a well known technique, that allows measuring changes in the refractive index in the vicinity of a metal surface. The geometry of the fabricated devices (integrated V-grooves with deep channels) allows to easily perform fiber-to-fiber measurements, thus, exploiting the high sensitivity of SPR, that would be probably higher when using coupled modes. For this, several possibilities may be studied, by filling the V-groves. In Figure 169, some ideas are proposed: using the V-grooves as micro/nano fluidic channels, studying cell interactions with the surface, or even resolving the vertical configuration of a media made of different liquids or having different compositions.

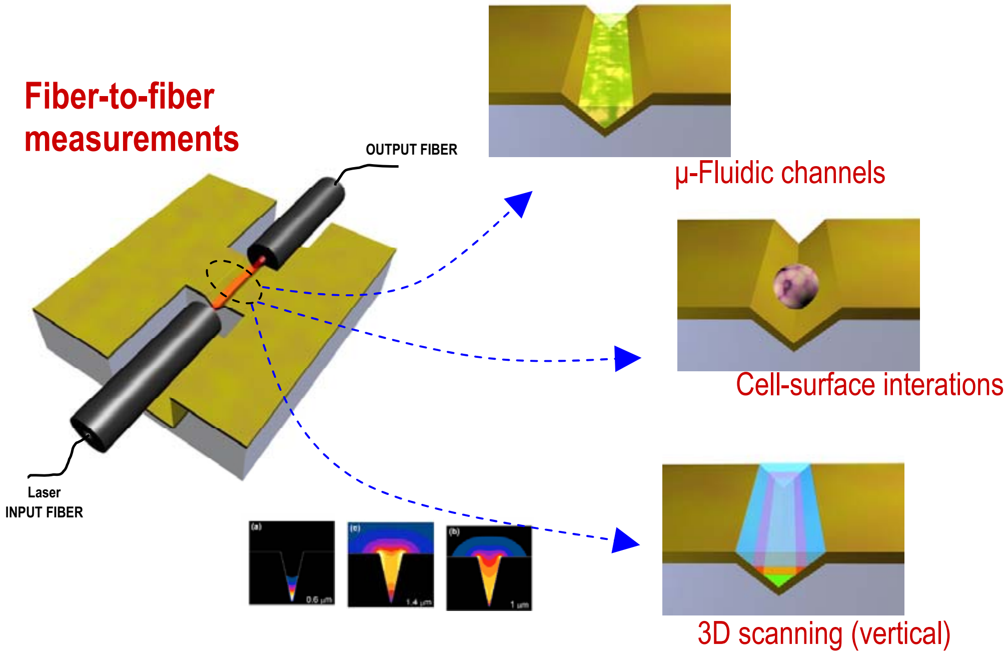

Figure 169. Schematic drawing of the possible use of the plasmonic devices for sensing and biosensing applications. Taking advantage of the integrated configuration, fiber to fiber measurements are easy. For this, the dependence of the transmitted light, or on the absorbed frequencies to excite plasmons, at different depths can be exploited for their utilization as microfluidic channels, to locally study the interaction of cells with the substrate, or to do verticall scanning of materials with different viscosities or refractive index, by tunning the incident wavelength.

7.5.- REFERENCES

[1] Balistreri, M.L.M., Gersen, H., Korterik, J.P., Kuipers, L. and van Hulst, N.F.,
Tracking Femtosecond Laser Pulses in Space and Time.
Science, 2001. **294**(5544): p. 1080-1082.

[2] Futamata, M. and Bruckbauer, A.,
ATR-SNOM-Raman spectroscopy.
Chemical Physics Letters, 2001. **341**(5-6): p. 425-430.

[3] Taminiau, H., Stefani, F.D., Segerink, F.B. and van Hulst, N.F.,
Optical antennas direct single-molecule emission.
Nature Photonics, 2008. **2**: p. 234-237.

[4] Maier, S.A.,
Excitation of Surface Plasmon Polaritons at Planar Interfaces,
in *Plasmonics: Fundamentals and Applications*, S. US, Editor. 2007. p. 39-52.

[5] Bozhevolnyi, S.I., Volkov, V.S., Devaux, E. and Ebbesen, T.W.,
Channel plasmon-polariton guiding by subwavelength metal grooves.
Physical Review Letters, 2005. **95**(4).

[6] Bozhevolnyi, S.I., Volkov, V.S., Devaux, E., Laluet, J.Y. and Ebbesen, T.W.,
Channel plasmon subwavelength waveguide components including interferometers and ring resonators.
Nature, 2006. **440**(7083): p. 508-511.

[7] Nielsen, R.B., Fernandez-Cuesta, I., Boltasseva, A., Volkov, V.S., Bozhevolnyi, S.I., et al.,
Channel plasmon polariton propagation in nanoimprinted V-groove waveguides.
Opt. Lett., 2008. **33**(23): p. 2800-2802.

[8] Fernandez-Cuesta, I., Nielsen, R.B., Boltasseva, A., Borrise, X., Perez-Murano, F., and Kristensen, A.,
V-groove plasmonic waveguides fabricated by nanoimprint lithography.
Journal of Vacuum Science & Technology B, 2007. **25**(6): p. 2649-2653.

[9] Volkov, V.S., Bozhevolnyi, S.I., Devaux, E. and Ebbesen, T.W.,
Compact gradual bends for channel plasmon polaritons.
Optics Express, 2006. **14**(10): p. 4494-4503.

[10] Balistreri, M.,
Coherent imaging of guided optical fields, in *Biomolecules and nanostructures*. 2000, University of Twente:
Promotor: Niek F. van Hulst.

[11] Heinis, D., Fernandez-Cuesta, I., Nielsen, R.B., Boltasseva, A., Pérez-Murano, F., et al.
Local probing of dispersion on guiding metal V-Grooves. in *Third International Conference on Surface Plasmon Photonics (SPP3)*. 2007. Dijon (France): Oral.

[12] Vernon, K.C., Gramotnev, D.K. and Pile, D.F.P.,
Channel plasmon-polariton modes in V grooves filled with dielectric.
Journal of Applied Physics, 2008. **103**(3).

[13] Barnes, W.L.,
Surface plasmon-polariton length scales: a route to sub-wavelength optics.
Journal of Optics a-Pure and Applied Optics, 2006. **8**(4): p. S87-S93.

[14] Hakala, T.K.,
Frequency conversion of propagating surface plasmon polaritons by organic molecules.
Applied Physics Letters, 2008. **93**(12).

Section 3

Interdigitated nanoElectrodes for (bio)sensing

"I have the pleasure of communicating to you, Sir, and through you to the Royal Society, some striking results at which I have arrived in pursuing my experiments on the electricity excited by the simple mutual contact of metals of different sorts..."

Discovery of the connection between chemistry and electricity

Alessandro Volta, 1793

The connection between chemistry and electricity is a very old one, going back to Alessandro Volta's discovery, in 1793, that electricity could be produced by placing two dissimilar metals on opposite sides of a moistened paper [1]. Since then, electrochemistry has become a useful tool that allowed the development of new types of sensors and biosensors.

Interdigitated electrodes have a very large panel of applications, running from organic devices to electrochemistry, and since more recently, to nano-biodetection. The high sensitivity exhibited relies on the electric field concentration in-between the digits. This becomes more remarkable when the electrodes dimensions are tailored for the recognition of an element of a given size, and especially when the dimensions are shrunk to the nanometric scale.

Interdigitated nanoElectrodes

In a generic way, an electrochemical sensor can be defined as a device able to detect changes in the activity of chemical species in a selective and reversible way, and quantify them by generating a proportional electrical analytical signal, susceptible of amplification and processing.

The oldest electrochemical sensors date back to the 1950s and were used for oxygen monitoring. More recently, as the Occupational Safety and Health Administration (OSHA) began requiring the monitoring of toxic and combustible gases in confined space applications, new and better electrochemical sensors have been developed. By the mid-1980s, miniaturized electrochemical sensors became available for detection of many different toxic gases, with the sensors exhibiting good sensitivity and selectivity. Currently, a variety of electrochemical sensors are being used extensively in many stationary and portable applications for personal safety. The physical size, geometry, selection of various components, and the construction of an electrochemical sensor usually depends on its intended use. Quite often, the final design results in a compromise between various performance parameters of the electrochemical sensor.

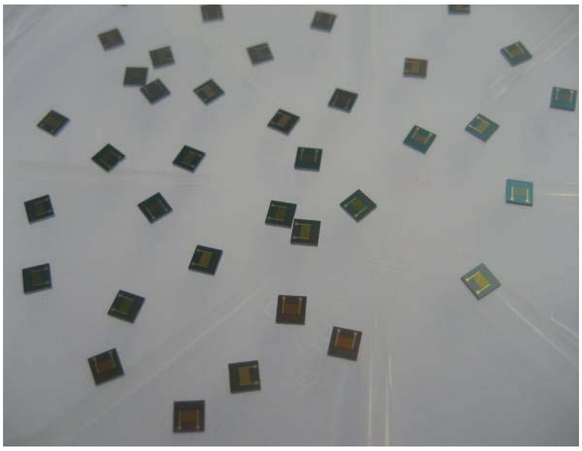

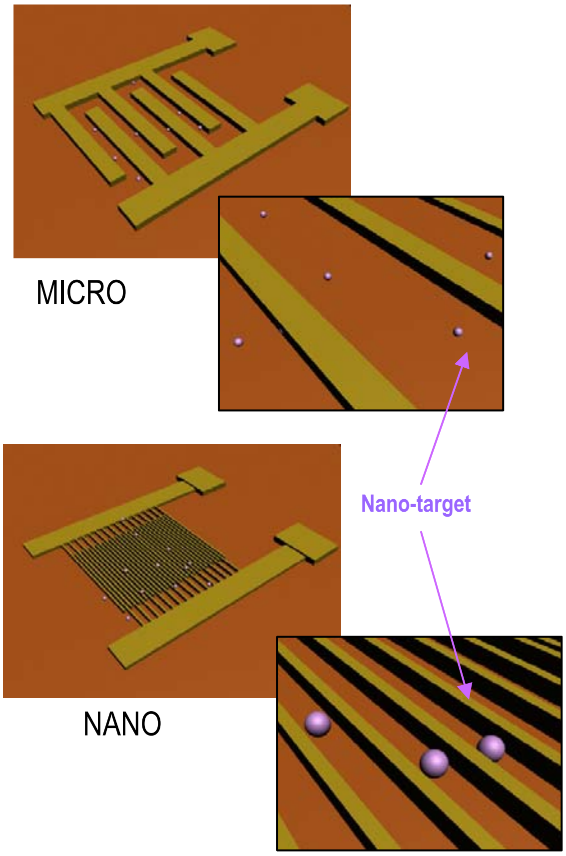

The combination of the **nanofabrication** capabilities and expertise with the knowledge about **electrochemistry** and **biosensing** of the GTQ group of CNM-IMB, opened new possibilities for exploring the new properties arising when shrinking the dimensions of the sensors to the nanoscale, in the framework of the project NILSIS.

In this section, the fabrication approaches developed for the fabrication of devices with nano-IDEs, and their characterization as electrochemical sensors and for impedimetric sensing. The detection of nanoparticles and DNA hybridization will be shown, as original applications.

Index of Section 3

Interdigitated nanoElectrodes for (bio)sensing

Chapter 8

Fabrication of Interdigitated nano electrodes (IDEs)

The fabrication of *complete devices* based on interdigitated electrodes with nanometric dimensions will be described in this chapter.

Three different approaches to define the mask in a resist onto the insulating substrate will be shown: a combination of optical lithography and electron-beam lithography, e-beam lithography alone, and nanoimprint lithography. Metallization and lift-off processes finish the fabrication of the chips with the metallic nanoIDEs, as will be described.

Also, the wire bonding and encapsulation steps will be described, what facilitates the connection of the chips to external equipments and enables working in liquid media.

8.1.- E-BEAM-BASED NANOFABRICATION PROCESS

By using electron beam lithography (EBL), the exposure strategies were optimized to fabricate with a high efficiency nanoelectrodes with lateral dimensions down to 80 nm, organized into interdigitated arrays of 250 nm pitch, extending over large areas.

Two generations of samples with different designs were developed. In the first one, the contacting pads were fabricated by optical lithography and the nanometric features, by EBL, using a modified SEM with e-beam capabilities. The second approach was developed afterwards, by using a new e-beam equipment (Raith 150 TWO) [2], so, by exploiting the possibilities for automatization of some processes of this machine, all the patterns (micro and nano) were defined by e-beam exposure.

8.1-1. First generation of devices

8.1-1:a.- Fabrication of the chips: Combination of EBL and Optical Lithography

Electron Beam Lithography is a commonly used tool to define features in the nanometric scale, but has some drawbacks for its use for the fabrication in larger (hundreds of microns) scales. In this work, the equipment used to fabricate the first generation of IDEs was a **LEO 1530 [3] modified with Raith capabilities** to perform e-beam writing (Figure 170).

Figure 170. Modified SEM: LEO 1530 with Raith electron-beam lithography capabilities, situated at CNM's cleanroom.

One of the problems of using a modified SEM without stitching capabilities is that the extension of the writing field is limited. The minimum size feature (maximum resolution) is directly related to the writing field. Thus, small lines cannot be effectively defined along large areas. For this reason, the areas of the first generation electrodes patterned with digits were restricted to few hundreds of microns (200 μm lateral size as maximum).

To minimize the fabrication time, and in order to increase the throughput and reliability of the process, the micrometric size patterns (i.e. the contacting pads) were first fabricated in parallel (wafer-scale) by **optical lithography**. Aligning marks were included in the design, to facilitate the posterior e-beam exposure. Figure 171 (a) shows the design of one of the chips, showing the contacting pads (blue) and the aligning marks (green), that were fabricated in the first lithographic step. Each single chip was 3 mm x 3 mm (standard size to be integrated later in PCB), and, as the area occupied by the IDEs was very small, two different sensors with different areas (100 x 100 μm^2 and 200 x 200 μm^2) were integrated in each chip. Two different configurations were fabricated, as shown in Figure 172. For both designs, two groups of aligning marks were necessary. The first ones were placed in the corners of the chip, for a rough align. The second ones were in the corners of areas where the digits should be written, to define the final writing fields. After the aligning step, the digits were defined by e-beam in the areas defined for this purpose (red lines in Figure 171 (b)).

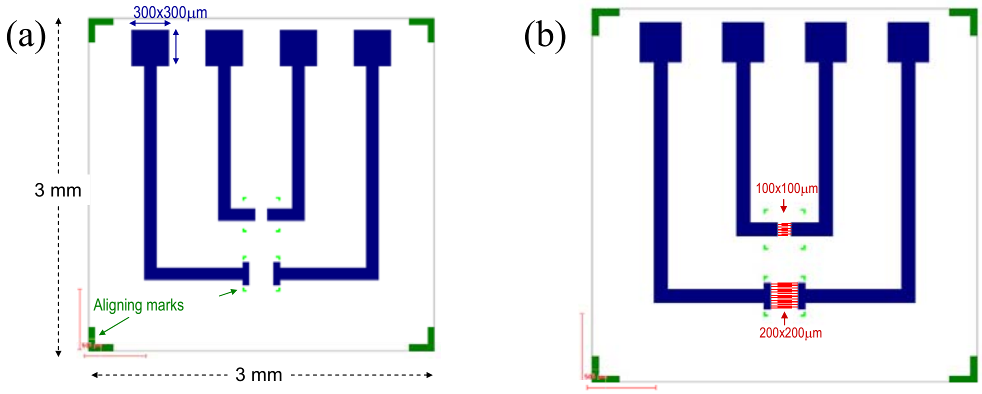

Optical Lithography

Electron Beam Lithography

Figure 171. GDS design of the patterns defined in each lithographic step: the micrometric contacting pads and aligning marks for the optical lithography step (a), and the nanometric digits, patterned by EBL, in-between the areas left for that purpose.

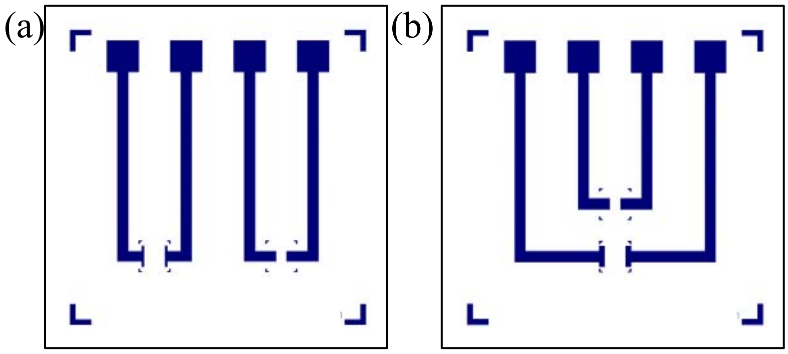

Figure 172. GDS design of two different configurations for the contacting pads distribution: symmetrical, so they have the same area in both sensors (a), and in a U-shape, so the sensing areas lie very close one to each other.

The details of the whole fabrication process are shown in the scheme of Figure 173:

Micrometric contacts and pads

a. 1.5 µm of SiO_2 are grown by thermal oxidation onto a silicon wafer.

b. The pads shape is defined with a conventional photolithography step (1.2 µm of a photo-sensitive resist, *HIPR6512*) onto the substrate.

c. A gold metal layer is deposited by sputtering (60 nm). To improve the adherence, a thin film of Titanium is previously deposited (8 nm).

d. A lift-off is performed (10 minutes in hot acetone, and 10 minutes in RT acetone with ultra sound agitation), to selectively remove the metal onto the resist. With this, the pads are finally defined.

Arrays of nano-electrodes

e. A thin film of PMMA (100nm) is spun onto the sample surface.

f. EBL is performed, defining the nanometric size digits between the contacting pads, in the areas left for this purpose, with the help of the aligning marks previously defined.

g. A thin metal layer is deposited by e-beam evaporation (15nm Au/8nm Ti).

h. After the lift-off, the nanometric digits, contacted to the pists and pads are defined in gold onto the insulating substrate.

a. Substrate (SiO_2/Si) b. Photolithography c. Sputtering (Au/Ti) d. Lift-off

e. Spin-coating of PMMA f. EBL g. Metal evaporation (Au/Ti) h. Lift-off

Figure 173. Fabrication process of the first generation of nanoIDEs. A thermal oxide (1.5 µm) layer is growth onto a silicon substrate (a). A photolithography step (b) followed by metallization of Au/Ti (60nm/8nm) (c) and a lift-off (d) is used to define the micrometric pads. The sample is spin-coated with 100 nm of PMMA (e), and the digits are patterned by EBL (f). Metal evaporation (Au/Ti, 15nm/8nm) (g) and lift-off (h) processes complete the fabrication of the nanoIDEs onto the insulating substrate (h).

The most critical step for the optimization of the fabrication process was the metallization and lift-off process needed to define the nanometric features. Lateral adhesion of the metal to the lines sidewalls was the main problem encountered. Substituting the metallization method (evaporation instead of sputtering) leaded to optimum results. Also, a thin film of titanium (~ 8 nm) below the gold was deposited to improve the adhesion to the substrate, as already mentioned above.

Figure 174 (a) shows a 3 mm x 3 mm chip, made in gold/titanium onto a SiO_2/Si substrate. Figure 174 (b) shows a SEM image of the 200 x 200 µm^2 patterned area. By proper chose of the exposure conditions the width of the digits as well as the gap between them can be tailored for the specific application of the sensor. Figure 175 (a) and (b) show SEM images of two IDEs with different nanometric dimensions.

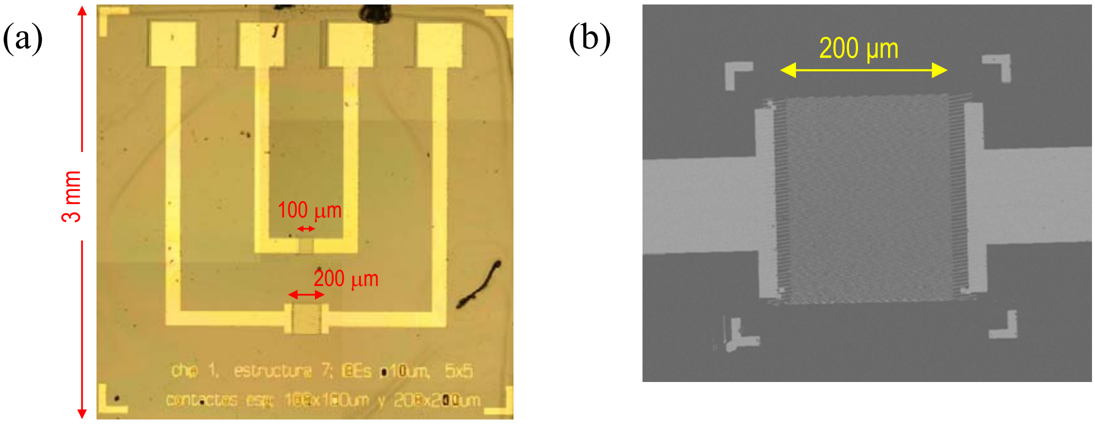

Figure 174. (a) Optical image of one of the fabricated devices, where the two integrated IDEs with different patterned areas can be seen. (b) SEM image of one of the IDEs areas (200 µm x 200 µm).

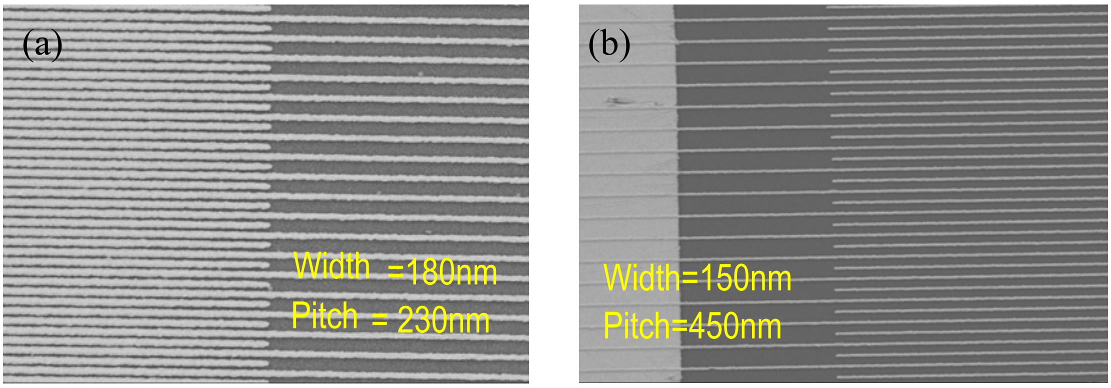

Figure 175. SEM images that show details of the nanometric digits of two different devices, where the lateral dimensions of the lines are different: 230 nm pitch and 180 nm electrode width in (a), and 450 nm pitch, 450 nm electrode width in (b).

8.1-1:b.- Wire bonding and encapsultaion

After the fabrication of the chips, they were encapsulated and bounded to a printed circuit board strip (PCB) (drawing of Figure 176 (a) and (b)), what facilitates the connection of the sensors to electronic equipments and protects the metal contacts, enabling to work in liquid media (Figure 176 (c)). A previous **local passivation** step (to cover the whole area of the chip but not the digits allows) restricting the sensing area to the nanometric size digits.

The PCBs used in this work are fabricated at CNM[*]. They have strip shape, and contain 5 metal lines, with the corresponding connection pads, as shown in Figure 176 (a). The hollow where the chip is stuck is 3 mm x 3 mm, which fixes the lateral size of the chips.

The gold contacting pads defined in the chips are connected to the metal lines of the strip by wire bonding, also at CNM[†]. Afterwards, the electric connection to external equipments is much easier, and done directly through the contacts in the top of the PCB.

The hole strip and the upper part of the chip are covered with an epoxy resin (Epotec®), to protect the contacts and the metal lines.

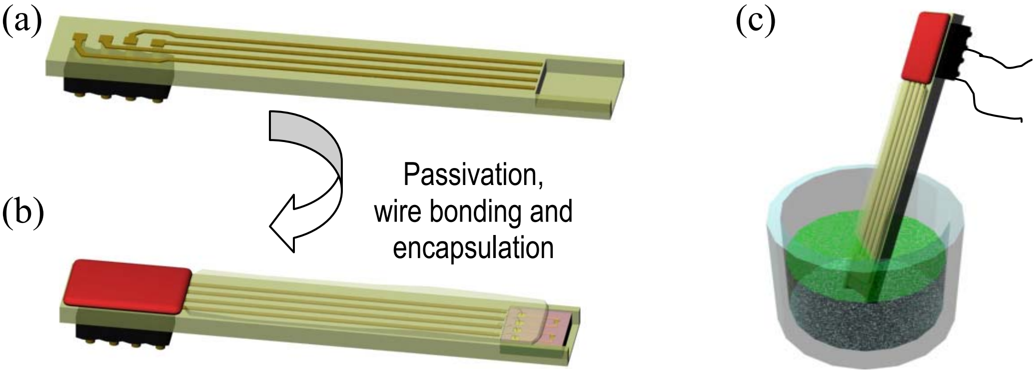

Figure 176. Drawing of the PCB used in the work: several metal lines lie onto a plastic strip (a). The fabricated chips are stuck into the hole, the pads are wire-bonded to the metal lines, and everything but the sensing area is covered with an epoxy resin (b). With this configuration, the devices can be easily connected to external electronic equipments, and used for sensing in liquid media (c).

---

[*] Angel Merlos, at the Printed Circuit Boards laboratory, in CNM.

[†] Alberto Moreno and María Sánchez, at the Wire-Bonding and Encapsulation laboratory, in CNM.

To avoid the damage of the nanometric IDEs, the sensor areas would be preferably protected and covered during the process. This requirement leaded to a more elaborated passivation of the chips. The steps of the passivation, bonding and encapsulation process of the samples, as developed within this work, are depicted in Figure 177:

a. The chips are covered with a 400 nm thick film of PMMA 35k
b. The areas covering the upper contacting pads were exposed by e-beam. The low molecular weight of the PMMA was chosen on purpose, to minimize the e-beam writing time needed to open large areas.
c. After development, the gold of the pads is open.
d. A second e-beam exposure is performed in the area where the digits are.
e. Before development, the chips were bounded and encapsulated to the PCB strip. The pads are welded to the metal lines of the strip, and everything but the bottom area of the chip is covered with a photocurable resist (epoxy in this case) to protect the contacts and the metallic tracks. This process is done manually and involves mechanical handling. The non-developed resist remaining on the area of the digits protected them from mechanical damage.
f. Finally, the exposed area is developed, leaving the digits open and ready for the electric characterizations.

Figure 176 (b) shows a scheme of the appearance of the strip, with the chip bounded and completely encapsulated, and Figure 178 shows a photograph of a device, with a zoom of the chip, where the structures and the areas with the IDEs can be seen.

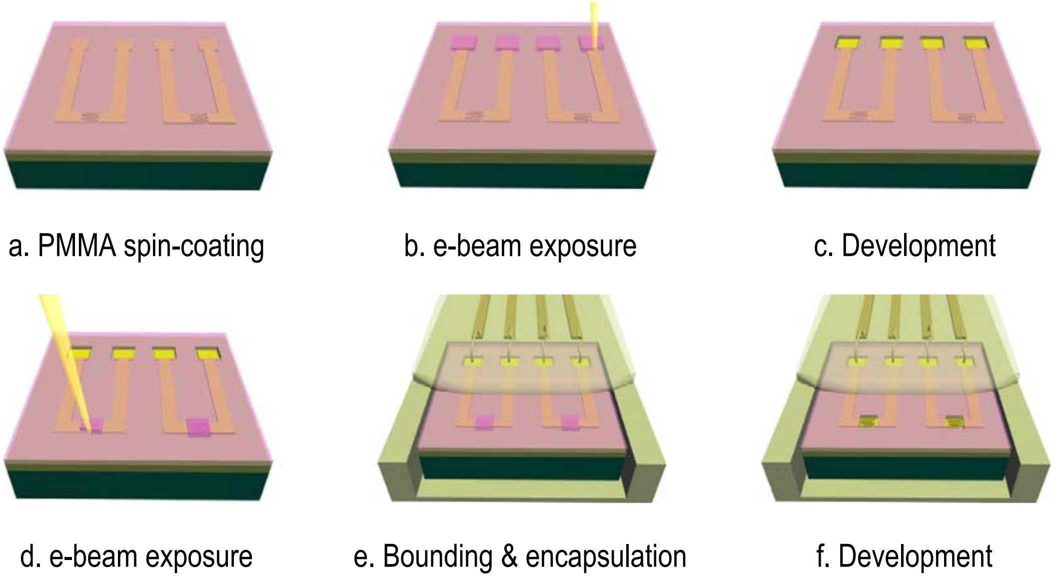

Figure 177. Passivation, wire-bonding and encapsulation process. The chips are covered with a PMMA film, 400 nm thick (a). The areas of the contacting pads are exposed by e-beam (b) and developed (c). The sensing areas with the nanometric digits are exposed by e-beam (d), and without removing the exposed PMMA, the chips are bonded and encapsulated into the PCBs. Thus, the fragile areas remain covered during the process, avoiding mechanical damaging. Finally, they are developed, so the areas are open and ready for electrochemical characterizations (f).

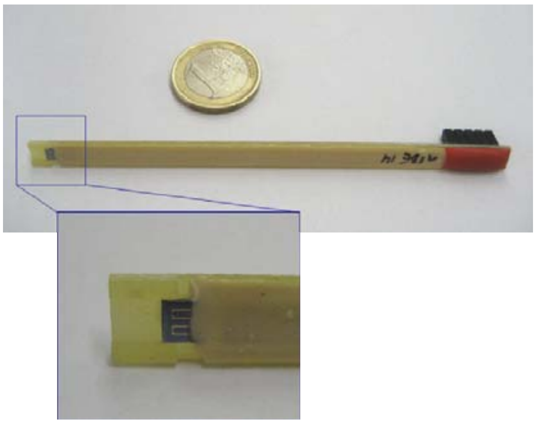

Figure 178. Photograph of a chip in a PCB. The size of the strip is compared to a 1 € coin. In zoomed photo, the chip can be seen.

After the whole process, the IDEs were ready to be characterized and/or used as (bio)chemical sensor.

This fabrication method is robust (several tens of devices were fabricated), and suitable for the applications that will be described later, in the next chapters (the gaps can be adjusted to the detection elements, and the areas, even small, are large enough to give a signal that can be measured for very low concentrations. It can be compared to the signals obtained for micrometric sensors, to study the new properties arising of their nanometric dimensions. However, even though the pads were massively fabricated (wafer scale), then, the area with the digits for each sensor had to be aligned and written individually, making the process arduous and time consuming. On the other hand, non-structured and micrometric-size IDEs are fabricated by screen printing or optical lithography, what leads to effective sensing areas of several millimetres of lateral size. Thus, in order to do an apropriate comparison, the more similar the area that the digits occupy, the better.

8.1-2. Second generation of devices

8.1-2:a.- Fabrication of the chips: all e-beam writing

After developing and optimizing the whole fabrication process described in the previous section, a new e-beam writer was available in the Institute. This, a Raith 150 Two [2], allows stitching small fields with ~ 20 nm accuracy, and most of the aligning procedures can be automatically done. Thus, very large areas can be written with nanometer features. The micrometric-size pads integrated in the design and defined by e-beam. This makes the exposure time much larger, but the process flow simpler, as the number of steps of the fabrication process is reduced.

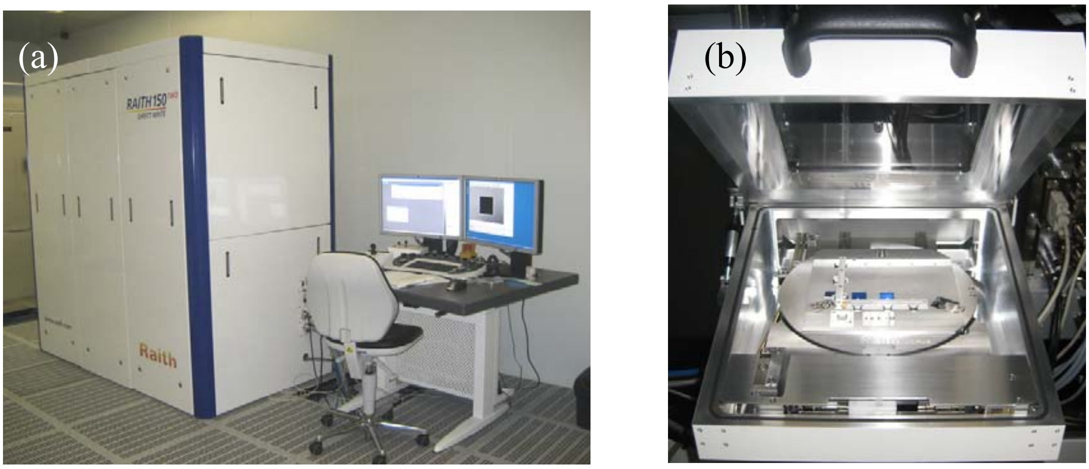

Figure 179. Raith 150 Two e-beam writer [2], placed at CNM's cleanroom (a), and it interferometric stage (b), with stitching capabilities, where the x, y and z positions are controlled with piezoelectrics.

Figure 180 shows an example of an interdigitated array of nanoelectrodes, that extends to a **1 mm x 1.5 mm** area together with the contacting pads, defined in a 100 nm thick PMMA film (left image),. The right image corresponds to a zoomed detail of the lines, that are 130 nm wide with a separation gap of 120 nm.

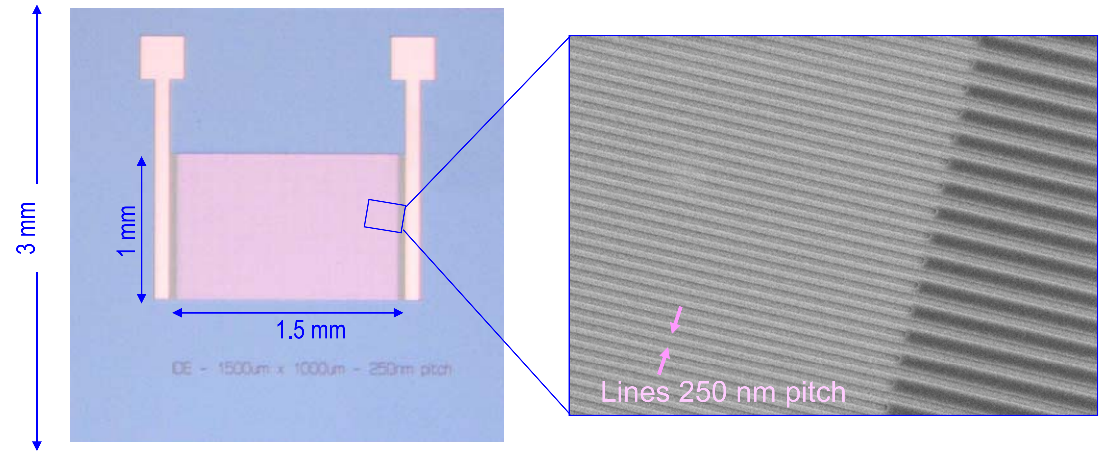

Figure 180. Optical image of a pattern defined entirely with the Raith 150 Two EBL equipment. A general view of the chip (3 mm x 3 mm) can be seen in the left image, where the area patterned with the nanometric digits extends up to 1 mm x 1.5 mm. The SEM image on the right shows a zoom of the lines, that are 250 nm pitch, 120 nm wide.

It should be noticed that Figure 180 (left) has the same lateral dimensions (3 mm x 3 mm) as Figure 174 (a). By comparison, the significant increase in the effective area (area covered by the digits) is evidenced.

After EBL, a metallization (gold/titanium) followed by a lift-off was performed, to define the structures in metal onto the insulating substrate.

This method is somehow automatic: several devices can be written in the same chip, saving time for loading and unloading the samples, and which allows parallel post processing. After dicing the samples, several chips are obtained (). Never the less, the time needed to pattern one single chip with one single array of nano-IDE is several hours (~ 3h), so, to obtain a large number of chips, complete days of e-beam writting are needed.

Figure 181. Photo of multiple devices obtained by EBL (several days long exposure) and parallel post-processing of the sample (metal and lift-off). After dicing the sample, the sensors can be individually encapsulated and used.

Also, for EBL, there are limitations in the substrate requirements: very insulating substrate present charging effects, severely affecting the resolution and the quality of the final structures. This is why NIL-based fabrication was considered as an alternative method for the fabrication of nanoIDEs with high resolution and throughput.

8.1-2:b.- Electric field characterization of the samples

During the electrochemical characterization of these devices (as will be described and shown in next chapter), a wrong asymmetrical response was systematically observed comparing the signals measured individually by each matrix. A closer look up to the electrodes revealed a gap between one of the contacting pads and the lines, probably due to a miss-match between the design and the pattern generator scaling of the features.

As the gap size was very small (< 20 nm) electric field measurements with the AFM were performed, to check if it impeded the current flow and represented and actual unplugging. Figure 182 (a) shows an AFM topographical image of the micrometric contact and the union with the digits, where the gap can be clearly seen. Figure 182 (b) corresponds to the phase image, obtained in Lift Mode[‡], with a conductive tip, and by polarization of the electrode at 0.5 V (so, it can be interpreted as a representation of the voltage distribution in the structures). Here, the contact appears polarized, but the voltage is not maintained across the gap despite its very small size, so the digits appear disconnected.

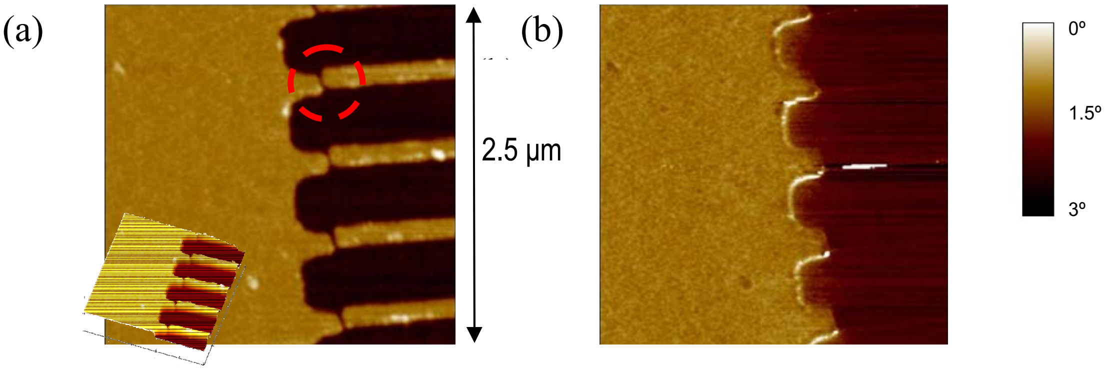

Figure 182. AFM topographical image (a) of the junction of the lines and the micrometric pads, where a discontinuity (gap) can be seen (vertical scale: 40 nm). In the phase image (b), obtained by polarizing the pads, the voltage distribution can be seen as a contrast. The gap is electrically disconnecting the pad and the digits, as they do not appear polarized in the image.

This type of defects did not appear for the other matrix (at the opposite side of the device). Figure 183 shows the electric field image (obtained again by measuring the change in the phase) of the nano-IDEs. Here, the voltage was applied to the other contacting pad. A contrast between the digits and the substrate is observed only for those connected to the polarized pad, but not for those of other matrix. The voltage was switched off when scanning the upper part of the area.

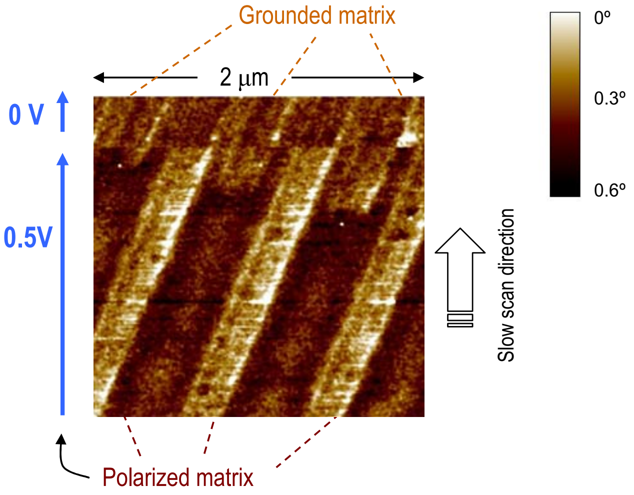

Figure 183. Electric field image of an electrode. The image was scanned upwards, and a voltage of 0.5 V was applied to one of the pads (that of the bottom of the image). A contrast can be seen between the substrate and the connected metal digits. The digits connected to the non-polarized pad do not show relevant contrast. The voltage was switched off at the top part of the image.

[‡] Lift Mode: a first scan is done in tapping mode, to obtain the topography of the sample surface. Then, the tip is lifted several nanometers (10 – 20 nm) from the surface, and the scan is repeated precisely following the surface map, but maintaining the vertical separation. Meanwhile, the phase is recorded.

Due to the appearance of this gap, most of the devices of the second generation could not be effectively used for electrical characterizations, as only one of the matrix was useful for electrochemical current measurements. Further improvement of the devices fabrication and re-design of the exposed layers is currently under study. This will lead to properly fabricated devices, that will be used for electrochemical sensing application soon.

8.2.- NIL-BASED NANOFABRICATION PROCESS

Nanoimprint Lithography is a good solution to overcome the drawback derived from the EBL-based fabrication process, as, once the stamp is fabricated, various IDE-based chips can be replicated in parallel, in a process that takes less than 1 hour. Also, insulating substrates (such as Pyrex) that are very convenient for further performance of the sensors, can be utilized with no additional effort.

8.2-1. Stamp

The typical steps needed to fabricate a stamp starting from previously defined structures are shown in Figure 184. First, by means of OL and/or EBL, metallization and lift-off the features are defined (Figure 184 (a)). Then, they are used as a mask for a RIE (Figure 184 (b)), so, after removing the metallic mask, the stamp is fabricated (c). To facilitate and make the process more robust, a silicon substrate is preferred to a SiO_2 one, as the etching process is easier, and the variation of the lateral dimensions is lower.

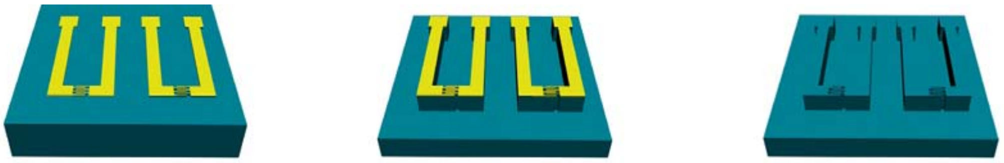

a. Metal Structures

b. Reactive Ion Etching

c. Stamp

Figure 184. Stamp fabrication process. The metallic structures (a) are used as a mask for a RIE (b), to etch down the pattern into the silicon substrate. After removing the metal (c), the stamp is fabricated.

The RIE process was a critical point in the fabrication of the stamp. For some of the applications where a very small separation between the electrodes was requiered, the lateral under-etching widened it, thus, making the design a non-robust and non reliable process. Also, when the width of the lines was very small, often, the under-etching leaded to discontinuities in the structures, as can be seen in the SEM images of Figure 185, corresponding to the mask (a) and the silicon structures after RIE (b). The width of the lines was reduced from 200 nm down to ~50 nm or below due to the overetching, even leading to discontinuities. This is an important problem, as discontinuous digits were, obviously, useless for the correct device performance.

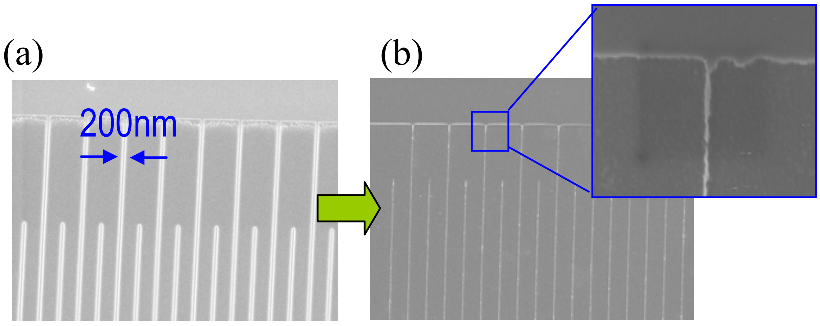

Figure 185. Metallic mask having 200 nm wide digits (a), and structures transferred into the substrate by a non-optimized RIE process (b). Here, it can be seen that the lateral underetching may lead to discontinuities in the lines.

For this reason, and as part of a collaboration within the project NILSIS (already introduced in Chapter 4), the RIE processes were done at Tekniker. Here, a Plasmalab80+ from Oxford Instruments was used, and with the optimized processes (the details of the recipe are listed in Table 6), the lateral underetching was reduced to few nanometers, so the stamps for nano-IDEs fabrication could be successfully fabricated.

Table 6. Recipe for etching the nano IDEs into the silicon substrate, in the Oxford Instruments Plasmalab 80+, at Tekniker.

SF_6:	20 sccm
C_4F_8:	30 sccm
Pressure:	15 mT
Backside He:	10 Torr

ICP Power:	220 W
RF Power:	15-20 W
Temperature:	20 °C

Figure 186 and Figure 187 show two examples of silicon stamps.

The first one (Figure 186) was fabricated by defining the structures by combining OL and EBL, with a similar process as described above previously for the fabrication of the first generation of devices, substituting the substrate for a silicon one, and by carving the structures with a RIE. The structures shown in the stamp of Figure 187 were defined just by using e-beam lithography (as described for the second generation of devices), with the Raith 150 Two equipment.

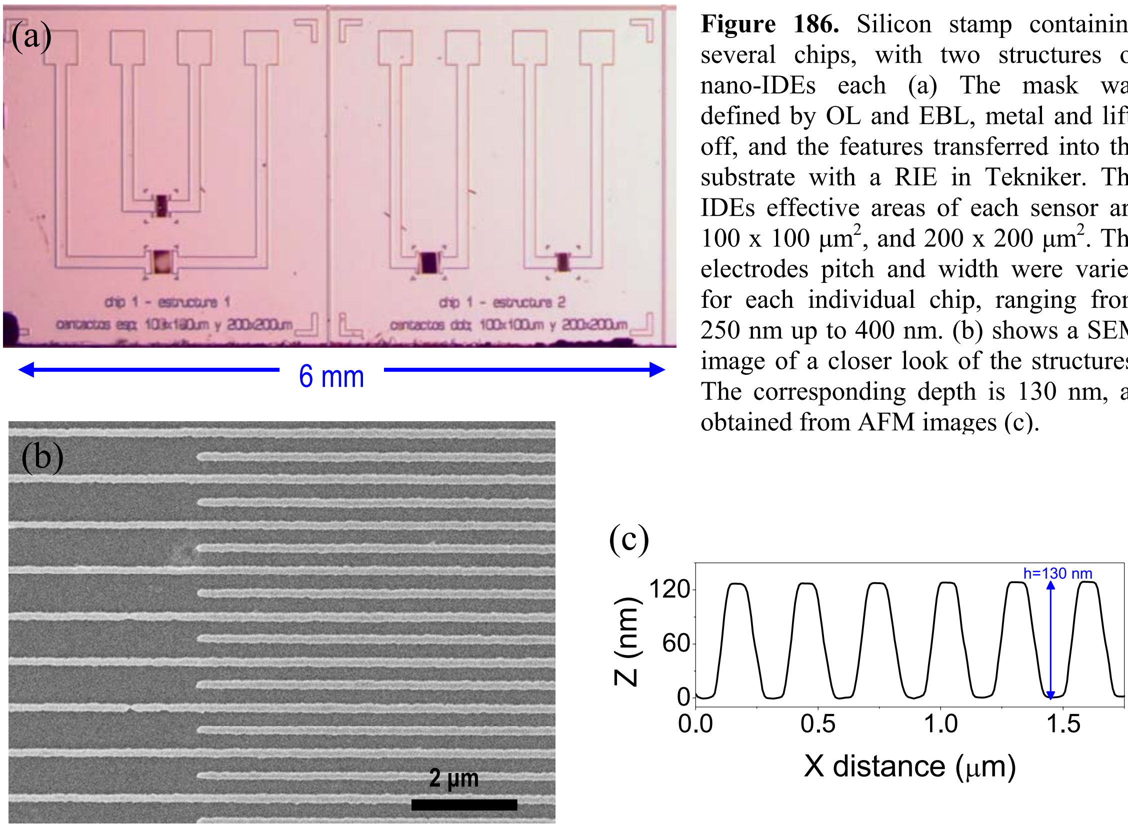

Figure 186. Silicon stamp containing several chips, with two structures of nano-IDEs each (a) The mask was defined by OL and EBL, metal and lift-off, and the features transferred into the substrate with a RIE in Tekniker. The IDEs effective areas of each sensor are 100 x 100 µm^2, and 200 x 200 µm^2. The electrodes pitch and width were varied for each individual chip, ranging from 250 nm up to 400 nm. (b) shows a SEM image of a closer look of the structures. The corresponding depth is 130 nm, as obtained from AFM images (c).

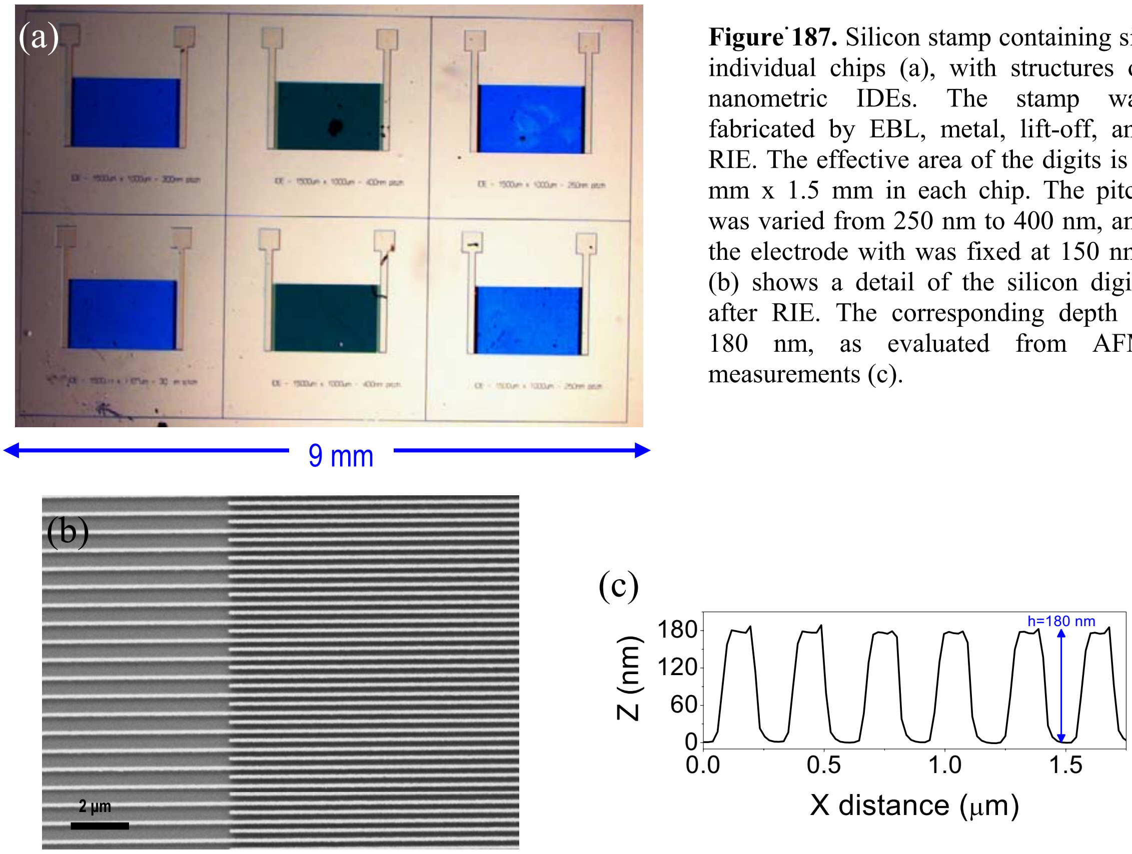

Figure 187. Silicon stamp containing six individual chips (a), with structures of nanometric IDEs. The stamp was fabricated by EBL, metal, lift-off, and RIE. The effective area of the digits is 1 mm x 1.5 mm in each chip. The pitch was varied from 250 nm to 400 nm, and the electrode with was fixed at 150 nm. (b) shows a detail of the silicon digits after RIE. The corresponding depth is 180 nm, as evaluated from AFM measurements (c).

8.2-2. Imprinting-based fabrication

8.2-2:a.- Micrometric-size IDEs

To prove the viability of the fabrication of IDEs by NIL, first, micrometric electrodes were fabricated. A mask§ containing various designs of IDEs with pitch varying between 6 µm and 20 µm was used for OL. After a metallization, lift-off and RIE, a stamp was obtained. This was imprinted in PMMA, and, after removal of the residual layer, metallization and lift-off, the structures were successfully patterned in metal onto the substrate. Figure 188 shows optical images of the different steps (stamp, imprint and final structures) of the fabrication of micro-IDEs. Each stamp included several similar chips.

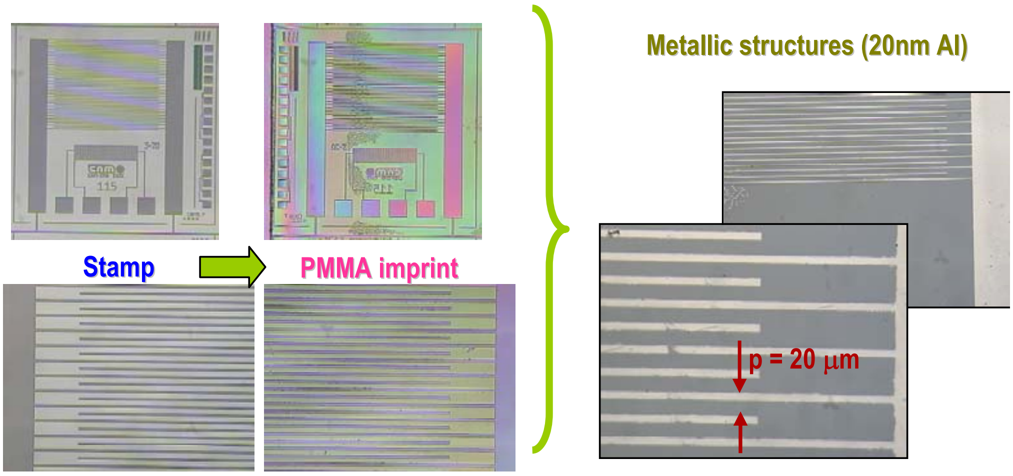

Figure 188. Micro-IDEs fabricated by NIL. The Si stamp is shown in the left images (general view in the top, zoomed area of the digits in the bottom). The PMMA imprint can be seen in the middle images, and the metallic (Al) electrodes in the right images, successfully transferred by metallization and lift-off.

---

§ Courtesy of Antoni Baldi.

8.2-2:b.- Nanometric-size IDEs

For the stamps used in this work, similar to those already shown in Figure 186 and Figure 187, several problems were encountered to successfully transfer the pattern onto the substrate. The main problem, that is a generic problem of NIL, is due to the combination of structures with very different filling factors, such as the large contacting pads and the arrays of nanometric electrodes, that have a difference in size of 3 orders of magnitude.

This leads to the bending of the stamp, and in most of the cases, to the cracking of the lines, as can be seen in Figure 189 (a). Nevertheless, by lowering the applied pressure and increasing the temperature, the obtained results were significantly improved, as shown in Figure 189 (b).

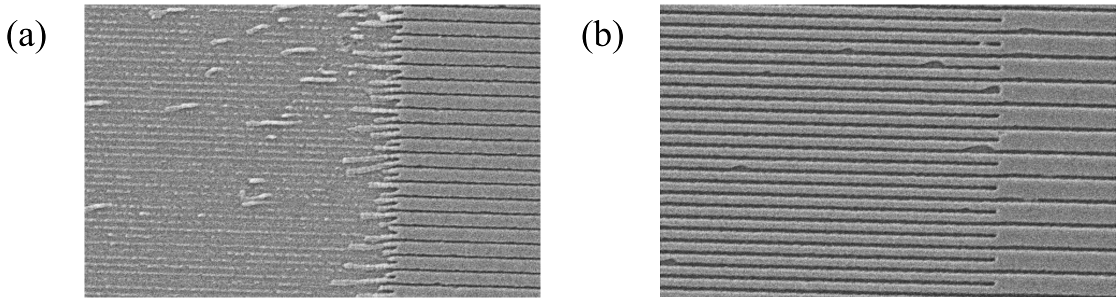

Figure 189. SEM images of imprinted IDEs. Pulled-off lines (a) appear as a consequence of stamp bending. Nicely imprinted lines result when lowering the pressure (b). Nevertheless, the quality is not equally good in the whole area.

Another problem is that NIL is very sensitive to the presence of defects. Figure 190 shows gold nano-IDEs fabricated onto a Pyrex® wafer, defined by NIL, metallization, and lift-off. In (a), the presence of a dust particle or a defect onto the resist leaded to the damage of a large area around it. In (b), the appearance of the structures is better. But, with a closer look, like shown in (c), the presence of residues, cracks, scratches and non-homogeneous lines can be observed. Some of the areas presented nicely transferred lines (d), but the quality is not homogeneous in all the patterned area.

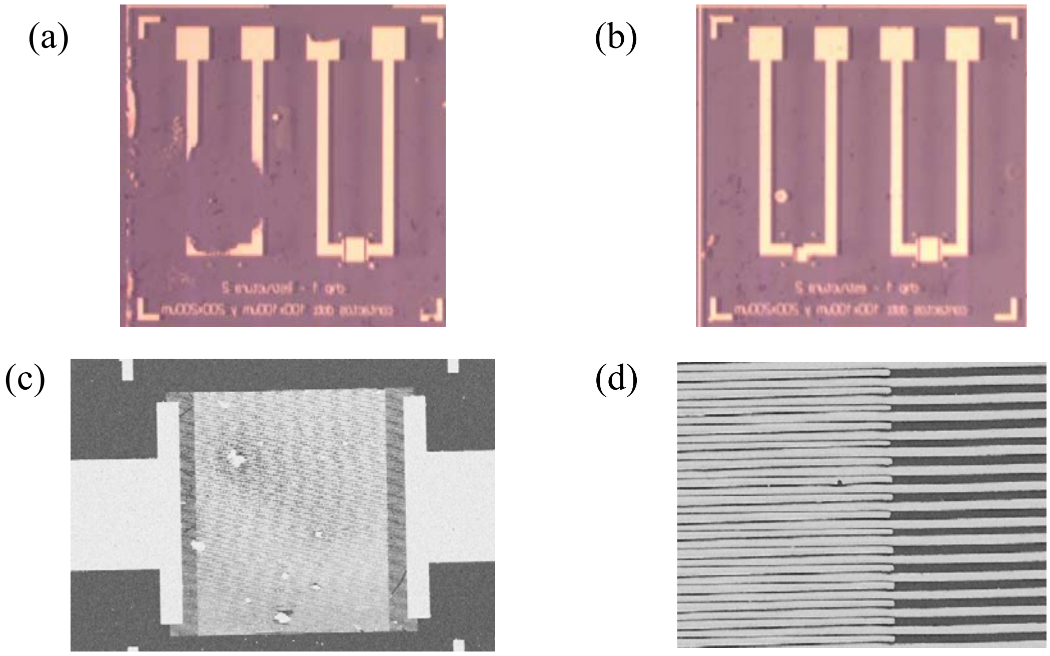

Figure 190. Images of electrodes fabricated in gold onto a pyrex substrate by NIL, metallization and lift-off. (a) shows an optical image of a complete chip (3 mm x 3 mm), where the presence of a dust particle leaded to a very large defected area. In (b), this problem was solved, and the pattern looks much nicer. A closer look to the areas patterned with the nanometric digits show the presence of inhomogeneities, contamination particles and scratches (c), even though most of the lines are defect-less (d).

When imprinting a stamp where the area covered by the nanometric digits is larger (1 mm x 1.5 mm), the sensitivity to the presence of defects becomes even more significative, and the stamp bending leaves a non-homogeneous residual layer distribution, as can be deduced from the different colours appearing in the optical image of Figure 191.

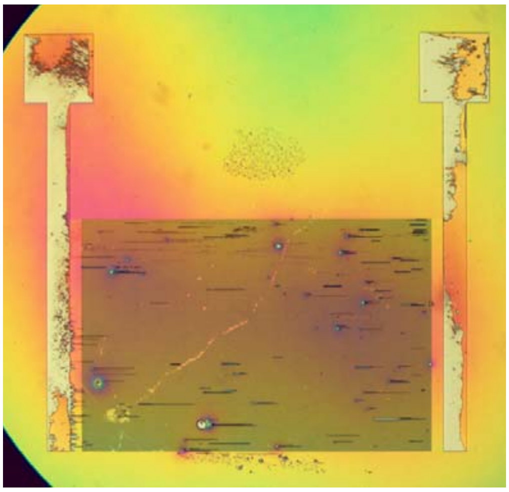

Figure 191. PMMA imprint of an electrode where the area patterned with the nano-IDEs is large (1 mm x 1.5 mm). The different colours are related to different thickness of the residual layer. This is a consequence of the stamp bending, due to the presence of patterns with very different filling factors (i.e., the pads and the digits matrix).

The devices obtained by NIL are not suitable yet for their use in electrochemical or impedimetric characterizations, as the defects could cause a shortcut of the two matrixes, and/or the broken lines do not serve to measure the current flow.

Thus, the optimization of the experimental set-up for electrical characterizations, the study and analysis of the electrochemical response of nanometric IDEs and the first developments of ideas for new applications were all done with the first generation of devices.

In parallel, the optimization of NIL for the fabrication of IDEs in a parallel, fast and simple way was (and is still) being developed. For this, new strategies are being addressed:

- Re-design of the stamps, with compensation features, to avoid critical stamp bending.
- Fabrication of two stamps, each one containing the features with the dimensions in the same scale (the micrometric pads in one, the nanometric digits in the other).
- Change of the geometry of the pads, so hollow reticules, of few microns of lateral size, would serve as contacts.

8.3.- REFERENCES

[1] Leicester, H. and Klickstein, H.,
Source Book in Chemistry, 1900 - 1950, ed. H.U. Press. 1952.

[2] *Raith, GmbH. Dortmund (Germany)* www.raith.com

[3] *LEO Electron Microscopy is the Nano Technology System Division of Carl Zeiss SMT,* *http://www.smt.zeiss.com/nts*.

Chapter 9

Electrode characterization I: Electrochemical measurements

A **sensor** is a device that measures a physical or chemical property and converts it into a signal which can be read by an observer or by an instrument. Sensors contain two basic functional units: the **receptor** (recognition element) and the **transducer** (part capable of transforming the energy carrying the information about the sample into a useful analytical signal).

In this chapter, the use of the nano-IDEs as electrochemical sensors will be described. A short description of the basics about chemical sensors and electrochemical methods will be first introduced. Then, the results obtained for different substances will be shown and discussed.

9.1.- CHEMICAL SENSING

A **chemical sensor** (Figure 192) is a device that can translate the chemical information of a sample into an analytical signal. The receptor part of chemical sensors may be based on various principles: physical, chemical or biochemical.

In the first case (*physical)*, the refractive index, absorbance, temperature or mass change, conductivity or capacitance are measured.

In the second case (*chemical)*, a reaction involving the analyte gives the analytical signal. The third case (*biological)*, can be regarded as a special case of the second, namely (bio)chemical sensors, where the source of the signal is a biochemical process.

Since the world of chemical sensors is so vast, only electrochemical and electrical sensors will be introduced here, summarizing the most relevant concepts related to the utilization of the nano-IDEs as (bio)electrochemical sensors. Thus, an **electrochemical sensor device** is basically a chemical sensor using an electrochemical transducer: it transforms the effect of an analyte-electrode electrochemical interaction into a useful analytical (electrical) signal. Such effects, in the cases studied within this work, are electrically stimulated by applying a voltage to the metallic electrodes.

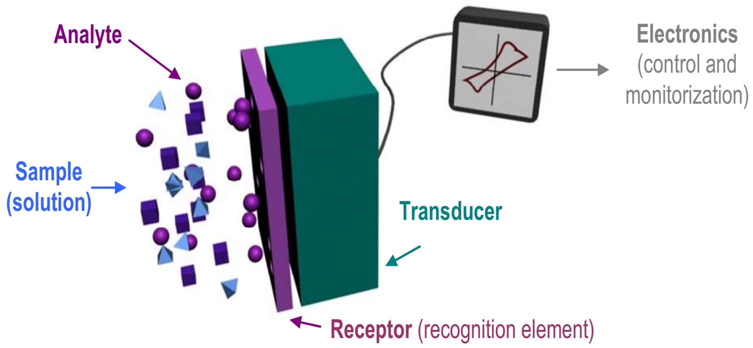

Figure 192. General scheme of a sensor: it consists on a receptor (recognition element), that is sensitive and selective to the presence of the analyte (target), that generally appears immersed in a solution. The second part of the sensor is the transducer, that is able to translate the information given by the receptor into an analytical (electrical) signal.

9.2.- INTRODUCTION TO ELECTROCHEMISTRY

Electrochemistry is a branch of chemistry that studies chemical reactions which take place in a solution at the interface of an electron conductor (a metal or a semiconductor) and an ionic conductor (the electrolyte), that **involve electron transfer** between the electrode and the electrolyte or species in solution. Electrochemical reactions can be driven by an external applied voltage (as in electrolysis), or a potential can arise from a chemical reaction (as in a battery). Chemical reactions where electrons are transferred between molecules are called oxidation-reduction (redox) reactions.

More precisely, **redox reactions** cover all chemical reactions in which atoms have their oxidation number (oxidation state) changed. Oxidation and reduction always occur in a paired fashion such that one specie is oxidized when another is reduced. This paired electron transfer is called a redox reaction. Oxidation is defined as an increase in oxidation number, and reduction as a decrease in oxidation number. A transfer of electrons is most generally the cause of the change in the oxidation number. Table 7 summarizes the processes taking place.

Table 7. Scheme of the reduction and oxidation (redox) reactions, and the processes taking place.

Reduction	**Oxidation**
Oxidant + e^- → Product	Reductant → Product + e^-
(gain of electrons) (oxidation number decreases)	(loss of electrons) (oxidation number increases)

Redox potential sensors

The standard oxidation-reduction potential corresponds to the equilibrium potential, relative to the standard hydrogen electrode, generated at the interface between a noble metal electrode and an aqueous solution containing electroactive redox species. Oxidation-reduction measurements are commonly performed using a combined redox electrode, which consists of a sensitive electrode (where the oxido-reduction process takes place) and a reference electrode (e.g. Ag/AgCl). The electroactive material of the electrode is commonly a metal (gold, in this work). By applying the appropriate voltage difference, V, the process can become somehow selective for the analyte under study.

9.2-1. Electrochemical methods

Electrochemistry is a wide research area where plenty of measurement methods have been developed. Electroanalytical methods are a class of techniques in analytical chemistry which study an analyte by measuring the potential (V) and/or current (I) in an electrochemical cell containing the analyte. These methods can be split into several categories depending on which aspects of the cell are controlled and which are measured. The three main categories are:

I. Potentiometry: the difference in electrode potentials is measured.
II. Voltammetry: the cell's current is measured while actively altering the cell's potential.
III. Chronoamperometry: the cell's current is measured over time.

The two last were used in this work to characterize the response of the nano-IDEs. The instrumentation used for the measurements and the electrochemical techniques utilized are described next.

9.2-1:a.- The Electrochemical cell: three electrode configuration and Potentiostat

Voltammetric and chronoamperometric techniques are commonly applied in electrochemical cells with a **three electrode configuration**. Three electrodes with different functionalities are immersed in the *electrolyte* (generally, aqueous solution with ions), where the analytes (or active red-ox species) are dissolved. The electrolyte facilitates the cell reaction and carries the ionic charge across the electrodes efficiently. It forms a stable potential with the reference electrode and needs to be compatible with the other materials in use. The electrodes are connected to a (bi)potentiostat, to perform the measurements. A schematic view of the set-up is shown in Figure 193.

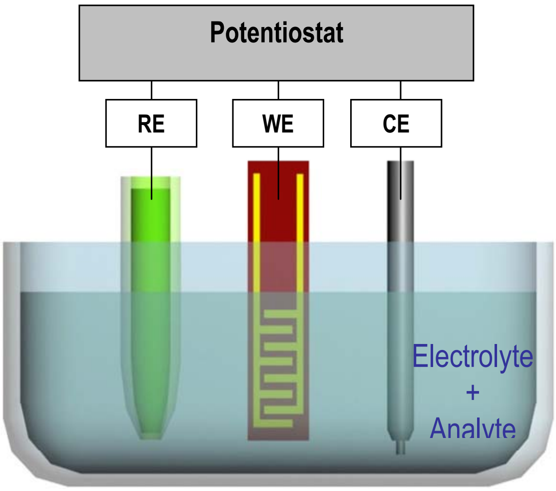

Figure 193. Scheme of an electrochemical cell on a three-electrode configuration: the electrodes (reference electrode RE, working electrode WE and counter electrode CE) are immersed into the sample solution, and connected to a potentiostat.

(i) The studied electrode (the nanoIDEs in our work) is the so-called sensing or **working electrode (WE)**, that is where the reactions take place. Typically, it is made from a noble metal.

(ii) The potential applied to the WE is measured by comparison to another electrode, that has a well-known fix potential: the **reference electrode (RE)**. There are various types of RE, that generally consist on a redox pair at equilibrium, therefore having a fix potential with respect to the hydrogen electrode (that is 0V). No current flows to or from the reference electrode. In this work, an Ag/AgCl electrode was used (E^0 = 0.22V). The RE is very important, as in reality, the sensing electrode potential does not remain constant due to the continuous electrochemical reactions taking place on the surface of the electrode and the reference electrode maintains the fix value of the applied voltage at the sensing electrode

(iii) The third electrode is the auxiliary or **counter electrode (CE)**. The CE often has a surface area much larger than that of the working electrode to ensure that the reactions occurring on the working electrode are not surface area limited by the auxiliary electrode. The current is measured between the working electrode and the counter electrode. Thorough this electrode, the potentiostat is able to pass current through the analyte solution without passing current into or out of the reference electrode. Thus, reference voltage variations due to electrode polarization are eliminated. In this work, a platinum CE was used.

The **potentiostats**, that are the equipments generally used for electrochemical characterizations, apply the desired potential between the WE and the RE, meanwhile the current flow, arising from the chemical reactions taking place in the cell, is measured. An adequate potentiostat needs to compensate for potential deviations at the surface of the WE from the set value. A commercial potentiostat/galvanostat (PGSTAT100 from Autolab [1]), shown in Figure 194 (a), was used during this work.

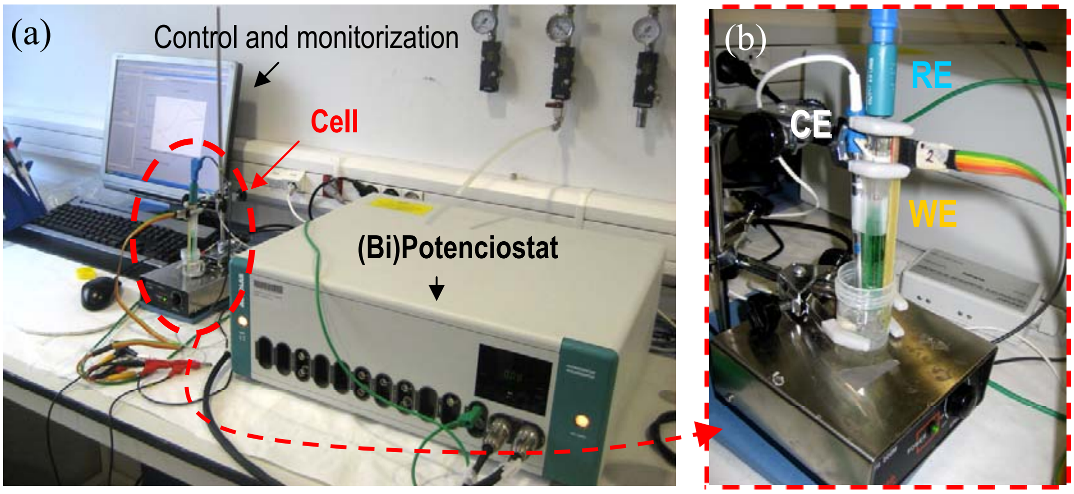

Figure 194. Photo of the Autolab equipment used for the experiments (a) and of the electrochemical cell (b), with the CE, RE and WE immersed in the liquid sample.

Figure 194 (b), shows the electrochemical cell, where the platinum counter electrode (CE), the Ag/AgCl reference electrode (RE) and the PCB strip with the gold IDEs working electrode (WE) can be seen, immersed in the liquid sample.

The software that controls the Autolab (*GPES*) allows controlling the electric parameters of the cell and performing different electrochemical characterizations. As mentioned above, cyclic voltammetry and chronoamperometry were the methods utilized to characterize the electrochemical response of the nano-IDEs.

9.2-1:b.- Cyclic Voltammetry

In general, in a voltammetric method, a voltage (or series of voltages) is applied to the electrode and the corresponding current flow is monitored [2, 3].

In this work, **linear sweep voltammetry** was used. It consists on measuring the current at the working electrode while the potential between the WE and the RE is **swept linearly** in time (Figure 195 (a)). Oxidation or reduction of species is registered as a peak or trough in the current signal at the potential at which the species begin to be oxidized or reduced (Figure 195 (b)).

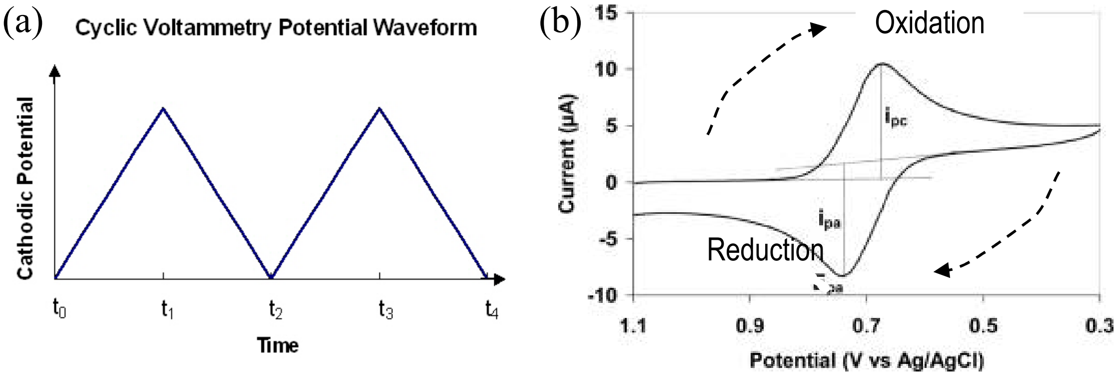

Figure 195. Scheme of the applied potential vs time (a) and the typical voltammogram obtained for the measured current (b) in the linear voltammetry.

When the specie in the solution is not electrochemically active (or the applied potentials are not in the right range) only the capacitive current due to the charge and discharge of the metal is measured.

9.2-1:c.- Chronoamperometry

Chronoamperometry is another electrochemical technique in which the potential of the working electrode is fixed (or stepped along large intervals of time), and the resulting current coming out from the reduction or oxidation processes occurring at the electrode/electrolyte interface is **monitored as a function of time**.

Generally, the standard procedure consists on maintaining the electrode at a fix potential, that is favourable for one of the half-cell reactions to occur, and adding a certain quantity of the active specie to the solution at intervals of several tens of seconds. Meanwhile, the current is continuously monitored, and a step appears right after each addition.

In this work, the process was slightly modified, to improve the calculation of the sensitivity and resolution of the nano-IDEs. Thus, the applied voltage was instantaneously switched from one value V_1 to another V_2 (Figure 196 (a)), and the resulting current was then measured as a function of time for a solution with a **fix concentration**. The process was then repeated for different solutions with different concentrations.

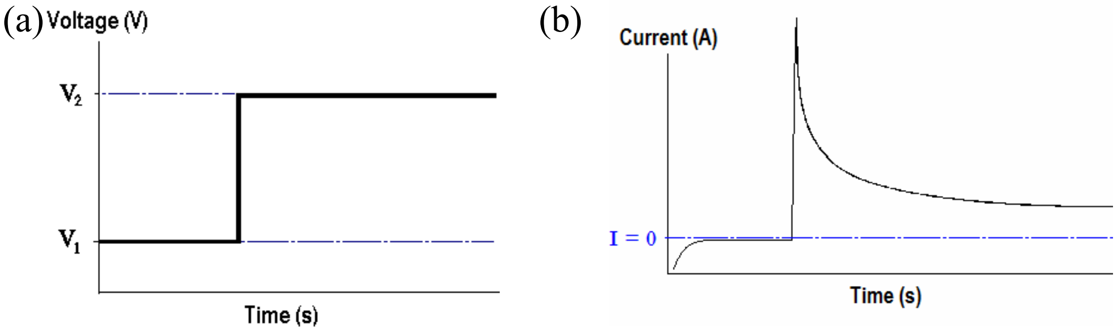

Figure 196. Scheme of the applied potential vs time (a) and the corresponding current (b) in the two-steps voltage chronoamperometry.

The voltage range was set such that at V_1 the reduction or oxidation of the active species was thermodynamically unfavourable. The second value of voltage (V_2) was selected so that any species close to the electrode surface were oxidized or reduced, depending on the case. Under these conditions the current response is like that shown in Figure 196 (b): the current rises instantaneously after the change in voltage and then begins to drop as a function of time.

This trend is observed since the process is **governed by diffusion,** as is schematized in the diffusion profile and colour scheme of Figure 197. The instant before the voltage step, the surface of the electrode is completely covered with reactant and the solution has a constant and homogeneous composition (a). Once the voltage (V_2) is applied, the reactant is converted to product and a large current begins to flow. However, for the reaction to continue, a supply of fresh reactant in the electrode surface is needed. This happens via **diffusion** in stagnant solutions (without agitation). The rate of diffusion is controlled by the concentration gradient. Thus, the supply of reactant to the surface (and therefore the current flowing) depends upon the diffusional flux. At short times, the diffusional flux is high, as the change in concentration between the bulk value and that at the surface occurs over a short distance (b). As the reaction continues, the material diffuses further from the electrode and the concentration gradient drops (c). As the concentration gradient drops, so does the supply of reactant to the surface and, therefore, the current also decreases.

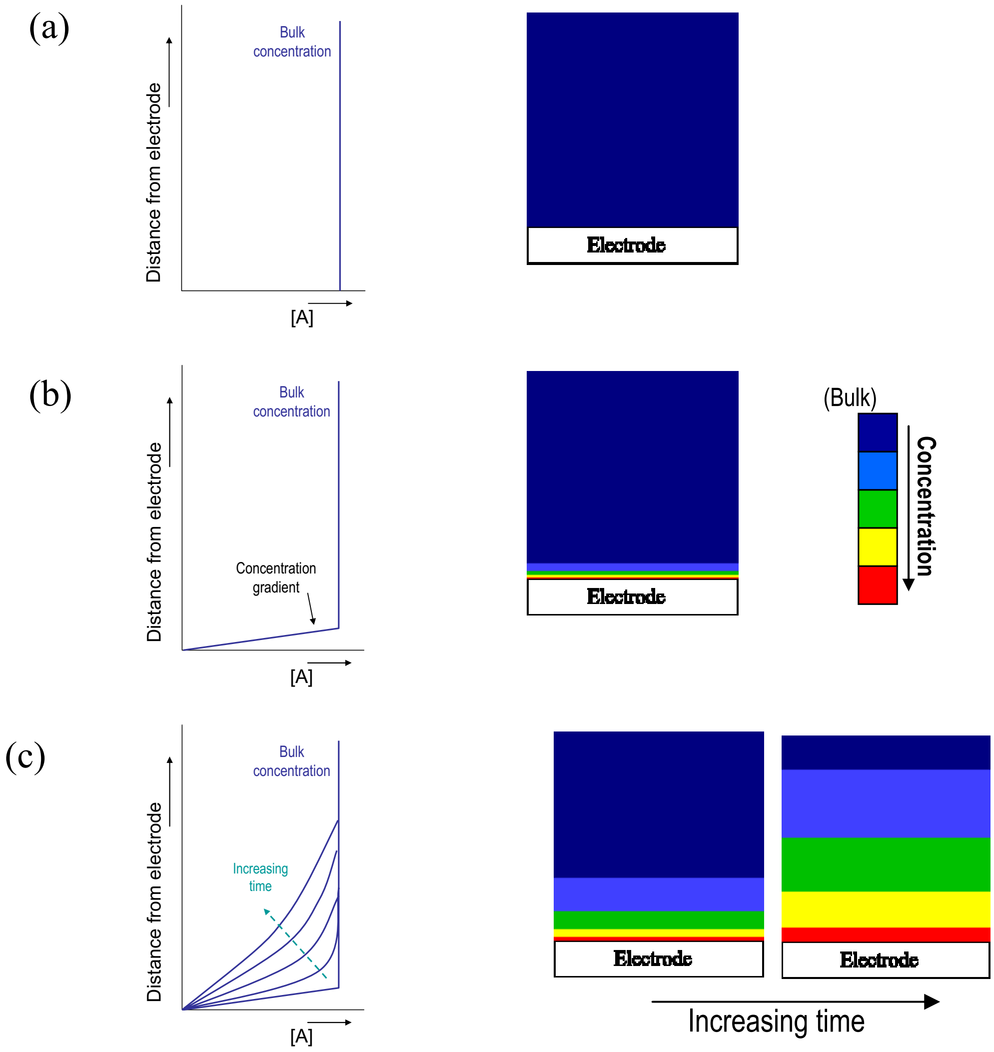

Figure 197. Evolution of the concentration of the active specie in the vicinity of the electrode surface, before polarization of the elctrode (a), just after applying V2 (b), and several seconds afterwards (c and d). The graphs in the left show the concentration distribution profiles as a function of the distance from the electrode, and, on the right column, the colour schemes.

Thus, the current can be studied from a diffusive point of view. The mass transport of reactant through the diffusion layer owes Fick's laws of diffusion given in (30). The x coordinate corresponds to the distance in the perpendicular direction to the electrode surface, [A] is the concentration of the reactant, and D_A its diffusion coefficient.

$$\frac{\partial [A]}{\partial t} = D_A \left(\frac{\partial^2 [A]}{\partial x^2} \right) \qquad (30)$$

The expression for the electrolysis current for a reduction reaction with a constant k_{red} happening in an electrode with a given total surface (S) is given by (31), where F is the Faraday constant, and n the number of electrons involved in the reaction This expression was re-written by Cottrell [4], showing that it is possible to solve the mass transport equation in terms of the current flux..

$$I_c = -nFSk_{red}[A] \qquad (31) \qquad \longrightarrow \qquad |I| = \frac{nFS[A]_{bulk}\sqrt{D_A}}{\sqrt{\pi}\sqrt{t}} \qquad (32)$$

This expression explains the current intensity measured during the chronoamperometry, **as I depends linearly on** $1/\sqrt{t}$**,** when the reaction is governed by diffusion.

This method is a reliable way of **calibrating** a sensor. It allows measuring a stable electrochemical current coming from redox reactions of the species in the solution as a function of the concentration, minimizing the noise/background signal that may arise from the charge or discharge of the electrodes or the double layer, as may happen in the voltammograms.

9.3.- ELECTROCHEMICAL CHARACTERIZATIONS OF THE IDES

The measurements reported in this chapter had the objective of studying the electrochemical behaviour of the electrodes, and optimize the cleaning process, the procedure parameters and the analyte concentrations. For this purpose, the measurements were done by **short-circuiting the two independent matrix** of interdigitated electrodes, so all the results were obtained as a sum of both, unless the contrary is specified. The electrodes from the first generation (see Chapter 8) were mainly used. Eventually, some of the second generation were also used; when so, it will be clarified.

9.3-1. Cleaning and activation

Prior to the electrochemical measurements, we observed that an activation process was needed. Right after the fabrication, the electrodes *appeared passivated*, probably due to contamination of the surface during the encapsulation process, or to the presence of remaining PMMA. Superficial oxidation of the metal at air was sometimes also observed.

For the cleaning process, the electrode was immersed in a KNO_3 0.1M solution, and the voltage was swept between -0.5 V and -1.5 V for several (~ 10) cycles. Under these conditions the water hydrolyzes and the H_2 (gas) bubbles and mechanically removes the passivating or contaminating elements that may lie onto the electrode surface. This method could be too aggressive for the nanometric electrodes, as the high current flow warmed up the metal and peeled off the digits. To avoid this, the maximum current was limited at 100 nA, which avoided fatal damage of the devices.

Figure 198 shows current vs time plots, for KNO_3 and ferricyanide solutions, obtained before and after the activation of the electrodes. It proves the efficiency of this method for the activation of the electrodes.

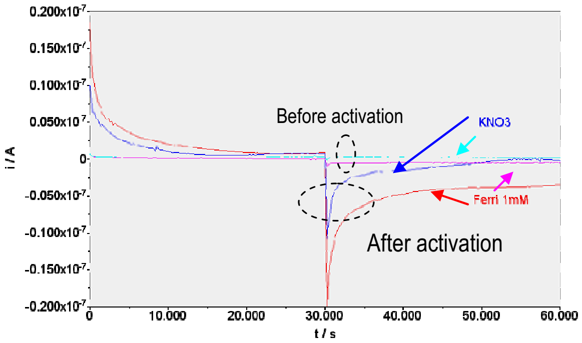

Figure 198. Comparison of the measured current before (light blue and pink lines) and after activation (red and dark blue lines) of the electrodes, for KNO_3 and Ferricyanide 1mM solutions.

All the measurements shown from now on were obtained after the activation of the electrodes.

9.3-2. Calibration and measurements for different substances

9.3-2:a.- Ferricyanide

One of the substances used to study the electrochemical signal obtained with the nano-electrodes was ferricyanide. The redox reaction for this specie is given in (33). An aqueous solution of KNO_3 (0.1 M) was used as support electrolyte.

$$Fe(CN)_6^{3-} + 1e^- \leftrightarrow Fe(CN)_6^{4-} \qquad (33)$$

Voltammograms

Figure 199 (a) shows a voltammogram obtained at a scan rate of 0.1 V/s for a blank solution (KNO_3 0.1M), that is not active (light blue line), and for a solution of ferricyanide 1mM in KNO_3 0.1 M (dark blue line). In the first case, only the charge and discharge of the electrodes and the double layer is observed. When active specie is added to the solution, the oxidation and reduction peaks appear added to the previous signal. This proofs that the electrodes are sensitive to the presence of the ferricyanide.

From this graph, **the potentials at which the oxidation and reduction reactions take place for the experimental conditions of this work can be obtained**. The oxidation peak appears at +0.22 V, and the reduction one at 0.11 V (referred to the Ag/AgCl reference electrode), as shown in Figure 199 (b). The distance between peaks is 0.110 V. This value is quite far from *theoretical value*, for a reaction involving 1 electron, predicted from Nernst equation [3] for a reversible reaction, that is 0.059 V. Slow electron transfer at the electrodes surface (i.e., “irreversibility”) causes the peak separation to increase. The cyanides in the solution cause the poisoning of the gold surface, making the reaction less reversible.

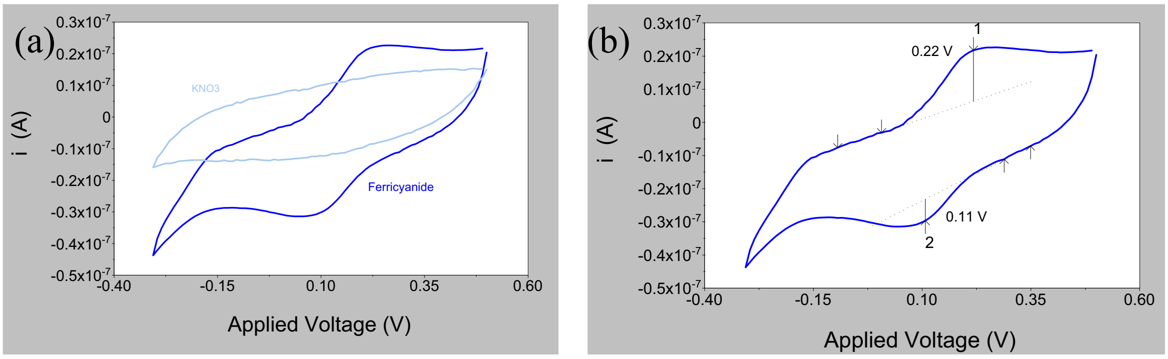

Figure 199. Voltammograms at 0.1 V/s. (a), comparison between the blank solution of KNO_3 0.1M (light blue line) and a solution of Fe(CN)63- 1mM in a 0.1M KNO3 electrolyte (dark blue line). The peak calculation is shown for the ferricyanide solution in (b).

Chronoamperometry

As it was mentioned above, the typical chronoamperometry procedure (measurement of the electrical current flow vs time, for a fix applied voltage) consists on starting with a blank solution, and adding a fix amount of active specie at fix intervals of time, so, afterwards, a calibration can be done.

Figure 200 shows a graph, obtained by adding 1 mL of ferricyanide every 60 s to 100 mL of KNO_3 0.1M. The noise introduced by the agitation was comparable to the signal increment, which difficulted the analysis and quantification of the obtained data.

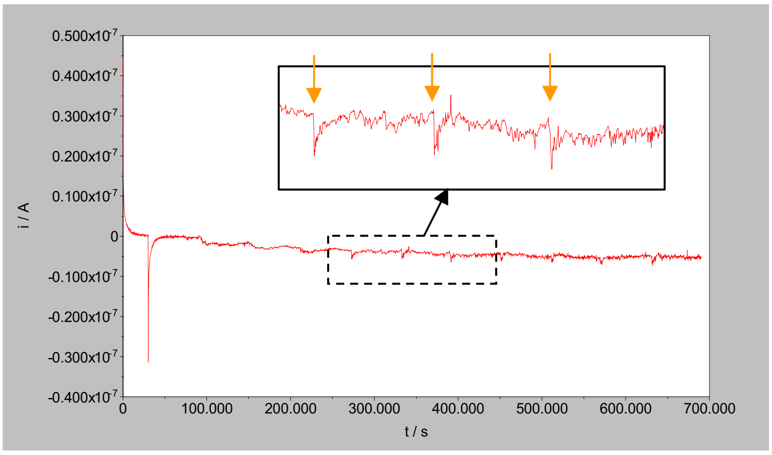

Figure 200. Current intensity vs time plot, obtained for a nano-IDEs, by adding 1mL of ferricyanide to 100 mL of KNO_3 every 60 seconds. The electrode was polarized at + 0V.

For these reasons, the chronoamperometric process was slightly varied from the conventional procedure, in order to get a better control and more reproducible measurements, and to measure with high accuracy the minimum detection limit. For this, as already described, the applied voltage was stepped, and the resulting current measured as a function of time for solutions with a fix concentration.

Figure 201 (a) shows the current intensity vs. time obtained for a blank solution, KNO_3 0.1M (cyan line) and for ferricyanide 1mM in KNO_3 0.1M (dark blue line). The cell was maintained at +0.5V for 30 seconds, and then 0 V applied. This over-potential was chosen according to the results obtained in the voltammograms (Figure 199).

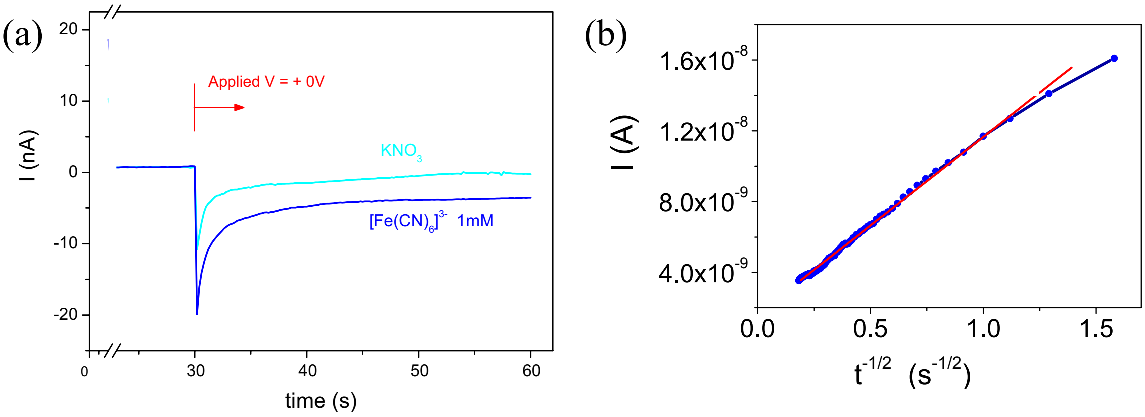

Figure 201. (a) Current intensity vs time plot, obtained for a blank solution (KNO3) and for a ferricyanide solution, 1mM. The voltage was swept from +0.5 V to 0 V at t = 30 s. (b) current intensity vs $1/t^{1/2}$ plot. The linear dependence proves that the process is diffusion controlled.

For both dissolutions a peak is observed when switching the voltage. This has two contributions: (1) the charge of the double layer and the electrode, that is discharged quickly, and (2) the fact that, when the voltage is applied, the concentration at the electrode interface is very high, so a large current intensity begins to flow.

As has been mentioned above, when the voltage is applied, the concentration of $Fe(CN)_6^{3-}$ at the electrode surface is the concentration of the solution (bulk). As time goes by, the analyte is consumed: the ions react and are transformed into $Fe(CN)_6^{4-}$ so the $Fe(CN)_6^{3-}$ run down. According to this, the current intensity depends linearly on $1/\sqrt{t}$, which is a state controlled by diffusion. Figure 201 (b) shows the dependence of I on $1/\sqrt{t}$, and its linear fit. The distance between points is 0.2 s, so in less than 1s the discharge of the double layer has occurred, and the diffusion controlled regime starts.

After few seconds, the current becomes almost constant. In the KNO_3 solution, after 15 s approximately, the current becomes zero, as corresponding to a non electrochemically active solution. In the case of the ferricyanide, the stable value is that resulting from the redox reactions taking place in the vicinity of the electrodes surface.

By repeating the chronoamperometric measurements using different concentrations of ferricyanide (Figure 202 (a)), the sensors can be calibrated. Figure 202 (b) shows the current values at t = 45 s (15 seconds after applying the active potential) as a function of the concentration of ferricyanide. The detection limits and sensitivity for very low concentrations were studied.

- The minimum current that can be detected by the equipment was ~0.1nA, and the noise in the signal ± 0.2 nA. The minimum concentration that can be detected is **~10^{-6} M** (i.e. **0.3 mg/L**), that gives a signal of 0.5 nA.
- As can be seen in the calibration plot of Figure 202, two regimes appear. For very low concentrations (below $5 \cdot 10^{-4}$M) the sensitivity is ~8 nA/mM. For higher values (up to mM) an increased sensitivity was observed: **~ 50 nA/mM** (i.e. **150 nA/(mg/L)**).
- It was been observed for other similar sensors that for increasing concentrations, the sensitivity was reduced again, in a factor of 10. Thus, the optimal sensing range for these sensors is from **$5 \cdot 10^{-4}$ M to 10^{-3} M.**

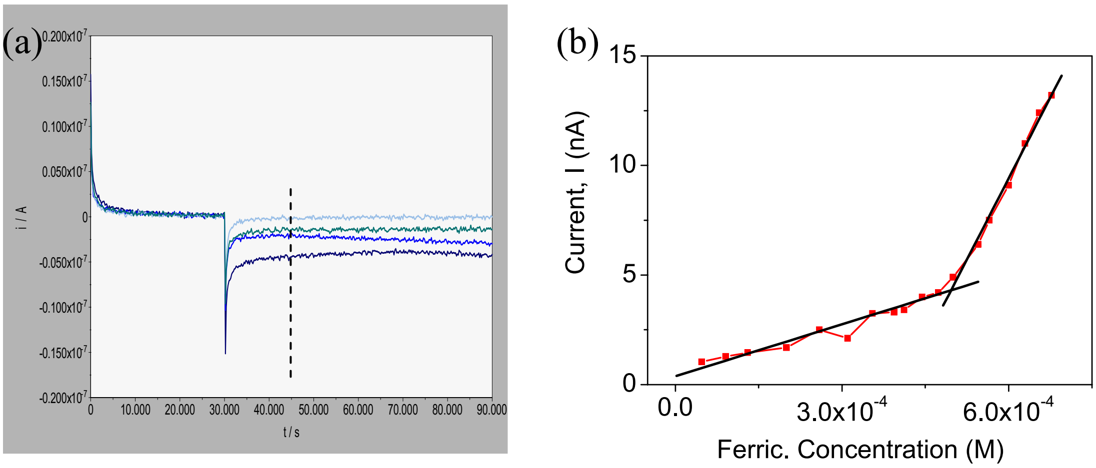

Figure 202. (a) Current intensity vs time plots, obtained for different concentrations of ferricyanide in a KNO_3 0.1M solution, for an applied voltage of + 0V. (b) shows the current intensity dependence on the ferricyanide concentration. This is a calibration plot, so the concentration of an unknown solution can be estimated by measuring the current at these conditions.

The typical values that can be found in the literature for the minimum concentration and the sensitivity of other types of electrodes for different electroactive species are similar to those obtained here. For example, in [5] they reported a sensitivity of 200 nA/(mg/L) and a 0.08 mg/L for the detection of free chlorine by using gold ultra-micro-electrodes, with an active area of 1.62 mm^2. In [6], they obtained a minimum detection limit of, $5 \cdot 10^{-9}$M, and a sensitivity of 10^6 nA/M for the detection of arsenic using a gold–carbon composite electrodes, consisting on flat areas of 18 mm^2.

Nevertheless, there are many other state-of-the-art sensors that show much better sensitivity and resolution, having very large effective areas, and that have been specifically designed and fabricated for the detection of a certain substance.

On the other hand, it is very difficult to establish a reliable comparison with the characteristics of other electrodes, as the properties, geometry, area and substances and media used significantly differ ones from the others.

Comparison with micrometric IDEs.

For this reason, similar devices to those used along this work were also fabricated, but having micrometric size matrix. For this, in the same mask designed and used for the fabrication of the contacting pads that were used for the e-beam lithography, some micrometric-size electrodes were also included and fabricated. The sensors geometry was exactly the same as the nanometric ones: two active areas were integrated in the same chip (200 µm x 200 µm and 100 µm x 100 µm). The gold layer of the micro IDEs was thicker than in the case of the nanometric digits (~ 60 nm, compared to 15 nm of the nanometric structures).

They were characterized in the same experimental conditions, and the results used to compare the resolution and the sensitivity with those already reported above.

Figure 203 shows optical images of the sensors. The area used for characterization of the micrometric IDE is shown in (a) and that corresponding to the nanometric IDE is shown in (b). In the first case an area of 200 x 200 μm^2 was used. Meanwhile, the area of the sensor used for comparison was smaller (100 x 100 μm^2). The insets of the figure show a detail of the digits in both cases. The micrometric IDE consisted on an array of electrodes, 5 µm wide with a separation of 5 µm (i.e., a pitch of 10 µm). The nanoIDE was formed by a matrix of IDEs 90 nm wide, with a gap of 280 nm (which is 370 nm pitch).

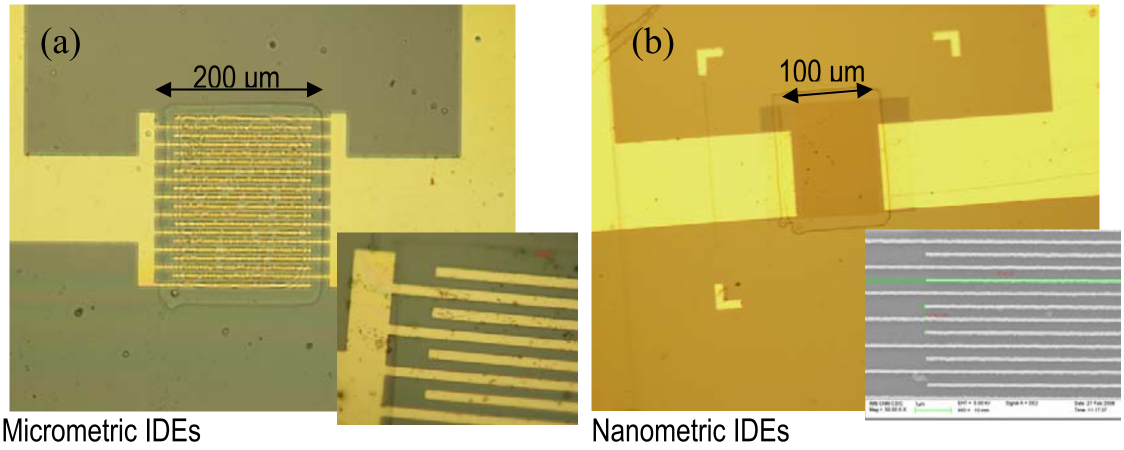

Figure 203. Images of the micrometric IDEs fabricated by OL (a) compared to the nanometric IDEs (b) used above. In the first case, the sensor had an area of 200 µm x 200 µm, filled with electrodes 5 µm wide, 10 µm pitch. In the second case, the area was 100 µm x 100 µm, with electrodes 90 nm wide, 370 nm pitch.

A simple calculation reveals that the total gold area of the micrometric IDE is more than the double of that corresponding to the nanometric one.

It can be clearly seen in the calibration plots of Figure 204 that the current flow for a given concentration is much higher in the nanoelectrodes. When using the microelectrode (red line), a higher concentration is needed in order to get a measurable signal, so the minimum concentration limit is higher than those previously shown for a similar nanometric electrode. Also, as deduced from the slope of the trends, the sensitivity at low concentrations is much higher when the dimensions are in the nanometric scale. Nevertheless, it has been observed that the saturation point (the sensitivity drops) is achieved for lower concentrations in the nano-IDE, meaning a shorter optimal optimal detection range. For the micrometric IDE, this range lies between 0.01 M and 0.5 M.

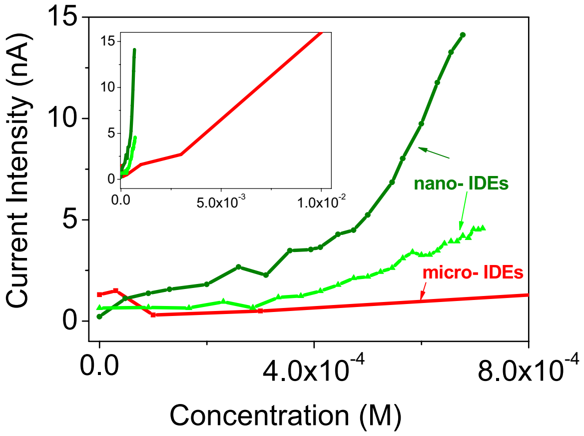

Figure 204. Calibration plot (I as a function of the analyte concentration) for a microelectrode (red line), compared to two different nanoelectrodes (green lines). The graph is a zoom for the lower concentrations range (0 – 0.8 mM), and in the inset a larger range is shown (0 – 10 mM).

Nevertheless, for the characterization in ferricyanide solutions, several problems were encountered. One is related to the poisoning of the gold surface due to the presence of cyanides in the solution, what causes the degradation of the signal intensity after few measurements. An activation process effectively cleaned the electrodes. On the other hand, filtration effects of the ions thorough the PMMA passivation layer were observed during the measurements, as this lead to a dramatic increase in the signal when the electrode had been immersed in ferricyanide solutions for several hours. After leaving the sensor in water for few hours, the filtered substances were removed. This impeded the correct characterization of the electrodes for high concentrations of ferricyanide (≈ 0.1 M or above), as when repeating the measure, the current didn't stabilize, but incremented continuously.

9.3-2:b.- Ruthenium complexes

The response of the electrodes was also studied in solution of ruthenium complexes ($Ru(NH_3)$). These species are commonly used for standard electrochemical characterizations, and have the advantage, compared to ferricyanide, that do not poison or passivate the gold surface of the electrodes.

The redox reactions for the ruthenium complexes is:

$$Ru(NH_3)^{3+} + 1e^- \leftrightarrow Ru(NH_3)^{2+} \qquad (34)$$

And also in this case, an aqueous solution of KNO_3 0.1M was used as support electrolyte.

The electrochemical measurements in ruthenium complexes were done using electrodes of the *second generation*. These had an active area of 1 mm x 1.5 mm, what means higher current intensities, compared to those obtained using the electrodes of the first generation in ferricyanide solutions.

Voltammograms

Figure 205 (a) shows a voltammogram obtained in a $Ru(NH_3)^{2+}$ solution, 1mM. The oxidation and reduction peaks appear at -0.155 V and -0.252 V respectively (referred to an Ag/AgCl RE). This means 0.097V between peaks, which is closer to the theoretical value (0.059 V) than the distance between peaks obtained for the ferricyanide solutions, what means that the ruthenium complexes do not passivate the gold surface, so the redox reaction along a cycle is more reversible.

Figure 205 (b) shows two voltammograms obtained in a $Ru(NH_3)^{2+}$ solution, 1mM, at two different scanning ratios: 0.1 V/s (blue line) and 0.01 V/s (red line). In comparison with the plot obtained in (a), it should be pointed out that the electrodes used had similar characteristics, but the pitch in the second one was larger, for a same electrode width. This leads to less pronounced peaks, which may be similar to an ultramicroelectrode array (UMEA) behaviour [7-9]. This means that the peak is not clearly marked, but instead, a constant value for the current is achieved and maintained for voltages above the oxidation one, or below the reduction one.

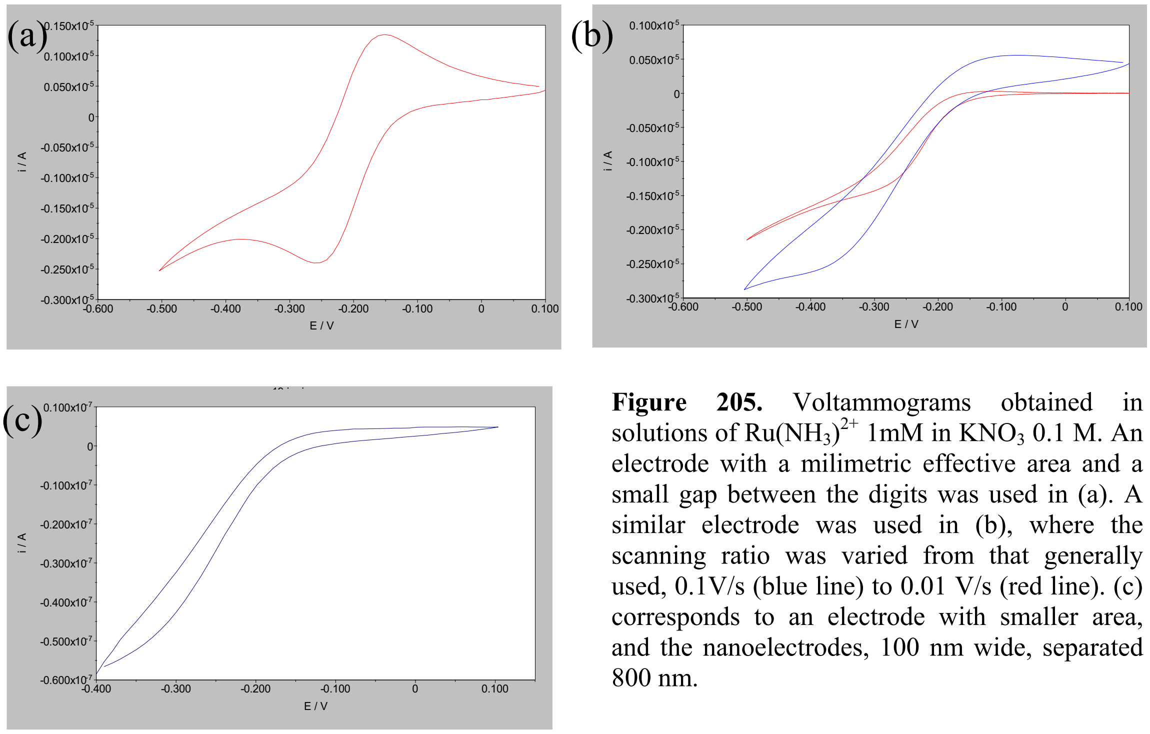

Figure 205. Voltammograms obtained in solutions of $Ru(NH_3)^{2+}$ 1mM in KNO_3 0.1 M. An electrode with a milimetric effective area and a small gap between the digits was used in (a). A similar electrode was used in (b), where the scanning ratio was varied from that generally used, 0.1V/s (blue line) to 0.01 V/s (red line). (c) corresponds to an electrode with smaller area, and the nanoelectrodes, 100 nm wide, separated 800 nm.

Some of the electrodes, especially those having large gaps, exhibited a very pronounced ultramicroelectrode behaviour. This was also very clearly seen when one of the two matrixes of the IDEs was disconnected, and the voltammograms obtained only by measuring the current thorough the other one (with this, the pitch of the active electrode was doubled). Figure 205 (c) shows an example: the oxidation limit current is reached and maintained for voltages above -0.15 V. The used IDE had an electrode width of 100 nm, and a pitch of 450 nm. By disconnecting one of the matrix, the pitch is 900 nm (the gap between active electrodes is then 800 nm).

Ultramicroelectrode behaviour

Ultramicroelectrode arrays [7-9] (UMEAs) are arrays of electrodes that have a low relation between the electrode width (w) and gap between them (g). The electrodes size has to be in the order of few microns or below (25 µm as maximum), and the main requirement is that the separation between them has to be larger than their width, i.e. $g/w \geq 3$.

As has already been mentioned above, in steady solutions, the evolution of the electrochemical reactions is governed by diffusion. When the voltage is applied, the reaction consumes the species around the electrode, and a gradient in the concentration profile appears. This is the **diffusion layer** (Figure 206), that extends up to a distance *d* from the electrode, and the fresh reactant has to diffuse thorough it to arrive to the metal electrode. In normal electrodes, the diffusion layer is larger than the distance between electrodes, so they overlap, and the net flux of reactant is vertical (Figure 206 (a)). In the UMEAs, the diffusion layer achieved in a readily accessed experiment is smaller than the distance between electrodes, so the current flux is radial (Figure 206 (b)), and the current flux (~ current intensity/gold area) in each electrode is higher than in the previous case. This configuration leads to a high signal-to-noise ratio on one side, and to a better exploitation of the total area on the other. For these reasons, UMEAs are convenient for the detection of very low concentrations of specimens.

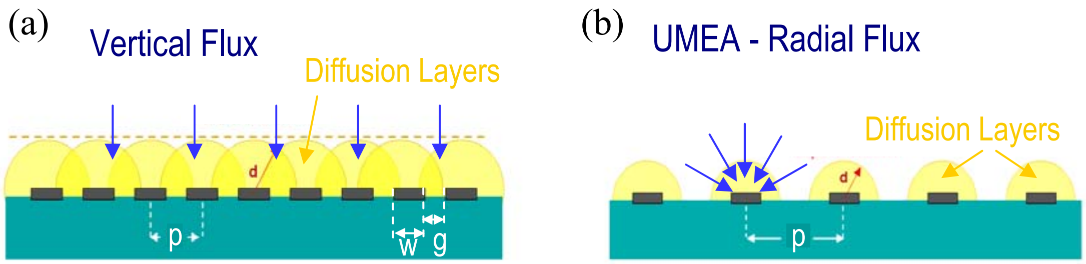

Figure 206. Schemes of the diffusion layers distribution in normal structured electrodes (a) and in a ultramicroelectrode array (b). When the separation between electrodes is smaller than the extension of the diffusion layer, they overlap, and the flux of fresh reactive is vertical. In the UMEA, the distance between the electrodes is larger than the radio of the diffusion layers, so they are independent, and the flux at each one is radial.

This especial geometry leads to current trends like those shown in Figure 205, as the drop of the current when the diffusion layer increases (this is, the peaks) is not so pronounced as in conventional electrodes.

Some of the electrodes used in this work comply with these requirements, so the current flow in each digit is higher than in other cases, which makes the nIDEs suitable for the sensing and quantification at very low concentrations of specimens.

9.3-2:c.- Dopamine

A more complex specie, this is, dopamine, was also used to test the electrochemical response of the nIDEs. Its detection and quantification is a very interesting and challenging task in biomedicine [10, 11], as dopamine acts as a neuromodulator in the brain [12], and its lack or anormal levels are related to degenerative diseases of the nervous system [13].

The redox reactions of this specie involve 2 electrons:

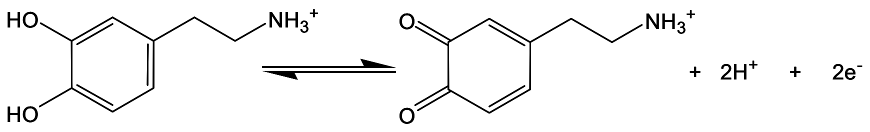

(35)

One of the main problems to study the dopamine signal in vivo is a pH shift. Changes in extracellular pH cause broad changes in the background of the electrode signal as a result of protonation and deprotonation of surface groups, and changes in the peak positions [14]. To reproduce the optimal media for the reactions, an alkaline buffer solution of phosphate with a pH= 7.4 (i.e., the blood pH) was prepared as supporting electrolyte for the dopamine solutions.

Electrodes of the first generation were used for these measurements.

Voltammograms

For this substance, it was very challenging to obtain a clear definition of the redox peaks in the voltammograms. Even for further activation processes and wider voltages sweep (up to 0.8 V) no real definition of the peaks was observed. Nevertheless, a clear difference in the signal when compared to the blank solution (phosphate) was observed, as can be seen in Figure 207 by comparing the dotted line with the solid ones, obtained for different concentrations of dopamine.

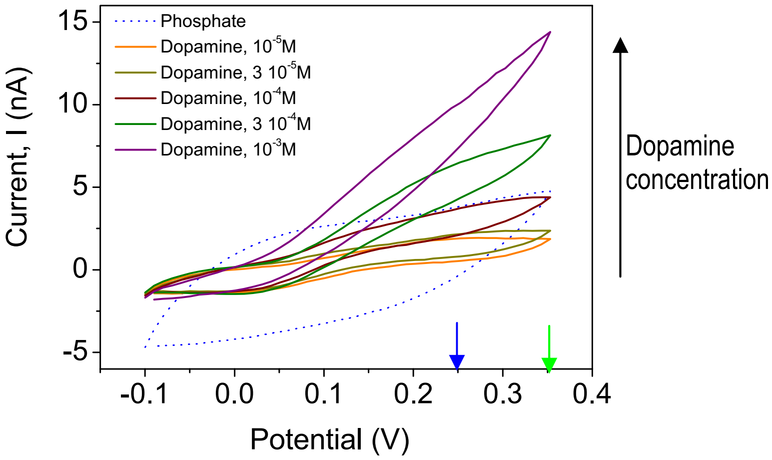

Figure 207. Voltammograms obtained in phosphate solutions, having different concentrations of dopamine., at a scanning ratio of 0.1 V/s.

As a tentative calibration, a plot of the current intensity at maximum (green line) and at the oxidation voltage (~ 0.25V) (blue line) as a function of the different concentrations is shown in Figure 208, with the corresponding sensitivities calculated without taking into accounting current intensity value obtained for the higher concentration of dopamine (0.9 mM).

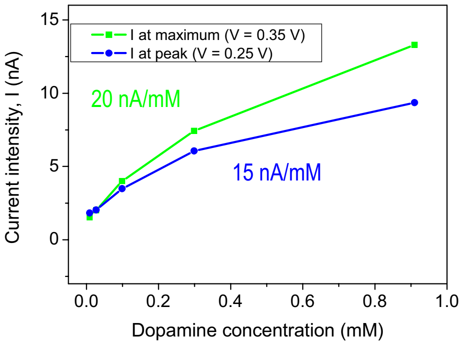

Figure 208. Dependence of the current at different voltages on the concentration of dopamine, obtained from the voltammograms of Figure 207.

Chronoamperometry

The chronoamperometric measurements were performed in a similar way to that described above. The potential was stepped from 0V to + 0.5V. Figure 209 shows the intensity profiles vs time trends for various concentrations of dopamine in the buffer solution, ranging from 10^{-5}M up to 10^{-3}M.

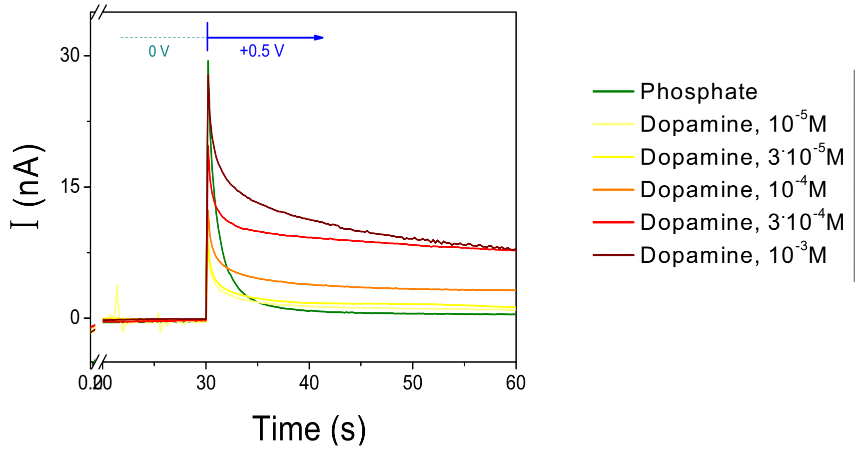

Figure 209. Current intensity vs time plots, obtained in dopamine solutions (in a phosphate buffer) by polarizing the electrodes at 0.5 V (at t=30s).

A calibration plot was obtained as well from these data. Figure 210 shows the dependence of the current intensity on the concentration. It shows a linear tendency for concentrations below 0.5 mM. After that, the sensor reaches a saturation range, and the sensitivity decreases. For that optimal range, **a sensitivity of 26 nA/mM** was obtained.

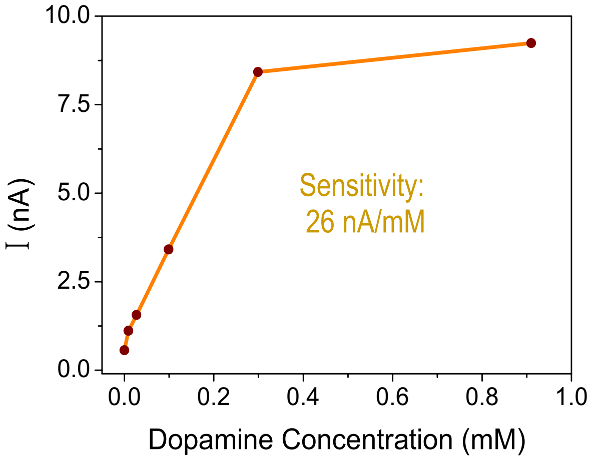

Figure 210. Calibration plot for dopamine in phosphate. This current intensity plot vs dopamine concentration allows to determine the concentration in an unknown solution, measured with this electrode at similar conditions.

In comparison with the calibration plot obtained from the voltammograms, in this second case, a linear trend is still observed for higher concentrations, and more accurate measurements can be performed for low concentrations, as the noise is lower and resolution and the sensitivity higher.

All these data show the correct performance of the nano-IDEs for electrochemical sensing and biosensing. The figure of merit of the electrodes places them among the electrodes that can be found in the literature, showing good sensitivity and resolution for low concentrations of the active species, as other ultra-micro-electrode arrays which typical dimensions are micrometric, and that have much larger active areas.

9.4.- REFERENCES

[1] Autolab Instruments, from the Eco Chemie group. http://www.ecochemie.nl/.

[2] Kissinger, P. and Heineman, W.,
Laboratory techniques in electroanalytical chemistry. 2nd ed., rev. and expanded ed. 1996, New York: Marcel Dekker, Inc.

[3] Kissinger, P.T. and Heineman, W.R.,
Cyclic voltammetry.
Journal of Chemical Education, 1983. **60**(9): p. 702.

[4] Cottrell, F.G.,

Z.Physik.Chem., 1902. **42**: p. 385.

[5] Olivé-Monllau, R., Orozco, J., Fernández-Sánchez, C., Baeza, M., Bartrolí, J., et al.,
Flow injection analysis system based on amperometric thin-film transducers for free chlorine detection in swimming pool waters.
Talanta, 2009. **77**(5): p. 1739-1744.

[6] Simm, A.O., Banks, C.E., Wilkins, S.J., Karousos, N.G., Davis, J., and Compton, R.G.,
A comparison of different types of gold–carbon composite electrode for detection of arsenic(III).
Analytical and Bioanalytical Chemistry, 2005. **381**(4): p. 979-985.

[7] Ordeig, O., Banks, C.E., Davies, T.J., Campo, F.J.d., Muñoz, F.X., and Compton, R.G.,
Gold Ultra-microelectrode Arrays: Application to the Steady-State Voltammetry of Hydroxide Ion in Aqueous Solution.
Analytical Sciences, 2006. **22**(5): p. 679.

[8] Jürgen, H.,
Ultramicroelectrodes in Electrochemistry.
Angewandte Chemie International Edition in English, 1993. **32**(9): p. 1268-1288.

[9] Orozco, J., Suárez, G., Fernández-Sánchez, C., McNeilb, C. and Jiménez-Jorquera, C.,
Characterization of ultramicroelectrode arrays combining electrochemical techniques and optical microscopy imaging.
Electrochimica Acta, 2007. **55**(2): p. 729-736.

[10] Feng-Lin, C., Wen-Ying, C., Li-Min, K., Chih-Heng, L., Shi-Wei, W., et al.,
An electrochemical dopamine sensor with a CMOS detection circuit.
Journal of Micromechanics and Microengineering, 2008(7): p. 075028.

[11] Robinson, D.L., Venton, B.J., Heien, M.L.A.V. and Wightman, R.M.,
Detecting Subsecond Dopamine Release with Fast-Scan Cyclic Voltammetry in Vivo.
Clinical Chemistry, 2003. **49**(10): p. 1763-1773.

[12] Garraux, G., Peigneux, P., Carson, R.E. and Hallett, M.,
Task-Related Interaction between Basal Ganglia and Cortical Dopamine Release.
Journal of Neuroscience, 2007. **27**(52): p. 14434-14441.

[13] Heien, M.L.A.V., Khan, A.S., Ariansen, J.L., Cheer, J.F., Phillips, P.E.M., et al.,
Real-time measurement of dopamine fluctuations after cocaine in the brain of behaving rats.
Proceedings of the National Academy of Sciences of the United States of America, 2005. **102**(29): p. 10023-10028.

[14] Davis, J. and Cooper, J.M.,
Electrochemical manipulation of localised pH: application to electroanalysis.
Journal of Electroanalytical Chemistry, 2002. **520**(1-2): p. 13-17.

Chapter 10

Electrode characterization II: Impedance Spectroscopy

Applications:

Nanoparticle quantification and DNA hybridization detection

Impedance spectroscopy is a powerful method that allows detecting small changes in a liquid media and/or in the electrode surface, that can be related to several phenomena. For example, a change in the specimen concentration, an affinity binding, a selective recognition, or many other events that may difficult to "observe", can be detected with this technique.

In this chapter we will introduce the fundamental concepts of impedimetric spectroscopy and the equivalent circuit models. Standard characterizations performed with the nanometric IDEs to study the response of the devices under different conditions will be reported.

Two applications showing the use of the devices for (bio)sensing will be presented: the detection and quantization of nanoparticles, and the detection of DNA hybridization on the electrodes surface.

10.1.- INTRODUCTION TO IMPEDANCE SPECTROSCOPY

Impedance spectroscopy is a very versatile electrochemical tool to characterize **intrinsic electrical properties** of any material or solution and its interface [1]. It analyzes the impedance ($Z \equiv V/I$) of the observed system as a function of the frequency and exciting signal. This analysis provides quantitative information about the conductance, the dielectric coefficient, the static properties of the interfaces of a system, and its dynamic change due to adsorption or charge-transfer phenomena. A low amplitude is generally used, which facilitates a non-invasive observation of any sample without any or less influence on the electrochemical state.

10.1-1. Impedances

The alternating current (a.c.) measurements exploit their ability to scan the frequency domain, allowing separate excitation of different **processes with different time constants**. Therefore, slow processes like chemical reactions and fast processes like ionic conduction can be studied individually this way.

For a sinusoidal signal with an amplitude V_0, the applied voltage, V(t) can be expressed as:

$$V(t) = V_0 sen(\omega t) \equiv V_0 e^{i\omega t} \qquad (36)$$

As a consequence, a sinusoidal current is generated, I(t), that may have a phase delay, φ, with respect to V(t). Its expression, in the stationary regime, is given by:

$$I(t) = I_0 sen(\omega t + \varphi) \equiv I_0 e^{i\varphi} e^{i\omega t} \qquad (37)$$

Thus, by combining (36) and (37), the impedance of the media is obtained:

$$Z = \frac{V_0}{I_0} e^{i\varphi} \qquad (38)$$

This assumption needs a linear dependence of the current intensity on the applied potential, which is not usually true when dealing with electrochemical systems. An example of non-linear system is shown in Figure 211 (a). Nevertheless, if the amplitude of the a.c. signal is small, the obtained response can be considered linear (Figure 211 (b)), and the expressions obtained for Z(ω) are valid.

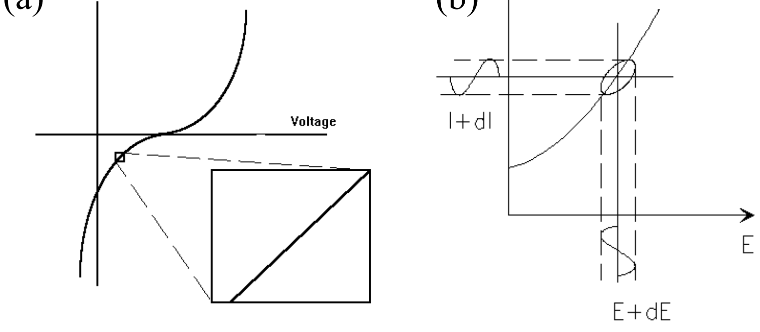

Figure 211. Current dependence on voltage for nonlinear systems: pseudo-linearity (a) and a.c small signal approximation (b) to analyze the pseudo-linear region, i.e. the impedance value.

The impedances corresponding to the conventional components of an electric circuit can be easily calculated from their relations between I and V. These are listed in Table 8.

Table 8 – Circuit elements, relationship between V and I, and the corresponding expression for the impedance, Z.

Resistor	$V = I \cdot R$	$Z = R$
Capacitor	$I = C \cdot \frac{dV}{dt}$	$Z = \frac{1}{j\omega C}$
Inductor	$V = L \cdot \frac{dI}{dt}$	$Z = j\omega L$

The total impedance of a circuit with different elements can be calculated by adding their corresponding impedances if they are combined in serie, or their inverses, if they appear in parallel, as schematized in Figure 212.

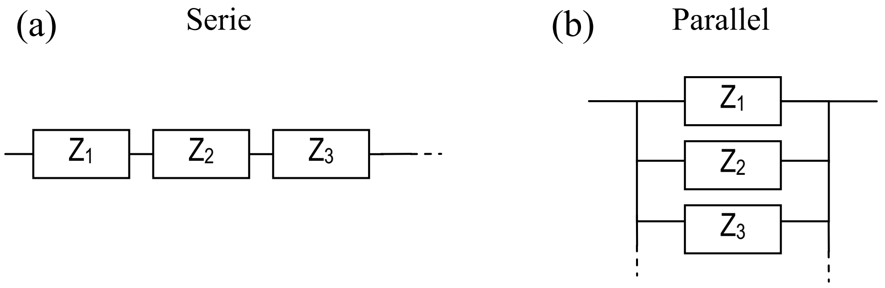

$$Z_{tot} = Z_1 + Z_2 + \ldots \qquad \frac{1}{Z_{tot}} = \frac{1}{Z_1} + \frac{1}{Z_2} + \ldots$$

Figure 212. Combination of impedances, in series (a), and in parallel (b), and the corresponding expression to calculate the resulting total impedance of the system.

10.1-2. Impedance spectra

The impedance can be expressed in terms of a real (Z’) and an imaginary part (Z”):

$$Z = Z' + jZ'' \qquad (39)$$

The understanding of the impedance in this form leads to the most common representation of the experimental data: the so-called **Nyquist plot** (Figure 213 (a)). Here, the real part is plotted on the X axis and the imaginary part on the Y axis of a chart. Each point on the Nyquist plot is the impedance at one frequency. Usually, for the data obtained in electrochemical cells, the frequency increases leftwards.

From this representation the frequency value or its ratio of increment cannot be deduced, so it is generally complemented with **Bode plots** (Figure 213 (b)), where the impedance modulus (top) and the phase angle (bottom) are explicitly plotted as a function of the frequency (log).

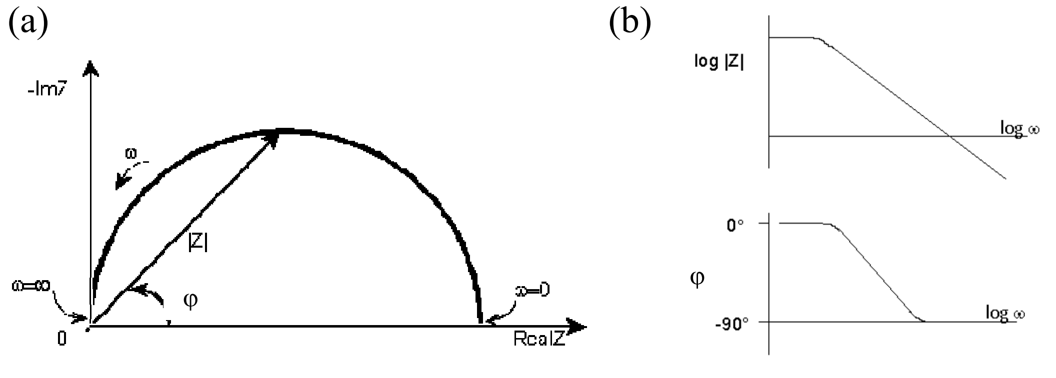

Nyquist plot

Bode plot

Figure 213. Data representation: Nyquist plot (a), where the imaginary part of the impedance (Z”) is plot as a function of the real part (Z’) for each frequency. In the example of the figure, low frequencies are in the right part of the graph, and high ones in the left. In the Bode plots (b), the modulus of the impedance (|Z|) and the phase angle (φ) are plot as a function of the frequency, as shown in the top and bottom graphs respectively.

10.1-3. Equivalent circuits

How does this apply to an electrochemical cell?

The general behaviour of an electrode immersed in a (liquid) media excited with an a.c. signal can be explained with an equivalent electric circuit, where the different responses and movements of the charges involved can be represented with resistors, capacitors or inductors. The equivalent circuits can be further used for a deeper understanding of the system behaviour, for modellization and for the calculation of the values of various parameters.

10.1-3:a.- Equivalent Circuit Elements

The study of the elements involved in an equivalent circuit may be very complicated, as the cells and the reactions involved sometimes are very complex. For example, redox reactions taking place at the electrode can be represented as a *charge-transfer resistance*. Diffusion processes (needed also for the red/ox reactions) can create an impedance known as the *Warburg impedance*, that depends on the frequency of the potential perturbation. To simplify, here we will describe briefly only the terms related to the response of the IDEs immersed in inert pure liquids or aqueous solutions.

Figure 214 (a) is a drawing of the different zones that contribute to the impedimetric signal when the electrodes are polarized: the double layer (A), the media (B) and the substrate (C).

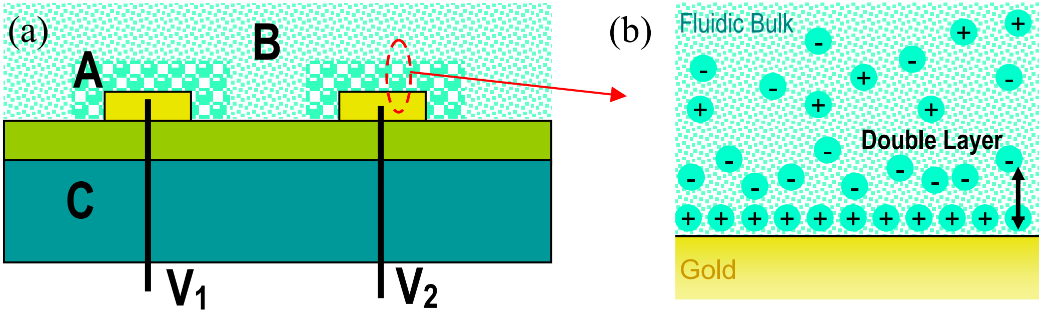

Figure 214. Different parts of the polarized electrodes in a solution, necessary to describe the electric model (a). Three parts appear: the double layer (A), the liquid (B) and the substrate (C). In (b), a scheme of double layer is shown: when the electrode is polarized, a high concentration of ions with the opposite charge are attracted very close to the surface. Ions of the opposite charge form a second layer next to the first ones, screening the charge accumulation.

A. The double Layer appears as a consequence of the polarization (charging) of the metal electrodes: the ions in the liquid media, having the opposite charge of that of the electrode, are attracted and surround the metal surface. To screen this charge accumulation, the concentration of ions of the opposite charge increases in the vicinity (Figure 214 (b)). These two charges distributions with opposite signs form the double layer, that acts as a capacitor. The value of the double layer capacitance (C_{dl}) depends on many variables including electrode potential, temperature, ionic concentrations, types of ions, oxide layers, electrode roughness, impurity adsorption, etc.

It should be taken into account that what we consider as capacitors in the equivalent circuits, actually, in impedimetric spectroscopy experiments often do not behave ideally. Instead, they act like **a constant phase element** (CPE) as defined in (40), where $0 \leq \alpha \leq 1$. For an ideal capacitor, $\alpha = 1$.

$$Z_{CPE} = \frac{1}{C(j\omega)^{\alpha}} \tag{40}$$

B. The liquid media (or solution) where the electrode is immersed, has itself a certain resistance (R_s) and capacitance (C_{diel}), that also depend on the presence of mobile charges. The solution resistance is often a significant factor in the impedance of an electrochemical cell. The resistance and capacitance of an ionic solution depend on the ionic concentration, type of ions, temperature and the geometry of the area in which current is carried.

C. The substrate parasitic capacitance and resistance appears as a consequence of the dielectric nature of the SiO_2/Si substrate. The current flow thorough the substrate can be neglected, compared to that in the liquid, but the charge storage (parasitic capacitance) needs to be taken into account for modelling the equivalent circuit. It can be easily measured from an impedimetric spectra obtained with the electrode at air.

10.1-3:b.- Equivalent circuit models

Whit these elements, an equivalent circuit that reproduces the electric behaviour of the polarized electrodes in a liquid media can be constructed.

The simplest representation of a solid electrolyte cell in terms of an equivalent circuit and the correspondent impedance spectrum are depicted in Figure 215. Each semicircle (b) is associated to a RC sub-circuit (a), that is, to a time constant τ (τ =1/RC) and subsequently to a process in the cell.

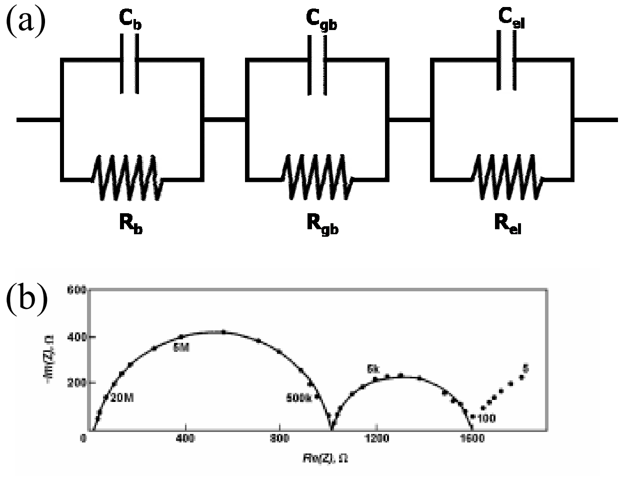

Figure 215. Simplest cell of an electrolyte cell in terms of equivalent circuits (a), and the correspondent impedance spectrum (b), where each semicircle is associated with a RC sub-circuit, and that has an typical time constan.

This model is a simple model, and it is usually varied, so more elements are needed, in different combinations and configurations.

10.1-4. Electric model for Interdigitated nanoelectrodes

Impedimetric spectroscopy allows direct detection, avoiding the use of radioactive, fluorescent, enzymatic or electrochemical labels or signal enhancement. In principle, IDEs have several advantages over conventional electrodes for bio-sensing. The main one is an improved sensitivity compared to non-structured electrodes, owing to the electric field concentration in the area in-between the digits, what can be exploited for the sensing of target elements of size similar to this gap. Thus, when the target element is very small (i.e., in the nanometric scale), the nano-IDEs can be tailored to improve the sensitivity, compared to micrometric electrodes.

The electric field distribution in-between the digits and in the area surrounding the electrodes can be theoretically calculated from Laplace equation, under the appropriate boundary conditions, where φ is the electric potential.

$$\nabla^2\varphi = 0 \qquad (41)$$

This was solved in [2], and the resulting plot for the current flow around the digits is shown in Figure 216. A very important conclusion that can be extracted from this graph is that almost all the current and the "activity" is taking place below a vertical distance that is in the same order of magnitude of the pitch of the array (*L*): 95% is below L, and >99% below 2L. This means that, in order to maximize the sensitivity of the device, it is convenient to fabricate electrodes which characteristic dimensions are in the same range of the size of the target element. In addition, when the sensor surface is functionalized for selective recognition, the changes will take place also in a vertical distance ~L. This fact has to be borne in mind for the design of the geometric parameters for each specific application.

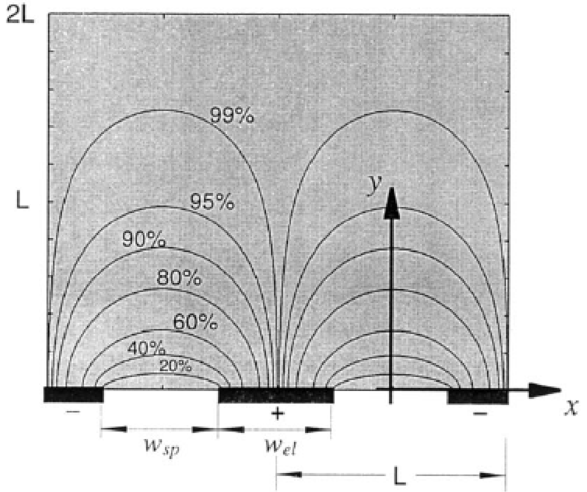

Figure 216. Calculated current comprisement of interdigitated electrodes. The gap between the electrodes is equal to the electrode width. A curve of e.g. 80% means that 80% of the current flows beneath the curve. [2]

The circuits associated to the metallic nano-IDEs into a liquid are a little bit more complex than the basic cells shown previously. Figure 217 (a) shows the model proposed by Gerwen et. al. [2, 3]. The **upper half plane represents the solution** with its resistance (R_{sol}) and capacitances (C_{diel}) and the double layer capacitance (C_{dl}). The **bottom half plane represents the dielectric** layer on top of the silicon substrate. It can be seen that for an oxide thickness larger than the pitch of the electrodes array, the capacitances C are negligible compared to the capacitance C_{ox} in the bottom half –plane. The electrodes that were used in this work had an oxide layer of 1.5 μm, and the typical pitch of the electrodes was < 400 nm. This allows us to neglect the capacitance C when building the equivalent circuit. As it has been mentioned above, a measurement of the capacitance at air gives the value of the remaining C_{ox}, (parasitic capacitance). Subtracting this value to the rest of the measurements (in liquid media) allows obtaining rough information of only the upper part of the cell (Figure 217 (b)).

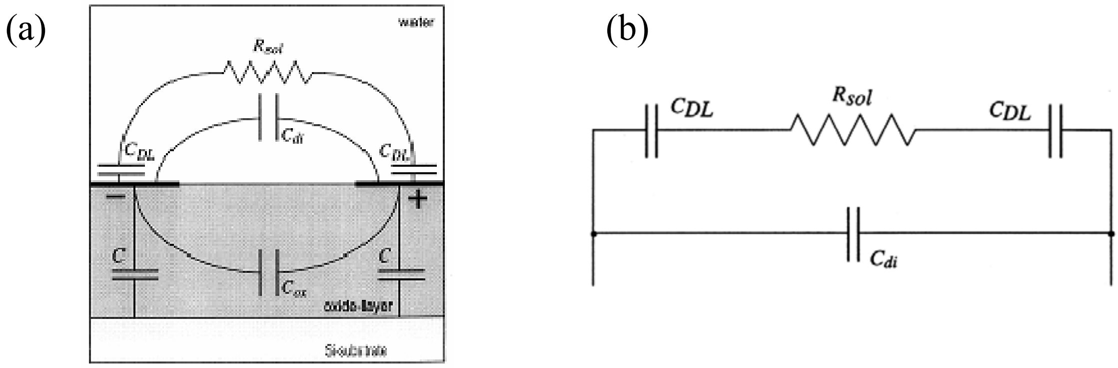

Figure 217. Equivalent circuits. (a) Unity cell with different impedance components. The lower half plane contains the capacitance through the oxide Cox and the capacitance C going to the conductive Si substrate. The upper half plane contains two paths: the dielectric capacitance C_{di} of the solvent, i.e. water, and the path containing the resistance of the solution R_{sol} in series with the double layer capacitances C_{dl} at the electrodes. (b) A simplified equivalent circuit representing the impedimetric response of IDEs in aqueous solution. This circuit contains the upper half plane of (a). [2]

This model reproduced quite well our experimental results. But, for a finer fit, slight modifications had to be considered as will be shown next, for the results obtained from standard characterizations.

10.2.- GENERAL CHARACTERIZATION

The general dependence of the impedance of the electrodes/solution system on the frequency was studied for two cases: for solutions with various conductivities (aqueous solutions with different concentrations of NaCl) and for different ε_r (pure liquids of different natures).

10.2-1. Experimental set-up

For the experiments, a Solartron equipment [4] was used, as shown in Figure 218 (a). A detail of the electrode connected to the equipment and immersed in a liquid sample can be seen in Figure 218 (b).

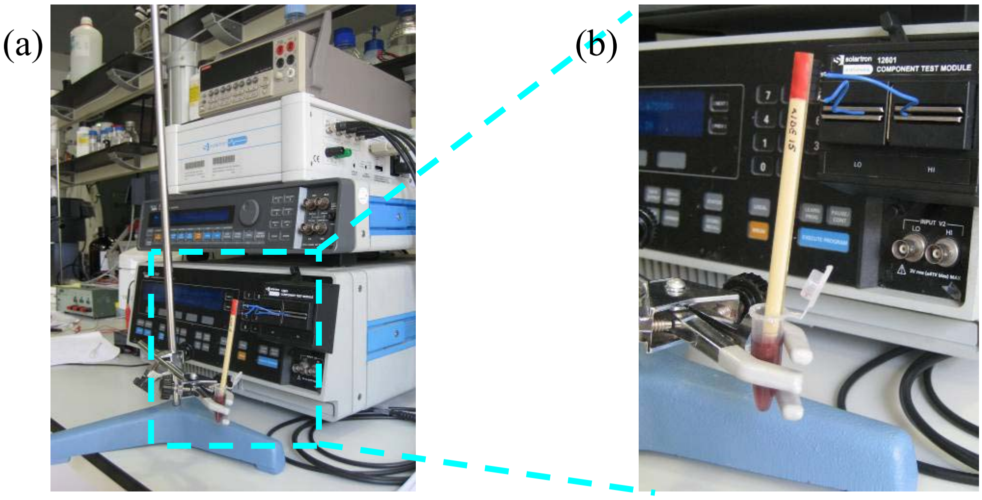

Figure 218. Equipment used (a) with the potentiostat and the frequency response analyzer, from Solartron, and detail of one electrode (b), connected for impedance spectroscopy performance, immersed in the liquid sample.

10.2-2. Dependence on the conductivity

To characterize the impedimetric signal of the nano-IDEs for medias with different conductivities, the impedance-frequency response was studied to aqueous solutions with **different NaCl concentrations**. The salt dissolved in DI water adds ions to the media, increasing its conductivity. Solutions with concentrations varying from 10^{-4} M to 0.1 M were prepared. Figure 219 shows the dependence of various parameters (|Z|, φ and C) on the frequency (a, b and c, respectively) and the Nyquist (Z' vs Z") plot (d), for each dissolution.

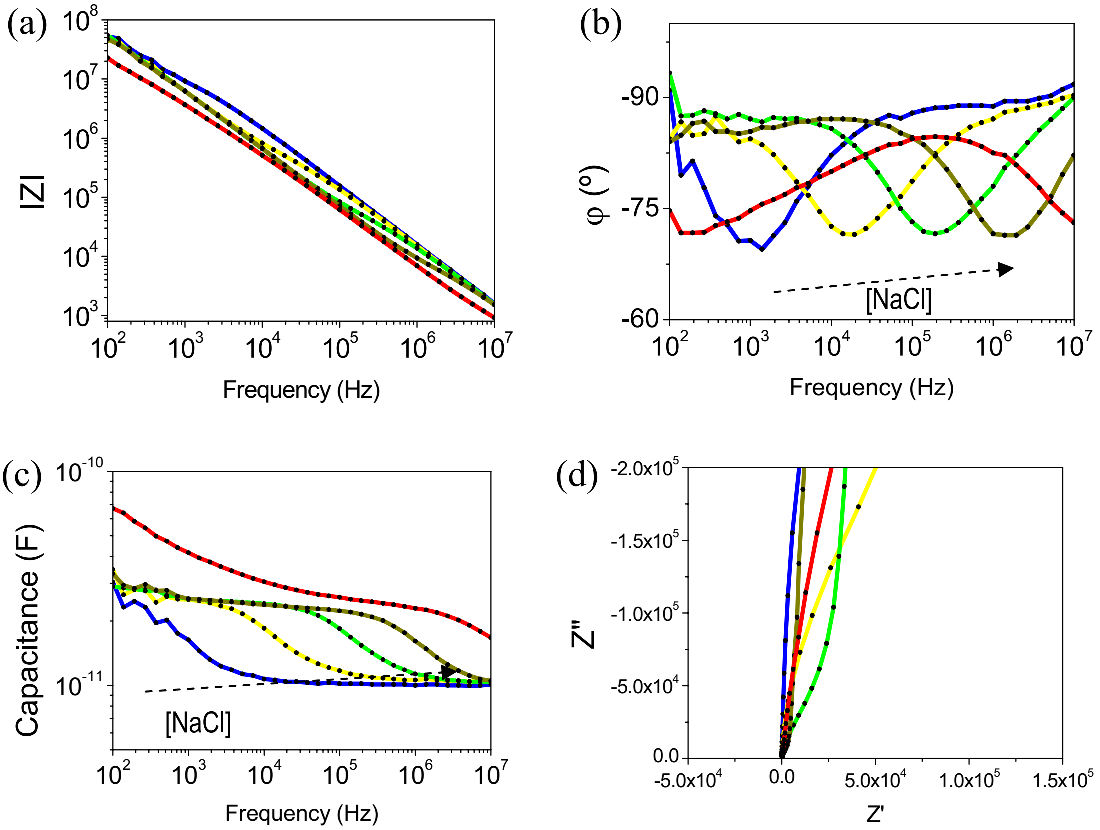

Figure 219. Bode plot (|Z| and φ as a function of the frequency) (a) and (b) respectively, obtained for different H2O and different concentrations of NaCl (aq.). (c) shows the dependence of the capacitance on the frequency, and (d) the Nyquist plot for the solutions.

All the parameters show different responses for each concentration of NaCl, showing that the number of ions present in the media influences the signal. For the nano-IDEs studied, the parameter where the differences can be more clearly observed is the **capacitance**. In the spectrum shown in Figure 219 (c) it can be observed that there are two values for the capacitance: the low-frequency one, (28 pF) and the high frequency one, (10 pF). **The frequency at which C drops from one value to the other one depends on the concentration of the solution.**

For a deeper study of the results, the spectra were fitted attending to electric models based on that shown previously in (Figure 217(b)). The simulations of the frequency response of the equivalent circuits were done with the same software used to record the experimental data (*Zplot* and *Zview*). Figure 220 (a) shows the experimental data (green line) and the modelled response obtained using two different equivalent circuits that are shown in Figure 220 (b) and (c). First, the double layer was represented as a capacitor (Figure 220 (b)), but the resulting trend (dashed line) didn't fit the slope of the capacitance for low frequencies. If the double layer was simulated with a constant phase element (CPE) (circuit in Figure 220 (c)), the concordance with the experimental results was improved (dash-dot line).

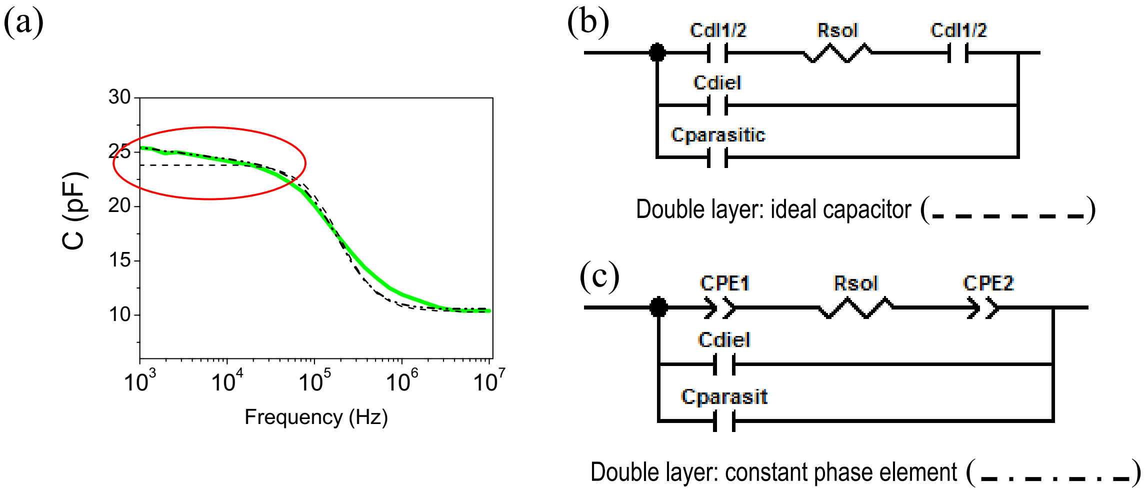

Figure 220. (a) Comparison of the measured capacitance as a function of the frequency for an aqueous solution of NaCl, 10^{-3} M (green line), with the simulations obtained with the equivalent circuits shown in (b) and (c) (discontinuous black lines). In (b), the double layer is modelled as an ideal capacitor (dash-dot line in (a)). In (c), it has been modelled as a constant phase element (CPE) (dashed line in (a)). Both models fit quite well the experimental response for frequencies above $5 \cdot 10^4$ Hz, but below that (the double layer is the dominant capacitance), the circuit in (c) shows the best fit.

By using the electric model of Figure 220 (c), the values of the C_{diel}, $C_{parasitic}$, CPE(double layer) and R_{sol} can be estimated for the studied solutions.

Figure 221 shows the experimental spectra obtained for DI water (blue line), and for two dissolutions with different NaCl concentrations (10^{-3}M - green line, and 10^{-2}M - dark yellow line). The black lines correspond to the fitting plots obtained with the equivalent circuit. Table 9 shows the values of R_{sol} and C_{diel} obtained for different concentrations. The values of CPE (common for all the spectra) are 40 pF, and α=0.97, which, as expected, is very close to 1, indicating that the double layer capacitance is almost an ideal capacitor. The capacitance of the substrate ($C_{parasit}$) is ~9 pF, as obtained from the fit, and that agrees with the measurements with the electrode at air.

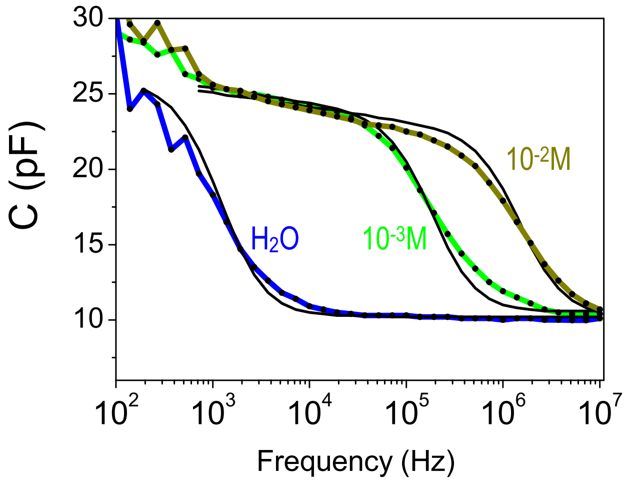

Table 9. Tabulated values for the different R and C of the circuit.

[NaCl]	R_{sol} (Ω)	C_{diel} (pF)
H_2O	$1.3 \cdot 10^7$	1.5
10^{-4}M	$6.5 \cdot 10^5$	1.8
10^{-3}M	$8.8 \cdot 10^4$	2.4
10^{-2}M	$1.4 \cdot 10^4$	2.3

$CPE_1=CPE_2=32$ pF, α=0.97

$C_{parasit}= 8.8$ pF

Figure 221. Simulations for C as a function of the frequency (black lines), obtained with the equivalent circuit shown in Figure 220 (c) compared to the experimental spectra for DI water (blue line), and NaCl aqueous solutions 10^{-3}M and 10^{-2} M (green and dark yellow lines, respectively). The modellization gave the general values for the electrode of the capacitance of the double layer (CPE_1 and CPE_2 and α) and that of the substrate ($C_{parasit}$) shown in Table 9, and, as listed, the values of R_{sol} and C can be also obtained for each concentration.

10.2-3. Dependence on the permittivity (ε_r)

Figure 222 shows the dependence of the capacitance on the frequency for liquids with different permittivity, such as water, acetonitrile, ethanol, tetrahydrofurane (THF), hexane and air.

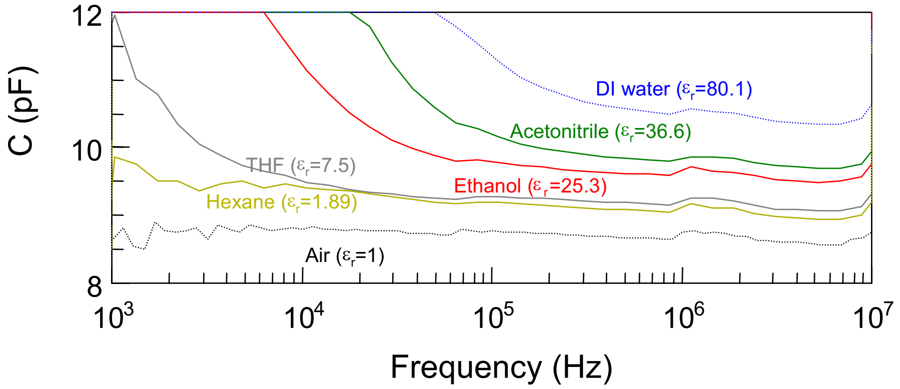

Figure 222. Dependence of the impedimetric signal (capacitance vs frequency) for various liquid medias with different permitivities: DI water (ε_r=80.1), acetonitrile (ε_r=36.6), ethanol (ε_r=25.3), tetrahydrofurane THF (ε_r=7.5), hexane (ε_r=1.89) and air (ε_r=1).

Each liquid responds in a different way to the a.c. voltage. For those with lower dielectric constants (ε_r), the capacitance of the media is reduced, obviously, as expressed for a capacitor.

$$C = \varepsilon_r \varepsilon_0 \frac{A}{d} \qquad (42)$$

Figure 223 shows the dependence of the capacitance on the dielectric constant of the media. The C values correspond to those measured at high frequency ($5 \cdot 10^6$ Hz), that is when the other possible slower processes that may contribute to the capacitance are not observed anymore. A linear relationship is observed, as the results are compared for the same electrodes (i.e., same A/d).

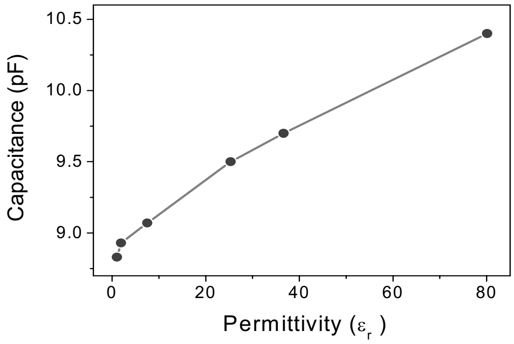

Figure 223. Dependence of the capacitance at high frequencies ($5 \cdot 10^6$ Hz) measured by the nano-IDEs on the dielectric constant of the liquid media.

Apart from the standard characterizations to study the impedimetric response of the electrodes, original applications were proposed, to take advantage of the high sensitivity of the electrodes, especially at short distances from the electrodes surface. Three different applications were addressed: detection of insulating nanoparticles, quantification of very small conductive gold nanoparticles and detection of the hybridization event of complementary DNA strands.

10.3.- APPLICATION I: NANOPARTICLE DETECTION

Inorganic nanoparticles [np] can nowadays be synthesized in a routinely way with a wide spectrum of materials and sizes. They can be used as connection elements for addressing small molecules. A large number of surface chemistry processes have been developed for functionalization of the np, so specific molecules and biomolecules can be attached to their surfaces. These advances enable to envision their use inside new generation biochips as specific labelling objects or for signal enhancement. This kind of application raises the problem of their on-chip detection. In this work, we propose to investigate the response of interdigitated nanoelectrodes in the presence of nanoparticles with different properties and sizes (i.e. metallic and insulating).

10.3-1. Conductive nanoparticles

The detection and/or quantification of gold nanoparticles is interesting for several reasons. One is that they can be easily synthesized with a good control of the diameter, and then functionalized (e.g., with thiols) for their use in selective recognition and/or signal enhancement. On the other hand, they are interesting themselves, as they are associated to contamination effects, and, due to their small size, they can have toxic effects in living organisms. Thus, a quantitative control of their concentration may have interesting applications for the use of the IDEs for security or environmental devices.

10.3-1:a.- Synthesis of the particles

The nanoparticles were provided by the group of Arben Mercoçi, from ICN[*], in the framework of the project Consolider NanoBioMed. Nanoparticles study is one of the major tasks of the project: synthesis, detection and functionalization for bio-medical applications.

The **gold nanoparticles** were home-made, synthesized following the procedures described in [5]. The resulting **diameter was 15 nm**, and, due to the process, they appear charged.

Dilutions from the original suspension were prepared (Figure 224), with concentrations from 0.05% in volume[†] down to $5 \cdot 10^{-5}$ % in volume.

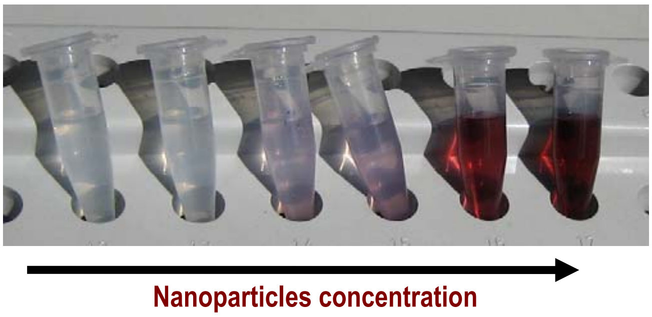

Figure 224. Different concentrations of the nanoparticles in aqueous suspensions, ranging from $5 \cdot 10^{-2}$ down to $5 \cdot 10^{-6}$ % in vol.

---

[*] ICN – Institut Català de Nanotecnologia. Campus de la UAB. 08193, Bellaterra (Spain).

[†] *% in volume*: percentage of liquid volume occupied by the nanoparticles. For nanoparticles with a diameter of 15 nm, 1% in vol. corresponds to $5.6 \cdot 10^{20}$ np/L.

10.3-1:b.- Spectra

The measurements were performed just by immersing the electrode in the eppendorf tubes containing the aqueous suspensions of Au nanoparticles, that were agitated just before, to ensure a good homogeneity of the [np] distribution.

The impedance spectra obtained for the different concentrations of Au np are shown in Figure 225. The lines corresponding to DI water and air have been plotted also (blue and black lines, respectively). These results are very similar to those shown in Figure 219, obtained for aqueous solutions with different concentrations of Na^+ Cl^- ions.

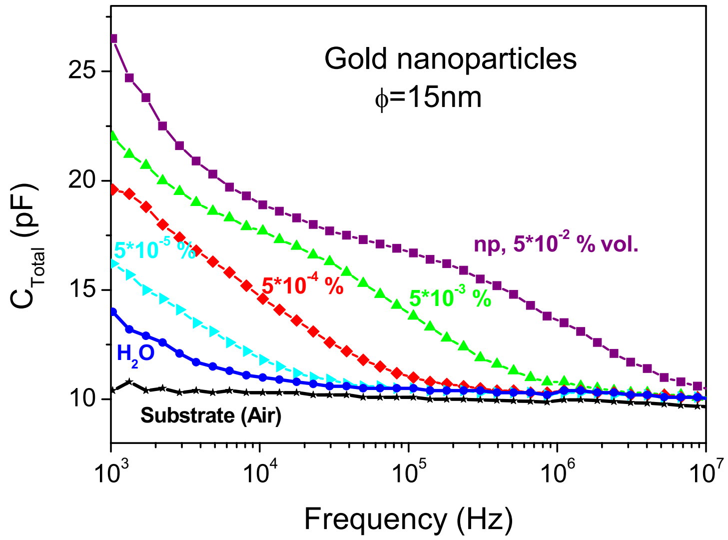

Figure 225. Capacitance measured for aqueous suspensions containing different concentrations of gold nanoparticles, as a function of the frequency.

As it has been mentioned above, the nanoparticles were negatively charged, and, as their diameter was very small compared to the typical dimensions of the electrodes, they would be able to follow the a.c. field that appears in-between the electrodes, behaving like the ions in the salt dissolutions previously shown. A schematic view of the situation is shown in Figure 226.

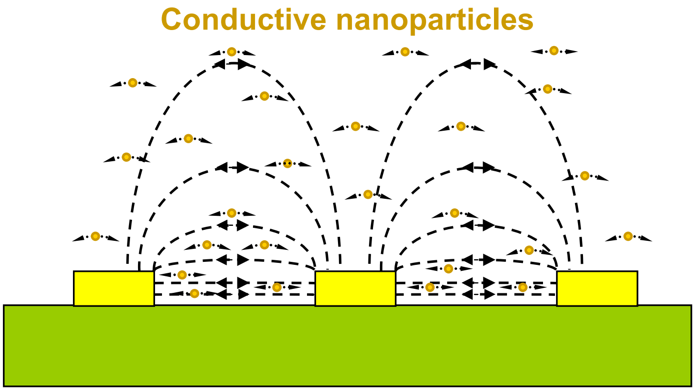

Figure 226. Scheme of the effect of the presence of the gold nanoparticles (15 nm diameter) in the aqueous media: their small size and the fact that they are charged improves the total capacitance of the media, as they can follow the electric field.

Figure 227 shows the capacitance as a function of the concentration of nanoparticles for different frequencies. A higher sensitivity is obtained for low frequencies (as could be already deduced from Figure 225), where a logarithmic dependence is obtained. By extrapolation of these lines, the lower limit for the nanoparticles concentration that can be detected by the sensor can be obtained for different frequencies.

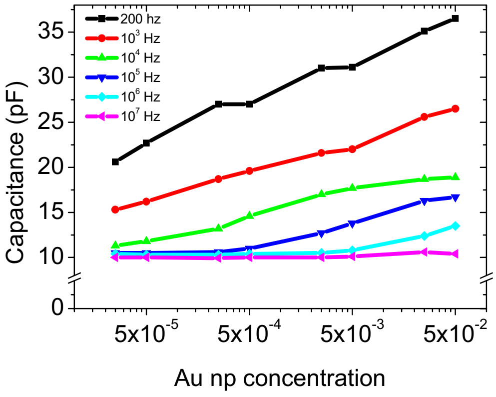

Figure 227. Dependence of the capacitance on the nanoparticles concentration for different frequencies.

The expressions obtained for the fit for the graph corresponding to 200 Hz and 1000 Hz are given in (43) and (44) respectively. The limit has been obtained by setting the minimum capacitance that can be detected as that corresponding to DI water for each frequency, that are 18.5 pF and 14 pF for the studied frequencies. This leads to a minimum detection limit of **$2.5{\cdot}10^{-8}$ % in vol.**[‡] and **$3.4{\cdot}10^{-9}$ % in vol.**[§] for 200 Ha and 1000 Hz respectively.

$$\text{Freq} = 200\text{ Hz} \qquad C([np]) = 5\text{pF} + \log([np]) + 40\text{ pF} \qquad [np]_{min} = 2.5{\cdot}10^{-8}\,\%\text{ vol} \qquad (43)$$

$$\text{Freq} = 1000\text{ Hz} \qquad C([np]) = 3\text{pF} + \log([np]) + 30\text{ pF} \qquad [np]_{min} = 3.4{\cdot}10^{-9}\,\%\text{ vol} \qquad (44)$$

It should be pointed out that the graph of Figure 227 is a **calibration** plot, that represents the dependence of a given parameter (C, in this case) on the nanoparticles concentration. With this, by measuring the capacitance and extrapolation or interpolation of the point, ***the concentration of gold nanoparticles of an unknown solution can be determined with the nanoIDEs sensors.***

In order to check the advantages of the nanodimensions of the electrodes, the measurements were repeated with a similar sensor with typical dimensions in the micrometric range. As already described in the previous chapter, a batch of similar sensors but having micrometric-size pitch and width was fabricated for this pourpose. Figure 228 shows a direct comparison of the results previously shown for a nanometric IDEs (left) and repeated for a micrometric IDEs (right). Both graphs have the same scale in the x and y axes. It should be remarked that the gold layer in the micrometric IDEs was ~ 100 nm thick, compared to ~ 20 nm in the nanometric case. Also, even if the patterned area was similar in both cases (200 µm x 200 µm), the total area of gold was the double in the micrometric case, as the electrodes were 10 µm picth, 10 µm wide, compared to 450 nm pitch 100 nm wide of the nanometric ones. Even though, an evident increase in the sensitivity and in the signal can be observed when using a device with nanometric electrodes.

[‡] $2.5{\cdot}10^{-8}$ % in vol = $1.4{\cdot}10^{10}$ np/L
[§] $3.4{\cdot}10^{-9}$ % in vol = $1.9{\cdot}10^{9}$ np/L

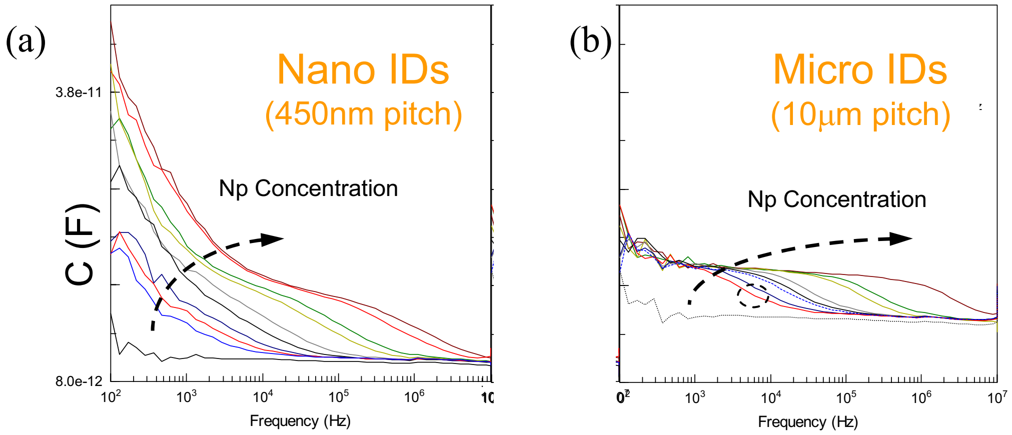

Figure 228. Comparison of spectra obtained for two different sensors, with different lateral sizes: nanometric (a) and micrometric (b) digits. The total capacitance was measured for different concentrations of AuNP in an aqueous media.

In this case, concentrations of $5 \cdot 10^{-5}$ % in vol. could not be distinguished from the DI water signal, or gave a signal below the water one. Even more, for this sensor, the sensitivity is lower, and the optimal range of frequencies for detection should be chosen as a function of the concentration, as the signal, for a fix frequency, does not change for all the variety of concentrations used here.

10.3-2. Insulating nanoparticles

The second type of nanoparticles to be detected and quantified by means of impedimetric spectroscopy using the nano-IDEs-based sensors were insulating "big" nanoparticles. For this, commercial **latex** and **silica nanoparticles**, **300 nm diameter**, were used.

This type of nanoparticles is interesting, as they can be functionalized and used for selective detection of species, proteins or other biomolecules that are more difficult to detect alone. It should be pointed out also that this type of "inert" and insulating nanoparticles are difficult to detect and/or quantify with other methods different from impedimetric spectroscopy, as they are non-interactive.

During the experimental characterizations, we found that the obtained data were not reproducible, as a consequence of the np precipitation onto the electrode surface. This made the direct measure of the np in the liquid suspension an arduous task.

For this reason, we changed the procedure. Instead of measuring directly in the liquid, the np were precipitated in a controlled way and the signal obtained afterwards was compared with that obtained previously without the nanoparticles.

For this, a drop of the liquid was deposited onto the sensor surface (in horizontal position), and left until the liquid completely evaporated, so all the nanoparticles of the drop precipitated onto the sensor surface.

In order to check the surface coverage obtained for different concentrations of nanoparticles, previous precipitation tests were performed on a non-patterned silicon surface, and the number of np per area measured from SEM images (Figure 229). Full-coverage of the surface was obtained for the suspensions containing 1% and 0.1% of np in volume[**]. For a concentration ten times lower (0.01%), 50 particles per 100 µm^2 were obtained, and 5 np/100 µm^2 in the most diluted case (0.001%).

[**] For these nanoparticles, 300 nm diameter, 1% in volume corresponds to $7.1 \cdot 10^{16}$ np/L

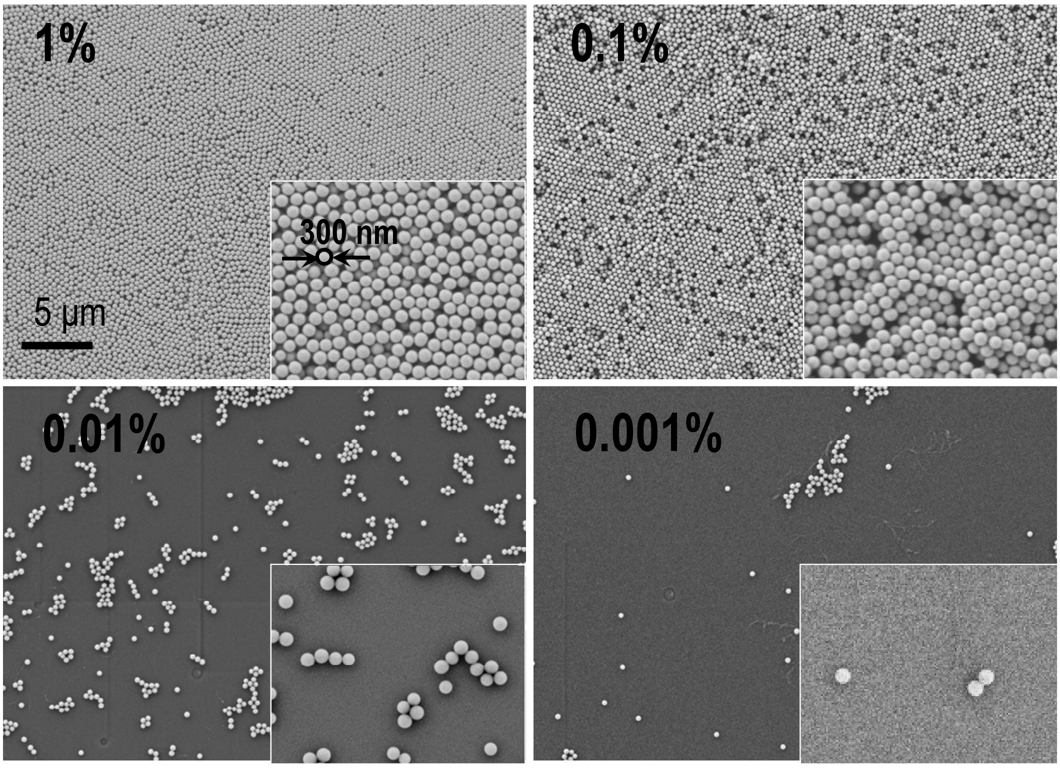

Figure 229. Concentrations of latex nanoparticles obtained by drying drops of aqueous suspensions of nanoparticles with different concentrations (% in volume) deposited onto a flat surface. The number of np/ µm^2 can be estimated from these images: Full-coverage is obtained for the suspensions of 1% and 0.1% in volume; 50 np/ 100µm^2 are counted for the 0.01%, and 5 for the 0.001% suspensions.

To analyze the impedimetric signal for the nano-IDEs covered with different concentrations of nanoparticles, a drop of suspension with the desired concentration was deposited onto the sensor surface. It was left until the liquid had evaporated, so all the nanoparticles had precipitated onto the surface. Then, the sensors were immersed in DI water, and the impedance spectra recorded. We checked with SEM images that they remained stuck to the surface even when immersed in water again. To minimize the possible desorption, the spectra where recorded with the electrode in an horizontal position. Figure 230 shows SEM images of the nanoparticles, precipitated onto the electrode surface. In this case, the electrodes gap was tailored (300 nm wide) so the nanoparticles (300 nm diameter) fitted in-between.

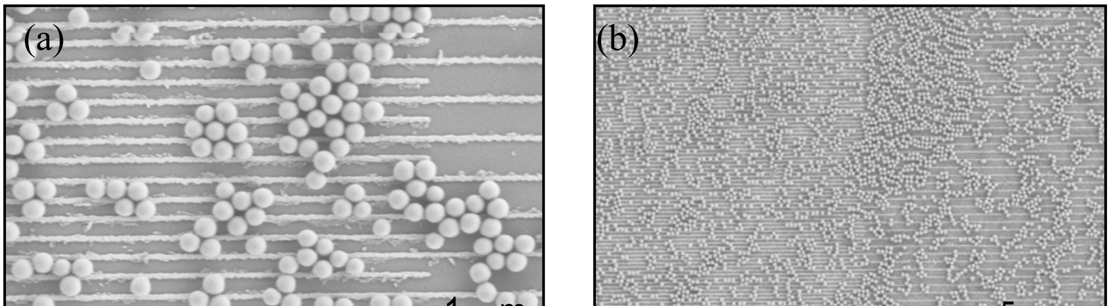

Figure 230. SEM images of silica nanoparticles deposited onto a nano-IDEs, with different magnifications. The gap in-between the digits was tailored to have the same size of the nanoparticles diameter (this is, 300 nm). As observed in the images, the particles stand in the gap in-between the digits.

Figure 231 shows the results obtained in two different cases: for very high and very low concentrations of nanoparticles. In the first one (Figure 231 (a)), the nanoparticles covered the major part of the area of the sensor. As a result, the total capacitance measured by the sensor significantly decreases, at high and low frequencies. In the second case, highly diluted suspensions were used. To obtain the different spectra shown in Figure 231 (b), one drop was deposited and left to dry, and then, the impedance recorded in water (green line). Then a second similar drop was deposited onto the same electrode and left to dry again, in order to obtain the double concentration of nanoparticles. The process was repeated once again, for a three-times concentration (red line), and so on. In this case, the changes were very small, but still detectable, especially at high frequencies, as can be seen in Figure 231 (b).

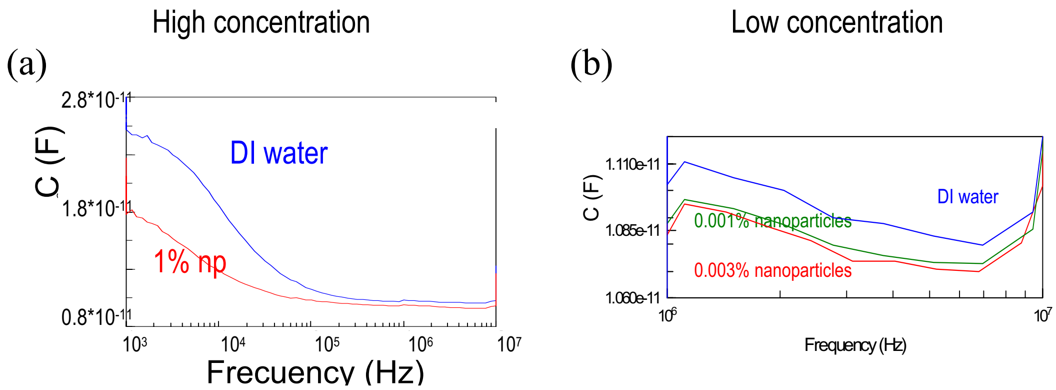

Figure 231. Spectras obtained measuring the total capacitance as a function of the frequency for different concentrations of the nanoparticles. In (a), a drop of a solution containing a very high concentration of nanoparticle s was dried onto the electrodes (total coverage). The capacitance is significantly reduced, as a consequence of the change in the dielectric constant in the area around the digits. In (b), very low concentrations were used (very few nanoparticles lie onto the sensor). The change in the high-frequency capacitance can be detected for concentrations as low as 0.001% in volume.

The presence of "big" insulating nanoparticles has completely different effect from that described for the conductive "small" ones described before. These nanoparticles lye in-between the digits, and inhibit the ions or molecules to be attracted to the electrodes when the electric field is created, as it is schematized in Figure 232. Thus, the capacitance measured by the sensor is reduced. The more nanoparticles deposited, the more it decreases, as a consequence of the decrease in the active area of the sensor.

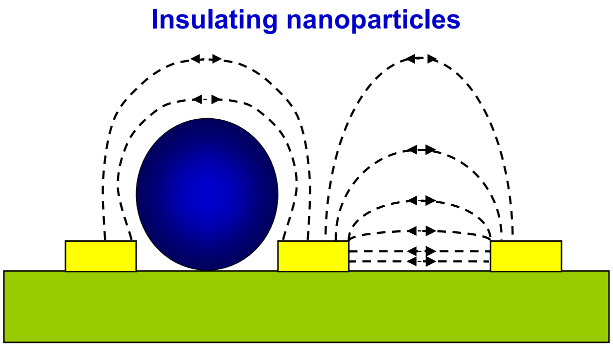

Figure 232. Scheme of the effect of the presence of an insulating "big" nanoparticle, sitting in the gap in-between the electrodes. They do not move, and they change the dielectric nature of the media in-between the digits.

The detection and quantification of different types of nanoparticles is an interesting task itself. For the case of gold nanoparticles, environmental or health security may profit of the sensitivity of these sensors, to determine and control the number of np in a volume. In the second case, the detection of insulating nanoparticles it's a challenging task, as they do not actively interact with the receptors. Impedimetric spectroscopy is a suitable technique for this task.

Even further, both types of nanoparticles can be functionalized, and used for more complex applications, such as specific recognition, or for signal enhancement, as schematized in Figure 233. The development and study of these applications leave an open research line for future works in the use of the nano-IDEs as (bio)sensors.

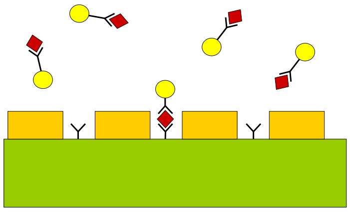

Figure 233. Scheme of one possible application of the detection of nanoparticles, for specific recognition or for signal enhancement.

Next, another different application will be described, where the gold nanoparticles were secondarily used, to enhance the signal obtained after hybridization of DNA.

10.4.- APPLICATION II: DETECTION OF DNA HYBRIDIZATION

The development of DNA-biosensors (**genosensors**), has been offering a valid alternative to the more classical methods for DNA analysis. In fact, these devices present several advantages in comparison with traditional approaches, such as low cost, rapid analysis, possibility of miniaturization and analysis in situ [6, 7]. Recently, among available electrochemical techniques, impedance spectroscopy [1] is rapidly developing as a tool for studying DNA hybridization [8]. This is due to its ability to directly probe the interfacial properties (capacitance, charge transfer resistance) of modified electrodes [9, 10].

The binding of target molecules to the probes (immobilised onto the biosensor surface) causes changes in the vicinity of the digits. Using an impedance spectroscopy with a nano-IDE sensor, these changes can be detected as a shift in the impedance, yielding a direct electrical signal related to the binding.

Taking advantage of the high sensitivity of the sensors to the changes at the sample surface and in-between the digits, the hybridization (or not) of DNA can be detected. This application is currently being developed in the framework of the project NanoBioMed, in collaboration with M. del Valle and A. Bonnani, from the Chemistry department of UAB[††].

[††] UAB – Departamento de Química. Universitat Autónoma de Barcelona. 08193 – Bellaterra (Spain)

10.4-1. Adenine (20 bases)

The first experiments were performed with *test* DNA strands (20 bases). All DNA stock solutions were prepared with sterilized and doubly distilled water and kept frozen until used. Their bases sequences are shown in Table 10:

Table 10. Lines and gene sequences used for the experiments

Probe: d(pT)20 (20 mer):
5'-TTTTTTTTTTTTTTTTTTTT-3'

Target: d(pA)20-bio (20 mer):
5'-AAAAAAAAAAAAAAAAAAAA-3' (modified with biotin in 5' end)

Target (negative control): d(pA)20 (20 mer):
5'-AAAAAAAAAAAAAAAAAAAA-3'

The protocol had been already optimized and used to detect these gene sequences using graphite–epoxy composite electrodes and measuring the change of interfacial charge transfer resistance using a redox marker[11].

In this work, we followed a similar procedure for the absorption and incubation of the different DNA, and the impedance spectra were recorded in DI water, as the electrodes were sensitive enough to directly detect changes in the capacitance.

The process protocol is schematized in Figure 234:

1. A first **blank measure** was performed in DI water, with clean IDEs surface.
2. **Physical absorption of the DNA probe**. A drop (10 µL) of a solution (TSC1[‡‡]) containing 30 pmol of the probe DNA was deposited onto the sensors surface, and left in an oven at 80ºC during 30 minutes, so the strands were physically absorbed to the surface. A washing step with TSC2[§§] buffer thus eliminated all remaining non-adhered material and/or salt from the solution.
3. **Hybridization of target**. The modified IDEs with DNA probe were incubated by dropping 30 pmol of *biotinylated* complementary target oligonucleotide in TSC1 buffer solution (total volume 10 µL). It was then incubated at room temperature during 30 min. This step was followed by a gentle washing step in TSC2 buffer solution.
4. **Adhesion of AuNP for signal enhancement.** A final incubation in a PBS[***] solution containing strept-AuNPs was performed, to induce the adhesion of the np to the hybridized target DNA, for signal enhancement. Streptavidin-coated gold nanoparticles (AuNPs) were used in this work to amplify the impedimetric signal generated in a biosensor detecting the DNA hybridization event.

[‡‡] TSC1: 0.75M NaCl, 0.075M trisodium citrate, pH 7.0
[§§] TSC2: 0.30M NaCl, 0.030M trisodium citrate, pH 7.0
[***] PBS: 0.1M NaCl, 0.01M sodium phosphate buffer, pH 7.0

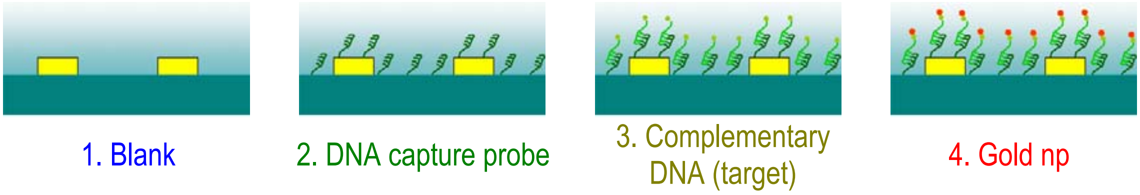

Figure 234. Steps of the procedure: starting from a clean electrode (a), the probe DNA is absorbed onto the surface, at 80º during 30 minutes (b). Then, it is incubated in a buffer solution, containing the complementary DNA, that is functionalized with biotin, and is left 30 minutes at room temperature to hybridize (c). A final incubation is done in a solution containing straptavidin-gold nanoparticles, for another 30 minutes at room temperature. The nanoparticles are bounded selectively to the target DNA.

A **negative control** essay was done in parallel, by using a non-biotinylated DNA target in the hybridization step. These electrodes were also immersed in the AuNps solution, to compare the results with the other essay.

Figure 235 shows the capacitance measurements as a function of the frequency obtained after each step of the process: blank measurement with the clean electrode (1), after the physical absorption of the ADN probe (2), after hybridization (3), and AuNp adhesion (4).

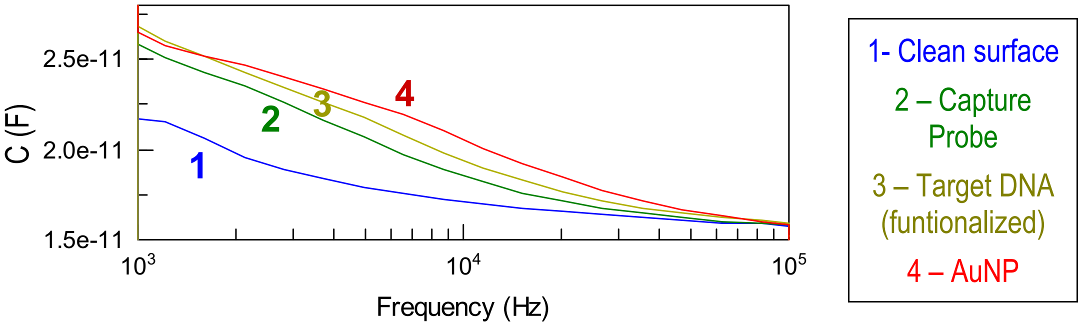

Figure 235. Spectra (capacitance vs frequency) obtained after all the incubations: blank, obtained with the clean electrode in DI water (blue line - 1); after hybridization of the probe DNA strands (green line – 2); when the target DNA is hybridized (dark yellow line – 3), and after the incubation with the gold nanoparticles (red line – 4).

The **DNA strands generally present negative charge**. So, **when they are immobilized onto the electrode surface, they increment the total measured capacitance**. Thus, after the first adsorption (of the probe), a significant increase compared to the clean surface is observed. The hybridization is also observed as another increment in C. Finally, as already described above, the AuNp are also negatively charged, which contributes again to increase the measured capacitance.

In the negative control (Figure 236), a similar tendency of the capacitance can be observed after the first adsorption and the hybridization, but no significative increment appears after the incubation with the AuNp, which means that the nanoparticles do not bind to the non-functionalized target.

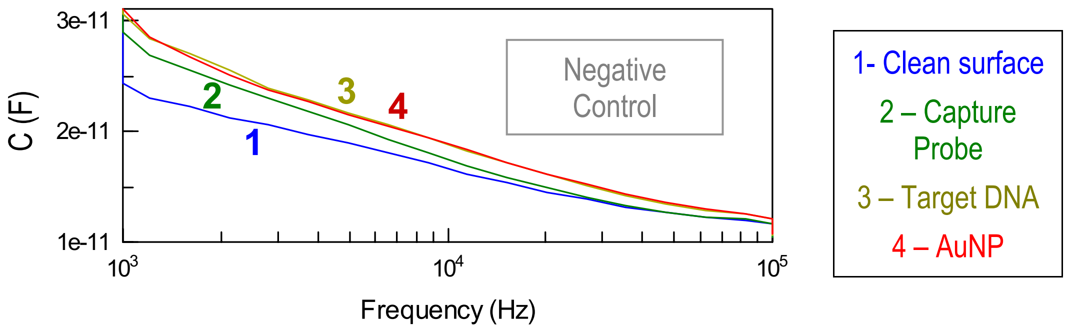

Figure 236. Spectra (capacitance vs frequency) obtained after all the incubations in the *negative control essay* (the target DNA was not functionalized with biotin): blank, obtained with the clean electrode in DI water (blue line - 1); after hybridization of the probe DNA strands (green line – 2); when the target DNA is hybridized (dark yellow line – 3), and after the incubation with the gold nanoparticles (red line – 4). No increment is observed between these last two lines.

The procedures (positive and negative control) were repeated in various different electrodes, so the results were averaged to obtain the mean value and the standard deviation.

To analyze the results, and to be able to compare the increase in the capacitance for each different electrode, the signal obtained from the clean surface was subtracted to all the others (Δsignal). Then, the corresponding increments (after the target hybridization and AuNP binding) were divided by the increment obtained when the capture probe was absorbed:

$$\Delta target_{norm} = \frac{\Delta target}{\Delta probe} \qquad (45) \qquad\qquad \Delta AuNP_{norm} = \frac{\Delta AuNP}{\Delta probe} \qquad (46)$$

The results are shown in the histogram in Figure 237. The line corresponding to a ratio of 1 (*no increment*) has been marked. It is remarkable that there is a significant increase in the signal after the hybridization (green column - 🟩), that can be directly detected. This increase is higher for the electrodes used in the negative control, as those used were more sensitive in average (the choose was arbitrary). After the incubation with the nanoparticles (red column - 🟥) the signal was highly enhanced in the positive essays, but not almost in the negative ones. This means that the nanoparticles were adhered mainly to the functionalized DNA strands (positive essays).

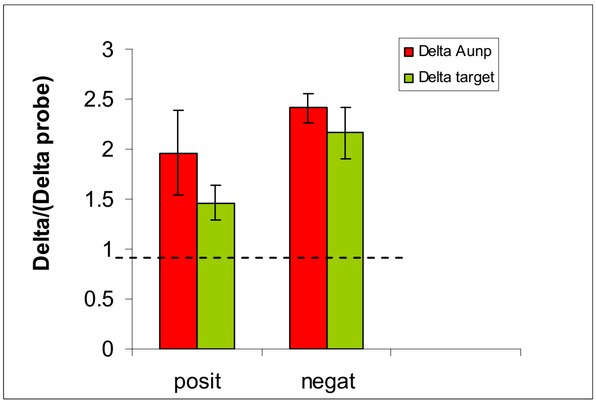

Figure 237. Histogram showing the mean values obtained for the increment of the capacitance (with respect to the water blank) after the hybridization with the target (green), and after the deposition of the nanoparticles (red), for the positive and negative controls, relative to (i.e. divided by) the signal obtained after the capture immobilization. In all the cases, a significant increment is observed, meaning that the hybridization can be successfully observed by an increase in C. In the negative control, the increment due to the nanoparticles is smaller, so no less inespecific binding of np is taking place in this case. The error bars correspond to the standard deviation.

To check the inespecific binding of the nanoparticles, the modified electrodes surface was inspected with the SEM. Figure 238 (a) shows an image of an electrode used for a positive essay and (b) for one used in the negative control.

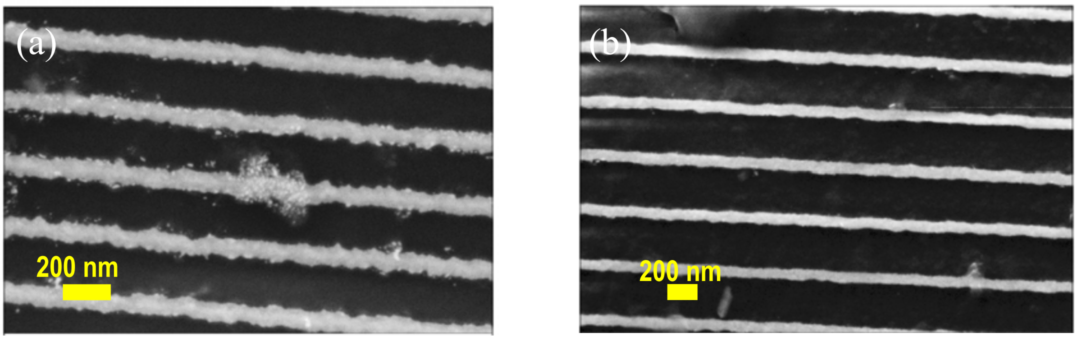

Specific binding

Negative control

Figure 238. SEM images of the electrodes, after completing all the steps of the procedure for DNA hybridization. (a) corresponds to the specific binding, so the Au nanoparticles can be seen, especially around the electrodes. (b) is an electrode used for the negative control: no nanoparticles can be seen. Thus, the increment in the signal after the last incubation can be univocally related to the specific binding of the AuNP to the target DNA.

It can be concluded that **the non-specific binding of the nanoparticles is negligible**, as could be already said from the capacitance spectra and the data analysis.

10.4-2. Mutant gene of BRCA1

A second batch of experiments was done, using different genes, that have medical interest, and a more complex sequence of steps. In this case **the presence of a mutant gene of BRCA1, that is related to breast and ovarian cancer, was the objective** of the work. The line 3061-3120 was used. In the mutant, a base is missing (T, at position 3099), compared to the non-mutant gene (*wild*). The other sequences for capturing, signaling and negative (arbitrary non-complementary) control are also shown in **Table 11**.

Table 11. Lines and gene sequences used for the experiments

Gen BRCA1 †††
Line 3061-3120. Detect the mutation 3099 of T.
CACCACTTTT TCCCATCAAG TCATTTGTTA AAACTAAATG TAAGAAAAAT CTGCTAGAGG

Wild:
5’-CACCACTTTT TCCCATCAAG TCATTTGTTA AAACTAAATG TAAGAAAAA-3’

Mutat (48-mer):
5’-CACCACTTTT TCCCATCAAG TCATTTGTTA AAACTAAAG TAAGAAAAA-3’

Capture probe:
5’-TTTTTCTTACTTTAGTTTTA-3’

Signaling probe:
5’-TGATGGGAAAAAGTGGTG-biotin-3’

No complementary (arbitrary, 48-mer):
5’- TGGGTGGAAGTGGGTGGGTGGGTGGAAGTGGGTGGGTGGGTGGAAGT-3’

---

††† http://www.ncbi.nlm.nih.gov/entrez/viewer.fcgi?val=U14680

Electrodes of the second generation (see Chapter 8) were used for this work.

The steps of the procedure are schematized in Figure 234:

a. **Absorption of the capture probe**. A first physical absorption step of a capture probe, that has a complementary sequence with the mutant gene was done. For this, a drop of 10 µL of buffer solution TSC1 containing 30 pmol of the DNA strands was deposited onto the electrodes surfaces, and left 30 minutes at 80 ºC. Afterwards, it was cleaned in a TSC2 buffer to eliminate the non-absorbed material and salt.

b. **Target hybridization.** Then, an incubation step in a solution (TSC1) containing the target DNA (30pM) was done for 20 minutes at room temperature. Depending on the target DNA of the solution (three different ones were used, as will be described next) it may hybridize to the capture probe.

c. **Signaling probe.** The sample was incubated with a similar solution containing a signaling probe, that has a sequence that hybridizes to a free part of the target strand, for another 20 minutes at room temperature. This signaling probe is functionalized with biotin.

d. **AuNp selective binding**. Finally, a last room temperature incubation in a PBS buffer containing gold-streptavidin nanoparticles was done, so the AuNP specifically adhere to the biotin.

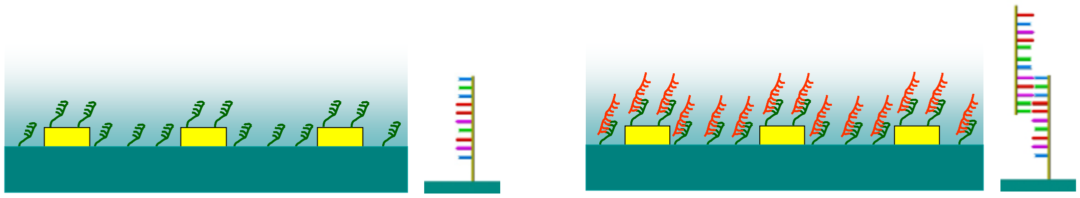

(a) Capture probe: physical adsorption (b) Mutant (target): hybridization.

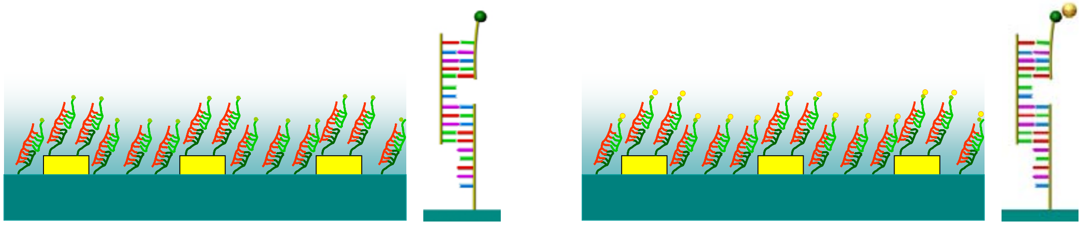

(c) Signaling probe: hybridization (d) AuNp: specific adhesion

Figure 239. Steps of the procedure: a first capture probe is absorbed onto the electrodes sample, during 30 minutes, at 80º (a). A solution containing the target DNA (mutant) is left for 30 minutes to hybridize, at room temperature (b). A signaling probe strand, with a common sequence with the mutant is incubated at room temperature, for another 30 minutes (c). These strands are functionalized with biotin. So, after the last incubation in a solution containing the gold nanoparticles (d), they specifically adhere to the signaling probe, that is hybridized to the mutant gene.

For a negative control, two different DNA sequences were used instead of the mutant probe for the incubations in step 2. The fist was the non-mutant gene (*wild*) that has one extra base (the one that is missing in the mutant) (Figure 240 (b)), and the second was an arbitrary non-complementary sequence (Figure 240 (c)).

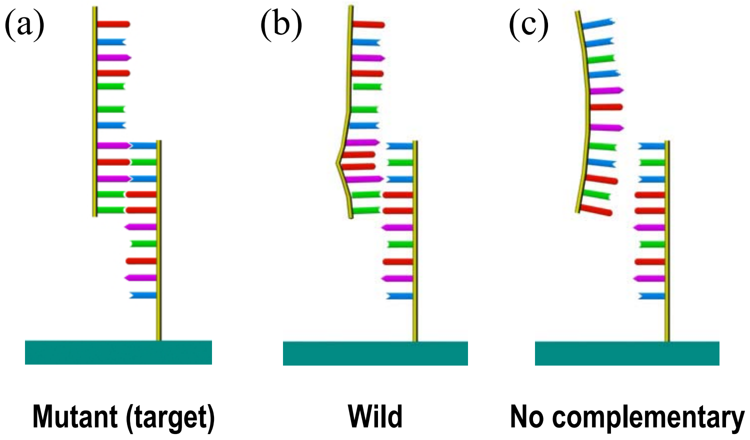

Figure 240. Scheme of the hybridization of the mutant (target) to the capture probe (a), and of the other two sequences used: the wild gene, with one extra base (b), and an arbitrary no complementary sequence.

Each experiment (positive, negative with the wild, and negative with the non-complementary) was repeated with various different electrodes, and then averaged to obtain the mean value and the standard deviation.

Figure 241 shows an histogram with the summary of the results. As already described above, the signal obtained with the clean surface is subtracted from the data obtained after the incubations (Δsignal). The columns on the left (🟩) show the increment in the capacitance after the incubation with the target (mutant, wild or non-complementary) divided by the capacitance measured after the absorption of the capture probe (47). The columns on the right (🟨) correspond to the signal measured after the incubation in the AuNP solution divided again by the capacitance after the absorption of the capture probe (48).

$$\Delta target_{norm} = \frac{\Delta target}{\Delta probe} \qquad (47) \qquad\qquad \Delta AuNP_{norm} \frac{\Delta AuNP}{\Delta probe} \qquad (48)$$

The line corresponding to no increment in the signal (delta = 1) has also been plotted.

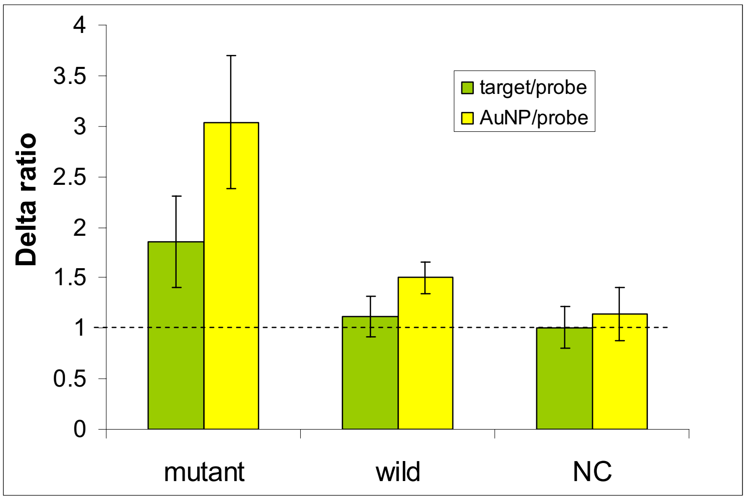

Figure 241. Histogram with the results, showing the increment in the signal after the incubation with the mutant, wild or nc (green) and after the binding of the AuNP (yellow). All the data are referred (divided) to the signal obtained after the absorption of the capture probe.

It can be clearly seen that the increment in the signal is much more significative in the mutant case. After the incubation with the gold nanoparticles, this is even more evident (2.24 in the mutant, compared to 1.46 and 1.23 for the wild and no complementary respectively).

This shows the successful detection of the complementary hybridization event with the nanoIDEs.

10.5.- REFERENCES

[1] MacDonald, J.R.,
Chapter 1,
in *Impedance Spectroscopy*, Wiley-Interscience, Editor. 1987: New York.

[2] Van Gerwen, P., Laureyn, W., Laureys, W., Huyberechts, G., De Beeck, M.O., et al.,
Nanoscaled interdigitated electrode arrays for biochemical sensors.
Sensors and Actuators B-Chemical, 1998. **49**(1-2): p. 73-80.

[3] Laureyn, W., Nelis, D., Van Gerwen, P., Baert, K., Hermans, L., et al.,
Nanoscaled interdigitated titanium electrodes for impedimetric biosensing.
Sensors and Actuators B-Chemical, 2000. **68**(1-3): p. 360-370.

[4] *Solartron Analytical, from Ametek.* www.solartronanalytical.com.

[5] Ambrosi, A., Castaneda, M.T., Killard, A.J., Smyth, M.R., Alegret, S., and Merkoci, A.,
Double-Codified Gold Nanolabels for Enhanced Immunoanalysis.
Analytical Chemistry, 2007. **79**(14): p. 5232-5240.

[6] Cattrall, R.W.,
Chemical Sensors. Vol. 52. 1997: Oxford Chemistry Primers.

[7] Mikkelsen, S.R.,
Electrochemical Biosensors for DNA Sequence Detection.
Electroanalysis, 1996. **8**(1): p. 15-19.

[8] Katz, E. and Willner, I.,
Probing biomolecular interactions at conductive and semiconductive surfaces by impedance spectroscopy: Routes to impedimetric immunosensors, DNA-sensors, and enzyme biosensors.
Electroanalysis, 2003. **15**(11): p. 913-947.

[9] Huang, H., Liu, Z. and Yang, X.,
Application of electrochemical impedance spectroscopy for monitoring allergen-antibody reactions using gold nanoparticle-based biomolecular immobilization method.
Analytical biochemistry, 2006. **356**(2): p. 208-214.

[10] Tlili, C., Korri-Youssoufi, H., Ponsonnet, L., Martelet, C. and Jaffrezic-Renault, N.J.,
Electrochemical impedance probing of DNA hybridisation on oligonucleotide-functionalised polypyrrole.
Talanta, 2005. **68**(1): p. 131-137.

[11] Bonanni, A., Esplandiu, M.J. and Valle, M.d.,
Signal amplification for impedimetric genosensing using gold-streptavidin nanoparticles.
Electrochimica Acta, 2008. **53**: p. 4022 - 4029.

Conclusions
&
List of publications

Conclusions

The work performed during the PhD has contributed in different ways to the development of Nanoimprint Lithography and its applications in different areas, like material sciences, plasmonics and biosensing.

It should be pointed out that the complete NIL technology was developed: stamps fabrication, functionalization with an antiadhesive layer, imprinting process, residual layer removal and corresponding post-processing (e.g. metallization and lift-off or replication in a different material).

Finally, to summarize in few lines the most important achievements of this work, it could be said that:

I. Nanoimprint technology was successfully started up, studied and optimized at IMB-CNM. AFM local anodic oxidation was originally proposed and studied as a fast method for the fabrication of stamps. Rheological studies allowed to quantify and visualize the residual stress that appears in the polymers after NIL process. The functionalization step was conveniently improved and adapted for the local modification of surfaces with other types of silanes. The homogeneity of the residual layer was studied for different conditions.

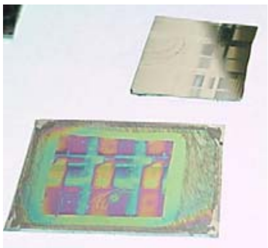

Stamp & Imprint

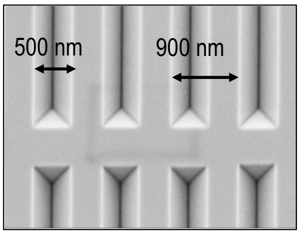

Stamp image

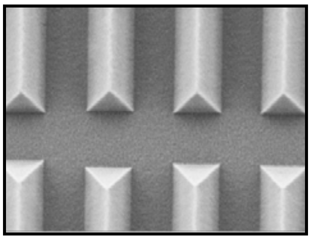

Imprint image

II. A fabrication process based on NIL was developed for the fabrication of integrated devices, based on **metallic V-groove waveguides**, to squeeze light in sub-micrometric channels. Optical characterizations (near field and far field) showed that it was possible to confine and guide light in the imprinted V-grooves. Fluorescent nanoparticles were introduced into the channels for characterizations, and as a first step for their use in sensing applications.

Device

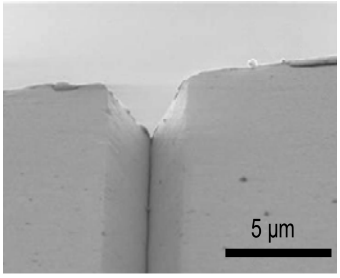

V-groove

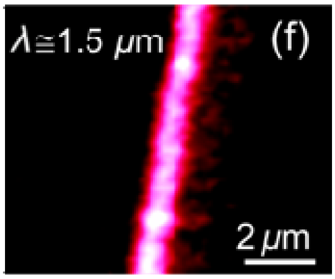

Performance

III. A technology was developed for the fabrication of interdigitated arrays of gold **interdigitated nanoelectrodes**, ranging from the lithographic process (e-beam, most commonly) to the encapsulation of the devices, to facilitate the connection to external equipments and handling and characterization in liquid media. Electrochemical measurements and impedance spectroscopy characterizations showed the good performance of the devices. The improved sensitivity compared to micrometric devices was shown. Two applications were proposed and successfully developed: the detection and quantification of nanoparticles of different types (insulating and conductive), and the specific detection of DNA hybridization.

Device

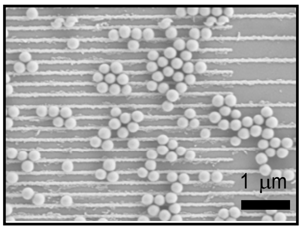

Image of the nanometric electrodes

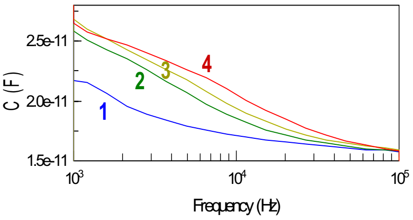

Performance

List of publications

[1] R.B. Nielsen, I. Fernandez-Cuesta, A. Boltasseva, V.S. Volkov, S.I. Bozhevolnyi, A. Klukowska, and A. Kristensen.
Channel Plasmon Polariton Propagation in Nanoimprinted V-Groove Waveguides
Optics Letters, 33(23): p. 2800-2802 (2008)

[2] R.B. Nielsen, A. Boltasseva, A. Kristensen, S.I. Bozhevolnyi, V.S. Volkov, I.F. Cuesta, and A. Klukowska.
Fabrication of plasmonic waveguides by nanoimprint and UV-lithography
art. no. 688304, in Advanced Fabrication Technologies for Micro/Nano Optics and Photonics. SPIE-INT SOC OPTICAL ENGINEERING: Bellingham. p. 88304-88304 (2008)

[3] I. Fernandez-Cuesta, X. Borrise, A. Retolaza, S. Merino, D.A. Mendels, O. Hansen, A. Kristensen, and F. Perez-Murano.
Determination of stress build-up during nanoimprint process in triangular Polymer structures
Microelectronic Engineering, 85(5-6): p. 838 (2008)

[4] D.A. Mendels, I. Fernandez-Cuesta, X. Borrise, A. Retolaza, S. Merino, O. Hansen, A. Kristensen, and F. Perez-Murano.
A finite element mesh tailored to full NIL process modelling: hot embossing, cool-down and stamp release
Microprocesses and Nanotechnology, Digest of Papers. 2007, JAPAN SOCIETY APPLIED PHYSICS: Tokyo. p. 278-279 (2007)

[5] C. Gourgon, N. Chaix, H. Schift, M. Tormen, S. Landis, C.M.S. Torres, A. Kristensen, R.H. Pedersen, M.B. Christiansen, I. Fernandez-Cuesta, D. Mendels, L. Montelius, and T. Haatainen.
Benchmarking of 50 nm features in thermal nanoimprint
Journal of Vacuum Science & Technology B, 25(6): p. 2373 (2007)

[6] I. Fernandez-Cuesta, R.B. Nielsen, A. Boltasseva, X. Borrise, F. Perez-Murano, and A. Kristensen.
V-groove plasmonic waveguides fabricated by nanoimprint lithography
Journal of Vacuum Science & Technology B, 25(6): p. 2649 (2007)

[7] A. Boltasseva, K. Leosson, T. Rosenzveig, R.B. Nielsen, R.H. Pedersen, K.B. Jorgensen, I. Fernandez-Cuesta, J. Jung, T. Sondergaard, S.I. Bozhevolnyi, and A. Kristensen.
Fabrication of plasmonic waveguides for device applications
art. no. 663804, in Photonic Metamaterials, SPIE-INT SOC OPTICAL ENGINEERING: Bellingham. p. 63804-63804 (2007)

[8] I. Fernandez-Cuesta, X. Borrise and F. Perez-Murano.
Atomic force microscopy local anodic oxidation of thin Si3N4 ayers for robust prototyping of nanostructures.
Journal of Vacuum Science & Technology B, 24(6): p. 2988 (2006)

[9] I. Fernandez-Cuesta, X. Borrise and F. Perez-Murano.
Atomic force microscopy local oxidation of silicon nitride thin films for mask fabrication
Nanotechnology,. 16(11): p. 2731 (2005)

In preparation:

[10] A. Bonanni, I. Fernandez-Cuesta, X. Borrise, F. Perez-Murano and M. Del Valle.
Detection of DNA hybridization with interdigitated arrays of nanoelectrodes

[11] I. Fernandez-Cuesta, R. B. Nielsen, A. Boltasseva, X. Borrise, F. Perez-Murano, and A. Kristensen.
Excitation of fluorescent nanoparticles by plasmons confined and propagating in V-grooves

[12] I. Fernandez-Cuesta, C. Fernandez-Sanchez, A. Baldi, X. Borrise and F. Perez-Murano
Interdigitated nanoelectrodes: fabrication and nanoparticle detection